Development of an all-fibre source of heralded single photons

Mcmillan, Alex

Award date:
2012

Awarding institution:
University of Bath

DEVELOPMENT OF AN ALL-FIBRE SOURCE OF HERALDED SINGLE PHOTONS

Alex Robert McMillan

A thesis submitted for the degree of Doctor of Philosophy

University of Bath
Department of Physics

September 2011

Abstract

The preparation of single photons in a pure quantum state is a subject of great interest in physics, enabling the control of light at an unprecedented level. The ease with which certain degrees of freedom of photon states, such as polarisation, can be manipulated, along with the inherent resilience of photons to decoherence, makes them well suited for use as qubits. Recent rapid developments in the transmission and processing of quantum information, as well as the likely technological impact of potential real-world applications such as quantum cryptography and quantum computation, mean that the demand for high performance single photon sources is likely to increase in the near future.

One approach to producing single photon states, which are known to be in a well-defined spatio-temporal mode without destructively measuring them, is to take advantage of nonlinear optics. Nonlinear processes can be used to realise frequency conversion by generating a single, correlated pair of photons from an intense pump laser source. The detection of one of the photons from a pair can then be used to indicate the presence of the other photon in the pair, a procedure known as heralding.

This thesis describes the development of a source of heralded single photons at 1550 nm, generated directly in the core of a photonic crystal fibre (PCF). By taking advantage of low loss fibre components for the required spectral filtering of the generated photon state, a heralding fidelity of 52% was achieved. The source was designed to be used with a picosecond pulsed fibre laser, making it relatively low cost and maintenance free. With 148 mW of average pump power a heralded output photon rate of 6.4×10^4 s^{-1} was observed, demonstrating the brightness of the source. The purity of the generated single photons was established by measuring non-classical interference, with a visibility of 70%, between the photons output from this source and a source based on a PPLN waveguide. The fabrication of a series of birefringent PCFs for the generation of spectrally pure state photons at 1550 nm is also discussed. These PCFs will be useful for incorporation in the next generation of high performance, fibre-based photon sources.

Acknowledgements

First and foremost I would like to thank my supervisor Dr. William Wadsworth, not only for giving me the opportunity to take part in this project but for always taking the time to assist me whenever I needed guidance. I have very much enjoyed my time spent studying at Bath for my PhD, and I think it is fair to say that I know considerably more about fibres, nonlinear optics and single photons than I did when I started.

I would also like to thank all of the other staff and students within the CPPM who I have had the opportunity to work with over the years. I would especially like to thank Chunle Xiong, Martina Delgado-Pinar, Laure Lavoute and Peter Mosley, all of whom have provided support on some aspect of this project.

In addition to everyone at Bath I am very grateful to Professor John Rarity and his group, past and present at the University of Bristol, including Jérémie Fulconis, Matthaeus Halder, Alex Clark and Bryn Bell, as well as Laurent Labonté and colleagues from the University of Nice, for their support and the opportunity to spend some time away from Bath as part of our collaborative project.

Finally, I would like to thank all of my friends, especially Leigh-Anne Thomas (it wouldn't have been the same without you dude!) and of course my family, especially my mum and dad for all of their support over the years.

Contents

List of Figures and Tables

List of Abbreviations

BBO	Beta-barium borate
CAR	Coincidence-to-accidentals ratio
CCD	Charge-coupled device
c-NOT	Controlled-NOT
CW	Continuous wave
ESM	Endlessly single mode
FBG	Fibre Bragg grating
FPGA	Field-programmable gate array
FWHM	Full-width half-maximum
FWM	Four-wave mixing
HOM	Hong-Ou-Mandel
ID	Inner diameter
InGaAs	Indium Gallium Arsenide
JSA	Joint spectral amplitude
KDP	Potassium dihydrogen phosphate
LBO	Lithium triborate
LED	Light-emitting diode
LP	Linearly polarised modes
LWP	Long-wave pass
MCVD	Modified chemical vapour deposition
MFD	Mode field diameter
NA	Numerical aperture
OD	Outer diameter
OSA	Optical spectrum analyser
PBS	Polarising beam-splitter

PCF	Photonic crystal fibre
PDC	Parametric down-conversion
PPLN	Periodically poled lithium niobate
PRF	Pulse repetition frequency
QI	Quantum information
QIP	Quantum information processing
QPM	Quasi-phase-matching
SEM	Scanning electron microscope
SHG	Second-harmonic generation
Si	Silicon
SLED	Superluminescent light-emitting diode
SMF	Single mode fibre
SPAD	Single photon avalanche diode detector
SPM	Self-phase modulation
SWP	Short-wave pass
TIR	Total internal reflection
WDM	Wavelength division multiplexer
XPM	Cross-phase modulation
ZDW	Zero dispersion wavelength

Chapter 1

Introduction

The study and control of the properties of light has long been a major goal in science. Early experiments into classical interferometry, as well as studies of the polarisation properties of light, provided seemingly incontrovertible evidence that light is a type of wave. However, the subsequent discovery of the photoelectric effect [1] and the proposed quantisation of the electromagnetic field in order to explain the observed spectral profile of blackbody radiation [2], both implied that at a fundamental level a light field is composed of discrete, particle-like packets of energy, known as photons. Along with further developments in the theory of quantum mechanics, the concept of photons proved to be of great use in understanding the way in which light and matter interact. However, due to the probabilistic nature by which photons are emitted from ensembles of atoms it was, at that time, not experimentally possible to produce a single isolated photon, as measuring such a state to determine its presence would necessarily result in its destruction.

While at first seemingly unrelated to the topic of single photon generation (and considered a solution looking for a problem at the time of its development), the initial demonstration of lasing in 1960 [3] was a significant moment in the story of the control of light. For the first time light could be prepared in a high power, low divergence beam with high coherence and narrow spectral bandwidth. Among other applications, this opened up the nascent field of nonlinear optics to experimentation for the first time. Nonlinear effects can occur when the light propagating in a material is so intense that the motion of the bound electrons in

response to the driving electric field is no longer linear due to the shape of the atomic binding potential. This electron motion sets up a time-varying polarisation response in the material, leading to the generation of light at new frequencies, first observed in 1961 for the case of second-harmonic generation [4].

Another major innovation that impacted on nonlinear optics, was the development of modern, clad optical fibres in the 1950s, capable of guiding light along a narrow core by total internal reflection [5]. Today optical fibres are most commonly associated with telecommunications applications, due to their remarkably low loss. However they can also be an efficient medium for nonlinear interaction, with the low inherent nonlinear coefficient of silica being compensated by the long interaction length that is achieved by tight confinement of laser light along its entire length of propagation. Experimental observations confirmed a variety of interesting nonlinear interactions could be realised within a guided mode of the fibre core, including degenerate four-wave mixing, in which intense pump light can generate a pair of correlated sidebands, symmetrically spaced in frequency about the pump, known as the signal and idler [6].

Due to the simplistic structure of standard telecommunications fibres, the parameters important to the nonlinear interaction, particularly the chromatic dispersion profile for light at different wavelengths, are largely fixed by the inherent properties of silica. This gives a limited scope for control over the wavelengths of light that can be generated by nonlinear processes. The development of the photonic crystal fibre (PCF) in 1996 enabled fibres with a much wider range of properties to be realised [7]. For PCF a fibre can be formed from pure silica, with the required lower index cladding implemented using a periodic array of air holes running along the fibre length. As the dispersion properties of a PCF are strongly affected by its cladding structure, nonlinear generation of photons with desired properties can be achieved with an appropriate choice of pump laser and fibre geometry.

Although the output intensity of a laser can be extremely stable, the constituent photons will be randomly distributed throughout the beam. This means photons will be output at random times with no way to tell when a single photon has been produced. Generation of photons by nonlinear processes such as four-wave mixing will similarly produce photons at random times, so this may seem to be no better suited to preparing single photon states. However, conservation of energy ensures that photons at the signal and idler wavelengths must always be produced together as a correlated pair. By detecting one of them, the presence of the

other can be inferred, providing a single photon state of known properties, localised in time. The use of waveguides, such as optical fibre, as a generation medium gives the significant benefit that such a state is also guaranteed to be spatially localised in a propagating mode of the structure.

In recent years, single photon sources have proven to be a valuable resource in the rapidly developing field of quantum information, both for fundamental tests of quantum mechanics and as non-classical light sources to enable investigation of a range of applications, such as quantum cryptography [8], metrology [9] and quantum computation [10]. Experiments in these areas are often limited by the available brightness (output rate of photons) of current photon sources. These applications all have the potential to be of great technological importance in the future, highlighting the need for further development of high performance single photon sources.

This thesis describes the development and characterisation of a source of heralded single photons at 1550 nm, based on four-wave mixing in a PCF. The theoretical background to this project is first discussed in Chapters 2 and 3. Chapter 2 focuses on the basic properties of light guidance in optical fibres, before dealing with the subject of nonlinear optics. Chapter 3 presents theory related to single photon states and non-classical Hong-Ou-Mandel interference. The theory of four-wave mixing in the single photon regime is also described, including details on how purity of the generated single photon state can be achieved. This chapter also summarises previously demonstrated photon sources and some of the potential applications for these sources. Chapter 4 describes preliminary work on the fabrication of a PCF-based single photon source, with separation and spectral filtering of the correlated photon pairs realised with free-space optics. In Chapter 5 this work is extended to incorporate narrowband filtering into the source, leading to an all-fibre source of pure state single photons. Chapter 6 describes an experiment in which this all-fibre source was used to demonstrate Hong-Ou-Mandel interference between photons from the source based on PCF with those from a source based on periodically poled lithium niobate for the first time. Chapter 7 describes the design, fabrication and evaluation of birefringent PCF suitable for generating narrowband idler photons at 1550 nm by cross-polarised four-wave mixing, which will be of use for the future development of the fibre-based photon source. Finally, this thesis is concluded in Chapter 8, with a summary of the important experimental results achieved, and a discussion of plans for possible future work.

Chapter 2

Photonic Crystal Fibre and Nonlinear Optics

For the purposes of producing a source of single photons, optical fibres are an invaluable component. Their waveguiding nature enables a light beam to remain tightly confined to the fibre core over great distances, allowing even the smallest levels of light, single photons, to be reliably transmitted to where they are required with high efficiency. With the advent of high power lasers allowing access to a new regime of nonlinear optics, fibres demonstrated their uses not just as passive carriers of light but as a medium in which light at one frequency could lead to the generation of light at new frequencies, defined by the fibre properties. This allows photon sources to take advantage of this remarkable structure right from the point of photon generation to their delivery.

This chapter describes the principles of light propagation in optical fibres, first for conventional fibres and then for the more recently developed photonic crystal fibre that allows far more control over the fibre properties than can be achieved with the standard design. Important properties relating to the propagation of classical pulses in the linear regime including fibre modes, optical losses and dispersion are discussed in Section 2.1. After this, Section 2.2 deals with important nonlinear effects that manifest when dealing with the propagation of high intensity laser pulses. In particular, the effect of four-wave mixing will be considered in detail, as it is the mechanism by which photons are generated in the fibre-based heralded single photon devices described in later chapters. The manufacturing process for optical fibre is outlined in Section 2.3. This chapter concludes with a short discussion of joining fibres by low loss fusion splicing in Section 2.4.

2.1 Light Propagation in Optical Fibres

This section describes some of the basic properties of light propagation in optical fibres. Knowledge of the linear guidance properties of fibres is essential to understand the nonlinear effects that are discussed in Section 2.2.

2.1.1 Light Guidance Mechanism in Conventional Fibre

An optical fibre is a type of waveguide designed to confine light to a narrow core region so that it can easily be transferred over large distances with minimal levels of loss. Early work, showed that narrow silica strands in air were capable of guiding light along their length through total internal reflection at the air-glass interface, a property that was already well known from the similar effect that can be observed using jets of water [11]. Later work showed that the properties of fibres could be improved by taking advantage of a cladding layer [5]. Most conventional optical fibres still rely on this straightforward geometry.

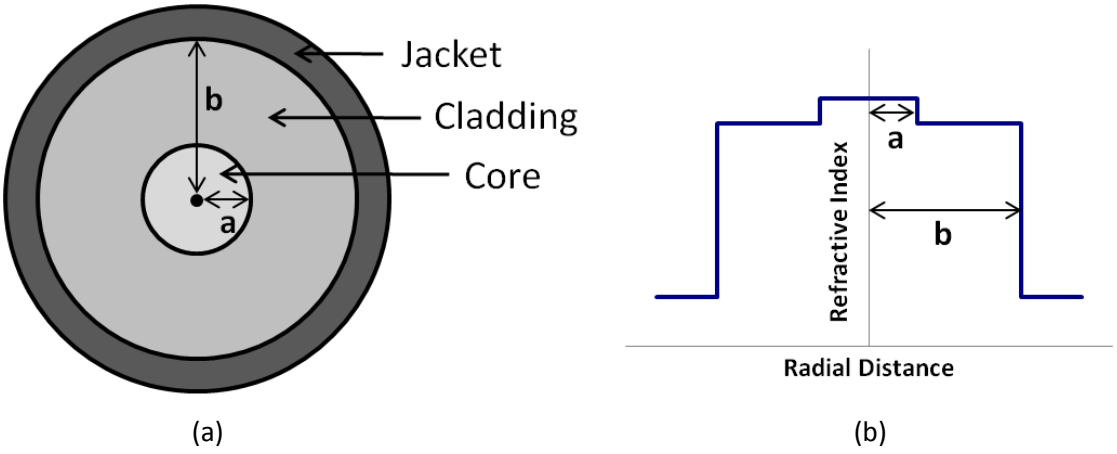

Figure 2.1: (a) Schematic representation of a conventional step-index fibre. The core size in this case would correspond to a multimode fibre; (b) Refractive index profile of the step-index fibre.

The structure of a standard step-index fibre can be seen in Fig. 2.1. Such a fibre consists of a narrow circular region, known as the core, surrounded by a material of slightly lower refractive index, the cladding. Due to its excellent optical and mechanical properties, fused silica is generally the preferred material for use in both the core and cladding, with a low level of chemical dopant added to either the cladding or core region to provide the required index profile. Fibres typically also include a polymer jacketing layer to improve their mechanical strength. Due to the rapid exponential decay in the field strength of guided light with

increasing distance from the core, the presence of this jacketing layer should not influence the optical properties of the fibre.

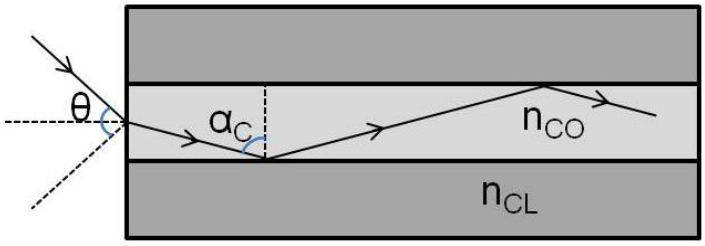

Figure 2.2: Schematic representation of ray propagation in a large core multimode step-index fibre. n_{CO} and n_{CL} are the refractive indices of the core and cladding materials respectively.

A simple intuitive understanding of the principle of index guidance in a step-index fibre can be gained using a ray optics model. Consider a monochromatic light ray directed onto the end face of a fibre at an angle θ as shown in Fig. 2.2. Some of the light will be immediately lost by the Fresnel reflection from the air-glass interface. The remaining light will be launched into the core and propagate for some distance before encountering the core-cladding interface. If the angle between the ray and the normal to the interface α exceeds the critical angle α_C then total internal reflection (TIR) will occur and the light will remain confined to the fibre core. The critical angle is defined by

$$\alpha_C = \sin^{-1}\frac{n_{CL}}{n_{CO}}, \tag{2.1}$$

where n_{CL} and n_{CO} are the refractive indices of the cladding and core respectively. As long as the initial launch angle θ of the light is close enough to the fibre axis to allow TIR, light can propagate along the entire length of the core in this manner. Two rays launched at different angles θ_1 and θ_2 will propagate through the fibre with different effective velocities due to the unequal path length for the two beams as they travel along the fibre. While the ray model gives a simple qualitative understanding of the guidance, it fails to account for effects that become important when the size of the core is comparable to the wavelength of the guided light.

In order to understand how the wave nature of light influences the guidance properties of the fibre it is necessary to solve Maxwell's equations for this step-index fibre geometry.

For a dielectric non-magnetic medium such as silica

$$\nabla \times \mathbf{E} = -\frac{\partial}{\partial t}(\mu_0 \mathbf{H}), \tag{2.2}$$

and

$$\nabla \times \mathbf{H} = \frac{\partial}{\partial t}(\varepsilon_0 \mathbf{E} + \mathbf{P}), \tag{2.3}$$

where $\mathbf{E}$ and $\mathbf{H}$ are the electric and magnetic field vectors, ε_0 and μ_0 are the permittivity and permeability of free space and $\mathbf{P}$ is the induced electric polarisation of the material. These equations can be combined and further simplified by ignoring the effects of loss, and (for now) considering only the linear term in the polarisation $\mathbf{P}$. Both are valid since the optical fibre will be used in a wavelength range that is far from any resonances of the material. The resulting equation for the electric field distribution (expressed in the frequency domain) is given by

$$\nabla^2 \tilde{\mathbf{E}}(\mathbf{r}, \omega) + n^2(\omega)\frac{\omega^2}{c^2}\tilde{\mathbf{E}}(\mathbf{r}, \omega) = 0, \tag{2.4}$$

where ω is the angular frequency of the light wave, $n(\omega)$ is the frequency dependent refractive index of the medium, $\tilde{\mathbf{E}}(\mathbf{r}, \omega)$ is the Fourier transform of the electric field vector $\mathbf{E} = \mathbf{E}(\mathbf{r}, t)$ and c is the speed of light in a vacuum.

After expressing Eq. (2.4) in cylindrical polar coordinates (ρ, ϕ and z) it can be solved by a separation of variables [12] to find the general solution for the z-component of the electric field, which is given by

$$\tilde{E}_z = A(\omega)F(\rho)\exp(im\phi)\exp(i\beta z), \tag{2.5}$$

where $F(\rho)$ is the solution of the differential equation for Bessel functions:

$$\frac{d^2F}{d\rho^2} + \frac{1}{\rho}\frac{dF}{d\rho} + (n^2k_0^2 - \beta^2 - \frac{m^2}{\rho^2})F = 0, \tag{2.6}$$

where $k_0 = \omega/c$ is the free-space wavenumber, m is an integer and β is the propagation constant. Appropriate boundary conditions are then applied to Eq. (2.6). These are that the refractive index profile is as shown in Fig. 2.1, that the electric field is finite at all points, and

that the electric field strength should decay to zero far from the fibre (as the light should be guided). Each value of the integer m gives several potential values for the propagation constant, β_{mn}. Each of these solutions represents a potential guided mode that is supported by the structure. The meaning of this is apparent from Eq. (2.5), the transverse spatial profile of light launched into a single mode of the fibre will be constant as it propagates, apart from a phase shift given by the factor $\exp(i\beta z)$. The shape of the modes is defined by the solution to Eq. (2.6), which are Bessel functions. Comparing the role of β here to the simple ray optics case that was considered previously, it is apparent that the propagation constant is analogous to the component of the wavevector k in the direction of propagation. This allows an effective index of the mode, n_{eff}, to be defined according to

$$\beta(\omega) = n_{eff}(\omega)\frac{\omega}{c}, \tag{2.7}$$

where n_{eff} is dependent on the angular frequency of the wave ω. For each potential value of β_{mn} the corresponding mode is designated HE_{mn} (similarly EH_{mn} modes can also be found by considering solutions for the z-component of the magnetic field $\tilde{H}_z$). For modes to be guided by the structure, the propagation constant β must lie within the range [13]

$$n_{CL}k_0 \leq \beta \leq n_{CO}k_0, \tag{2.8}$$

It is common to express the modes of the waveguide instead in terms of linearly polarised modes (LP modes) that can be found from a superposition of the HE and EH modes [14]. These modes can also be obtained directly from the wave equation (Eq. (2.4)) in the case of weakly guiding fibres [15]. The fundamental LP_{01} mode and some of the higher-order modes for a step-index fibre are shown in Fig. 2.3.

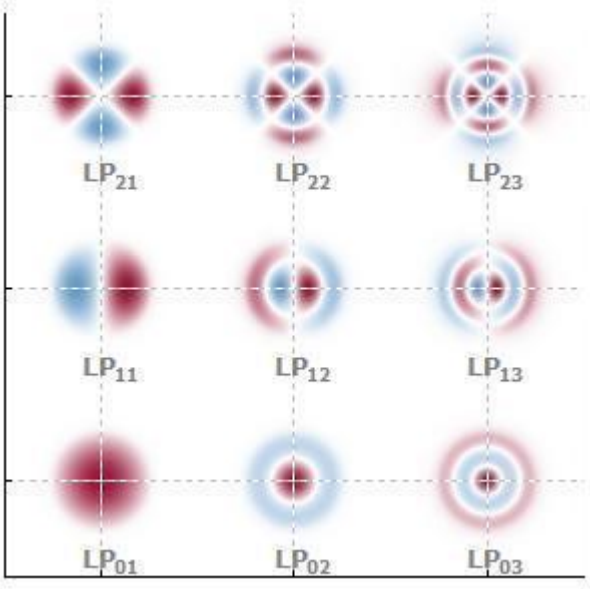

Figure 2.3: Spatial profile of some of the linearly polarised (LP) modes for a step-index fibre. The red and blue areas represent regions of opposite phase where the electric field has high magnitude. (Image from [16]).

An important parameter of fibres is the refractive index contrast between the core and cladding. One of the reasons for this is that it defines the numerical aperture (NA) of the fibre which gives the maximum input angle θ_{max} over which the fibre will accept light according to

$$\mathrm{NA} = \sin\theta_{\max} = \sqrt{n_{CO}^2 - n_{CL}^2}\ . \tag{2.9}$$

For standard fibres the index contrast is limited to a narrow range because the high levels of dopant required to achieve a significant index mismatch also result in high levels of loss and a fibre with poor mechanical properties [17]. Another important parameter is the normalised frequency V, which defines how many modes will be guided by the structure at a specific wavelength. For a given index contrast, V can be defined as

$$\mathrm{V} = k_0 a\sqrt{(n_{CO}^2 - n_{CL}^2)}\ , \tag{2.10}$$

for a wavelength of light λ, where k_0 = 2π/λ and a is the fibre core radius. As the V value is reduced, such as by considering fibres with smaller cores or by working at longer wavelengths, the effective mode index for all the fibre modes is reduced. When the effective index for a mode falls below the cladding index that mode ceases to be guided and is 'cut-off'. It can be shown [18] that for V < 2.405 only the fundamental mode of the fibre is guided, and all higher order modes become cut-off (the fibre will always support the fundamental mode). Under

these conditions the fibre is described as single-mode. For a given structure it is therefore always possible to define the cut-off wavelength beyond which the fibre exhibits single-mode behaviour. For shorter wavelengths the fibre will be multimode.

Single-mode operation is desirable for a number of reasons. It is generally difficult to couple light into only a single mode of a multimode waveguide, and since different modes have different propagation constants, an initially well defined pulse that is launched into multiple modes will broaden as it propagates. Also, the spatial profile of the light in a multimode waveguide will be complex in shape, being given by a superposition of the excited modes, and will vary along the waveguide, making coupling of this light into other fibres difficult. Finally, the nonlinear process described in Section 2.2.3 can only be designed to operate efficiently at the desired wavelengths for one individual mode, meaning that power in other modes of the fibre is wasted. Likewise, fibre components such as Bragg gratings are only designed to operate for a single-mode input.

In addition to the mode field shape, it is useful to consider to what extent the electric field of the light is confined to the core of the fibre. For the case of the fundamental mode, the electric field distribution is entirely determined by the variation in the term $F(\rho)$ in Eq. (2.5), and follows the shape of the first Bessel function J_0 inside the core. Outside the core the Bessel function shape is combined with an exponential decay that dominates the mode field profile far from the core. This can be approximated with quite high accuracy as a Gaussian profile, so that in Cartesian coordinates

$$F(x, y) \approx \exp[-(x^2 + y^2) / w^2], \tag{2.11}$$

where w is the $1/e^2$ width of the Gaussian profile for the fundamental mode. Fig. 2.4 shows the calculated variation in w for different values of the normalised frequency V.

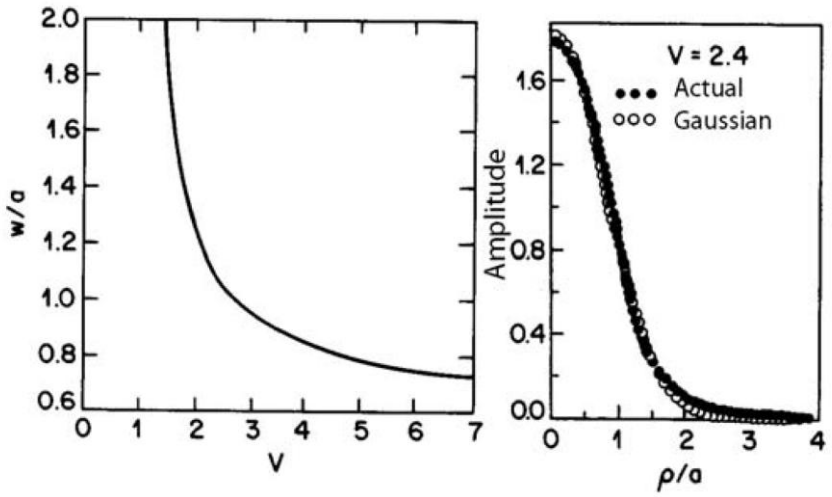

(a) (b)

Figure 2.4: (a) Width of the fundamental mode as a function of the V-value, assuming a Gaussian mode distribution; (b) Comparison between the Gaussian approximation and the actual mode field profile. (Images from [12]).

As shown in Fig. 2.4, for wavelengths below the second mode cut-off the mode field of the light expands and a significant proportion of the light propagates outside the core. This leads to an increase in the susceptibility of the fibre to bend loss which explains why the loss for single-mode fibres increases dramatically when operated far from the cut-off wavelength (and hence why they can only be designed to have ideal low loss in a narrow wavelength range). The consideration of the mode field diameter is also important when considering guidance in photonic crystal fibres (Section 2.1.2) and the dispersion properties of fibres (Section 2.1.6). The width of the mode is also relevant for nonlinear processes (Section 2.2) where the strength of the interaction is dependent on the intensity of light, and therefore its cross-sectional effective area during propagation A_{eff}, where

$$A_{eff} = \pi w^2 . \tag{2.12}$$

For fibres with a more complex core shape, the mode field profile for the fundamental mode will differ from the Gaussian profile seen in a circularly symmetric structure. For these types of fibres the distribution of optical power in the core (and hence the effective mode area) cannot be described by the simple formula shown in Eq. (2.12). In this case the effective mode area can be found through integration of the of the mode field distribution $F(x,y)$ and is defined to be [12]

$$A_{eff} = \frac{\left(\int\int_{-\infty}^{\infty} |F(x,y)|^2 \, dxdy \right)^2}{\int\int_{-\infty}^{\infty} |F(x,y)|^4 \, dxdy}. \tag{2.13}$$

2.1.2 Guidance Mechanisms in Photonic Crystal Fibre

In 1996 a new type of optical fibre was developed, the photonic crystal fibre [7]. Unlike conventional fibres with cladding and core regions formed by two different materials (typically silica with different dopant levels), in a photonic crystal fibre (PCF) the cladding region is formed from an array of air holes in the glass that run along the fibre length. For this reason PCF is sometimes referred to as 'holey' or 'microstructured' fibre in the literature.

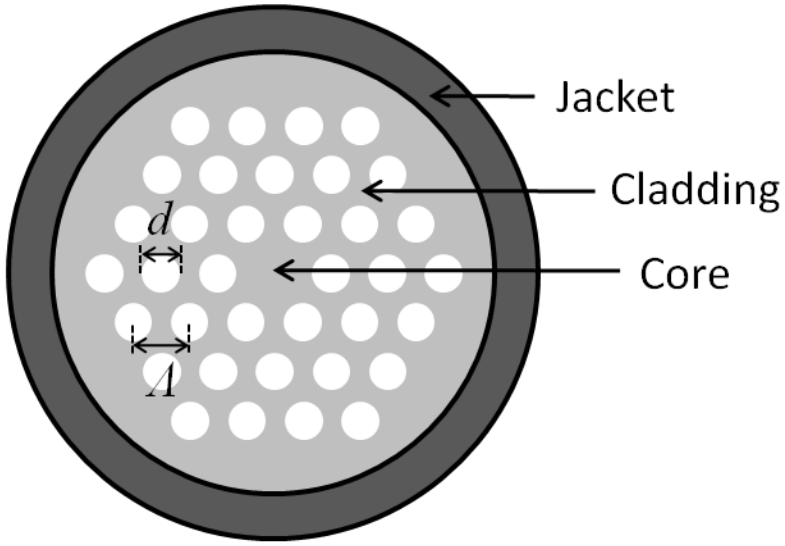

Figure 2.5: Schematic representation of a PCF structure. In real fibres the scale of the holey cladding would typically be smaller relative to the overall diameter of the fibre. The cladding hole diameter d and the pitch Λ are shown.

When light propagates in the core of a PCF structure, such as that shown in Fig. 2.5, part of the field will extend into the cladding region. The effective index experienced by light in the cladding region is an average of the air and silica regions, and consequently lower than the solid silica core. Light can therefore be guided by total internal reflection in such a structure following a similar theory to that developed for conventional fibre in Section 2.1.1. However, in contrast to conventional fibres, where the requirements for low loss single mode guidance fix the values of the physical parameters of the fibre, for PCF there is far more scope for engineering the fibre properties through the geometry of the cladding. In particular, the possibility of producing cladding with a high air filling fraction allows for a strong contrast between the cladding and core indices that cannot be achieved in conventional fibre. As discussed in Section 2.1.6, this leads to a significant waveguide contribution to the fibre dispersion that can be that can be tailored to a required dispersion profile, unlike the material dispersion contribution that dominates in conventional fibre.

For some PCFs the guidance of light is instead due to the existence of a photonic bandgap. In this case the periodic structure of the cladding leads to spectral regions where light of a given frequency is unable to propagate for a range of values of the propagation constant β, meaning it cannot propagate in the cladding region [19]. By introducing a defect into the periodic cladding, forming the core, light can be forced to propagate along the core as it is unable to enter the cladding region. This type of guidance can exist in all-solid fibres [20], although it is most applicable to hollow-core designs [21] which cannot be achieved through index guiding. All the fibres described in this thesis are index guiding so this guidance mechanism is not discussed further.

2.1.3 Endlessly Single-Mode Guidance

As discussed in Section 2.1.1, standard single-mode fibres only exhibit single-mode guidance for light above a particular cut-off wavelength. For PCF it is possible to design the structure such that it exhibits single-mode guidance at all possible wavelengths. Such a fibre is described as being endlessly single-mode (ESM). This property can be understood by considering how the V-value, described in Eq. (2.10) varies with wavelength for PCFs with different ratios of the cladding hole diameter to the pitch d/Λ [22]. In conventional fibres, as the wavelength of the light is reduced the V-value increases, tending to infinity, and eventually exceeds the critical value for single-mode guidance. In PCF, as the wavelength is

reduced the light in the cladding becomes increasingly confined to the silica regions [23]. The result is that the effective index experienced by light in the cladding region increases, reducing the core-cladding index contrast which acts to lower V. In contrast to conventional fibres, the V value for PCF tends towards a finite value as the $\lambda \rightarrow 0$, with the value determined by the d/Λ parameter of the structure.

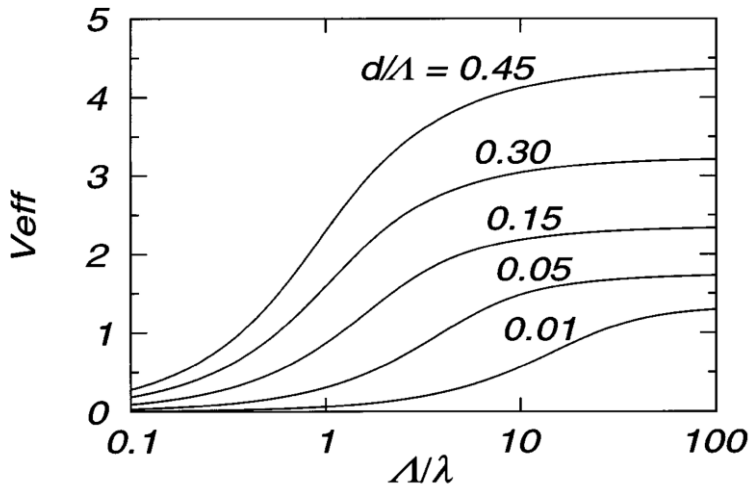

Figure 2.6: Calculated V-values for PCF structures with differing d/Λ. The V-value can remain finite as $\lambda \rightarrow 0$. The dashed line shows the critical V-value for single mode guidance in conventional fibre. (Image from [22]).

As shown in Eq. (2.10), for conventional fibres the V-value is in part determined by the core radius *a*. In order to describe the V-value for a PCF, it is necessary to define a similar quantity based on the structural parameters of the fibre. The variation of the effective V-value with wavelength, for a variety of PCF structures, is shown in Fig 2.6, for the case where *a* is defined to be equal to the fibre pitch Λ. For this choice of scaling for the fibre core size, the critical V-value at which the second mode is cut off, is calculated from numerical modelling to be $V_C = 4.1$ [24]. This indicates that for fibres with $d/\Lambda < 0.4$, the effective V-value of the fibre will remain below the critical V-value at all wavelengths, such that the fibre is endlessly single-mode. For a better choice of the definition of the core size for a PCF ($a = 0.625\ \Lambda$), the critical V-value is found to more closely match to that of conventional fibre with $V_C = 2.4$, but in either case the requirement on the PCF structure to observe ESM guidance remains the same.

This analysis of the conditions for endlessly single mode guidance assumes a PCF structure based on the standard hexagonal air hole array. For birefringent PCF of the type discussed in

Chapter 7 the enlarged air holes around the core act to reduce the effective index of all the guided modes. In this structure the cut-off conditions for single-mode guidance become dependent on the relative size of the enlarged air holes to the other cladding holes, and can allow endlessly single-mode guidance for values of d/Λ in excess of the limit found for the standard non-birefringent PCF structure [25].

2.1.4 Birefringence

Birefringence was first noted as a property of certain anisotropic materials, such as calcite, whereby the crystal structure defines an optical axis, with a difference in the refractive index of the material depending on whether light is polarised parallel or perpendicular to this axis. While silica glass itself is an isotropic material, asymmetry in a waveguide can also lead to birefringence. Even in fibres that support only a single guided mode there are still two possible distinct modes of polarisation. In the case of a perfectly symmetrical waveguide the propagation constant is degenerate for these polarisation modes, but for an asymmetrical design there will be a variation in β for the two modes, defining fast and slow axes of the fibre. If light is launched into the fibre with a linear polarisation that is not aligned to one of these axes, the state will periodically evolve to an elliptic state and then back to a linear polarisation state as it propagates, due to the relative phase difference that accumulates between the components of the light on the two axes of the fibre, as illustrated in Fig. 2.7.

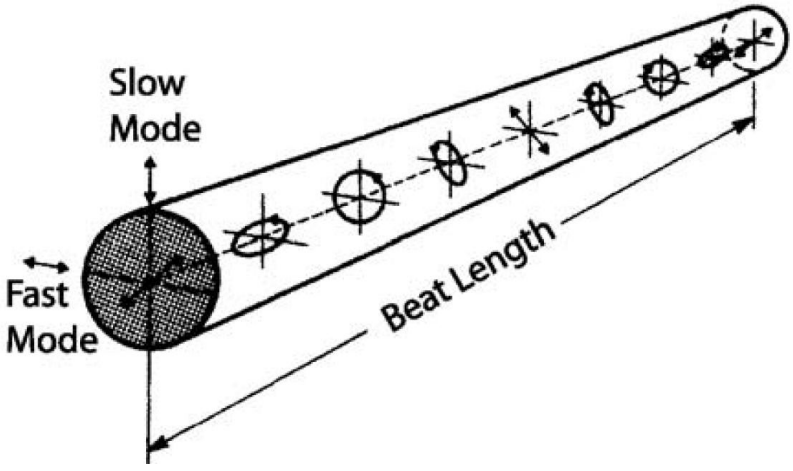

Figure 2.7: Evolution of the polarisation state of an initially linearly polarised input beam as it propagates through a fibre with birefringence. (Image from [12]).

The spatial period over which the light undergoes this transition and returns to its initial polarisation state is known as the beat length (L_B), which is given by

$$L_B = \frac{2\pi}{\left|\beta_{fast} - \beta_{slow}\right|}, \tag{2.14}$$

where β_{fast} and β_{slow} are the propagation constants for the fast and slow fibre axes. The beat length is a measure of the strength of the birefringence, and is shorter for more strongly birefringent fibres. Linearly polarised light aligned with either the fast or slow axis will not experience a change in polarisation as it propagates

In reality, even for fibre that is designed to be symmetrical, small unintentional variations in the fibre parameters generally lead to slight difference in the propagation constant for the two modes, and therefore birefringence. As these fluctuations in the fibre are random along its length this leads to the fast and slow axis repeatedly changing in orientation and scrambling the polarisation of the input light. While the evolution of the polarisation of light in such a structure is deterministic, it is in practice impossible to predict. In addition, bending of the fibre can induce birefringence [26] that will also influence the output polarisation state.

In order to maintain the polarisation state during propagation, it is necessary to keep the fast and slow axes of the fibre well defined by introducing an intentional strong birefringence that dominates over any random fluctuations in the structure or the influence of bending. In conventional fibres this is achieved either through an elliptic core shape [27] or via stress-induced anisotropy in the core by incorporating a material with a different thermal coefficient to silica in the structure during manufacture [28]. Polarisation-maintaining guidance can be easily realised in PCF by introducing asymmetry in the cladding structure during manufacturing, for instance by enlarging two of the air holes in the cladding, one on either side of the core, in order to produce an elliptic core shape and anisotropic cladding index [29]. By using differential pressure in these two holes relative to the rest of the cladding structure during manufacture the diameter of the holes, and therefore the strength of the resulting birefringence can be accurately controlled. As well as allowing the polarisation state of light to be maintained during propagation, the controllable polarisation mode dispersion arising in strongly birefringent PCF can be used to achieve phase-matching for nonlinear interactions, as described in Section 2.2.6.

2.1.5 Loss

One of the most attractive features of light propagation in optical fibres is the exceptionally low transmission losses that can be achieved. Achieving low loss is of particular importance when dealing with the delivery of single photons through optical fibre in order to realise a high performance single photon source. The loss of the fibre can be characterised by the attenuation constant α, which is commonly given in units of dB/km. When light of power P_0 is launched into a fibre, after propagation through a distance L the expected remaining power P_L is related to α by

$$\alpha = -\frac{10}{L}\log\left(\frac{P_L}{P_0}\right) \text{ dB/km.} \tag{2.15}$$

Commercially available conventional fibre can exhibit loss as low as 0.2 dB/km at 1550 nm, close to the theoretical limit for silica. At longer wavelengths the loss increases due to vibrational resonances of the material. For wavelengths shorter than about 200 nm, the loss is also significant due to electronic absorption. In the transparency window of silica, from around 500 nm – 2 μm, the main contribution to the loss is the intrinsic Rayleigh scattering caused by density fluctuations in the material which scales as the inverse of λ^4. Low levels of contamination of water in the fibre can also cause a source of significant loss near 1.4 μm due to the vibrational resonance of OH bonds, although this can be reduced by taking extra care during the fabrication process to avoid this contamination [30].

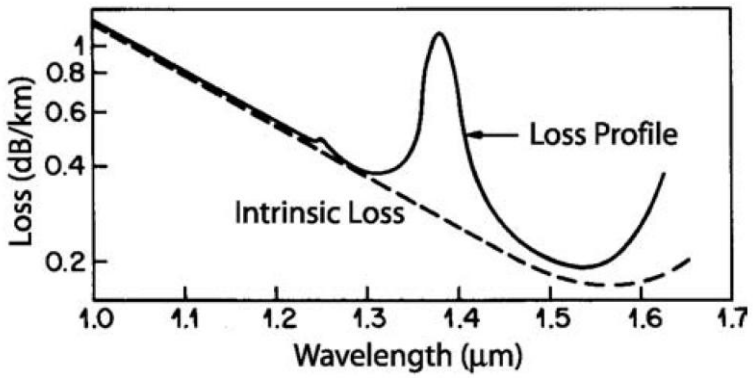

Figure 2.8: Comparison between the theoretical minimum loss in silica fibres and a typical measured loss. The intrinsic loss is dominated by Rayleigh scattering over most of the range shown. The loss peak in the measured fibre is due to OH contamination. (Image from [12]).

In solid core PCF an additional source of loss arises due to surface roughness at the glass-air interfaces in the fibre. Even when considering idealised conditions in the manufacturing process, fluctuations in the boundaries still occur which are thermodynamic in origin and are subsequently frozen in during the glass formation. The scattering from these features may be more than two orders of magnitude greater than that from Rayleigh scattering at similar wavelengths [31], giving PCF losses ~100 dB/km for small core fibres. For PCF with core size similar to that of conventional fibre effect is far less pronounced, with losses ~5 dB/km demonstrated. While the propagation loss is higher, the length of PCF required to observe the type of nonlinear effects described in Section 2.2 is typically ~1 m, so the loss should not be significant over this length.

As well as the intrinsic losses present in uniform waveguides, both standard fibres and PCF exhibit loss associated with microscopic and macroscopic bending [32]. In both cases the bending of the structure induces coupling between the guided mode and the lossy cladding modes. Care should be taken not to coil any fibre too tightly (to a bend radius < 20 mm for standard telecommunications fibre) in order to avoid this effect.

In addition to the losses that occur during the propagation, some light will be lost when launched into a fibre due to the imperfect coupling of a free-space light source (such as a laser) to the guided mode of the fibre. In a single-mode PCF, in order to minimise this loss the mode field profile of the input light should be matched as closely as possible to the fundamental mode of the fibre by means of a focussing lens, to avoid coupling to the lossy cladding modes. In the case of a laser source with an approximately Gaussian field profile the optimum coupling is achieved when the minimum spot size of the focussed beam is equal to the core size of the fibre. For typical solid-core PCFs this leads to relatively short focal lengths that can be achieved with microscope objective lenses [14]. Typical input coupling efficiency for single mode PCFs is ~70%, but may be higher with optimised launch optics [33]. Coupling efficiencies for multimode fibres may be ~95%, limited by the Fresnel reflection at the silica-air interface.

The final type of loss that is important in the context of this thesis is the loss that occurs between fibres that have been joined by fusion splicing. Techniques for minimising the loss due to splicing will be covered in Section 2.4.

2.1.6 Dispersion

As discussed in Section 2.1.1, the propagation constant β varies for the different guided modes of the structure. However, even for a single mode the propagation constant is dependent on wavelength, meaning that light at different wavelengths will travel through the fibre at different speeds. This effect is known as chromatic dispersion and occurs for both conventional optical fibres and PCF. In telecommunications systems an understanding of the properties of dispersion is crucial because pulses of light will tend to broaden as they propagate, due to the relative phase difference that accumulates between the different wavelength components of the pulse, which can limit the achievable data transfer rate. In the case of nonlinear effects the dispersion properties of the fibre play a crucial role in achieving phase-matching between light at different wavelengths, as described in Section 2.2.4. There are two contributions to the dispersion observed in fibres. The first is the material dispersion due to the silica glass in which the light propagates, and the second is the waveguide contribution due to the difference in the relative size of the waveguide features for different wavelengths of light. For standard optical fibres the material contribution generally dominates the overall dispersion profile, while for PCF the magnitude of the contribution from waveguiding can be comparable.

The origin of the material contribution to the dispersion is due to the oscillation of the bound electrons within the silica glass in response to the applied electric field from the propagating light. This leads to a wavelength dependent refractive index that is determined by the resonance frequencies at which absorption occurs in the material as described by the Kramers–Kronig relations [34]. While silica glass has extremely low loss in the wavelength range of interest here, from 500 – 2000 nm, strong absorption due to electronic excitation in the ultraviolet region, and vibrational resonances in the infrared lead to a characteristic dispersion profile for silica glass. In the transparency region, far from these resonances, the refractive index can be approximated by the Sellmeier equation [35]

$$n^2(\omega) = 1 + \sum_{j=1}^{m} \frac{B_j \omega_j^2}{\omega_j^2 - \omega^2}, \tag{2.16}$$

where n is the refractive index of the material and B_j is the relative strength of the j^{th} resonance occurring at angular frequency ω_j , and the sum extends over all nearby contributing resonances. The parameters B_j and ω_j are obtained experimentally and are well

known for silica glass [36]. When considering the propagation of a pulse in a medium, consisting of a spread of frequencies, it is useful to consider the group velocity v_g at which the pulse envelope will travel, for which the group index n_g can be defined as

$$n_g = \frac{c}{v_g} = c\frac{\mathrm{d}\beta}{\mathrm{d}\omega} = n(\omega) + \omega\frac{\mathrm{d}n}{\mathrm{d}\omega}. \tag{2.17}$$

In order to demonstrate the effects of dispersion it is common to express the propagation constant as a Taylor expansion about some central frequency ω_0

$$\beta(\omega) = \beta_0 + (\omega - \omega_0)\beta_1 + \frac{1}{2}(\omega - \omega_0)^2\beta_2 + ..., \tag{2.18}$$

where

$$\beta_m = \left(\frac{\mathrm{d}^m\beta}{\mathrm{d}\omega^m}\right)_{\omega=\omega_0} \qquad (m = 1, 2,....). \tag{2.19}$$

By comparing with Eq. (2.19) with Eq. (2.17), it can be seen that the first derivative term is related to the group velocity, and therefore the second derivative term (the rate of change of β_1 with respect to ω) is responsible for group velocity dispersion [12], where

$$\beta_1 = \frac{1}{v_g}, \tag{2.20}$$

and

$$\beta_2 = \frac{\mathrm{d}}{\mathrm{d}\omega}\left(\frac{1}{v_g}\right) = -\frac{1}{v_g^2}\left(\frac{\mathrm{d}v_g}{\mathrm{d}\omega}\right). \tag{2.21}$$

Generally the higher order terms in Eq. (2.18) can be disregarded for quasi-monochromatic pulses where the spectral width is significantly less than the central wavelength such that $(\omega - \omega_0) << 1$, however, these higher order terms become important for the phase-matching of nonlinear processes close to the zero-dispersion wavelength of the fibre, where $\beta_2 = 0$ (see Section 2.2.4).

The dispersion profile of a fibre is commonly described using the dispersion parameter D, which is related to the group velocity dispersion coefficient β_2 by

$$D = -\frac{2\pi c}{\lambda^2}\beta_2, \tag{2.22}$$

at a wavelength of λ. D is normally given in units of ps·nm^{-1}·km^{-1}, as this then indicates the expected temporal broadening, per nanometre of pulse bandwidth, after propagation through a kilometre of the fibre.

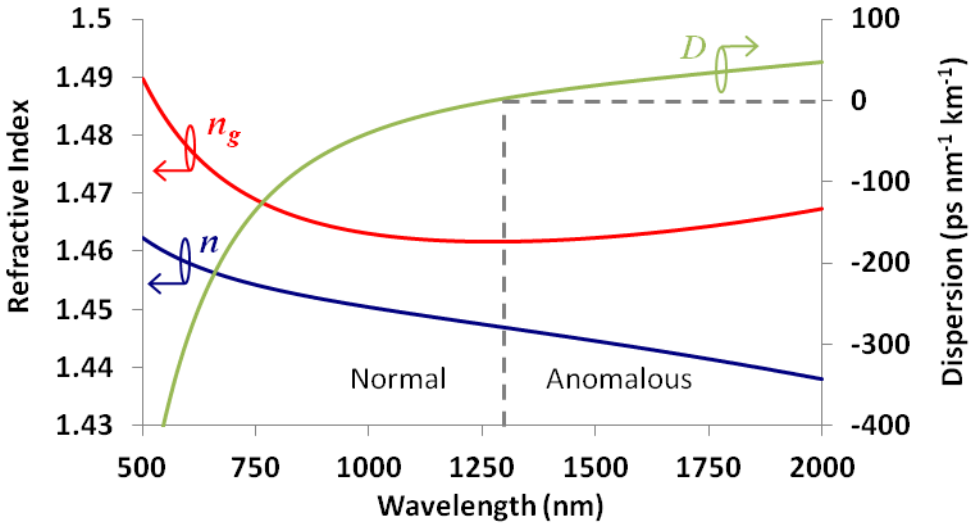

Figure 2.9: Refractive index n, group index n_g and dispersion parameter D calculated for bulk silica glass using Eq. (2.16).

The calculated profiles of n, n_g and D are shown in Fig. 2.9. It can be seen that D = 0 (and consequently β_2 = 0) for a wavelength of 1.27 µm. This point is the zero-dispersion wavelength (ZDW) of the material. Although D = 0, chromatic dispersion still occurs at this point due to the presence of the higher order dispersion terms in the expansion of Eq. (2.18). The ZDW marks the boundary between two different propagation regimes of the material. For wavelengths below the ZDW, the material displays normal dispersion, where long wavelength components travel faster than shorter wavelength components (or 'red' light travels faster than 'blue' light). On the long wavelength side of the ZDW the dispersion is anomalous, and the situation is reversed so that the blue components of the light are faster than red.

In addition to the material contribution to the dispersion, the confined light guided in a fibre also experiences a waveguide contribution to the dispersion and the overall dispersion D can be approximated by their sum [37]

$$D = D_m(\lambda) + D_{wg}(\lambda), \tag{2.23}$$

where D_m and D_{wg} are the dispersion contributions from the material and waveguiding respectively. For standard step-index fibres with a low index contrast between the core and cladding, the waveguide contribution to the dispersion is small. Fig. 2.10 shows the measured dispersion curve for a standard single-mode fibre. The resulting dispersion profile is very similar to that of bulk silica, with a slight increase in the ZDW, from 1.27 µm to 1.31 µm. While it is possible to tailor the dispersion of conventional fibres by structuring the refractive index profile of the cladding (for instance, in dispersion flattened fibres [38]), this adds complexity to the manufacturing process. Additionally, for conventional fibres the waveguide contribution to dispersion usually acts to shift the ZDW to longer wavelengths [17].

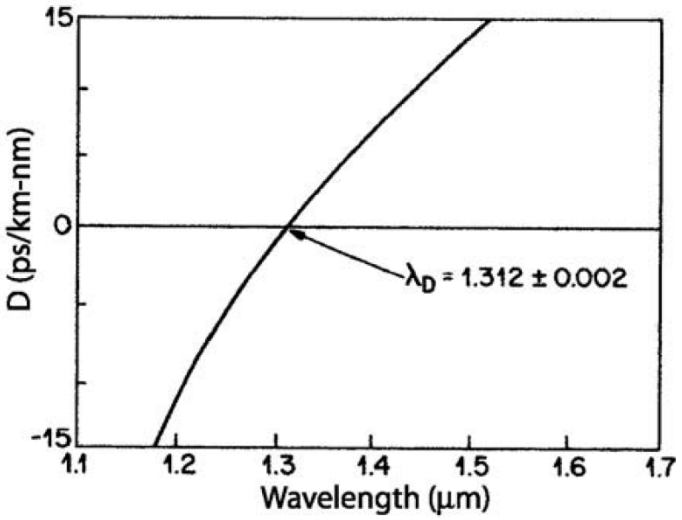

Figure 2.10: Typical dispersion curve for a standard conventional fibre. λ_D is the ZDW. (Image from [60]).

The waveguiding contribution to dispersion is more important when considering structures with strong index mismatch. Fig. 2.11 shows the calculated waveguide dispersion properties for narrow strands of material with a constant refractive index of 1.5, embedded in a second material of refractive index 1, able to guide light by TIR. Both the mode index and dispersion parameter D are shown over a range of wavelengths, scaled relative to the radius of the high

index strand, ρ. These results approximate the waveguide contribution to dispersion that would be expected for a narrow silica strand in air.

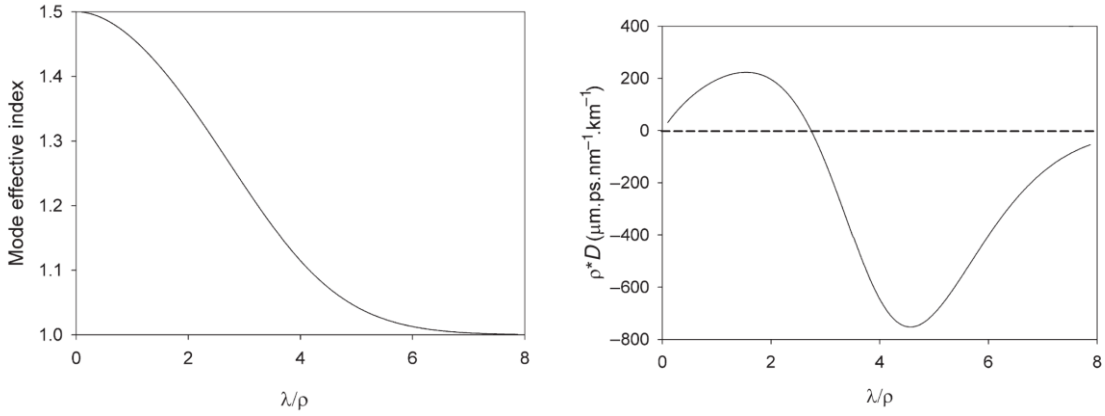

Figure: 2.11 (a) Calculated effective mode index for a silica strand in air, assuming a constant refractive index of 1.5 for silica and ignoring the effect of material dispersion. The variation in the mode index as the wavelength of propagating light is scaled relative to the strand radius is demonstrated; (b) The corresponding waveguide contribution to dispersion for this structure. (Images from [39]).

As seen in Fig. 2.11(a), in the limit where the strand radius is large compared to the wavelength of the propagating light, the effective mode index will approach that of the high index material (the light would be mainly confined to the silica region for the case of a strand of silica in air). However, when the strand diameter is reduced relative to the wavelength, a portion of the light will propagate outside the strand and the large index contrast will cause a departure of the dispersion from that of the high index material. Comparing these results to the material contribution to dispersion, shown in Fig. 2.9, it can be seen that for silica strands with a diameter similar to the wavelength of the propagating light, the large anomalous waveguide dispersion can be used to counter the inherent normal dispersion from the material in the case of a high index contrast waveguide. For narrow silica strands the ZDW will therefore be shifted towards the visible part of the spectrum, and for strands with sufficiently small diameter a second ZDW will be observed within the transparency window of silica.

Very narrow silica strands are typically difficult to manufacture and prone to damage. For PCF however, a very strong core to cladding index contrast can be readily achieved through enlargement of the air holes in the cladding to achieve a structure with high air filling fraction. The dispersion profiles for such a structure can closely approach that calculated for a silica strand of similar diameter to the PCF core, as demonstrated in Fig. 2.12. By controlling both

the pitch and air filling fraction of the PCF, the waveguide contribution to the dispersion profile can be readily tailored. For simple symmetrical cladding structures, the dispersion can be easily calculated from empirical relations [40], while for more complex structures, such as the birefringent fibre discussed in Chapter 7, it is necessary to use a numerical approach, such as modelling using plane wave methods [41] or finite element analysis [42].

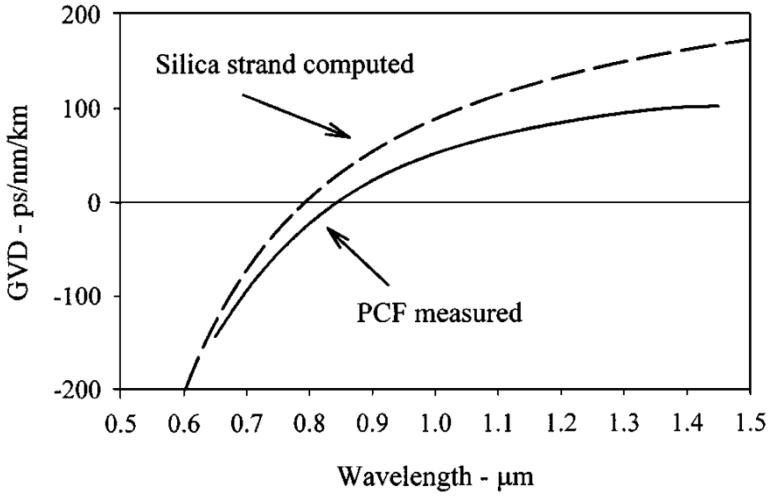

Figure 2.12: Comparison of the group velocity dispersion of a measured small core (diameter 1.45 μm), high air filling fraction (cladding hole diameter 0.62 μm; pitch 1 μm) PCF with the calculated dispersion of a silica strand in air of equal diameter to the PCF core. (Image from [ref 43]).

For nonlinear effects (which will be discussed in Section 2.2), qualitatively different behaviour is observed when comparing the normal and anomalous dispersion regimes, with the wavelengths at which these effects can be occur being limited by the intrinsic properties of silica in the case of conventional fibres. In particular, interesting nonlinear behaviour is anticipated when an intense laser pulse with wavelength close to the ZDW is propagated. The ability of PCF to dramatically shift the ZDW to shorter wavelengths allows these effects to be observed using robust, high power, short pulse length 1064 nm fibre lasers. For parametric nonlinear processes resulting in the generation of light at new frequencies from these laser pump pulses, the generated wavelengths are dependent on the dispersion properties of the fibre. Control of dispersion therefore allows the most desirable operating wavelengths to be selected through careful choice of the fibre parameters. Finally the effect of group velocity dispersion leads to limitations on the length of fibre over which pulses of different wavelength are able to interact through nonlinear processes. This 'walk-off length' will be discussed further in Section 2.2.7.

2.2 Nonlinearity

When light propagates in a dielectric material its electric field component causes bound electrons within the material to oscillate. At low field intensities the induced polarisation in the material from this effect is linear with field intensity and the electrons simply re-radiate light at the same frequency as the applied field, albeit with a slight time delay that leads to the lower speed of propagation for light in a material compared to free-space. For significantly intense applied electric fields the oscillation of the bound electrons becomes anharmonic due to the profile of the binding potential of the electron. In this case the induced polarisation of the material can no longer be related linearly to the electric field and it becomes possible for the material to radiate frequency components that were not present in the input light.

2.2.1 Nonlinear Susceptibility and Nonlinear Phase Shift

When an electric field $\mathbf{E}$ is present in a dielectric material the field induces an electric dipole moment, the polarisation of the material $\mathbf{P}$, such that the electric displacement field $\mathbf{D}$ is given by

$$\mathbf{D} = \varepsilon_0 \mathbf{E} + \mathbf{P}(\mathbf{E}), \tag{2.24}$$

where ε_0 is the permittivity of free space. For linear, isotropic, homogeneous materials

$$\mathbf{P} = \varepsilon_0 \chi \mathbf{E}, \tag{2.25}$$

where χ is the electric susceptibility of the material, related to the refractive index of the material via the relative permittivity of the material ε_r by

$$n = \sqrt{\varepsilon_r} = \sqrt{\chi + 1}. \tag{2.26}$$

This linear dependence of $\mathbf{P}$ on the electric field was assumed in Eq. (2.4) when considering the linear propagation properties of fibres. In the case of intense incident electric fields, the polarisation of the material is no longer able to respond in a linear fashion to the applied field. As the functional dependence of χ on the electric field intensity is generally not known, it can be approximated by a Taylor expansion [44], giving

$$\mathbf{P} = \varepsilon_0 \left(\chi^{(1)} \cdot \mathbf{E} + \chi^{(2)} : \mathbf{EE} + \chi^{(3)} \vdots \mathbf{EEE} + \cdots \right), \tag{2.27}$$

where $\chi^{(j)}$ is the j^{th} order susceptibility. For materials with inversion symmetry, such as silica glass, the second order susceptibility $\chi^{(2)}$ = 0, as this would otherwise imply a preferred direction for the material polarisation irrespective of the direction of the applied field. Since the nonlinear response is dominated by the lowest order non-zero term, the third order $\chi^{(3)}$ susceptibility is responsible for most of the nonlinear effects that can be observed in optical fibres, and higher order terms in the Taylor expansion can be disregarded. $\chi^{(3)}$ is often referred to as the Kerr nonlinearity. As the response time of $\chi^{(3)}$ is typically <<10 fs, its effect on an input light field is usually modelled as being instantaneous [12].

The linear expression for the refractive index given in Eq. (2.26) can be modified to account for the addition of the nonlinear contribution to the material permittivity from $\chi^{(3)}$, such that the refractive index $\tilde{n}$ is given by

$$\tilde{n}(\omega,|E|^2) = n(\omega) + n_2|E|^2. \tag{2.28}$$

Here *n* is the linear component of refractive index described previously, while the second term is the nonlinear contribution to the refractive index that is dependent on the intensity of the of the light in the fibre. n_2 is the nonlinear index coefficient and is related to $\chi^{(3)}$ by

$$n_2 = \frac{3}{8n}\mathrm{Re}(\chi^{(3)}_{xxxx}) \quad (\mathrm{m}^2/\mathrm{W}), \tag{2.29}$$

where $\chi^{(3)}_{xxxx}$ is the component of the nonlinear susceptibility that relates to the nonlinear interaction of co-polarised waves (see Section 2.2.3). The consequences of the nonlinear contribution can be seen by considering the difference in the relative phase experienced for an intense pulse as it propagated through the nonlinear medium, compared to that of a lower intensity pulse where the nonlinear component of the phase shift is negligible. A linearly polarised wave of frequency ω_{0a} propagating in the z-direction through a material with the refractive index profile given by Eq. (2.28) is described by the equation

$$\mathbf{E} = \frac{1}{2}\hat{x}\{E_a \exp[ik_{0a}nz + ik_{0a}n_2Iz - i\omega_a t]\} + c.c., \tag{2.30}$$

where $k_{0a} = \frac{\omega_a}{c} = \frac{2\pi}{\lambda_a}$, $I \propto |E_a|^2$, and *c.c.* is the complex conjugate.

The intensity dependent term in Eq. (2.30) gives the additional nonlinear component of the phase shift in the case of a material without loss. For a real material with loss it is common to define an effective length of propagation L_{eff}, that takes into account the reduction in the intensity I over the course of propagation through a physical distance L. For a fibre with attenuation constant α

$$L_{eff} = \frac{1}{\alpha}[1-\exp(-\alpha L)], \tag{2.31}$$

After propagation through a length of fibre L, the additional nonlinear phase shift experienced for a high intensity pulse is therefore given by [44]

$$\phi_{NL} = -n_2 k_{0a} L_{eff} I(t), \tag{2.32}$$

This effect is known as self-phase modulation (SPM), the intensity dependence of the nonlinear material response leads to a change in a light pulse as it propagates that is related to the initial pulse profile. For a pulse, where the intensity is time dependent, this leads to a time dependent shift in the instantaneous frequency across the pulse

$$\delta\omega(t) = \frac{\partial \phi_{NL}}{\partial t} = -n_2 k_{0a} L_{eff} \frac{\mathrm{d}I(t)}{\mathrm{d}t}, \tag{2.33}$$

where $\delta\omega$ is the shift in the instantaneous frequency away from the central carrier frequency ω_{0a}. Since the frequency shift is related to the slope of the pulse intensity, the effect is most pronounced for high peak power, short duration pulses. The frequency shift is positive for decreasing I, which leads to new blue-shifted frequency components being continuously generated near the trailing edge of the pulse as it propagates. Conversely, red-shifted components are generated at the leading edge. For an initially time-bandwidth limited Gaussian pulse profile this frequency shift results in a broadening of the spectrum, and since the frequency of the generated light varies across the pulse it also leads to a frequency chirp.

SPM can be a limiting factor in the peak power output that can be achieved in short pulse duration, high power fibre lasers. Increasing the initial peak power of the pulse through higher gain enhances the broadening of the output pulse that occurs after propagation through the fibre in the laser. Fig. 2.13(a) shows the variation in the instantaneous frequency shift expected for an initially unchirped pulse. Since new frequency components will be generated in pairs with a frequency dependent phase separation between them, this eventually leads to

a periodic structure developing in the pulse spectrum (Fig. 2.13(b)) when the maximum value of ϕ_{NL} becomes sufficiently large [14]. The reduction of peak power at the central wavelength reduces the useful power available for further nonlinear processes when using such a laser as a pump source.

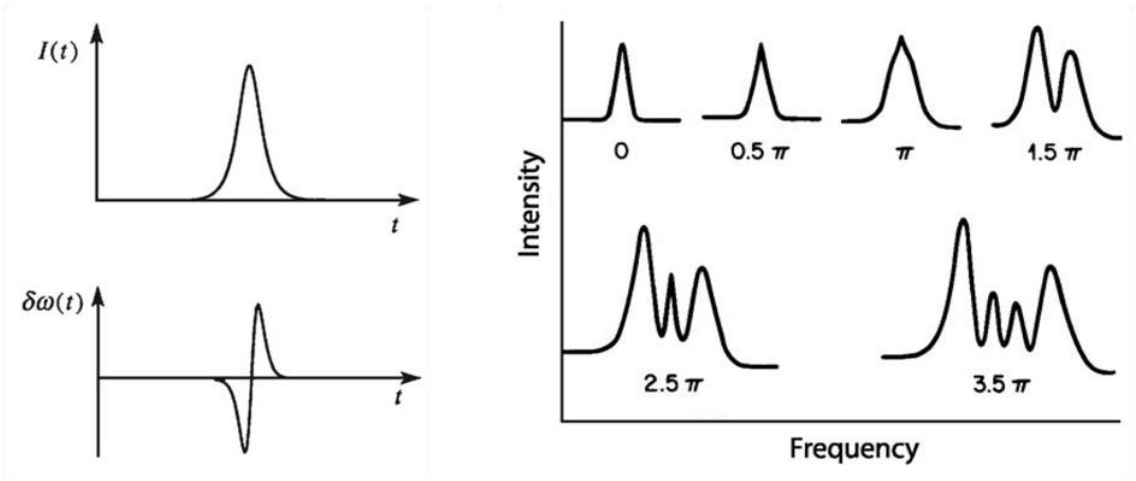

(a) (b)

Figure 2.13: (a) Temporal intensity profile of an initial pulse, and the resulting time dependent shift in the frequency after propagation due to SPM. (Image from [44]); (b) Output spectrum after propagation of a Gaussian high energy pulse due to SPM. The values refer to maximum nonlinear phase shift for the pulse. (Image from [45]).

The nonlinear phase shift that is experienced by a pulse can also be effected by the presence of another pulse, differing in frequency, polarization or propagation direction from the first, that is overlapped with it in time. If the analysis leading to Eq. (2.32) is repeated, but this time considering a total electric field given by the sum of two individual fields (both of the form of Eq. (2.30)) of different frequencies ω_{0a} and ω_{0b} and both polarised in the x-direction, the nonlinear phase shift for the field of frequency ω_{0a} is given by

$$\phi_{NL} = -n_2 k_{0a} L_{eff} \left(|E_a|^2 + 2|E_b|^2 \right), \tag{2.34}$$

where the first term is responsible for the SPM described previously and the second term is the contribution from cross-phase modulation (XPM).

In the case where both the propagating waves have the same central frequency ω_0, but are polarised orthogonally on the x and y-axes, the nonlinear phase shift experienced by the x-polarised wave will be

$$\phi_{NL} = -n_2 k_0 L_{eff} \left(\left| E_x \right|^2 + \frac{2}{3} \left| E_y \right|^2 \right), \tag{2.35}$$

where E_x and E_y are the electric field amplitudes for the x and y-polarised waves respectively. The reduction in the relative contribution of the XPM term in this case compared to the co-polarised case is due to the difference in the magnitude of the $\chi^{(3)}$ component by which the waves are coupled (see Section 2.2.3). In addition to the spectral broadening of short pulses, SPM and XPM effect the phase-matching conditions required to efficiently observe other nonlinear processes based on $\chi^{(3)}$.

2.2.2 Raman Scattering

Both SPM and XPM are parametric processes, meaning that although the material in which the waves propagate is involved in mediating the interaction, the state of the material is left unchanged afterwards. In other words, energy is not transferred to or from the material. In contrast to this, another nonlinear effect that is important in optical fibres, the Raman effect [46], can shift photons to either higher or lower frequencies, with energy conservation for this process satisfied by a change in the vibrational state of a molecule within the medium that the light is propagating in. The Raman response is a consequence of the imaginary part of $\chi^{(3)}$. Photons that are down-shifted to a lower frequency (with a corresponding increase in the vibrational energy of the material) form a field known as the Stokes, while the photons that are shifted to higher frequencies (with a decrease in the energy of the material) are known as the anti-Stokes. The Stokes field is generally several orders of magnitude brighter than the anti-Stokes, as in the latter case it is necessary for a pump photon to be overlapped with an excited vibrational state of the material. In thermal equilibrium the proportion of molecules in an excited state will be lower than the amount in the ground state by a factor of $\exp(\Delta E / k_B T)$, where ΔE is the difference in energy between the levels, T is the temperature and k_B is the Boltzmann constant.

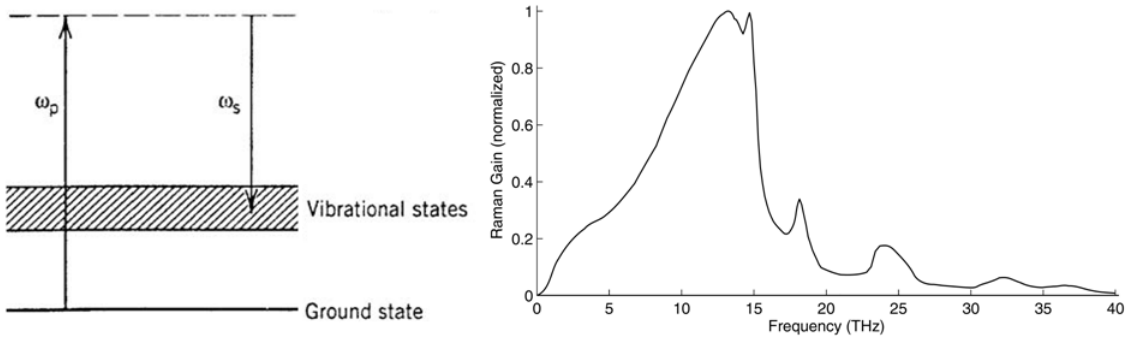

(a) (b)

Figure 2.14: (a) Schematic representation of the transfer of power from a bright pump to a frequency down-shifted Stokes beam; (b) Characteristic normalised Raman gain spectrum for silica. (Images from [12]).

The frequency shift observed in this process is characteristic of the distribution of vibrational states of the material, and for amorphous materials, such as silica glass, these form bands in which there is a continuum of states, allowing for frequency shifts with a broad range of energies. For silica, as shown in Fig. 2.14(b), the vibrational states give a gain spectrum with a peak for frequency shifts of 13 THz. As Raman scattering is a stimulated process, the growth rate of the intensity of the Stokes wave is proportional to both the intensity of the pump I_P and Stokes wave I_S along the length of the fibre as described by

$$\frac{dI_S}{dz} = g_R I_P I_S, \tag{2.36}$$

where $g_R = g_R(\omega_P - \omega_S)$ is the Raman gain coefficient and propagation is in the *z*-direction. In the case of a propagating intense pump pulse, where there is no initial power in the Stokes field, gain can still occur due to spontaneous Raman scattering, which is the amplification of quantum noise present at the required Stokes wavelength. As the gain increases exponentially with the Stokes intensity, this leads to the growth of a narrow Stokes peak at the peak value of the Raman gain. In the case where the Stokes power builds up significantly, the generated peak can itself undergo a Raman shift, leading to a series of peaks separated by 13 THz.

While the theory described here relates to the generation of high power Raman-shifted peaks from intense pump light, Raman scattering is also one of the main sources of noise in single photon sources based on parametric processes, operated at much lower peak pump power (see Section 3.4.3). In the low pump power regime, the pump power dependence of the gain for Raman scattering is found to differ significantly from that observed in the high gain regime.

Variation in the pump power dependence of gain is also seen for the process of four-wave mixing at low pump power, which will be covered in Section 2.2.5. It has been demonstrated that in the limit of low gain, the intensity of the light generated by Raman scattering will scale linearly with both the peak pump power and fibre length [47].

2.2.3 Four-Wave Mixing

In addition to the nonlinear phase shifts described by SPM and XPM, many other parametric processes, involving the interaction of waves with different frequencies, are also possible via the $\chi^{(3)}$ nonlinear susceptibility. This can be understood by considering the induced polarisation of the material in Eq. (2.27). The induced polarisation in the material $\mathbf{P}$ is associated with an oscillating electric dipole that will emit light with a frequency equal to its frequency of oscillation. If this frequency is the same as the input electric field $\mathbf{E}$ (as in the low power case where the contribution from the higher order terms of the susceptibility are negligible) the output light will be the same as the input, except for the relative phase shift from the refractive index of the material. This corresponds to the linear contribution to the polarisation $\mathbf{P}_{\mathrm{L}}$, if Eq. (2.27) is rewritten as

$$\mathbf{P} = \varepsilon_0(\chi^{(1)} \cdot \mathbf{E}) + \varepsilon_0(\chi^{(3)} \vdots \mathbf{EEE}) = \mathbf{P}_{\mathrm{L}} + \mathbf{P}_{\mathrm{NL}}. \tag{2.37}$$

In the nonlinear case, the induced nonlinear component of the polarisation, $\mathbf{P}_{\mathrm{NL}}$ (and hence the generated light) depends on the interaction of three electric fields via $\chi^{(3)}$. In the most general case this results in the coupling between four vector fields (due to the different possible polarisation states of the light) with different frequencies. $\chi^{(3)}$,as shown in Eq. (2.37) is a fourth order tensor, where its component $\chi^{(3)}_{ijkl}$ relates the component of the polarisation vector in the i-direction, $P_{NL\text{-}i}$, to the 3 contributing electric fields by [44]

$$P_{NL-i}(\omega_4) = \varepsilon_0 \sum_{jkl} \chi^{(3)}_{ijkl} E_j(\omega_1) E_k(\omega_2) E_l(\omega_3), \tag{2.38}$$

where the subscripts i,j,k and l can take the values x, y and z, representing the three orthogonal vector components in Cartesian coordinates. In the most general case there are a total of 81 components to the $\chi^{(3)}$ tensor, 27 relating each component of P to the 3^3 possible different polarisation configurations of the three incident fields. However, the isotropic nature of silica significantly reduces the number of non-zero elements in the tensor for a number of reasons. Firstly, each axis of the material must be equivalent so, for instance

$$\chi^{(3)}_{xxxx} = \chi^{(3)}_{yyyy} = \chi^{(3)}_{zzzz}. \tag{2.39}$$

While more than one index can appear in the subscript, an index cannot appear an odd number of times, since this would imply a preferred direction in the material. Also, for propagation in a fibre, only electric fields with a polarisation in the transverse directions x and y, are considered meaning that the terms involving z can be ignored. Finally, the resulting behaviour should be the same regardless of the chosen coordinate system, which leads to the remaining elements of the tensor being related to each other by

$$\chi^{(3)}_{xxxx} = \chi^{(3)}_{yyyy} = \chi^{(3)}_{xxyy} + \chi^{(3)}_{xyxy} + \chi^{(3)}_{xyyx}. \tag{2.40}$$

Note that in the case where two of the coupled fields are polarised orthogonally with the other two, the strength of the nonlinear susceptibility is only 1/3 that of the case where all four are co-polarised. This is the reason for the difference in the nonlinear phase shift associated with XPM for the case of waves of different polarisation in Eq. (2.35), compared to those of different frequency given by Eq. (2.34).

Although solutions to Eq. (2.38) with the electric fields polarised in different directions are clearly possible, considering the simpler case in which all four coupled fields are polarised in the same direction demonstrates much of the interesting nonlinear behaviour. For four such CW fields polarised in the x-direction the total electric field in the material will be given by

$$\mathbf{E} = \hat{x}\frac{1}{2}\sum_{j=1}^{4} E_j \exp\left[i(\beta_j z - \omega_j t\}\right] + c.c, \tag{2.41}$$

where in general the frequency of each field ω_j is distinct. Similarly, the total nonlinear polarisation $\mathbf{P}_{\mathrm{NL}}$ can be considered as a sum of polarisation components at each of the four frequencies associated with the coupled fields such that

$$\mathbf{P}_{\mathrm{NL}} = \hat{x}\frac{1}{2}\sum_{j=1}^{4} P_j \exp\left[i(\beta_j z - \omega_j t\}\right] + c.c. \tag{2.42}$$

By substituting these expressions for $\mathbf{E}$ and $\mathbf{P}_{\mathrm{NL}}$ into the nonlinear part of Eq. (2.37), the relationship between the amplitudes of the polarisation components and the electric field components is found to depend on a large number of terms involving the sum and difference of the frequencies and propagation constants, resulting from evaluating the product of the

total electric field with itself. For instance, considering the P_4 amplitude of the polarisation, part of the expression [12] is given by

$$P_4 = \frac{3\varepsilon_0}{4}\chi^{(3)}_{xxxx}\{|E_4|^2 E_4 + 2(|E_1|^2 + |E_2|^2 + |E_3|^2)E_4 + 2E_1E_2E_3^* \exp(i\theta_{FWM}) + ..\}, \quad (2.43)$$

where

$$\theta_{FWM} = (\beta(\omega_1) + \beta(\omega_2) - \beta(\omega_3) - \beta(\omega_4))z - (\omega_1 + \omega_2 - \omega_3 - \omega_4)t. \quad (2.44)$$

Different terms correspond to various third-order nonlinear effects, including SPM and XPM. Of particular interest is the term containing θ_{FWM} that gives rise to four-wave mixing (FWM). This term shows that a component of the material polarisation at frequency ω_4 can be induced as a result of the interaction between fields of frequency $\omega_1, \omega_2, \omega_3$, and this will then radiate, generating a new light field at frequency ω_4. The presence of the relative phase factor $\exp(i\theta_{FWM})$ means that generally the relative phase of the generated light will vary with both time and position such that the power in the generated wave cannot build up appreciably. However, for carefully chosen wavelengths, in the case where $\theta_{FWM} \approx 0$ the generated light remains in phase along the fibre, allowing the build-up of light at this frequency to occur with high efficiency. This is referred to as phase-matching and is discussed in Section 2.2.4.

The second part of Eq. (2.44), the time dependent part of θ_{FWM}, results from the requirement for energy conservation in this interaction and demonstrates the process of FWM. In FWM energy is redistributed, with a loss from the fields at frequencies ω_1 and ω_2, usually referred to as the pump fields and a corresponding gain in the amplitude of the fields at frequencies ω_3 and ω_4. Of particular interest is the special case known as degenerate FWM, when the pump source consists of a single intense monochromatic pump such that

$$\omega_1 = \omega_2 = \omega_P, \quad (2.45)$$

where ω_P is the frequency of the pump. The constraint of energy matching then leads to the two remaining frequencies ω_3 and ω_4 being spaced equally about the pump (in frequency) such that

$$\omega_P - \omega_3 = \omega_4 - \omega_P = \Omega, \quad (2.46)$$

where Ω is the frequency shift of these sidebands from the pump wavelength. The amplified fields with frequencies ω_3 and ω_4 are usually referred to as the idler ω_i and signal ω_s fields respectively, where

$$\omega_s > \omega_P > \omega_i . \tag{2.47}$$

While the energy matching condition seems to suggest that coupling can occur between signal and idler pairs of any wavelengths satisfying Eq. (2.46), in reality the first bracketed term in Eq. (2.44), which is related to phase-matching, means that the process is only efficient for specific signal and idler wavelengths, dependant in part on the dispersion properties of the fibre.

2.2.4 Phase-Matching Conditions for FWM

Since the induced polarisation in a material will be coherent with the phase of the pump pulse, the generated parametric (signal or idler) field generated as a result of it will also have a constant phase relationship to the pump at the point of generation. However, if the generated waves are travelling with a different phase velocity to the pump then in general they will tend to cancel out with the generated field produced at earlier points in the fibre. Only in the case where all three waves (the signal, idler, and two degenerate fields comprising the pump) maintain a constant phase relationship to each other is destructive interference avoided, allowing the amplitude of the generated waves to build up to a significant amplitude.

The phase-matching term relating the propagation constants in Eq. (2.44) can be shown to be only partially complete, as it neglects to account for the additional phase shift that occurs for the pump field due to SPM. An analysis of the coupled amplitudes of the fields, in the quasi-CW regime (assuming the pump beam is not depleted) [12] shows that

$$\omega_s + \omega_i - 2\omega_P = 0, \tag{2.48}$$

and

$$\kappa = \Delta\beta + 2\gamma P_P = 0, \tag{2.49}$$

where

$$\Delta\beta = \Delta\beta_m + \Delta\beta_{wg} = \beta(\omega_s) + \beta(\omega_i) - 2\beta(\omega_P). \tag{2.50}$$

Eqs. (2.48) and (2.49) are the energy and phase-matching conditions for FWM respectively. κ is the effective phase-mismatch which includes the difference in the propagation constants of the waves (seen in Eq. (2.44)), as well as the effect of SPM via the $2\gamma P_P$ term, where P_P is the peak pump power and γ is the nonlinear coefficient of the fibre at the pump wavelength, defined as

$$\gamma(\omega_P) = \frac{n_2(\omega_P)\omega_P}{cA_{eff}}. \tag{2.51}$$

The condition of perfect phase-matching, when $\kappa = 0$, determines the wavelengths at which the peak gain for FWM will occur. For small non-zero values of the phase mismatch κ, FWM will occur with lower efficiency, with the maximum tolerable phase mismatch determining the bandwidth of the gain for the process. The $\Delta\beta$ term in the phase mismatch is due to both the intrinsic material dispersion contribution $\Delta\beta_m$ and dispersion due to waveguiding. The ability to readily control the dispersion in PCF (see Section 2.1.6) means that the wavelengths at which phase-matching is satisfied can be selected through the choice of fibre parameters.

In the case of degenerate FWM the signal and idler frequencies can be expressed in terms of a frequency offset from the pump, as given by Eq. (2.46). This allows the phase-matching equation (Eq. (2.49)) to be rewritten as

$$\kappa = \beta(\omega_P + \Omega) + \beta(\omega_P - \Omega) - 2\beta(\omega_P) + 2\gamma P_P = 0. \tag{2.52}$$

By expanding the β terms about the pump frequency using a Taylor series, as in Eq. (2.18), this can be expressed as

$$\kappa = 2\gamma P_P + \beta_2(\omega_P)\Omega^2 + \frac{2\beta_4(\omega_P)\Omega^4}{4!} + \cdots = 0. \tag{2.53}$$

Note that only the even terms in the expansion of β contribute to the phase-matching, since the odd terms from the expansion of the propagation constant for the signal will cancel with those from the idler. Generally the β_2 term of the expansion will dominate, but close to the ZDW (where $\beta_2 = 0$) the higher order terms become important.

There are a number of ways to satisfy Eq. (2.53) so that phase-matching is achieved. In a multimode fibre where the pump is divided into different spatial modes, or the signal or idler are generated in different modes the difference in the propagation constant for the modes

can balance the inherent mismatch between different wavelengths from the material dispersion. For single-mode, non-birefringent fibres, the nature of the phase-matching depends on the sign of β_2, which is positive in the normal dispersion regime of the fibre and negative in the anomalous dispersion region by definition.

In the anomalous dispersion regime where the β_2 term is negative, phase-matching can be achieved via SPM. In this case, for sufficiently large pump powers the SPM term given by $2\gamma P_P$ can cancel the negative $\Delta\beta$ term in Eq. (2.53) near the ZDW. If the mismatch due to dispersion ($\Delta\beta$) is small, the generated signal and idler wavelengths will be strongly dependent on pump power. For typical pump power values in the quasi-CW regime, the frequency separation (Ω) of the signal and idler from the pump is small, usually only ~10THz [12]. While this can be increased with short pump pulses, Ω drops off significantly as the pump wavelength is moved further away from the ZDW and the importance of the β_2 term increases. The separation of the generated idler wavelength from the pump in the anomalous dispersion regime can be comparable in magnitude to the shift of the of the Raman Stokes line from the pump. FWM in the anomalous dispersion regime is often referred to as modulation instability, as it was first studied in the time domain by considering the effect of perturbations on a CW propagating wave [12]. While the phase-matching equation seems to predict a discrete pair of wavelengths will be generated through FWM, in reality the interplay between various nonlinear effects tends to lead to the formation of broadband supercontinuum when a high power pump pulse propagates close to the ZDW in the anomalous dispersion region of a fibre (see Section 2.2.8).

In the normal dispersion region of a fibre, both β_2 and the SPM term in Eq. (2.53) are positive, so far from the ZDW phase-matching cannot be achieved. However, close to the ZDW where β_2 becomes small, if the β_4 term in Eq. (2.53) is negative then for sufficiently large frequency shifts Ω, it can balance the other two terms, satisfying the requirement $\kappa = 0$. In this case it is seen that the generated wavelengths vary over a considerable range, often several hundred nanometres, in response to changes of only a few nanometres in the pump wavelength, and are not significantly affected by changes in the pump power [48,49]. Due to the potential for a large wavelength separation from the pump in the normal dispersion regime, there is less overlap between the narrow peaks generated through FWM with light generated by other nonlinear processes such as Raman scattered light, in contrast with the closely spaced parametric peaks for phase-matching in the anomalous dispersion regime.

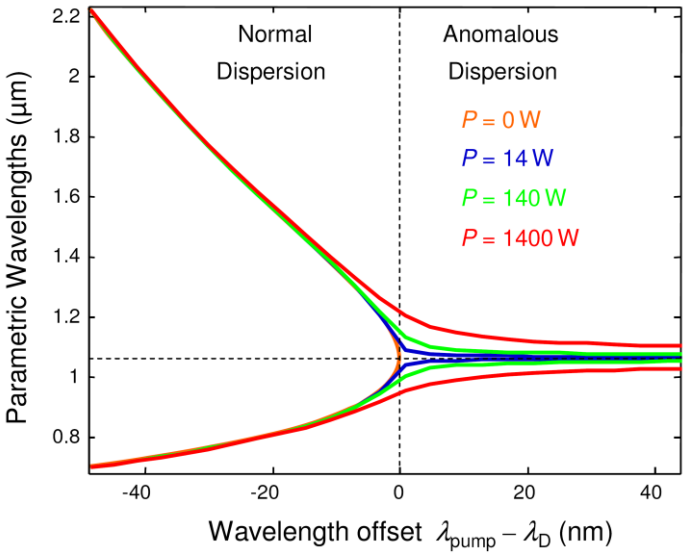

Figure 2.15: Calculated, phase-matched signal and idler wavelengths at different offset values of the pump wavelength from the ZDW (λ_D), for variety of peak pump power levels. These curves were calculated for a fibre with λ_D = 1090 nm (Image from [49]).

Since this type of phase-matching can only be realised close to the ZDW, in conventional fibre it limits the suitable pump source and the frequency about which the idler and signal are spaced because of the intrinsic material dispersion of silica. In PCF, the waveguide contribution to dispersion can be used to move the ZDW towards 1070 nm, so that this type of phase-matching can be obtained with high power Nd:YAG or Yb-doped fibre lasers. Theoretical predictions for an idealised fibre show that far from the ZDW, the phase-matching curves turn back on themselves and form closed loops, such that there will be a second phase-matched pair of signal and idler wavelengths with greater frequency separation from the pump [50]. In practice these peaks are usually difficult to observe as they occupy spectral regions where the absorption of silica is much higher.

2.2.5 Gain and Bandwidth of FWM

In order to evaluate the signal and idler gain for co-polarised FWM in the case of degenerate pump fields it is necessary to consider coupled equations for the field amplitudes. Combining Eqs. (2.2) and (2.3) gives a wave equation of the form

$$\nabla^2\mathbf{E} - \frac{n^2}{c^2}\frac{\partial^2\mathbf{E}}{\partial t^2} = \mu_0\frac{\partial^2\mathbf{P}_{NL}}{\partial t^2}, \tag{2.54}$$

where $\mathbf{P}_{NL}$ is the nonlinear polarisation as shown in Eq. (2.37) and n is the linear refractive index of the fibre. By substituting in a total electric field of the form given in Eq. (2.41) with three fields (j = 1, 2, 3), representing the pump signal and idler, where $E_j = E_j(\boldsymbol{r})$ is now allowed to vary spatially. This gives a set of three coupled equations for the field amplitudes [51], which can be reduced to two equations in the case that the pump field is undepleted by the interaction, such that

$$A_P(z) = A_P(0)\mathrm{e}^{i\gamma P_P z}, \tag{2.55}$$

where γ is the nonlinear coefficient described in Eq. (2.51), P_P is the peak pump power given by $P_P = \left|A_P(0)\right|^2$, and A_P is the pump amplitude function, which is related to the electric field amplitude by

$$E_P(r) = F_P(x,y)A_P(z), \tag{2.56}$$

where F_P represents the mode field distribution of the pump (the mode field distribution is assumed to be the same for all three waves for a single-mode fibre). The coupled amplitude functions for the signal A_s and idler A_i are given by [51]

$$\frac{dA_s}{dz} = i\gamma(2P_P A_s + P_P \mathrm{e}^{i(2\gamma P_P - \Delta\beta)z} A_i^*), \tag{2.57}$$

and

$$\frac{dA_i^*}{dz} = -i\gamma(2P_P A_i^* + P_P \mathrm{e}^{-i(2\gamma P_P - \Delta\beta)z} A_s). \tag{2.58}$$

By making substitutions $B_j = A_j \mathrm{e}^{-2i\gamma P_P z}$ for j = s, and i, these equations can be rewritten as

$$\frac{dB_s}{dz} = i\gamma P_P \mathrm{e}^{i(2\gamma P_P + \Delta\beta)z} B_i^*, \tag{2.59}$$

and

$$\frac{dB_i^*}{dz} = -i\gamma P_P \mathrm{e}^{-i(2\gamma P_P + \Delta\beta)z} B_s. \tag{2.60}$$

Solving these equations, the amplitude for the signal peak is then given by

$$B_s = [C_1 \mathrm{e}^{gz} + C_2 \mathrm{e}^{-gz}]\mathrm{e}^{i\kappa z/2}, \tag{2.61}$$

with a similar expression for the idler amplitude, where the parametric gain coefficient g is given by

$$g = \sqrt{(\gamma P_P)^2 - \left(\frac{\kappa}{2}\right)^2}\,. \tag{2.62}$$

The coefficients C_1 and C_2 are found by using the boundary condition that the signal and idler power at z = 0 are given by the initial launched powers, $P_s(0) = P_{s0}$ and $P_i(0) = P_{i0}$ [52]. The equations simplify considerably in the case that $P_{i0} = 0$ so that the idler power is initially zero and only pump pulse and a weak signal beam are launched into the fibre. After propagation through a length of fibre L, the gain for the signal and idler G_s and G_i in this case are given by [12]

$$G_s = \frac{P_s(L)}{P_s(0)} = 1 + (\gamma P_P L)^2 \frac{\sinh^2(gL)}{(gL)^2}, \tag{2.63}$$

and

$$G_i = \frac{P_i(L)}{P_s(0)} = (\gamma P_P L)^2 \frac{\sinh^2(gL)}{(gL)^2}, \tag{2.64}$$

where $P_j = B_j B_j^*$.

When the phase mismatch is small and the gain is large (gL >> 1) the gain in the signal and idler is exponential. In the limit of low gain and low pump power g becomes dominated by the phase mismatch term so that $g \approx \kappa/2$ and $\sinh(gL) \approx \sin(gL)$. The low power gain for FWM (G_{FWM}) is therefore given by

$$G_{FWM} = G_s - 1 = G_i \approx (\gamma P_P L)^2 \,\mathrm{sinc}^2(\kappa L/2). \tag{2.65}$$

For perfect phase-matching in the low power case, the generated signal and idler powers scale as the square of both the pump power and propagation length. The importance of the nonlinear coefficient γ, in determining the strength of the FWM interaction can now be seen. As shown in Eq. (2.51), γ depends on the nonlinear refractive index n_2 and the effective mode area A_{eff}. For silica glass $n_2 \approx 2\times10^{-20}$ m^2W^{-1}, which is relatively small compared to other

nonlinear materials, such as nonlinear glasses like chalcogenide [12]. However, the extremely low loss of silica means that the nonlinear interaction remains efficient over long lengths so that the generated parametric waves can build up to considerable levels. While n_2 is fixed by the material properties, PCF can be designed to have a high nonlinear coefficient by significantly reducing A_{eff} in fibres with small core diameters [53], although the effect this has on the dispersion properties of the fibre must be considered. Despite the $\chi^{(3)}$ susceptibility term, that is relevant in silica glass, being orders of magnitude weaker than the $\chi^{(2)}$ nonlinear susceptibility of relevance in nonlinear crystals, the long interaction length allowed by fibres means that the process can still be efficient. In bulk crystals a laser must usually focussed to a point to achieve a high intensity for nonlinear interaction, limiting the interaction length due to diffraction of the beam, whereas in a fibre A_{eff} remains small along the entire length of propagation.

The sinc^2 term in Eq. (2.65) defines the bandwidth of the generated signal and idler, with the width of its central peak determining the maximum tolerable phase mismatch. In theory, the bandwidth of the peaks scales as the inverse of the length of the fibre. In practice the bandwidth is usually broadened due to changes in the phase-matching conditions along the fibre length due to imperfections in the structure [52]. Furthermore, this result assumes quasi-CW fields. For FWM with pulses, walk-off will limit the maximum fibre length over which the three fields can interact, limiting the minimum bandwidth output that can be achieved (see Section 2.2.7).

Eqs. (2.63) and (2.64) show that the generated power in the signal and idler remains equal, with the initially launched signal beam amplified and the idler beam generated as a result. Since the generated power of both beams is always equal, at the single photon level the process can be understood as the generation of a signal and idler pair of photons, along with the destruction of two pump photons as required by energy matching. While FWM was considered here after the launch of a bright pump beam along with a weak signal beam, FWM can also occur spontaneously when just a bright pump is launched. In that case the process is seeded by quantum noise. The gain for this process, resulting from the probability of spontaneous emission along the fibre, is equivalent to that described in Eq. (2.65), assuming that the presence of a single virtual noise photon per mode [54].

2.2.6 Cross-Polarised FWM

In addition to the co-polarised FWM process discussed so far, phase-matching can also be achieved for cross-polarised FWM (XFWM) with degenerate pumping in birefringent fibres. In birefringent fibres the difference in the propagation constant between the fast and slow axes can be used to achieve phase-matching. For degenerate pumping, on the fast axis the signal and idler pair will be generated on the slow axis, and with the pump on the slow axis the generated signal and idler must both be on the fast axis in accordance with the symmetry properties of the $\chi^{(3)}$ tensor. In this case the phase-matching condition of Eq. (2.49) is modified such that [55]

$$\kappa = \frac{n_s \omega_s}{c} + \frac{n_i \omega_i}{c} - 2\frac{n_P \omega_P}{c} + 2\gamma P_P = 0\,, \tag{2.66}$$

where $n_{s,i}$ may be expressed as

$$n_{s,i}(\lambda) = n_P(\lambda) \pm \delta n(\lambda)\,. \tag{2.67}$$

Here the effective index for the signal and idler is modified by an additional term $\delta n(\lambda)$ to account for propagation on a different axis to the pump, with the sign dependent on which axis the pump propagates. The wavelength dependence of the refractive index difference $\delta n(\lambda)$ can be ignored without significantly affecting the qualitative results of the phase-matching calculation [56]. The addition of this extra birefringence related term in the phase-matching equation acts in a similar way to an additional positive or negative contribution to the pump power (depending on the pump polarisation axis) although it is usually much greater in magnitude than the $2\gamma P_P$ term.

Of particular interest are regions where the gradient of the phase-matching curves (relating the generated signal and idler wavelengths to the pump wavelength) becomes zero. Close to these regions the bandwidth of the generated signal and idler wavelengths becomes narrow, and independent of the pump bandwidth. These regions can be observed in the anomalous dispersion regime for the idler when pumping on the fast axis of the fibre, and in the normal dispersion regime for the signal wavelength when pumping on the slow axis of the fibre.

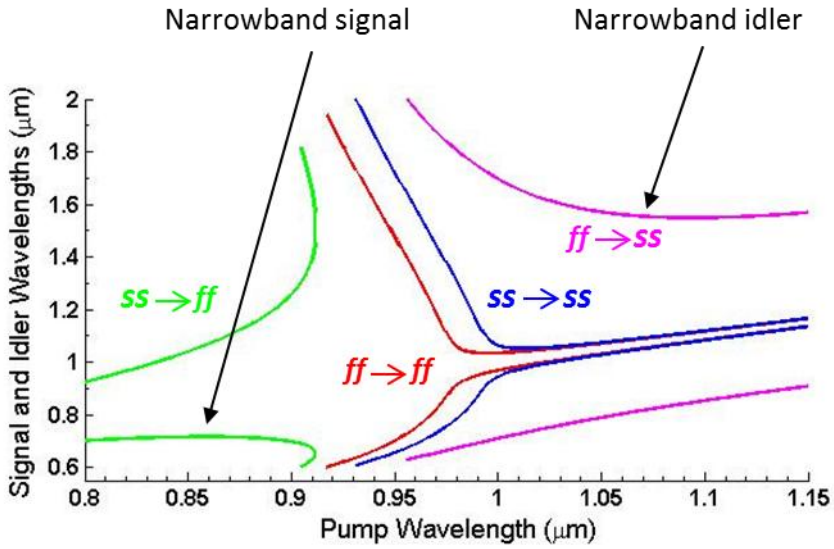

Figure 2.16: Calculated phase-matching curves for XFWM and co-polarised FWM. These results correspond to a PCF structure with Λ = 2.86 μm, d/Λ = 0.42 and D/d = 2.

The theory of XFWM is very similar to that of the co-polarised process. The most significant difference is that the gain for XFWM is around an order of magnitude lower, as the nonlinear coefficient for the process γ depends on n_2. In the case of a cross-polarised process the $\chi^{(3)}_{xxxx}$ coefficient in Eq. (2.29) should be replaced by $\chi^{(3)}_{xxyy} = \frac{1}{3}\chi^{(3)}_{xxxx}$ with n_2 reduced accordingly.

2.2.7 Pulse Walk-Off

The description of FWM in Section 2.2.3 and subsequent derivation of the parametric gain for the process in Section 2.2.5 both assume that the interacting fields are quasi-CW. In the case of a pulsed pump beam this represents the limit where the pump line-width is significantly less than the bandwidth of the parametric gain [52]. This simplifies the analysis significantly, as the time dependence of the electric field amplitudes can be ignored and only the spatial variation of the pulses (in the form of Eq. (2.56)) needs to be considered. In this approximation the pump, signal and idler fields remain overlapped in time throughout propagation through the fibre. In reality, group velocity dispersion leads to the three fields propagating with different group velocities so that the effective length of fibre over which parametric amplification of the signal and idler can occur is limited to the so-called 'walk-off length' for the three pulses. This is defined as the length scale over which the fastest travelling pulse completely moves through the slowest travelling pulse.

Fig. 2.9 shows the group velocity profile for bulk silica, which has a minima at the ZDW. The phase-matching requirement for FWM means that the pump pulse must be near the ZDW, and its group velocity will differ significantly from the generated signal and idler in the case of a large frequency offset Ω. Since the frequency separation of the signal and idler is symmetric about the pump, the difference in group velocity between them is much smaller, so that for co-polarised FWM the walk-off length L_{WO}, can be defined as

$$L_{WO} \approx T_P[v_g(\omega_P) - v_g(\omega_s)] \approx T_P[v_g(\omega_P) - v_g(\omega_i)], \tag{2.68}$$

where T_P is the temporal pulse width of the pump, which is assumed to be equal to the signal and idler pulse widths. The gain and bandwidth equations for FWM described in Section 2.2.5 are only valid over this length, and for longer lengths the overall effect can be considered as a summation of independent FWM interactions over fibre sections of length L_{WO}. This limits the minimum bandwidth that can be achieved by increasing the fibre length and also means that the power at the signal and idler wavelengths only increases linearly with fibre length for $L > L_{WO}$. Furthermore, when considering the generation of single photons through co-polarised FWM, lengths of fibre longer than result L_{WO} result in photons in a mixed state of comprised of multiple temporal modes (see Section 3.5.3).

While the issue of walk-off is also important for XFWM, in the case of birefringent phase-matching it is possible to match the group velocity of the pump with that of the signal or idler, and Eq. (2.68) then no longer applies. Under these conditions it is possible realise a narrowband signal (or idler) irrespective of the pump bandwidth. This is discussed further in Section 3.5.5.

2.2.8 Supercontinuum Generation

As described in Section 2.2.4, pumping in the normal dispersion regime of a PCF close to the ZDW leads to the generation of narrow signal and idler sidebands that are widely separated from the pump wavelength. By contrast, launching a high power pump pulse in the anomalous dispersion regime of a fibre often leads to the generation of supercontinuum, a broad output spectrum which may extend to more than 1000 nm in bandwidth in a fibre with an appropriate dispersion profile [57], with relatively little variation in the power across this range. The exact mechanism by which the supercontinuum is generated is complex, as it is dependent on a variety of nonlinear processes and varies significantly for different levels of

pump power and pump pulse duration [58]. Generally, the initial broadening of the pump occurs due to modulation instability or SPM, which leads to the formation of high order solitons in the anomalous dispersion regime of the fibre due to the interplay between dispersion and nonlinearity. These subsequently break up into fundamental solitons of different central wavelengths through soliton-fission, that shift to longer wavelengths through the Raman-induced soliton self-frequency shift, with an associated emission of nonsolitonic radiation on the short wavelength side of the spectrum [59].

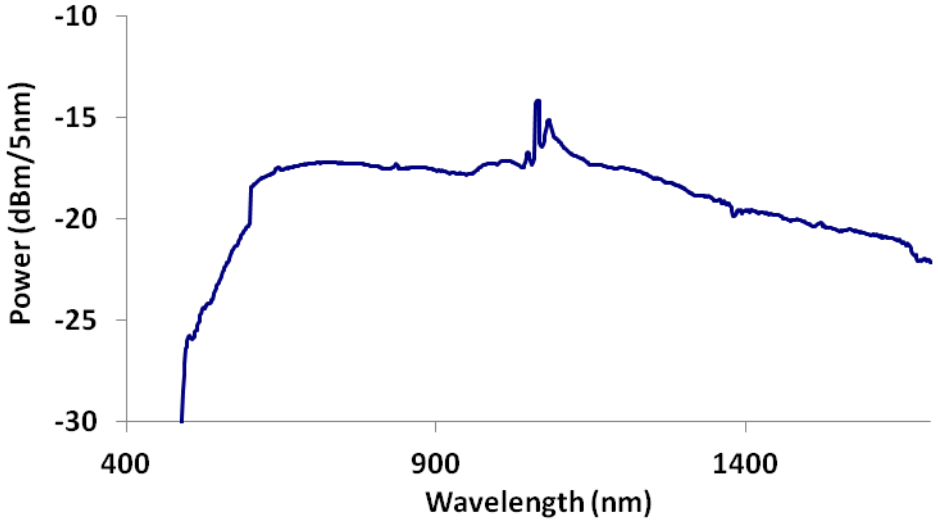

Figure 2.17: Measured generated spectrum for PCF-A, pumped using a high peak power, nanosecond pulsed microchip laser.

While supercontinuum generation is not the focus of the work presented in this thesis, it is relevant in two ways. Firstly, the broad and flat power spectrum of a supercontinuum, combined with the high power levels within a narrow spectral range make it a useful tool for characterising the transmission of fibre components. Combined with narrowband filtering, such a source can also provide light at a known reference wavelength for the purposes of calibrating wavelength sensitive components. Throughout the experimental work described in later chapters, a broadband PCF based supercontinuum source pumped with a high peak power, nanosecond-pulsed 1064 nm microchip laser (*Teem Photonics*, NP-10820) was used for these purposes. The PCF used (PCF-A) was a solid core fibre with a pitch (Λ) of 2.91 µm, a cladding hole to pitch ratio (d/Λ) of 0.35 and a calculated zero dispersion wavelength of 1061 nm. After pump pulse propagation through a 10 m section of this PCF the output spectrum spanned from 600 nm to more than 1700 nm as shown in the typical measured spectrum in Fig. 2.21. The narrow central peak at 1064 where the detector is saturated is the

residual unconverted pump light, and the two side bands are due to modulation instability. This PCF was similar in design to the supercontinuum PCF described in [49].

Supercontinuum generation is also relevant to this thesis because when attempting to observe very low levels of output light from a fibre, generated by some other nonlinear process, unintentional supercontinuum generation can be problematic if it overlaps with the wavelengths of interest. This situation is discussed in Chapter 7, where a birefringent PCF designed to generate photon pairs via XFWM in the anomalous dispersion regime of the fibre is described.

2.3 Manufacture of Optical Fibres

Both PCF and standard single-mode fibre are produced using a tower drawing process. Firstly, a macroscopic preform is fabricated. In the case of a standard fibre this will be a solid silica rod with the required index profile, and for PCF it will be a glass cane with the correct pattern of air holes to produce the desired fibre geometry. While the methods of producing the preform differ, the final stage of drawing the preform down to fibre is similar for both.

The preform for a standard fibre is fabricated from fused SiO_2 silica glass, with dopants added to either the core or cladding to produce the required index mismatch between the core and cladding. The glass for the preform needs to be of extremely high purity in order to achieve the low levels of loss associated with commercial fibre. In particular, care must be taken to avoid contamination of the preform with water, as the presence of OH-ions leads to a vibrational absorption peak that causes significant loss near 1.4 µm [60], in the desirable operating range close to 1550 nm, the wavelength of minimum attenuation.

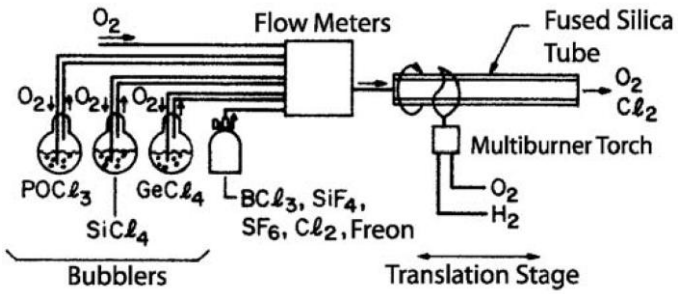

Figure 2.18: Schematic of the MCVD process, where silica is deposited on the inside of the silica tube to produce a fibre preform. (Image from [12]).

Fig. 2.18 shows a commonly used technique of preform fabrication based on modified chemical vapour deposition (MCVD). A multiburner torch is moved back and forth across the outside of a silica tube, uniformly heating the inside surface to around 1800°C. $SiCl_4$ and O_2 gases flow into the hot tube where they react to form small silica particles that fuse on the inner surface. Small quantities of boron or fluorine may also be added to lower the glass index in the cladding. After the cladding layer is formed $GeCl_4$ or $POCl_3$ dopants are added to the gas mixture to give a layer of higher index that will form the core. Finally, the burner temperature is raised, causing the tube to collapse into a solid preform rod, with the required index profile.

The technique required to produce a preform for PCF, is dependent on the desired fibre geometry and material. For fibres with unusual or irregular cladding geometries a preform can be produced by drilling a bulk sample of the glass, or softening the glass by heating and then extruding the material through a metal die [61]. These techniques are more commonly used when working with softer, highly nonlinear materials such as chalcogenide glasses. For preforms made from silica glass, the standard method is the stack and draw technique.

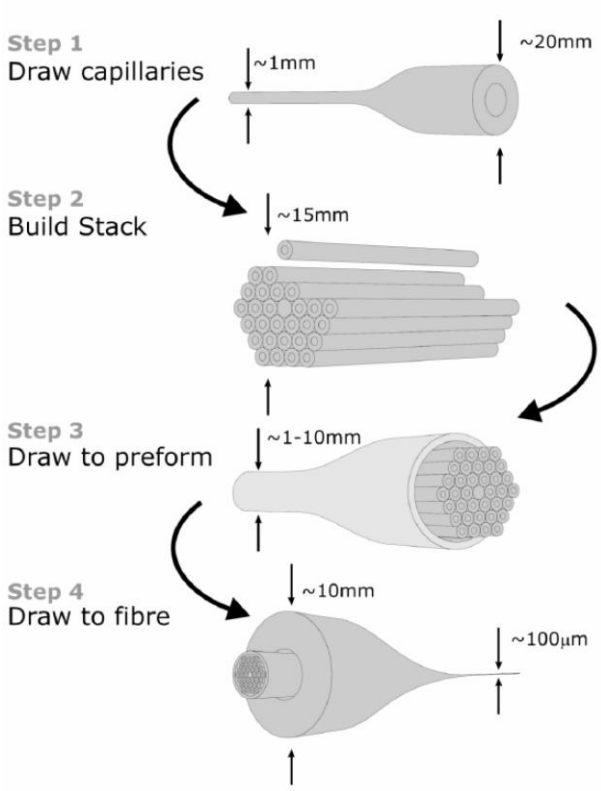

Figure 2.19: Stages of the manufacturing process of a PCF using the stack and draw technique. (Image from [62]).

Fig. 2.19 shows the various steps involved in the stack and draw technique in order to produce a PCF with a regular hexagonal cladding structure similar to that depicted in Fig 2.5. Firstly glass tubes of pure silica are drawn down in size to capillaries of around 1 mm diameter, using the same fibre drawing tower that is used to draw fibres from the preform in the final stage (step 1). Typically a single glass tube ~ 1m in length will produce a sufficient quantity of capillaries to produce the entire preform (also around 1 m in length). Additionally, a solid silica rod is drawn down to the same diameter as the capillaries, which will be used to form the core. The capillaries are then stacked into a hexagonal array with same geometrical arrangement required in the finished fibre, with the capillary at the centre replaced with the solid core rod (step 2). The whole structure is then placed within another silica tube and fused at one end, before being drawn on the fibre tower again to make a preform (step 3). Generally a vacuum is applied to the inside of the outer tube (with ambient pressure inside the capillaries), which encourages the small interstitial holes between the capillaries to collapse.

Before being drawn to fibre the preform is placed inside another silica tube to achieve the desired outer diameter for the fibre after drawing (step 4). The wall thickness of the glass tube in the first stage is selected such that the air filling fraction in the preform is close to that required in the final fibre. Similarly, the diameters for the capillaries and glass rod are chosen so that the when the structure is drawn down to fibre with cladding holes of the desired size, the outer diameter of the fibre will be close to that of standard single-mode fibre. This ensures that the fibre will have sufficient mechanical strength and is compatible with standard fibre accessories, such as bare fibre adaptors etc.

The final stage of drawing a preform down to fibre is similar for both PCF and conventional fibre. The preform is fed at a rate of a few $mm \cdot min^{-1}$ into a furnace at around 2000°C. Fibre is drawn off the bottom of the softened preform at a rate of a few ms^{-1} by the tension from a rotating capstan. As the total volume of material is conserved during this process, the difference in speed leads to the output fibre maintaining the same geometry as the preform, but with a greatly reduced diameter. A diameter monitor is used for feedback control of the draw speed to ensure the fibre remains uniform. A polymer coating is also applied to the outside of the fibre and cured before it reaches a winding drum. During this process, pressure of a few kPa is typically applied to the cladding holes in order to prevent them collapsing under surface tension. Adjusting this pressure allows PCFs with different cladding structures to be produced from a single preform.

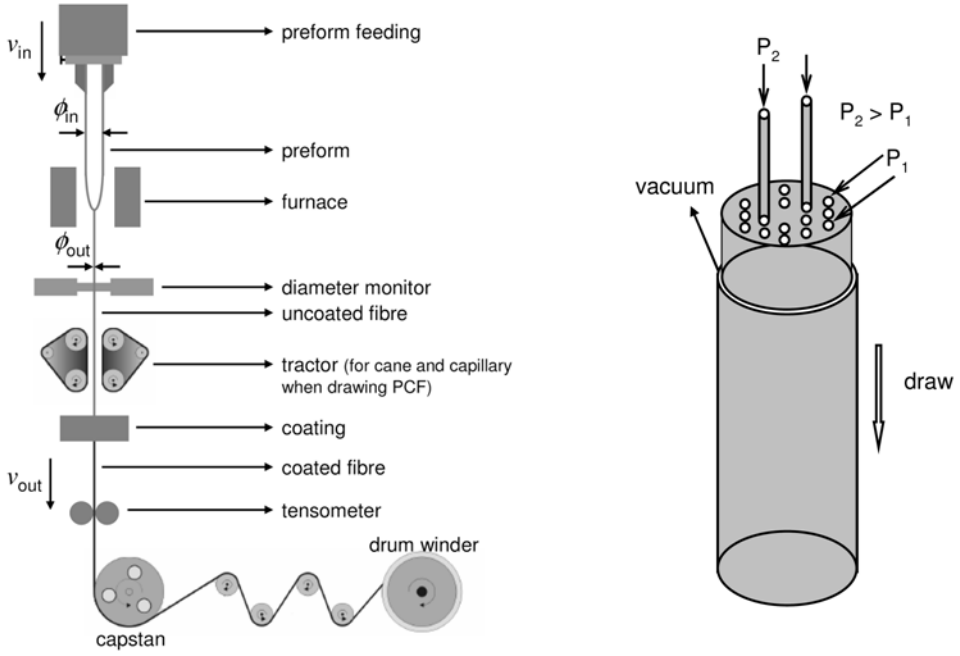

Figure 2.20: (a) Schematic diagram of a fibre draw tower showing a preform being fed into the furnace at the top and fibre drawn out at high speed from below; (b) Technique to manufacture birefringent PCF. Differential pressure is applied to the holes around the core of the preform compared to the rest of the cladding as it is drawn to fibre. (Images from [63]).

In order to produce birefringent PCF of the type discussed in Chapter 7, two holes on either side of the core need to be enlarged during manufacturing. In this case a differential pressure is applied in these holes relative to the rest of the cladding, by means of narrow capillaries inserted into these holes. Alternatively, during production of the preform for this type of fibre, these holes can be made initially bigger by using capillaries with a thinner wall thickness. This ensures that the fibre structure does not become distorted by excessive enlargement of these holes when the preform is drawn to fibre.

2.4 Splicing

Splicing is a technique that allows two individual fibres to be permanently joined, by first aligning the fibre cores and positioning them close together, and then heating the end region of the fibres to soften them. The heating can be achieved either by using a current carrying filament positioned around the splice position or by means of an electrical discharge around the fibres. As the fibres are heated they are pushed together slightly using motorised mounts, such that the glass at the interfaces fuses. Not only are splices mechanically robust and unable

to be misaligned, unlike free-space coupling, but for conventional fibres of the same type, losses of < 0.1 dB can be readily achieved using fully automated, commercial splicer systems.

Splicing of PCF to conventional fibre is usually considerably more difficult and the minimum loss level that can be achieved is dependent on the PCF structure. The two main reasons for the splice loss when splicing PCF are the mismatch of the mode fields of the two fibres and the deformation of the PCF structure that can occur upon heating [64]. Deformation will occur when the glass is softened, as the surface tension of the small air holes in the cladding will cause them to reduce in size. The reduction in the index contrast between the core and cladding will cause the mode field of light in the PCF to expand. At the relatively high temperatures involved for splicing of conventional fibres, the air holes may collapse entirely, meaning the structure is no longer waveguiding close to the splice region, leading to very high loss. In order to avoid this, the temperature and duration of the heating during splicing should be reduced. The extent to which the two fibres are pushed together during splicing should also be reduced, as the glass in the PCF will not be soft enough the fibres to be pushed together forcefully and would lead to bending of the fibres or damage to the PCF structure at the end face.

In order to achieve high overlap between the mode fields of a PCF and conventional fibre at a splice it is best if the mode field diameters (MFD) of the chosen fibres are similar in size. If achieving a low loss splice is important then the core size of the chosen PCF should therefore match the MFD of the chosen conventional single mode fibre. The splice loss can be further reduced if the MFD of the PCF is gradually expanded until it matches that of the conventional fibre by a controlled collapse of the cladding structure. In the case where the change in the cladding structure is gradual along the fibre length the theoretical minimum losses achieved by this method can be very low [65]. Experimentally this can realised by repeatedly applying short bursts from the heat source that was used to make the initial splice and monitoring the decrease in the splice loss, looking for the minimal loss that occurs when the MFDs of the fibres are matched [66].

Chapter 3

Single Photon Theory and Applications

In recent years, the ability to produce single photons in pure states has become highly relevant to the field of quantum information. As a result of their many desirable characteristics, photons are one of the most well studied systems used for the encoding and manipulation of quantum information in the form of qubits. The continued development of single photon sources will be of great importance, both in the short term as a resource for the study of more complex quantum information systems, and in the future to make commercial applications based on this work feasible.

While the theory of the generation of light at new frequencies by a nonlinear interaction in a PCF was discussed in some detail in Chapter 2, the focus there was on the regime of high pump power. This chapter will consider the theory relating to the underlying nature of the generated light fields, which becomes apparent when a low peak power pulsed pump source is used and only a single pair of signal and idler photons are produced on a given pulse of the pump laser. This will be important in later chapters of this thesis to understand the properties of the fabricated source of single photons that was based on this process.

Section 3.1 describes the concept and basic properties of a qubit and some of the reasons why photons are an attractive option for realising a physical qubit. A mathematical description of a pure photon state is defined in Section 3.2, and later in Section 3.3 it is seen that such pure state photons can demonstrate non-classical Hong-Ou-Mandel interference when brought together at a beam-splitter, if their states are not only pure but also indistinguishable.

Section 3.4 summarises some of the ways in which single photon states have previously been produced. In particular, Section 3.4.3 gives an introduction to the concept of heralded single photon sources based on parametric generation of correlated photon pairs, which was the approach taken to generate photons in the experimental work described in later chapters. Section 3.5 extends upon the theory of FWM given in Chapter 2, in order to understand the factors affecting the purity of the generated photons. This chapter concludes with a discussion of some of the potential applications of the photonic qubits that can be realised with a source of pure state single photons.

3.1 Qubits

The ultimate goal of quantum information (QI) science is to be able to understand and manipulate the quantum states of physical systems in order to represent, communicate and process information. Of particular interest are two-level quantum systems, known as qubits in analogy with classical bits. These represent a fundamental resource of many quantum information protocols. Like a regular bit that can take values of zero or one, a qubit can exist in either of two possible eigenstates of the quantum system. The difference arises due to the fact that a quantum system can also exist in a superposition of these eigenstates. The general state of the qubit can therefore be expressed as

$$\left|\psi_{qubit}\right\rangle = \alpha\left|a\right\rangle + \beta\left|b\right\rangle, \tag{3.1}$$

where $|a\rangle$ and $|\ b\ \rangle$ are the eigenstates of the system, α and β are arbitrary complex coefficients, and the state of the system is normalised such that

$$\left|\alpha\right|^2 + \left|\beta\right|^2 = 1. \tag{3.2}$$

In addition to the superposition states that can be obtained with a single qubit, multiple qubits can exhibit non-local correlations between their states which have no analogue in classical bits. For a system consisting of two qubits, both with eigenstates $|a\rangle$ and $|\ b\ \rangle$, the state of the overall system can be described by

$$\left|\psi_{2-qubit}\right\rangle = \alpha_{aa}\left|a\right\rangle_1\left|a\right\rangle_2 + \alpha_{ab}\left|a\right\rangle_1\left|b\right\rangle_2 + \alpha_{ba}\left|b\right\rangle_1\left|a\right\rangle_2 + \alpha_{bb}\left|b\right\rangle_1\left|b\right\rangle_2, \tag{3.3}$$

where the subscripts 1 and 2 refer to the two individual qubits and the amplitude coefficients α are again chosen such that the state of the system is normalised. For some values of these amplitudes it is possible to factorise the state of the system in the form of

$$\left|\psi_{2-qubit}\right\rangle = \left(\alpha_1\left|a\right\rangle_1 + \beta_1\left|b\right\rangle_1\right)\otimes\left(\alpha_2\left|a\right\rangle_2 + \beta_2\left|b\right\rangle_2\right), \tag{3.4}$$

such that the states of the two qubits are independent and the measurement of one has no effect on the other. However, for a general two-qubit state given by Eq. (3.3) it may not be possible to make this factorisation. In that case the states of the qubits are entangled. For example, the state

$$\left|\Phi^-\right\rangle = \frac{1}{\sqrt{2}}\left(\left|a\right\rangle_1\left|a\right\rangle_2 - \left|b\right\rangle_1\left|b\right\rangle_2\right), \tag{3.5}$$

is described as maximally entangled, since the measurement of one of the qubits gives complete information on the state of the other. This is the form of one of the four maximally entangled Bell states that are of significant interest in QI applications [67].

The mathematical description of idealised qubits given by Eq. (3.1) is quite general and there are many potential physical two-level quantum systems that could be used to realise them. There are several important criteria that a physical system must meet in order to be considered as a useful qubit [68]. The system must have two well defined quantum states and be able to be reliably initialised to a desired starting state before any experiment in order to encode information. For the purposes of quantum information processing (QIP) it is also necessary to be able to manipulate the state of the qubits after initialisation, including implementing interactions between the states of two separate qubits, and be able to reliably detect the output qubit state. Finally the qubit should be stable against decoherence of its quantum state due to interactions with the environment. This last requirement is necessary to ensure that the qubit state survives for long enough for a desired QIP task to be completed. In the case of qubits for quantum communications systems it is also necessary to be able to faithfully transmit qubits between locations without degradation of the qubit state.

Some examples of the types of systems that have been investigated for their use of qubits include the states of trapped ions [69], nuclear magnetic resonance in ensembles of molecules [70] and magnetic flux in loops of superconducting material [71]. Working with these qubits is usually challenging due to the difficulty of isolating molecules to minimise their interaction with their surroundings. For this reason such sources tend to exhibit short coherence times and often require operation at cryogenic temperatures in order to suppress thermal noise.

One of the most widely studied and promising qubit candidates is the single photon. There are several different degrees of freedom of a photon that can potentially be used as the qubit states. For instance, photons emitted from a source at different times could be used, with the two states given by the presence or absence of a photon in a given 'time bin'. Alternatively the photon could be sent into one of two paths through a system with the data being encoded based on which path the photon is present in. One of the most useful qubit representations for the photon is its polarization state. This has two orthogonal well defined states and can be easily manipulated by standard optical components such as wave-plates and beam-splitters. Furthermore, established detector technology for detecting single photon levels of light means the state of photonic qubits can be measured relatively easily.

The other major advantage of photons is that they are far more resistant to the effects of decoherence due to the weakness of the interaction between photons and a dielectric transmission medium such as silica glass. The long lifetime over which the qubit state remains viable with high probability means that photons have ideal properties for the transmission of qubits over large distances by taking advantage of waveguiding structures such as optical fibre (see Section 2.1.1). It was initially believed that the weak nonlinear coupling between photons via the transmission medium would rule out any possibility of interacting light pulses with each other at the single photon level and thus make QIP with photons unfeasible [116]. However it was later discovered that an effective interaction could be realised between single photons via by taking advantage of non-classical interference between identical photons (see Section 3.3) where the required nonlinearity is realised by the measurement of the photons [72]. For this reason the development of single photon sources that can produce exactly one photon with fixed properties, reliably and on demand remains one of the major areas of research in the field of QIP at present. The applications of single photons will be discussed further in Section 3.6.

3.2 Pure Single Photon States

Ever since the early experiments of the 20th century into the nature of light, such as the investigation of the photoelectric effect, it has been understood that at a fundamental level electromagnetic waves are composed of discrete quantised excitations of the electromagnetic field known as photons. A theory of light in which the field consists of discrete energy levels can be developed by considering the optical modes of a hypothetical bounded cavity [73]. This allows the energy states of the system to be described using the model of a quantum harmonic oscillator with energy levels E_n given by

$$E_n = \left(n + \frac{1}{2}\right)\hbar\omega_k \qquad n = 0, 1, 2,\ldots, \tag{3.6}$$

where ω_k is the angular frequency of the electromagnetic wave under consideration with wavevector k. The allowed values of ω_k are defined by the modes of the cavity in the case of the bounded system but become continuous for optical fields in free-space. For a monochromatic field of angular frequency ω_k the state of the system can expressed in terms of the number states (or Fock states) which are eigenstates of the harmonic oscillator with energy levels given by Eq. (3.6), so that

$$\hat{H}\left|n\right\rangle_k = E_n\left|n\right\rangle_k, \tag{3.7}$$

where $\hat{H}$ is the Hamiltonian operator of the system and $\left|n\right\rangle$ is a pure Fock state where there are exactly n photons in the mode of frequency ω_k.

In order to describe nonlinear processes in which photons are created in a mode of one frequency by the annihilation of photons in other frequency modes, it is useful to define a creation operator $\hat{a}_k^\dagger$, and annihilation operator $\hat{a}_k$. These act respectively to either create or destroy one photon in a mode with wavevector k when applied to the number state, such that

$$\hat{a}_k^\dagger\left|n\right\rangle_k = \left(n+1\right)^{1/2}\left|n+1\right\rangle_k, \tag{3.8}$$

and

$$\hat{a}_k\left|n\right\rangle_k = n^{1/2}\left|n-1\right\rangle_k. \tag{3.9}$$

Any number state of *n* photons can be therefore be expressed in terms of the vacuum state (containing zero photons) through successive application of the creation operator,

$$\left|n\right\rangle_k = \frac{1}{(n!)^{1/2}}\left(\hat{a}_k^\dagger\right)^n\left|0\right\rangle. \tag{3.10}$$

The relationship between the creation and annihilation operators for a mode and the number of photons in that mode can be further explored by considering the effect of applying both of these operators (as given by Eqs. (3.8) and (3.9)) on a pure number state, showing that

$$\hat{a}_k^\dagger\hat{a}_k\left|n\right\rangle_k = n_k\left|n\right\rangle_k. \tag{3.11}$$

The product $\hat{a}_k^\dagger\hat{a}_k$ is the number operator and for a general system state vector $\left|\psi\right\rangle$, which could be a superposition of number states, the average number of photons in the mode of frequency ω_k will be given by

$$\left\langle n_k\right\rangle = \left\langle\psi\left|\hat{a}_k^\dagger\hat{a}_k\right|\psi\right\rangle. \tag{3.12}$$

For the case where *n* = 1, the number state representation given in Eq. (3.10) provides a description of a single photon state of definite frequency ω_k. However, the assumption that the photon should be monochromatic means that this state represents an excitation that extends over all space and time, much like the theoretical plane waves of classical optics. This seems to go against the commonly held description of a photon as a particle-like quantum of energy, localised in some region of space and time [74]. Such a localised photon state can be realised by considering an integral over one photon Fock states of different frequencies [75]

$$\left|\psi(\omega_k)\right\rangle = \int d\omega\cdot f(\omega)\hat{a}^\dagger(\omega)\left|0\right\rangle, \tag{3.13}$$

where $\left|\psi(\omega_k)\right\rangle$ is a localised single photon state with frequency centred on ω_k and $f(\omega)$ is a weighting function resulting in finite bandwidth of the state. Experimentally the spectral bandwidth of the photon state and consequently the form of the function $f(\omega)$ are determined by the gain bandwidth of the process from which the photon is generated (see Section 3.5) and the profile of any subsequent spectral filtering that it undergoes (see Section 3.5.1). The inverse Fourier transform of the spectral profile of the state determines the coherence time of the photon wave packet $\Delta\tau_c$. Assuming a Gaussian spectral profile of FWHM bandwidth $\Delta\lambda$ and central wavelength λ_0, this will be given by

$$\Delta\tau_c = \frac{2\ln 2}{nc\pi}\frac{\lambda_0^2}{\Delta\lambda}, \tag{3.14}$$

where c is the speed of light and n is the refractive index of the material in which the photon is propagating. For photons of bandwidth $\Delta\lambda$ to be considered temporally indistinguishable from each other, in order to demonstrate non-classical interference (see Section 3.3), they must be overlapped in time to within $\Delta\tau_c$.

3.3 Hong-Ou-Mandel Interference

One striking result of the non-classical nature of single photon states is the observation of two-photon quantum interference that can be observed when indistinguishable single photon states are incident on the two input ports of a beam-splitter. The effect, which is known as Hong-Ou-Mandel (HOM) interference [76], results in photon bunching such that both photons exit from the same beam-splitter output.

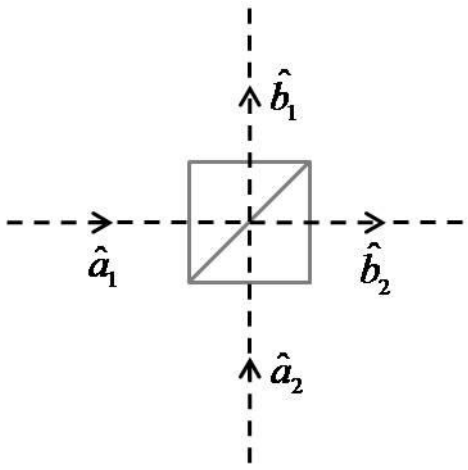

Figure 3.1: The input and output modes of a beam-splitter.

To understand the origin of HOM interference it is necessary to consider the relationship between a general input photon state to an idealised lossless beam-splitter and the resultant output state [77]. For a beam-splitter with input modes $\hat{a}_{1,2}$, output modes $\hat{b}_{1,2}$ and reflection and transmission coefficients r and t, the photon creation operators for the different paths are related by

$$\hat{a}_1^\dagger = r\hat{b}_1^\dagger + t\hat{b}_2^\dagger, \quad \text{and} \qquad \hat{a}_2^\dagger = t\hat{b}_1^\dagger - r\hat{b}_2^\dagger, \tag{3.15}$$

where the minus sign in the second expression is a result of the phase-shift required to satisfy conservation of energy [78]. For a single polarisation state these expressions are universal for all types of beam-splitters and are also applicable to fused-fibre couplers.

For a single photon input into one of the input arms of the beam-splitter described by

$$\left|\psi_{in}\right\rangle = \left|1\right\rangle_{a1} = \hat{a}_1^\dagger \left|0\right\rangle, \tag{3.16}$$

the final state after the beam-splitter will be a single photon in a superposition of the two output modes

$$\left|\psi_{out}\right\rangle = \left(r\hat{b}_1^\dagger + t\hat{b}_2^\dagger\right)\left|0\right\rangle_{b1}\left|0\right\rangle_{b2} = r\left|1\right\rangle_{b1}\left|0\right\rangle_{b2} + t\left|0\right\rangle_{b1}\left|1\right\rangle_{b2}. \tag{3.17}$$

While the photon can only be found in one of the two output arms after measurement, the probability amplitude of the photon wavefunction before measurement is non-zero in both arms. In the case where two photons are input simultaneously the beam-splitter these wavefunction contributions in the two arms can interfere.

When two indistinguishable single photon states are input to the system, one in each arm of the beam-splitter the two-photon state is described by

$$\left|\psi_{in}\right\rangle = \left|1\right\rangle_{a1}\left|1\right\rangle_{a2} = \hat{a}_1^\dagger \hat{a}_2^\dagger \left|0\right\rangle. \tag{3.18}$$

Using the input and output beam-splitter relations given in Eq. (3.15), the resultant state is given by

$$\begin{aligned}\left|\psi_{out}\right\rangle &= \left(r\hat{b}_1^\dagger + t\hat{b}_2^\dagger\right)\left(t\hat{b}_1^\dagger - r\hat{b}_2^\dagger\right)\left|0\right\rangle_{b1}\left|0\right\rangle_{b2} \\ &= \left(rt\hat{b}_1^\dagger\hat{b}_1^\dagger + \left(t^2 - r^2\right)\hat{b}_1^\dagger\hat{b}_2^\dagger - rt\hat{b}_2^\dagger\hat{b}_2^\dagger\right)\left|0\right\rangle_{b1}\left|0\right\rangle_{b2}.\end{aligned} \tag{3.19}$$

For the case of an ideal lossless 50:50 beam-splitter the reflectivity and transmittance must be equal, and sum to one in order to satisfy energy conservation so that.

$$\left|r\right|^2 + \left|t\right|^2 = 1 \qquad \text{and} \qquad r = t = \frac{1}{\sqrt{2}}. \tag{3.20}$$

Here r and t are assumed to be real, although a more general analysis allowing for complex reflection and transmission coefficients leads to the same result. For the 50:50 beam-splitter the output state in Eq. (3.19) therefore reduces to

$$\begin{aligned} |\psi_{out}\rangle &= \frac{1}{2}\left(\hat{b}_1^\dagger \hat{b}_1^\dagger - \hat{b}_2^\dagger \hat{b}_2^\dagger\right)|0\rangle_{b1}|0\rangle_{b2} \\ &= \frac{|2\rangle_{b1}|0\rangle_{b2} - |0\rangle_{b1}|2\rangle_{b2}}{\sqrt{2}}, \end{aligned} \tag{3.21}$$

where the difference of the factor of $\sqrt{2}$ in the denominator results from successive application of the creation operators (see Eq. (3.10)).

The output state shown in Eq. (3.21) demonstrates the effect of photon bunching that occurs for the two photon state as a result of HOM interference. As in the one photon case, the photons can still go either way at the beam-splitter, resulting in a superposition of having photons in the two output arms of the device. However, due to the cancellation of the $|1\rangle_{b1}|1\rangle_{b2}$ terms, both photons will always be found in the same output arm of the beam-splitter. It is important to note that in the derivation of this result it was assumed that the input photon states were identical. If the photons are partially distinguishable in some degree of freedom (see Section3.5) then the input state of the system cannot be described by identical pure photon states as in Eq. (3.18), leading to a reduction in the observed bunching effect due to only partial cancellation of the $|1\rangle_{b1}|1\rangle_{b2}$ terms. In particular, when the time of arrival of the two photons at the beam-splitter is varied (assuming indistinguishability in all other degrees of freedom) the measured coincident count rate between photon detectors placed at the two output ports of the beam-splitter will exhibit a pronounced reduction when the arrival time is exactly matched due to this bunching effect. This feature of the measured coincident count is often referred to as a HOM dip and is illustrated in Fig. 3.2.

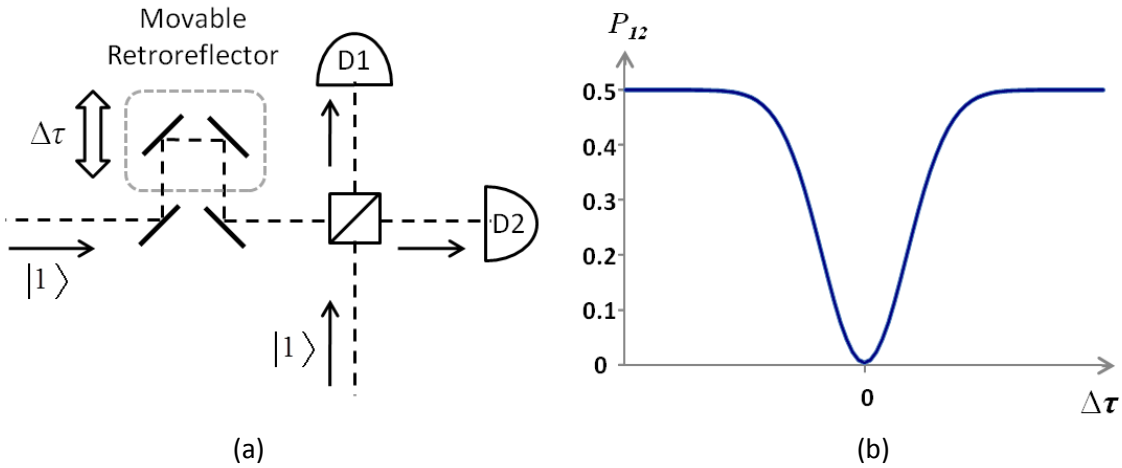

(a) (b)

Figure 3.2: (a) Experimental setup to observe HOM interference between two indistinguishable single photon states, input into the two input ports of a beam-splitter. The relative difference in the arrival times of the photons at the beam-splitter, $\Delta\tau$, can be controlled using the moveable retroreflector. D1 and D2 are single photon detectors. (b) Probability of observing two-fold coincidence between the detectors as $\Delta\tau$ is varied.

In for the case of indistinguishable spectrally filtered photons, the form of the HOM dip is given by [78]

$$P_{12} = \frac{1}{2}\left(1 - V\exp\left[-\frac{(\sigma\cdot\Delta\tau)^2}{2}\right]\right), \tag{3.22}$$

where P_{12} is the probability of seeing detections at both D1 and D2 given that two photons were input to the beam-splitter, $\Delta\tau$ is the time difference between the arrival of the two photons at the beam-splitter and V is the visibility of the interference feature, taken to have the maximal value of 1 in the case of Fig. 3.2. The visibility that will be observed for the HOM dip depends on the extent to which the photon states can be considered indistinguishable. The effects of timing jitter and polarisation state on the visibility are considered in Sections 3.5.3 and 3.5.4, and the importance of spectral purity is addressed in Section 3.5.1. The effect of higher photon numbers on the expected visibility is considered in Section 3.5.2.

As described in Section 3.2, for photon states which are temporally localised the photons must necessarily possess a finite bandwidth, as described by Eq. (3.13). This defines the bandwidth of the dip, given by the parameter σ in Eq. (3.22). For photon sources where filtering is used to achieve spectral purity, σ is given by the standard deviation of the width of the filter profile (see Section 3.5.1). If the photons are not spectrally filtered prior to the interference then the dip width is governed by the coherence length of the generated photon wave packets [79].

The initial interest in this interference effect was as a technique to measure the duration of short pulses of light in the low power regime due to the limited timing resolution of single photon counting detectors.

HOM interference is an inherently quantum effect and, unlike the more familiar examples of classical interference, affects the correlation between the electric field at two separate points in space as a result of the interaction between two sources. An analysis of the experiment illustrated in Fig. 3.2 using classical optics theory predicts a maximum observable interference visibility of 0.5 [80], while the result for the quantum analysis, described by Eq. (3.22) can demonstrate a perfect visibility of 1. This effect cannot be considered as simply an interaction between photons at a single point in space, but rather as a result of the indistinguishability of the two paths through the beam-splitter on the two-photon state amplitude. This distinction is clearly demonstrated by experiments in which, through an appropriate choice of optical delay in the input and output arms, HOM interference was observed between two single photon inputs, even though the photons were not present in the beam-splitter at the same time [81]. The correlation in the two photon state resulting from HOM interference means that the presence of a photon in one arm of a beam-splitter can influence the behaviour of another, despite the usual weak interaction between light beams at single photon levels of power, leading to several applications in QI (see Section 3.6.2). The HOM effect is also of importance in evaluation of the performance of single photon sources. Since the visibility of the HOM dip depends on the indistinguishability of the input photon states, measurement of HOM interference can be used to establish the purity of the generated photon state.

3.4 Generation of Single Photon States

The number state representation of optical fields considered in Section 3.2 allows for a simple theoretical description of a single photon state $|1\rangle$. There are two important factors to consider in the design of a single photon source capable of generating such a state. The first is quite obvious, in that the source should output exactly one photon upon operation, no more or less. This idealised source which is capable of deterministically producing single photons upon the input of some triggering signal is often referred to as a photon gun. Reliably producing such a single photon state in practice, without subjecting the photon to a destructive measurement to confirm its existence and purity, requires an understanding of the underlying statistics of the process by which the light is generated.

There are three main approaches for realising a single photon state which will be discussed further in the following sections. These are the strongly attenuated output of a coherent light source such as a laser, the photon emission from a single two-level quantum system such as a single atom or quantum dot, and the photons generated through nonlinear parametric interaction of an intense optical pump beam with a bulk medium.

The second criteria that an ideal source should adhere to, in addition to the limitation on the photon number, is that the photons should be output into a well defined quantum state which is invariant upon each operation of the source. Most commonly this would be a pure single mode state, although for some situations, most notably in certain quantum cryptography protocols, the requirements are less stringent [82]. As many of the applications in QI are dependent on the interference of two or more indistinguishable photons, it is also desirable to be able to select the characteristic properties of the generated photon states for manufactured sources in a reproducible manner. This enables multiple compatible sources to be produced with output states that are suitable for demonstrating high visibility interference with each other.

In order for single photons states to be considered indistinguishable they must be identical in all degrees of freedom. This includes their spectral properties, temporal mode (relative output time from the source), spatial mode and polarisation state. Achieving purity in each of these properties is discussed throughout the later sections of this chapter in the context of an optical fibre-based source. Achieving a single spatial mode output for generated photons will not be covered in this chapter, as it can be guaranteed by the use of single-mode fibres as described in Section 2.1.3.

3.4.1 Attenuated Coherent Light

In classical optics the most stable type of light source that can be realised is a perfectly coherent, single polarisation state, monochromatic beam, which is close to what can be achieved using a stable pulsed laser source. It may therefore appear logical to consider attenuating such a beam until it contains only a single photon per pulse on average. However it will be shown in this section that such a scheme gives a relatively poor approximation of the idealised single photon source described in Section 3.4, due to the underlying photon number statistics of a coherent light source.

The scalar electric field $E(z,t)$ of a classical coherent light source is described mathematically by

$$E(z,t) = E_0 \sin(kz - \omega t + \theta), \tag{3.23}$$

where the peak field amplitude E_0 and relative phase θ are both independent of time. The intensity I of such a light source defines the number of photons *n*, which would be expected to be present in a section of the beam of length L

$$\mu \equiv \langle n \rangle = \frac{IA}{\hbar\omega}\frac{L}{c}, \tag{3.24}$$

where A is the cross-sectional area of the beam and μ is the average number of photons in the given length. In the limit where the length of the section under consideration becomes very small or the beam intensity is low, the particle like nature of the photons constituting the light beam becomes apparent. These photons are randomly distributed throughout the beam so that in the limit $\mu \to 0$ there will be a significant variation in the number of photons contained in each section relative to the average number due to shot noise and virtually every section will contain either one or zero photons. If the beam section of length L is divided into N subsections each with probability p_1 of containing one photon where

$$p_1 = \frac{\mu}{N}, \tag{3.25}$$

then the probability of the length L containing exactly n photons, $P(n,\mu)$, for a given average expected number μ is given by

$$P(n,\mu) = \frac{N!}{n!(N-n)!}\, p_1^n \left(1 - p_1\right)^{N-n}. \tag{3.26}$$

For $N \to \infty$ this can be shown to be equivalent to the Poisson distribution [67], where

$$P(n,\mu) = \frac{\mu^n e^{-\mu}}{n!} \qquad n = 0, 1, 2,\ldots \tag{3.27}$$

An equivalent quantum representation of the classical coherent states [83] can be expressed in the number state basis (see Section 3.2) as

$$\left|\alpha_{\mu}\right\rangle = \exp\left(-\left|\alpha\right|^{2}/2\right)\sum_{n=0}^{\infty}\frac{\alpha^{n}}{\sqrt{n!}}\left|n\right\rangle, \tag{3.28}$$

where $\left|\alpha_{\mu}\right\rangle$ is the coherent state with average photon number μ, $\left|n\right\rangle$ are the number states described previously and $\left|\alpha\right|^{2} = \mu$. Since the coherent state is defined as a superposition of individual number states, the number of photons found upon repeated measurement will show variation as expected due to the shot noise.

This quantum representation of the coherent state likewise has photon number statistics that follow the Poisson distribution described in Eq. (3.27), and can be applied to the case of a strongly attenuated pulsed laser, where n and μ are the number of photons passing through the attenuating element on a given pulse of the laser, and the expectation value of the number of photons transmitted per pulse respectively. The shape of the Poisson distribution is shown for several values of μ in Fig. 3.3.

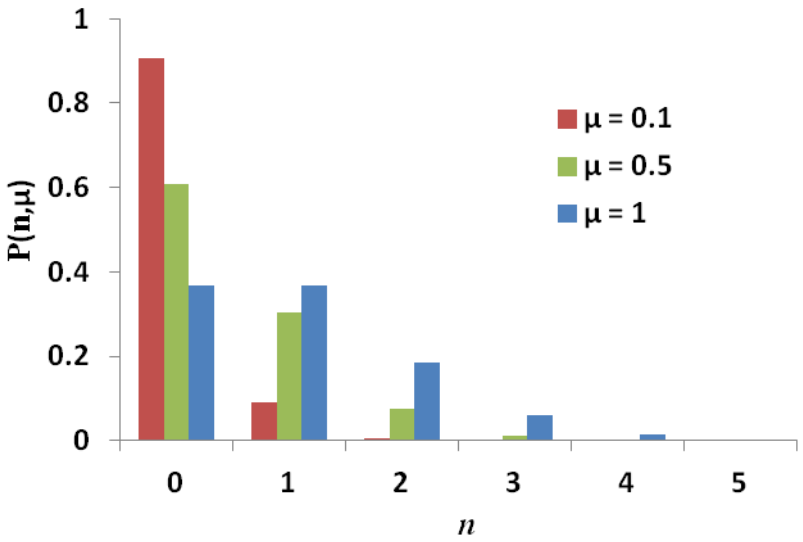

Figure 3.3: Poisson distribution showing the probability of producing exactly n photons for different average expected photon numbers μ.

The coherent state described in Eq. (3.28) has the highest probability of being found in the number state closest to the average value of μ, but has a finite probability of being found in the number states of higher and lower value around this peak value. Operating with $\mu = 1$means there will be a significant probability (~ 18%) that the source will output two photons. The only way to reduce the multi-photon emission probability, as required for an

ideal single photon, is to reduce the average number of photons emitted from the source per pulse, typically so that $\mu \leq 0.1$. However, in that case the $|0\rangle$ number term will dominate the state and most of the laser pulses will not produce any photons. Due to the stochastic nature of the exact number of photons that will be transmitted through any attenuating element there is no way to tell without a destructive measurement which of the laser pulses produced a single photon. The attenuated coherent source therefore cannot be used to generate the pure $|1\rangle$ state and the vacuum contribution to the output state renders it useless for most QI applications (see Section 3.6).

3.4.2 Single Emitter Sources

As described in Section 3.4.1, the probabilistic nature of photon emission for classically stable coherent sources, makes it impossible to predict exactly when a photon will be output from the source. This is in contrast to the idealised photon source described in Section 3.4, which should emit exactly one photon on demand. One approach to achieving such a deterministic output is by using the photons produced by electronic transitions in a single quantum emitter. This type of source was first demonstrated by observing the fluorescence seen from single isolated atoms pumped into an excited energy state using a laser [84]. Due to the time required for such a system to relax into its ground state by photon emission, only a single photon can be output from such a source if the laser pulse used to pump the atom into its excited state is sufficiently short. In addition to atoms, many other types of systems, possessing well defined energy levels and allowing only a single excitation, have been demonstrated to generate single photons, including trapped ions [85], dye molecules [86], quantum dots [87] and nitrogen vacancy defects in diamond [88]. Quantum dots and N-V centres in diamond are of particular interest, as their larger physical size allows them to be more easily incorporated into solid state cavities in order to enhance the emission rate of generated photons into a desired output spatial mode [89].

While single emitter sources may one day offer high brightness and pure single photons on demand, there are several common drawbacks currently preventing their widespread adoption for QI applications. For atom-based sources there is the inherent difficulty of maintaining the isolation of a single atom for an extended period of time. For solid state sources based on quantum dots or N-V centres it is difficult to reliably reproduce emitters with identical properties, such that the outputs from two sources are identical pure states that

could be used to demonstrate high visibility interference effects (see Section 3.3). These sources also commonly require cryogenic operating temperatures in order to suppress thermal broadening of the spectral line-width of the emission process, which would otherwise reduce the purity of the generated photons [83].

3.4.3 Parametric Generation and Heralding

An alternative approach for generating single photon states is to take advantage of parametric interaction that can be observed when an intense pulse of laser light propagates through a nonlinear medium. As discussed in Section 2.2, such parametric processes result in a transfer of energy from the pump to generated light at other frequencies, determined by phase-matching conditions. For degenerate FWM (see Section 2.2.3), signal and idler photons are generated at frequencies spaced symmetrically about the pump. As in the case of a photon source based on an attenuated laser (see Section 3.4.1) the number of photons that will be generated at the signal and idler wavelengths in a given time window, or on a given pulse of the laser in the case of a pulsed pump, is inherently probabilistic (the distribution of the number of generated photons will be discussed further in Section 3.5.2).

The significant advantage of using the photons generated by parametric interaction for a photon source, rather than those from the pump laser itself, is that due to the requirement of conservation of energy in the interaction, the signal and idler photons must always be produced together in pairs. As the photons in these pairs are produced simultaneously [90,91], detecting one of them allows the presence of a localised one photon state to be inferred without the need to measure it [92]. This procedure, known as heralding, significantly improves the output state of parametric sources by eliminating the vacuum contribution through post-selection of events where at least one pairs is generated. As with the case of an attenuated laser, the maximum rate at which photon pairs can be generated for this type of parametric-based sources is similarly limited by the requirement of having a negligible probability of generating more than one pair of photons on a given pulse of the laser (or in a time-bin defined by the photon coherence length for a source pumped with a CW laser). In the absence of optical losses, if the average pair generation rate is sufficiently low, the output from this type of source will approach that of a true one photon Fock state.

The first sources based on parametric processes [76,90,93] generated photon pairs via spontaneous parametric down-conversion (PDC) in $\chi^{(2)}$ nonlinear crystals such as potassium

dihydrogen phosphate (KDP) or beta-barium borate (BBO). While these sources displayed high brightness compared to other types of photon sources at the time, based on atomic cascades, collection of the generated photons was experimentally challenging. This is due to the phase-matching conditions in bulk crystal, which result in the generated signal and idler photons being emitted from the crystal over a range of angles dependent on their frequencies. Carefully matched spatial filtering of the output signal and idler beams is therefore required in order to select only the photons at the desired wavelengths. Furthermore, this broad angular distribution of the output makes coupling to single mode fibres challenging. In recent years progress has been made in techniques to optimise this coupling efficiency [94,95], leading to the development of fibre-coupled sources based on PDC with high brightness and low loss [96,97]. However, the bulky free-space optics used in these sources requires careful alignment and is unlikely to be well suited to future commercial applications. Currently the main focus of development for photon sources based on nonlinear crystals is on PDC in periodically poled bulk crystals or waveguides [98,99,100], although even in the case of waveguided PDC, the difficulty in interfacing the output mode from these waveguides with the circular core mode of an optical fibre remains one of the main drawbacks for this type of source.

For practical photon sources, efficient coupling of the signal and idler photons into single-mode optical fibre outputs is desirable, particularly for quantum communications applications where they may need to be transmitted over long distances. By taking advantage of FWM in single-mode optical fibres, the signal and idler photons can be generated directly in the guided fundamental mode, thus avoiding the issue of coupling efficiency. A schematic representation of a fibre-based photon source, demonstrating the principle of heralding by detection of the signal photons, is illustrated in Fig. 3.4. Note that, for the purposes of illustration, the generation rate of pairs shown in this figure is far higher than would be typical for the operation of such a source, due to the detrimental effect of multiple pair generation on a single pulse of the pump laser, which is not considered in this figure (see Section 3.5.2). Furthermore, this figure shows the idealised case of perfect transmission, in which no idler or signal photons are ever lost.

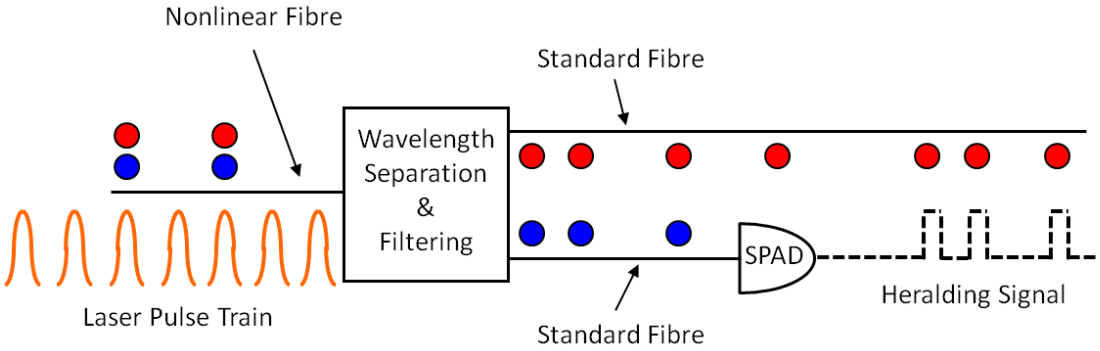

Figure 3.4: Schematic representation of a heralded single photon source based on FWM in an optical fibre. Signal and idler photons (shown by the blue and red circles) are generated simultaneously in pairs by a pulsed pump laser in a nonlinear fibre. The signal photons are later detected using a single photon avalanche diode detector (SPAD) to give an electronic heralding signal synchronised with the idler photon output.

The first fibre-based photon sources were based on photon pair generation in conventional dispersion-shifted fibres [101], while many of the subsequent sources took advantage of the increased possibilities for dispersion engineering in PCF [102,103]. These sources were all designed to operate with the pump wavelength close to the ZDW in the anomalous dispersion region of the fibre. This meant that the generated signal and idler wavelengths were typically separated from the pump wavelength by < 50 nm. Because of this, Raman-shifted pump light was a significant source of background noise in all of these systems. Photon sources were subsequently demonstrated with pumping in the normal dispersion regime of a fibre [104,105,106], where the signal and idler are more widely separated from the pump (see Section 2.2.4), greatly reducing the influence of Raman-shifted pump light on the performance of these later sources. Table 3.1 summarises some of the more recent advances in sources for the generation of high purity single photon states.

Source Type	Pump Properties	Average Pump Power	Generated Wavelength	Output Photon Bandwidth	Detected Output Photon Rate	Heralding Fidelity	Year	Ref.
PDC in bulk $KNbO_3$	CW 532 nm	< 50 mW	1550 nm	6.9 nm	~ 50 kC/s	60%	2004	[97]
PDC in bulk BBO	fs pulsed 780 nm (frequency doubled)	79 mW	780 nm	10 nm	950 C/s	83%	2005	[96]
PDC in periodically poled KTP waveguide	fs pulsed 800 nm (frequency doubled)	15 µW at 400 nm	810 nm	2 nm	850 kC/s/mW	85%	2004	[100]
Degenerate PDC in bulk PPKTP	ps pulsed 776 nm	~ 15 mW	1552 nm	~ 2 nm*	~ 50 C/s/mW	~20%	2011	[107]
FWM in PCF	ps pulsed 1064 nm	20 mW	1548 nm	5.8 nm	250 C/s	~25%	2010	[108]
FWM in PCF	ps pulsed 740 nm	~ 0.5 mW	800 nm	0.3 nm	3.8 kC/s	18%	2009	[105]
XFWM in birefringent PCF	fs pulsed 705 nm	-	597 nm	0.13 nm*	-	~35%	2009	[55]
XFWM in conventional birefringent fibre	ps pulsed 715 nm	-	848 nm	~ 0.3 nm*	177 kC/s	85%	2011	[109]

Table 3.1: Summary of the operating parameters and performance results for a selection of reported heralded photon sources, based on a variety of different technologies.
*In these sources the photons were generated in a naturally narrowband, spectrally uncorrelated state (see Section 3.5.5).

For the photon sources described here, the most important performance criteria are the detected output photon rate and the heralding fidelity. The output photon rate corresponds to the source brightness and the heralding fidelity is the probability that a photon will be output from the source, given that a heralding signal was generated (heralding fidelity is discussed in more detail is Sections 4.3 and 5.3.3). In order to achieve a high heralding fidelity, optical losses in the system should be minimised. The source brightness depends on both the level of loss and the photon pair generation rate.

As shown in Table 3.1, typical values for the brightness, heralding fidelity and pump power requirements vary significantly between sources depending on type of nonlinear material chosen for photon generation, and on other factors such as the required wavelength and bandwidth of the heralded photons. The sources described here all output heralded photons into a single-mode collection fibre, with the photon wavelength designed for operation either near the telecoms wavelength of 1550 nm or within the optimum range for detection with efficient Si-based photon detectors (550 – 850 nm).

The highest heralding fidelity for a source operating at 1550 nm is 60%, reported by Fasel et al. [97] for PDC in a bulk crystal. Near 800 nm, even higher heralding fidelity of >80% has been demonstrated by U'Ren et al. for waveguided PDC in a $\chi^{(2)}$ material [100]. However, the bandwidth of the prepared photons for these sources was relatively broad, due to the requirement of low loss free-space filtering. This typically limits such sources to operating with bulky and expensive short pulse length lasers, such as a Ti:Sapphire, or working in the CW regime where photons are no longer synchronised with a laser pulse but randomly distributed in their time of emission. Due to the high nonlinear coefficient associated with $\chi^{(2)}$ PDC crystals, the source brightness per unit of pump power can be very high [100].

In recent years, filtered PCF-based photon sources have been developed that exhibit high brightness over a narrow spectral range. By confining light in a 2 µm diameter core over much longer lengths than is possible in a PDC bulk crystal, Ling et al. demonstrated a source of heralded photons at 800 nm with a brightness of 4.5 X 10^4 photon pairs $(s \cdot nm \cdot mW)^{-1}$ [105]. However, for spectrally filtered photon sources based on FWM in PCF heralding fidelity values are usually less than 20%. This is due to the loss of the typical narrowband filtering used to achieve spectral purity and the need to couple the generated photons out of the PCF into free-space for spectral filtering and then back into single-mode fibre. The use of birefringent fibre for XFWM to generate naturally narrowband, spectrally uncorrelated photon pairs can

circumvent many of the difficulties associated with these earlier fibre-based sources. As this type of fibre can be designed to produce heralded single photons in a pure state without narrowband filtering, the use of lossy free-space filters can be avoided, leading to improved brightness and heralding fidelity. Söller et al. have demonstrated a source of heralded photons at 848 nm based on this principle with a detected output photon rate of 177 kC/s and a heralding fidelity of 85% [109]. The development of a birefringent PCF for generation of naturally narrowband idler photons at 1550 nm will be the focus of Chapter 7.

One inherent difficulty with all the types of probabilistic source described in this section arises when combining the output of multiple sources in any QI application requiring more than one heralded photon to operate. In such an experiment, even if the photon sources are pumped using synchronised pump pulses, because each source only operates on a given pulse with some probability (less than one) the overall probability of all of the sources producing a heralded single photon on the same pump pulse diminishes as the required number of photons increases. If P_1 is the probability that a single source outputs on any given pulse of the laser, then the probability that M photons will be heralded and output on a given pump pulse, P_M, scales as

$$P_M = (P_1)^M . \tag{3.29}$$

In order to minimise the probability of a single source generating multiple photon pairs on a given pulse of the laser, the pump power is chosen so that typically $P_1 \sim 0.1$ (see Section 3.5.2). This restricts the number of photons that can be used in any QI application, so that the time taken for an experiment to run is reasonable. Much of the interest in developing new higher brightness photon sources is to enable these higher photon number experiments to become feasible.

3.5 Photon Pair Generation by FWM

An overview of the process of FWM in optical fibre was described in Section 2.2.3, in which idler and signal wavelengths are generated via a nonlinear interaction with an intense pump pulse, at wavelengths defined by phase-matching conditions specific to the fibre (see Section 2.2.4). The generated intensity of the signal and idler pulses was shown in Eq. (2.65) to depend on the square of the fibre length and pump power. As described in Section 3.4.3, one standard approach to producing a single photon source is to generate pairs of signal and idler

photons via some type of nonlinear interaction and detecting one member of the photon pair to provide a heralding signal. The theory developed in Section 2.2.3 was based on the interaction between classical oscillating fields. While it was posited that in the low power regime this process could proceed in a spontaneous fashion, seeded by quantum vacuum fluctuations, it is not clearly apparent from this treatment whether the results for the gain of the FWM process would remain valid in this limit. Additionally, as the pump beam was assumed to be quasi-monochromatic, this approach does not quantitatively describe the influence of the pump bandwidth on the widths of the generated signal and idler, which becomes relevant for short duration pump pulses.

The quantum treatment of FWM has been studied by many groups [110,111,112] due to the applications of the resultant two-photon signal and idler state as a basis for heralded single photon sources (see Section 3.4.3). It is usual adopt a semi-classical approach in which the states of the idler and signal fields are quantised and interact with a classical pump field.

For describing the generation of light by parametric processes is often simpler to work with the interaction picture of quantum mechanics. The main difference between this approach and that of the more commonly used Schrödinger picture is that instead of the calculating the how the state of the system evolves over time, the time dependence of the system is moved to the quantum mechanical operators (such as the creation operator $\hat{a}_{\mathrm{k}}^{\dagger}$) which can then be used to determine how an observable property of the system evolves in time from a known fixed initial state [113]. In this representation the time evolution for any general operator $\hat{A}(t)$ is found from

$$\frac{\mathrm{d}\,\hat{A}(t)}{\mathrm{d}\,t} = -\frac{i}{\hbar}\left[\hat{A}, \hat{H}_{tot}\right], \tag{3.30}$$

where $\hat{H}_{tot}$ is the total Hamiltonian for the system and the brackets describe the commutator of the operators

$$\left[\hat{A}, \hat{H}_{tot}\right] \equiv \hat{A}\hat{H}_{tot} - \hat{H}_{tot}\hat{A}\,. \tag{3.31}$$

If the Hamiltonian of the system is known, then by solving Eq. (3.30) for the creation operators for idler or signal photons it is possible to see how these operators vary with the time. This

then allows the expectation value for the number of photons generated in the signal and idler modes from an initial zero-photon number state, $|0\rangle_s|0\rangle_i$, to be calculated.

For the case of FWM, the total Hamiltonian can be expressed as a sum of the unperturbed Hamiltonian $\hat{H}_0$ of a harmonic oscillator (the energy in the signal and idler fields without a pump beam present) and an interaction Hamiltonian $\hat{H}_{\text{int}}$ due to the additional energy associated with the nonlinear coupling between optical fields of different frequencies [74]

$$\hat{H}_{tot} = \hat{H}_0 + \hat{H}_{\text{int}}, \tag{3.32}$$

where

$$\hat{H}_0 = \hbar\omega_s(\hat{a}_s^\dagger\hat{a}_s + \tfrac{1}{2}) + \hbar\omega_i(\hat{a}_i^\dagger\hat{a}_i + \tfrac{1}{2}), \tag{3.33}$$

and

$$\hat{H}_{\text{int}} = \int_V \mathrm{d}V \cdot \varepsilon_0 \chi^{(3)} E_p^2 E_s E_i . \tag{3.34}$$

Here $E_{p,s,i}$ are the electric fields at the pump, signal and idler wavelengths and the volume integral extends over the entire region V in which the fields are interacting. The strength of the nonlinear coupling for FWM is determined by the nonlinear susceptibility $\chi^{(3)}$ as in the classical case described in Section 2.2.3.

The classical pump electric field in $\hat{H}_{\text{int}}$ can be described by

$$\varepsilon_p(\omega) = \frac{E_{p0}}{2} \cdot \exp\left(-\frac{\omega^2\sigma^2}{2}\right) \cdot \{\exp(-i\delta) + \exp(i\delta)\} \cdot e_p(\vec{r}), \tag{3.35}$$

with

$$\delta = (\Omega_p + \omega)t - (k_p - \gamma P_p)z . \tag{3.36}$$

Eq. (3.35) describes a single component of the of finite bandwidth pump pulse centred on a frequency Ω_p with peak field amplitude given by E_{p0}. The first exponential term is a weighting function defined by the pump pulse, ensuring that the correct relative amplitude for each frequency component of the pump pulse. The pulse shape is assumed to be Gaussian with

standard deviation σ. From Eq. (3.36) it is apparent that this description of the pump pulse also includes the effects of SPM, through the inclusion of the term involving the nonlinear coefficient γ and peak pump power P_p. The $e_p(\vec{r})$ term describes the transverse spatial variation of the field and is normalised such that

$$\int \left| e_p(\vec{r}) \right|^2 \mathrm{d}r\mathrm{d}\theta = 1. \tag{3.37}$$

Since the case of interest here is FWM in only the fundamental mode of a fibre, the transverse field profile does not affect the end result of the calculation and only the variation of the field in the direction of propagation needs to be considered, as in the treatment for FWM in the classical regime (see Section 2.2.5).

In order to account for the quantum nature of light for the generated signal and idler beams, E_s and E_i are described by the quantum electric field operators [114]

$$E_\alpha = \sqrt{\frac{\hbar\omega_\alpha}{2\varepsilon_\alpha}} \frac{1}{\sqrt{\ell}} \sum_{k\alpha} \left(\hat{a}_\alpha^\dagger \exp(-ik_\alpha z) e_\alpha(\vec{r}) + \mathrm{h.c} \right), \tag{3.38}$$

where the subscript α denotes the signal or idler, ℓ^3 is the volume in which the FWM interaction occurs and $\mathrm{h.c}$ is the Hermitian conjugate. As discussed in Section 3.2, the operator $\hat{a}_\alpha^\dagger$ describes the creation of signal or idler photons only into a single mode. The summation in Eq. (3.38) accounts for the fact that in general FWM can have a gain bandwidth that allows for generation of signal and idler into multiple spectral modes.

Substitution of Eqs. (3.38) and (3.35) into the expression for the interaction Hamiltonian, given in Eq. (3.34) allows an expression for the time dependent creation operator $\hat{a}_\alpha^\dagger(t)$ to be found from the solution of Eq. (3.30), in the limit that the interaction volume $\ell^3 \to \infty$. The expectation value for the number of photons signal and idler photons can then be found, similarly to Eq. (3.12), by taking the inner product of the this operator acting on the initial state $|0\rangle_s |0\rangle_i$ to show [112]

$$\langle N_s \rangle = \left(\varepsilon_0 \chi^{(3)} \frac{E_{P0}^2}{4} \sqrt{\frac{\omega_s \omega_i}{4 \varepsilon_s \varepsilon_i}} \right)^2 \left(\frac{IL}{2} \right)^2 \left(\frac{\sqrt{\pi}}{\sigma} \right)^2$$

$$\times \iint \mathrm{sinc}^2 \left(\frac{\kappa L}{2} \right) \exp \left(- \frac{\left(\Delta\omega_{ks} + \Delta\omega_{ki} \right)^2 \sigma^2}{2} \right) \frac{\mathrm{d}\Delta\omega_{ks}}{v_{gs}} \frac{\mathrm{d}\Delta\omega_{ki}}{v_{gi}}, \tag{3.39}$$

where L is the length of the optical fibre in which the interaction occurs, v_{gs} and v_{gi} are the signal and idler group velocities in the medium, κ is the phase-mismatch (described similarly to Eq. (2.52) for the case of co-polarised FWM in the high power regime in Section 2.2.4), and I is an overlap integral between the pump, signal and idler mode field profiles. $\Delta\omega_{ks}$ and $\Delta\omega_{ki}$ are frequency shifts for the signal and idler frequencies away from the peak values ω_s and ω_i that satisfy the energy matching requirement for the peak pump wavelength. The double integral over these frequency shifts therefore accounts for the bandwidth of the pump by allowing the energy matching to occur over a range of signal and idler frequencies. While Eq. (3.39) describes the expectation value for the number of signal photons, the procedure for determining the number of idler photons is similar and leads to the same result, further emphasising that the signal and idler must always be generated in pairs.

Looking at the terms in brackets outside the integral in Eq. (3.39) and comparing the expression to that developed previously in Section 2.2.5 for the gain of FWM using classical theory in Eq. (2.65), the derived pump power dependence of the process is found to be the same in both. The sinc^2 function within the integral is also found in Eq. (2.65) and leads to the finite bandwidth of the generated signal and idler even for a monochromatic pump due to a maximum tolerable phase-mismatch, which is determined by the fibre length. The other contribution to the gain, given by the exponential function inside the integral, is due to the additional broadening in the signal and idler bandwidths that occur by considering a pump of finite spectral width. These terms can be grouped together into a single function f, which is dependent on the generated signal and idler wavelengths according to

$$f(\omega_s, \omega_i) = \alpha(\omega_s + \omega_i) \phi(\omega_s, \omega_i) = \mathrm{sinc}^2 \left(\frac{\kappa L}{2} \right) \cdot \exp \left(- \frac{\left(\Delta\omega_{ks} + \Delta\omega_{ki} \right)^2 \sigma^2}{2} \right), \tag{3.40}$$

where $\phi(\omega_s, \omega_i)$ is determined by the phase-matching conditions of the fibre and $\alpha(\omega_s + \omega_i)$ describes the pump envelope function. Since all the dependence of the number of generated

pairs on their wavelengths is contained within this function, the distribution of $f(\omega_s, \omega_i)$gives the joint spectral amplitude (JSA) for the pair and demonstrates the degree of correlation between the signal and idler wavelengths (see Section 3.5.5).

Considering the effect of a broadband pump pulse also allows the dependence of the signal and idler bandwidths on the width of the pump pulse to be investigated. By considering both the phase-matching conditions and the energy matching for a pump pulse of FWHM frequency bandwidth $\Delta\omega_p$ it can be shown that [112]

$$\Delta\omega_{ks} = \frac{2\pi c}{|\Gamma_s - \Gamma_i|L} + 2\left|\frac{\Gamma_i - \Gamma_p}{\Gamma_s - \Gamma_i}\right|\Delta\omega_p, \tag{3.41}$$

and similarly,

$$\Delta\omega_{ki} = \frac{2\pi c}{|\Gamma_i - \Gamma_s|L} + 2\left|\frac{\Gamma_s - \Gamma_p}{\Gamma_i - \Gamma_s}\right|\Delta\omega_p, \tag{3.42}$$

where

$$\Gamma_\alpha = \left(\omega_\alpha \left.\frac{\partial n_\alpha}{\partial \omega}\right|_{\omega_\alpha} + n_\alpha\right), \tag{3.43}$$

where the subscript α denotes the pump, signal or idler field and the effective refractive index of the structure at that wavelength given by n_α. These expressions for the generated signal and idler bandwidths are seen to consist of two terms. The first is independent of $\Delta\omega_p$ and applies even to a monochromatic pump. This displays the $1/L$ variation of the bandwidth that was predicted in the previous analysis of FWM in the absence of pulse walk-off (see Section 2.2.5). The second term accounts for the bandwidth of the pump pulse, where the combination of factors multiplying this bandwidth is related to the slope of the phase-matching curves. This term is minimised when the gradient of the corresponding phase-matching curve (for the signal or idler) becomes zero, leading to narrowband generated photons for pump wavelengths satisfying these conditions. In Section 3.5.5 these points are shown to coincide with the group velocity at the pump wavelength being matched to the group velocity of either the signal or idler wavelength.

3.5.1 Spectral Filtering

As discussed in Section 3.4.3, one way in which a single photon source can be realised is by taking advantage of some form of parametric interaction to generate signal and idler photon pairs and herald the presence of one through the detection of the other. In order to observe high visibility interference effects using photons produced in this manner it is necessary to ensure that the heralded single photon is in a pure quantum state (see Section 3.3). In general, the generated signal and idler photons from a parametric process such as FWM will be strongly correlated in frequency due to the requirements of energy and phase-matching (see Section 2.2.3). When one of the pair, say the signal photon, is detected as a herald, information can in principle be extracted about the spectral state of the two photon system and therefore provide information about which state the idler photon is in. However, since realistic single photon detectors are unable to resolve which spectral mode the heralding photon is in, this information is not generally experimentally accessible to the observer of the system with standard single photon detectors [115]. When the signal and idler wavelengths are correlated, the result is that the measurement of the signal photon projects the idler into a state which is a statistical mixture of its available pure states, also known as a mixed state. The mixed state is described by a density matrix ρ of the form [116]

$$\rho = \sum_j S_j \left|\psi_j\right\rangle\left\langle\psi_j\right|, \tag{3.44}$$

where $\left|\psi_j\right\rangle$ possible pure states for the heralded state and S_j are the corresponding probabilities that the system will be found to be in that state upon measurement. As only pure states are expected to show HOM interference (described in Section 3.3), the visibility of interference between identically prepared heralded mixed state will be reduced according to the number of pure states in the mixed ensemble.

The correlation between the signal and idler frequencies, which results in an undesirable mixed state after heralding, can be demonstrated through the JSA, given by the shape of the function $f(\omega_s, \omega_i)$ defined in Eq. (3.40). A typical plot of the JSA for the pair photon state resulting from co-polarised FWM in a PCF is shown in Fig. 3.5, along with pump envelope function and phase-matching function from which it is calculated. The correlation is clearly evident in this case from the slope of the JSA.

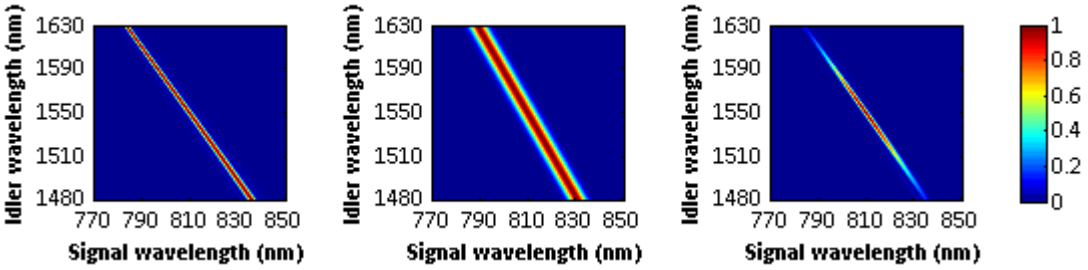

(a) (b) (c)

Figure 3.5: Example plots of: (a) the phase-matching function; (b) the pump envelope function; and (c) the resulting JSA of the generated idler and signal photons. The data shown is for co-polarised FWM in a PCF with Λ = 2.93 µm and d/Λ = 0.32, with a fibre length of 10 cm and average pump power of 100 mW. The pump bandwidth in this case was 10 nm in order to better illustrate the shape of the JSA.

In order to avoid producing a mixed state through heralding, narrowband spectral filtering of the signal and idler can be incorporated as part of a photon source to ensure that photons can only be output into a single temporal mode. As described in Section 3.2, the temporal width, or coherence length of the signal and idler photon wave-packets that are generated by FWM are given by the inverse of the gain bandwidth. This coherence length defines the width of a single temporal mode of the photon state. Photons can be generated at any point within the time window of the laser pump pulse, which could be larger than the photon coherence length, allowing the photons to be generated into multiple temporal modes which cannot be distinguished by realistic detectors. The effect of filtering on the photons will reduce their spectral width and thus increase the coherence length of the photon state. If the filtering is sufficiently narrow so that the coherence length is approximately equal to the pump pulse duration then only a single temporal mode can contain photon pairs and the desired single photon state will be pure upon heralding [117].

The effect of filtering can also be seen in the altered form of the JSA. Narrowband filtering of either the signal or idler photons can be incorporated into the JSA picture by multiplying the result by an appropriate filter function. As the filtering bandwidth tends to zero, the resultant JSA function becomes progressively more symmetrical, such that the degree of correlation between the generated signal and idler wavelengths is reduced [118]. An example of this can be seen in Fig. 3.6.

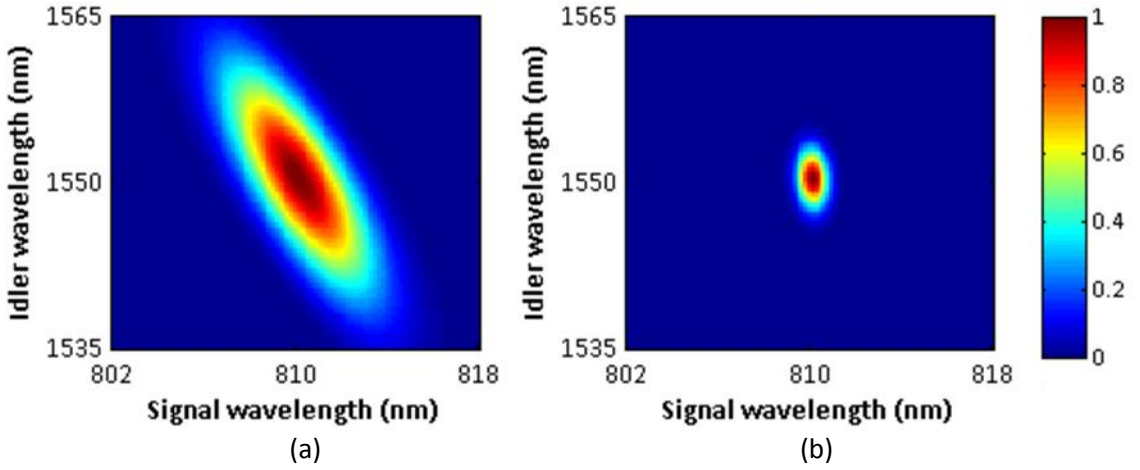

Figure 3.6: Demonstration of the effect of filtering on the shape of the JSA function. These results were calculated by applying energy-matched Gaussian filter profiles to the JSA shown in Fig. 3.5. The filtering FWHM bandwidths for the signal and idler were: (a) 3 nm and 12 nm respectively; and (b) 0.5 nm and 2 nm.

The visibility of HOM interference that can be observed at a beam-splitter, between the heralded photons from two separate parametric-based sources with narrowband filtering, depends on both the chosen filtering width and the accuracy with which the filter central frequencies are matched.

For each individual source the two-photon wave function [119] for the signal and idler pair before the heralding photon reaches its detector and the other photon reaches the beam-splitter is described by [120]

$$\Psi(t_1,t_2) = \alpha \int \mathrm{d}\omega_s \mathrm{d}\omega_i \mathrm{d}\omega_{p1} \mathrm{d}\omega_{p2} F_p(\omega_{p1}) F_p(\omega_{p2}) F_s(\omega_s) F_i(\omega_i) \\ \times \phi(\omega_s,\omega_i)\delta(\omega_s+\omega_i-\omega_{p1}-\omega_{p2})\exp[i(\omega_s t_s+\omega_i t_i)], \quad (3.45)$$

where the functions $F_{s,i}$ describe the form of the spectral filtering in the case of the signal and idler frequencies. These are chosen to be energy matched with a Gaussian profile of standard deviation σ. For the pump, which is unfiltered, F_p is the pump envelope function, which is also assumed to be Gaussian with a standard deviation of σ_p from the central frequency. $\phi(\omega_s,\omega_i)$ again gives the phase-matching function for the fibre, and energy matching is ensured by the Dirac delta term. The relative arrival time of the signal and idler photons at their detectors is also accounted for by the terms t_s and t_i in the exponential function. When the idler photons from two such sources are input into the two input ports of a beam-splitter and subsequently

detected as in Fig. 3.2(a), and the signal photons are also detected at two other detectors, the resultant four-photon wavefunction is given by

$$\Psi_{4-photon} = T\Psi_{14}\Psi_{23} - R\Psi_{13}\Psi_{24} \tag{3.46}$$

where R and T are the reflectivity and transmittance of the beam-splitter and the subscripts 1-4 signify the possibilities by which photons produced from two sources (1 and 2) can arrive at two detectors (3 and 4) after the beam-splitter.

Performing the time integral of the probability amplitude of the four-photon wavefunction [121] in Eq. (3.46) gives the probability of seeing a four-fold coincidence between all of the detectors as

$$P_{4-fold} = \mu^2 M\left(R^2 + T^2 - 2VRT\exp\left[\frac{-\Delta T^2\sigma^2}{2\left(1+\sigma^2/2\sigma_p^2\right)}\right]\right), \tag{3.47}$$

where M is a normalising factor, μ is the average number of generated photon pairs per pulse. The exponential term is responsible for the interference effect and defines the shape of the HOM dip, where ΔT is the difference in the arrival time of idler photons from the two sources at the beam-splitter. The maximum visibility V that will be observed is given by

$$V_{\max} = \frac{\sqrt{1+\sigma^2/\sigma_p^2}}{1+\sigma^2/2\sigma_p^2}. \tag{3.48}$$

As expected, the visibility of the interference feature is dependent on the width of the spectral filtering of the signal and idler photons, relative to the pump bandwidth. Although the purity of the heralded photon states only becomes absolute in the limit where the filter bandwidths tend to zero, a visibility ~95% can be obtained when the filter bandwidths are energy matched to the pump width so that $\sigma \approx \sigma_p$.

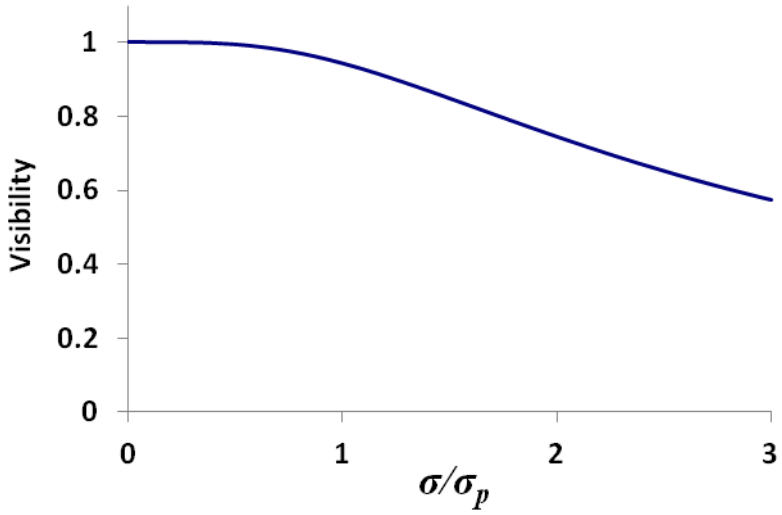

Figure 3.7: Plot of the anticipated HOM interference visibility for different values of the signal and idler filtering bandwidths (σ), relative to the pump bandwidth (σ_p), calculated using Eq. (3.48).

The purity that can be achieved through filtering which is matched to the pump bandwidth is sufficient for most practical applications. The main drawback of narrowband filtering is the reduction in the brightness of the source that results from the optical losses of such filters, although by taking advantage of fibre-based components it is possible to realise narrowband filtering with relatively low loss (see Section 5.2).

3.5.2 Photon Statistics for FWM

One of the key requirements of a single photon source is that only one photon should be output upon operation. In Section 3.4.3, the concept of heralding was introduced for sources based on the generation of time-correlated pairs of photons. Ignoring pulses of the laser in which no pairs are generated allows sources of this type to approach the pure number state of an idealised source by eliminating the vacuum component of the generated state.

Despite this significant improvement, even when disregarding the effects of noise photons and detector dark counts, the purity of the heralded photon state will always be limited by the possibility of generating additional pairs of photons by FWM that are uncorrelated with the heralding signal. Since the generation of pairs by nonlinear processes is inherently probabilistic, for a given laser repetition rate, the higher-order photon number terms can only be reduced at the expense of reducing the average pair generation rate of the source. Any detected photons which are uncorrelated with the heralding signal are described as accidental

counts, and the ratio of the accidentals count rate to the count rate of the true heralded photons is a key measure of source performance (this coincidence-to-accidentals ratio is discussed in more detail in Section 4.3). When both the accidentals count rate is low and the heralding fidelity is high, the heralded state approaches that of a true single photon.

Due to the limiting effect of the higher-order photon number terms on the source performance it is important to quantify how the number distribution of generated pairs varies with the average pair generation rate. When observed over a sufficiently long time period, the distribution of the number of photon pairs generated by FWM on each pulse of a pump laser is found to follow a Poisson distribution, as shown for the case of the coherent source in Section 3.4.1. However, on short time scales the number distribution for spontaneous emission processes deviates from the Poisson distribution and is instead found to follow a thermal distribution [83], where the number of photon pairs within the measurement period is given by [122]

$$P(n,\mu) = \frac{\mu^n}{(1+\mu)^{n+1}}, \tag{3.49}$$

and μ is the expectation value for the number of pairs measured. The change in the number distribution is related to intensity fluctuations from photon bunching in the light field, which are too rapid to observe with most detectors under usual circumstances [123]. These photon number distributions for the two limiting cases of the measurement duration can both be derived directly from the interaction Hamiltonian for a parametric process of the form

$$\hat{H}_{\text{int}} = i\hbar \mathrm{X}\left(\hat{a}_{\text{s}}^{\dagger}\hat{a}_{\text{i}}^{\dagger} - \hat{a}_{s}\hat{a}_{i}\right), \tag{3.50}$$

where X is a function that incorporates both the peak pump power and the appropriate nonlinear susceptibility coefficient of the interaction. Solving for the state of the system shows that the distribution of the number states obeys Eq. (3.49) exactly only when the photons are constrained to be generated in a single mode, and tends towards the Poisson distribution as the number of available modes becomes large [124]. As Eq. (3.50) can describe both $\chi^{(2)}$ and $\chi^{(3)}$ processes with an appropriate choice of X, this result can be applied to both.

The Poisson distribution is commonly assumed for the light generated by FWM. However, for the case of a single photon source the goal is to try and achieve emission into single mode, where this distribution may no longer be valid. The statistics of the photon number

distribution can be classified according to the value parameter $g^{(2)}(0)$, where $g^{(2)}(\tau)$ is related to the probability that, given that there is a photon at a time $t = 0$, there will be a second photon found at some later time $t = \tau$. $g^{(2)}(\tau)$ is defined by the fluctuations in the intensity $I(t)$ of the light field according to

$$g^{(2)}(\tau) = \frac{\langle I(0) \cdot I(\tau) \rangle}{\langle I(0) \rangle \cdot \langle I(\tau) \rangle} \tag{3.51}$$

For pulsed light sources the $g^{(2)}(\tau)$ parameter needs to be considered for values of τ that lie within the pulses. In the case of a coherent light source that follows the Poisson distribution, photons are distributed randomly within each pulse. This means that the intensity at $t = 0$ is totally uncorrelated with that at all later times $I(t)$, and therefore $g^{(2)}(\tau) = 1$ at all times, including when $\tau \to 0$. Light with $g^{(2)}(0) > 1$ exhibits greater intensity fluctuations than that of Poissonian light and is described as bunched, since photons are more likely to occur in groups. For the thermal distribution described by Eq. (3.49), $g^{(2)}(0) = 2$. Experimental measurement of $g^{(2)}(\tau)$ can therefore be used to determine the underlying distribution of photons for a given light source. It should be noted that for an ideal photon source outputting only the $|1\rangle$ state, the light will be anti-bunched with exactly one photon on each heralded pulse giving $g^{(2)}(0) = 0$. Sub-Poissonian light with $g^{(2)}(0) < 1$ is a clear signature of the quantum nature of the state, as this represents a state with less intensity fluctuation than even coherent light.

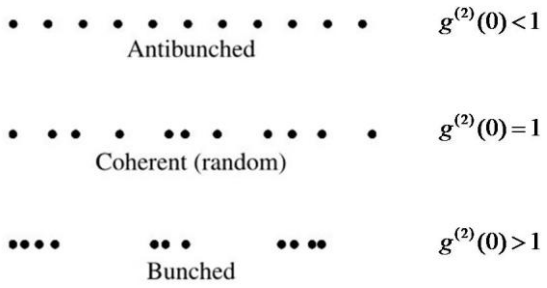

Figure 3.8: Illustration of the statistical distribution of photons for different regimes of the second-order coherence parameter $g^{(2)}$. (Image from [67]).

The photon statistics for the number of pairs generated by the nonlinear process of spontaneous parametric down-conversion (PDC) has previously been studied experimentally [125]. In this case one of the generated photons from a down-converted pair was sent through spectral filtering before being sent through a beam-splitter with a single photon

avalanche photodiode detector on each output. The timing information for coincidences between the two detectors allowed $g^{(2)}(\tau)$ to be measured. As expected, when the spectral filtering defined a coherence length for the down-converted photons that was significantly shorter than duration of the pump pulse (around 10% of its value) the $g^{(2)}(0)$ value approached 1. For extremely narrowband filtering where the filtered photon coherence length was around 10 times larger than the pump pulse duration the $g^{(2)}(0)$ tended to a value of 2, characteristic of thermal light. For a single photon source it is usually preferable to work somewhere between these two extremes in order achieve a compromise between the output photon rate and purity. When the filtering frequency bandwidth was approximately energy matched to that of the pump, $g^{(2)}(0)$ was found to be ~1.2. As this is reasonably close to the value expected of the Poisson distribution, this should provide a good approximation of the true photon number distribution of the source under these filtering conditions.

The photon number distribution will also clearly affect the HOM visibility that can be observed by the presence of multi-photon pair contribution to the total state vector that will not interfere. The importance of this contribution to the visibility can be seen by following the same analysis used to determine the output state from HOM interference as shown in Section 3.3, but for an input state of

$$\left|\psi_{in}\right\rangle = \frac{1}{\sqrt{2}}\left(\hat{a}_1^{\dagger}\right)^2 \hat{a}_2^{\dagger}\left|0\right\rangle. \tag{3.52}$$

This corresponds to the state in which one of the two photon sources providing an input to the experiment accidentally produces two pairs of signal and idler photons on a single laser pulse. By taking an average for the maximum visibility expected for this state and all the other possible combinations of states where the sources produce less than three pairs of photons, weighted according to the probability of generating each state, the overall HOM visibility is shown to be [126]

$$V_{\max} \approx \frac{1+8\mu}{1+12\mu}, \tag{3.53}$$

where μ is average number of pairs generated per pulse. Since this analysis neglects the effect of photon number generation events of more than two pairs it is only valid when $\mu \leq 0.1$ [120]. Eq. (3.53) demonstrates that the visibility can be made arbitrarily close to unity (assuming the photons are identical in all other degrees of freedom) by reducing the average

pair generation rate, although clearly this will also lower the output rate of photons from the sources. As a trade-off between the considerations of purity and source brightness it is common to operate such probabilistic sources at around $\mu = 0.1$, unless a specific application requires higher purity. At this average generation rate the maximum visibility can still exceed 80%, significantly higher than the visibility for the interference feature that can be expected classically.

It is apparent from this discussion on the number distribution of pairs from FWM that one of the major limitations preventing these sources from achieving higher count rates is the unavoidable generation of multiple pairs of photons when moving to higher values of μ, as unlike the $|0\rangle$ state these higher photon number states cannot be easily eliminated by post-selection. This is due to the fact that the most common single photon detectors currently in use are based on avalanche photodiode technology that is not able to discriminate between the detection of one photon and multiple photons. Some schemes have been proposed that can reduce the contribution of multi-photon events by post-selection using cascaded arrays of standard avalanche photodiode detectors [127,128]. Looking to the future, single photon detectors based on new technologies such as superconducting nanowires may one day offer the ability to reliably herald on the presence of exactly one photon pair, allowing the average pair generation rate to be increased closer to $\mu = 1$. While such detectors have already been demonstrated to show photon number resolving capabilities, they currently lack the necessary maximum counting rates and low timing jitter to be able to replace existing detectors [129].

3.5.3 Limitations on the Temporal Purity Due to Walk-Off

As shown in Section 3.5.1, the finite bandwidth of heralded single photon states, determined either by the gain bandwidth of the nonlinear process from which they are generated or by subsequent spectral filtering, allows a coherence length of the photon state to be defined. One factor that was not considered in this analysis was the effect of pulse walk-off between the pump and generated photon pairs that occurs in a dispersive medium (see Section 2.2.7). It was shown that high visibility interference could be achieved when the photon coherence length approaches the time window defined by the temporal profile of the pump pulse. This time window defines the number of available temporal modes due to the uncertainty about which point within the pump pulse the photon pair was generated. However, this approach is only valid when the effects of walk-off are negligible.

If the section of fibre that is used for FWM is longer than the walk-off length, then the time window within which the photon pair is generated will be broadened by an additional contribution to the timing uncertainty. The origin of this broadening is the unknown timing offset between the pump pulse and generated pair from walk-off due to differences in the position in the fibre at which the FWM interaction occurred. For a given photon coherence length, walk-off will therefore increase the number of available temporal modes, thus reducing the purity of the generated state as compared to the case where walk-off is absent. When attempting to interfere two single photon states (from separate sources with synchronised pumping) at a beam-splitter, the walk-off effect manifests as a timing jitter in the output time of the photon states from the sources from one pulse to the next. This reduces the temporal overlap between the photons at the beam-splitter and hence the visibility that can be achieved. In order to generate photons in close to a pure temporal state it is therefore important to ensure that the FWM medium in which they are generated does not exceed the walk-off length.

3.5.4 Degree of Polarisation of the Generated Photon State

The ideal photon source outlined in Section 3.4, should produce photon states which are indistinguishable in all degrees of freedom. As shown in Section 3.5.3, consideration of the effect of pulse walk-off is critical due to its influence on the number of temporal modes available to the heralded photon state. In the case of FWM in a non-birefringent fibre, the effect of walk-off also indirectly effects the degree of purity that can be achieved for the polarisation state of the heralded photon. This discussion is relevant to the results presented in Chapter 5 where such a source was realised experimentally.

For the case of FWM in a birefringent fibre, it is clear to see how a pure polarisation state for the generated signal and idler photons can be achieved. When using a single pump wavelength where the light is launched entirely onto one of the axes defining the birefringence (*s*-axis or *f*-axis), the pump light will remain linearly polarised along this axis throughout propagation. The difference in the propagation constant for at a given wavelength on the two axes as a result of the birefringence will mean that the phase-matching for a desired signal and idler pair will only be obtained for either the co-polarised FWM or XFWM process. Since there is only a single possibility for the polarisation of the signal and idler pair, the heralded single photons will be in a pure polarisation state.

For FWM in a non-birefringent fibre it is less obvious what the polarisation state of the generated photon pairs at the output of the fibre will be. As described in Section 2.1.4, a realistic nominally non-birefringent fibre will have a small but randomly varying birefringence determined mainly by fluctuations in the structure or any bending of the fibre. In order to theoretically describe such a fibre it is helpful to consider the overall structure as consisting of a series of short sections of birefringent with random alignments between their polarisation axes [130]. During propagation through each of these segments of the fibre the pump beam will undergo change in its polarisation state as described in Section 2.1.4. When the pump pulse leaves one segment of the fibre the amount of light launched onto the slow and fast axis of the next segment can be found by decomposing its current polarisation state in two orthogonal components aligned to the axes.

In each segment of the fibre the generation of photon pairs will be predominantly co-polarised with the pump due to the greater magnitude of the $\chi^{(3)}$ component for the co-polarised FWM process. Since there may in general be power on both the *f*-axis and *s*-axis, this segment will give some probability of generating a pair of photons on either axis. Photons generated in this segment of fibre will then propagate to the output of the fibre with their polarisation state evolving in a similar manner to the pump. If two orthogonal axes are defined at the output of the fibre, denoted by H and V for horizontal and vertical polarisations, then the overall probability of generating a photon on H at the output can be found by summing the probability contributions to that polarisation state from each individual segment. The state generated at the output of the fibre (considering only one member of the pair, for instance the idler photons) can be expressed as

$$\left|\psi_{sig}\right\rangle = M\left(\left|0\right\rangle + \sqrt{\mu}\left(c_H\left|1\right\rangle_H + c_V\left|1\right\rangle_V\right) + \mu\left(c_H\left|2\right\rangle_H + c_V\left|2\right\rangle_V\right) + ...\right), \tag{3.54}$$

where M is a normalising constant, μ is the average number of photon pairs per pulse and c_H and c_V are constants determined by a sum of the probability amplitudes of generating photons on the H or V axis from each segment of the fibre. Concentrating only on the $\left|1\right\rangle$ terms, in the basis for the polarisation (H and V) chosen here, the one photon state consists of a superposition of two available modes. A superposition of photon states of this kind can be shown to have similar polarisation properties to that of a classical light beam [131], representing circularly polarised, elliptically polarised, or linearly polarised photon states, at some angle to the H and V axes. Since the polarisation evolution of all the beams through the

system is deterministic and the input polarisation of pump is the same on each pulse, the output photon state will likewise be the same on each pulse, as described by Eq. (3.54). This means that each photon produced will have the same polarisation state and through an appropriate choice of wave-plates at the output of the fibre it is possible to transform from this state to any other desired state (for instance, linearly polarised).

The number states in Eq. (3.54) only allow for distinguishability in a single degree of freedom, the polarisation. As described in Section 3.5.3, if the fibre is longer than the walk-off length photons can be generated in more than one temporal mode. If the fibre is long enough to allow photon generation in N temporal modes, then N different amplitudes c_{HN} and c_{VN} will be required to describe the contributions into to the H and V polarisation components from the fibre as a whole. While the photons output into each temporal mode will be in a well defined polarisation state, generally this will vary from one length of the fibre to the next due to the random nature of the birefringence. In this case it would not possible to totally extinguish the component of light on one polarisation of the fibre through the use of wave-plates alone.

3.5.5 Generation of Photons with Naturally Narrow Bandwidth

As discussed in Section 3.4, an ideal photon source should produce an output of heralded single photons in a pure state. While it is relatively straightforward to achieve single spatial and polarisation mode operation for photons generated by FWM in optical fibres, it is more difficult to generate a spectrally pure heralded photon state. This is due to the spectral correlations that are usually present in the signal and idler JSA as a result of energy conservation and phase-matching (see Fig. 3.5(c)). While spectral filtering can be used to approximate a pure state by reducing this correlation, an alternative approach is to look for fibre dispersion profiles that minimise this correlation, and hence allow the generation of photons in naturally narrowband pure states without the need for filtering.

A general two-photon state generated by FWM can be expressed in the form

$$\left|\Psi\right\rangle \propto \iint d\omega_s d\omega_i \, f\left(\omega_s,\omega_i\right)\hat{a}_s^{\dagger}\left(\omega_s\right)\hat{a}_i^{\dagger}\left(\omega_i\right)\left|0\right\rangle, \tag{3.55}$$

where $f\left(\omega_s,\omega_i\right)$ is the JSA function described previously in Eq. (3.40). In analogy with the expectation value for the number of photons present in a single mode given by Eq. (3.12), the

generated number of photon pairs N_{pair} with frequencies ω_s and ω_i for the two-photon state is given by [132]

$$\begin{aligned}\left\langle N_{pair}(\omega_s,\omega_i)\right\rangle &= \left\langle \Psi \left| \hat{a}_s^{\dagger}(\omega_s)\hat{a}_i^{\dagger}(\omega_i)\hat{a}_s(\omega_s)\hat{a}_i(\omega_i) \right| \Psi \right\rangle \\ &= \left| f(\omega_s,\omega_i) \right|^2 . \end{aligned} \tag{3.56}$$

For signal and idler pairs that are uncorrelated in frequency, the probability of generating a pair at any given signal and idler frequencies must be expressible as a product of two functions, one dependent only on the signal frequency, and the other on only the idler frequency. The condition for the generation of spectrally uncorrelated photon pairs, and hence pure heralded single photons is therefore that the JSA be factorable such that

$$f(\omega_s,\omega_i) = f_s(\omega_s) f_i(\omega_i) . \tag{3.57}$$

As shown in Eq. (3.40), the JSA is composed of two contributing functions, $\alpha(\omega_s+\omega_i)$ and $\phi(\omega_s,\omega_i)$. The shape of the pump envelope function is fixed by the conversation of energy and always forms an angle of -45° to the signal frequency axis (when plotted as a function of frequency) on a JSA plot. The width of the function about the line described by $\omega_s+\omega_i = 2\omega_{p-peak}$, where $\omega_{p\text{-}peak}$ is the peak pump frequency, is defined by the spectral bandwidth of the pump pulse. In contrast, the angle of the function $\phi(\omega_s,\omega_i)$ on the JSA plot can be rotated through choice of the dispersion properties of the fibre. In general it is also important to consider the influence of any chirp on the pump pulse, which can introduce correlations in the time domain that are not apparent from the shape of the overall JSA in the frequency domain [132], although this is neglected here for brevity.

The anticipated shape of the phase-matching function $\phi(\omega_s,\omega_i)$ can be calculated analytically by using a linear approximation of the phase-mismatch κ given in Eq. (2.49) using a Taylor expansion of each of the propagation constant terms $\beta_{j\text{-}peak}(\omega_{j\text{-}peak})$ that contribute to it about their central frequencies $\omega_{j\text{-}peak}$. It is also assumed that the sinc term in the phase-matching function can be approximated by a Gaussian of the same FWHM. It can then be shown that the angle that $\phi(\omega_s,\omega_i)$makes to the signal frequency axis, θ_{pm}, is given by [50]

$$\theta_{pm} = -\arctan\left(\frac{\xi_s}{\xi_i}\right), \tag{3.58}$$

with

$$\xi_j = L\left[\beta_p^{(1)}\left(\omega_{p-peak}\right) - \beta_j^{(1)}\left(\omega_{j-peak}\right)\right], \tag{3.59}$$

where $\beta_j^{(1)}$ is equivalent to the expression for β_1, described previously in Eq. (2.20), for either the signal or idler wavelength, and L is the fibre length. There are two possible ways of achieving the factorable JSA described by Eq. (3.57). In the first method (symmetric group velocity matching) the fibre is designed such that for some desired combination of signal, idler and pump wavelengths, the corresponding values of β_1 mean that the slope of $\phi\left(\omega_s, \omega_i\right)$ lies at θ_{pm} = +45°, orthogonal to the slope of $\alpha\left(\omega_s + \omega_i\right)$. For a given pump bandwidth the fibre length can then be selected such that the widths of these two functions are matched, leading to no overall correlation in the JSA. On a plot of the JSA plot, of the kind shown in Fig. 3.5(c), this corresponds to the distribution of the JSA function becoming circular, centred on the peak signal and idler phase-matched wavelengths. This is also the state that is approximated by narrowband spectral filtering of both the signal and idler, as shown in Fig. 3.6(b).

The alternative approach (asymmetric group velocity matching) involves choosing the fibre parameters such that θ_{pm} = 0° or 90°. In this case, if the pump pulse is sufficiently broad compared to the width of the phase-matching [133] then the JSA function will form an ellipse with its major axis aligned with the signal wavelength axis or idler wavelength axis respectively. In this case, either the signal or idler will become narrowband, depending on the alignment of the JSA function, with the bandwidth determined by the width of $\phi\left(\omega_s, \omega_i\right)$. This type of JSA distribution occurs when either ξ_s or ξ_i is made equal to zero. As β_1 is the inverse of the group velocity (from Eq. (2.20)) it can be seen from Eq. (3.59) that these conditions correspond to the group velocity of the pump being matched to either the signal or idler group velocity. An example of the JSA distribution for the case of narrowband signal photon generation, with the idler group velocity matched to that of the pump, is shown in Fig. 3.9.

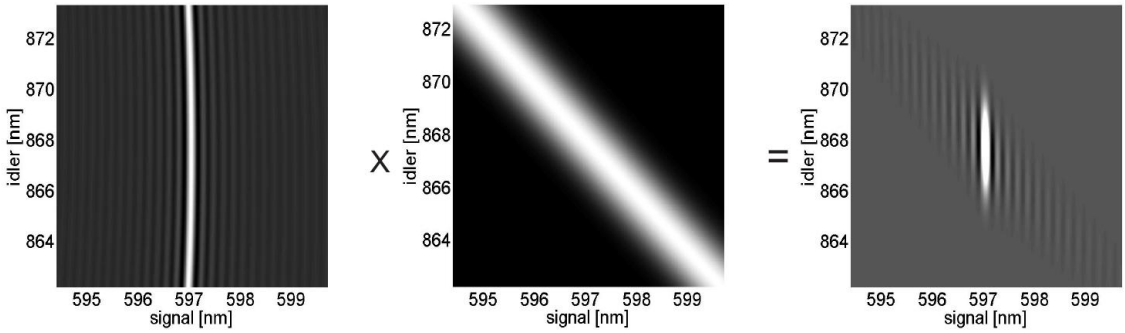

(a) (b) (c)

Figure 3.9: (a) The phase-matching function; (b) pump envelope function; and (c) the resulting JSA for a birefringent PCF designed to generate naturally narrowband signal photons at 597 nm from a pump wavelength of 705 nm (Image from [55]).

The slight curvature seen in the phase-matching function in Fig. 3.9(a) results from the higher order terms in the expansion of κ that were discarded previously. This limits the range of the central pump frequency over which the heralded photon state from this JSA will be pure. As seen in Fig. 3.9(c), the central peak of the JSA function exhibits almost no correlation of the signal and idler wavelengths. However, using the correct sinc profile for the phase-matching function, rather than a Gaussian approximation, leads to low intensity outlying peaks in the two-photon state which are correlated, and thus reduce the purity of the generated state. The influence of these peaks on the interference visibility that can be observed with the heralded output photons can be reduced, either using spectral filtering, or by increasing the length of the fibre used for FWM.

3.6 Applications of Single Photons

Among the first uses of photons prepared in well-defined states, were tests to verify the validity of quantum mechanics itself. One prediction made by quantum theory states that particles or photons can be 'entangled' in such a way that their individual quantum states become correlated and a measurement on one can instantaneously effect its partner, regardless of the distance between them (see Section 3.1). This phenomenon led to an apparent paradox, as described in the seminal paper of 1935 by Einstein, Podolsky and Rosen [134], as it seemed to violate the idea of local realism in the universe. This led some who doubted the validity of quantum mechanics to instead favour hidden variable theories, where the final state of the photons after measurement was determined by some unknown, but fixed, variable which was inaccessible to measurement. In 1964, J. Bell proposed a possible test that set an upper limit on the amount of correlation in the states of particles that a

hidden variable theory can account for [135]. Pioneering work by A. Aspect et al., using correlated photon pairs produced by atomic cascades in calcium [136] demonstrated that Bell's inequality can be violated, providing further experimental support for the basis of quantum mechanics. Later work using photon sources based on parametric down-conversion (see Section 3.4.3), further improved the statistical significance with which the violation of Bell's inequality was observed [137]. This ruled out most classes of hidden variable theories that could otherwise be permissible due to loopholes allowed by the previous experimental procedures.

In recent years, interest in the use of single photons has shifted from fundamental tests of quantum mechanics to future real-world applications of technological importance. One field of interest is quantum metrology, where it has been demonstrated that by taking advantage of photons suitably prepared in an entangled state, interferometric phase measurements can be realised with greater accuracy than usually permitted by the shot noise limit [9]. A closely related area of study is quantum lithography. Here control over the state of the photons used in an optical lithography process can allow features smaller than the wavelength of the incident light to be fabricated in photosensitive material [138]. To date however, the main focus for research into single photons has been on the implementation of photonic qubits (see Section 3.1) for the transmission and processing of quantum information.

3.6.1 Quantum Cryptography

One of the most well-known and well developed applications of single photons is that of quantum cryptography [8,139,140], enabling provably secure communications. This is usually achieved by quantum key distribution, where the data describing an encryption key is encoded onto a series of qubits, for example, by using two orthogonal polarisation states of a photon to represent a binary one and zero. Once the qubits have been exchanged between two parties so that they share the same key, further communications can take place securely over a regular classical communications channel using this key for encryption.

The security of this system is guaranteed by the fact that the result of a destructive measurement on a single qubit cannot be used to fully reconstruct its state without additional information on how the state was prepared, making it impossible to duplicate an unknown quantum state [141]. Thus, if a hidden eavesdropper attempts to incept photons from the key and then resend them, they cannot reliably reproduce the correct photon state to resend. This

leads to a characteristic rise in the error rate of bits in the key, above the baseline rate due to noise and optical losses. For an ideal photon source emitting only a single photon at a time, if this rise in the error rate is not seen then the key is guaranteed not to have been intercepted. It is therefore important to limit the probability of emission of multiple photons from the source (within the time window corresponding to the transmission of a single bit of the key), as the security of communication may otherwise be compromised by the so called 'photon number splitting attack' [142].

It should be noted that quantum key distribution is one of the few QI applications for which the photon state from an attenuated laser (see Section 3.4.1) can be used to approximate a single photon source. However, the maximum bit rate at which a key can be sent is limited both by sources of noise in the detection (commonly detector dark counts) and the optical losses in the transmission channel, which increase with transmission distance. By using a true single photon source for the transmission of a quantum key, the detected noise can be reduced (by triggering the detector only when a photon is known to be present) and the transmission length over which a key can be exchanged in a reasonable period of time is significantly increased.

3.6.2 Quantum Information Processing

The other main application for photonic qubits that has generated much interest in recent years is quantum information processing (QIP), with the eventual aim of developing a scalable architecture for quantum computation [10,116]. As with classical computation, the fundamental goal of QIP is to implement some mathematical operation which relates one or more input states to a desired output state. In classical information processing, these input states are represented by a number of bits taking values of one or zero. In the case of QIP with qubits, the inputs may be in superposition states, as well as being entangled with each other (see Section 3.1). For solving certain computational problems, this leads to a significant reduction in the time required to solve a problem of a given complexity, compared to classical computation. Well known examples include Shor's algorithm for determining the prime factors of large numbers [143] and Grover's algorithm for database searching [144]. A quantum computer would also be well suited to the simulation of complex quantum systems [145].

One approach to performing this type of information processing is the scheme of linear optical quantum computation [72,146], in which the input photons are passed through a series of logic gates in order to implement the processing task. The required interaction between photons is achieved through non-classical interference at a beam-splitter (see Section 3.3). Only a single type of two-photon logic gate, the controlled-NOT gate (c-NOT), is required to realise universal quantum computation [67]. In other words, any desired QIP task can be performed by combining the output from this type of gate with one-photon logic gates (implemented using linear optical components such as wave-plates and beam-splitters), in an appropriate arrangement for the desired task.

The operation performed by a c-NOT gate on a target qubit is similar to that of a NOT gate in classical electronics, as it reverses the probability amplitudes of the two state components of the qubit. Whether or not this operation is performed is determined by the state of a second control qubit and thus the gate implements the required interaction between the two photons. The c-NOT gate has been successfully demonstrated experimentally in both free-space [147] and waveguided configurations, including in a fibre-based system [148]. This would be compatible with heralded single photon sources based on the generation of photon pairs in optical fibre (see Chapter 5). As the operation of these logic gates depends on non-classical interference, their fidelity of operation will be limited by the purity of the heralded single photon state that the chosen single photon source is able to deliver. As a general processing task may require the concatenation of multiple gates to implement, the purity of currently available single photon sources is one of the factors limiting the scalability of experimental QIP to higher photon numbers.

Chapter 4

Heralded single photon generation in PCF

The goal of the work presented throughout this thesis was a single photon source operating near 1550 nm, based on FWM in a PCF. This particular wavelength was selected because of its importance in telecommunications, being the wavelength of minimum transmission loss in silica optical fibres (see Section 2.1.5). Since much of the current study into the quantum communications applications of single photon sources (see Section 3.6.1) is with the intent of integrating them with existing telecoms networks, sources at this wavelength are highly desirable for use in research. Furthermore, fabricating a useful source requires high quality fibre components, particularly low loss filtering elements. Working at this operating wavelength means that relatively cheap and, more importantly, low loss, fibre components are readily available.

This chapter describes the development of a single photon source based on the concept of parametric generation of correlated pairs of photons, with the detection of one photon used to herald its partner, as outlined in Section 3.4.3. Section 4.1 describes the pump laser source and PCF that were used to generate the required photon pairs by FWM. This PCF was then incorporated with free-space optics, used for the separation and filtering of the generated photons, in order to produce a single photon source. Details of the construction of this source are discussed in Section 4.2. In Section 4.3 the source performance is evaluated from measurements of the coincident count rate between the signal and idler photons generated by FWM. Finally, in Section 4.4 the wavelengths of the signal and idler photons were measured in order to allow for the selection of appropriate components for the later

development of an all-fibre source of heralded single photons, which will be the focus of Chapter 5.

4.1 Choice of PCF and Pump Source for FWM

The photon source described in this chapter was based on the generation of correlated pairs of photons through FWM in a PCF. As the dispersion of PCF can be easily tailored to allow phase-matching for FWM over a wide wavelength range (see Section 2.2.4), the choice of pump source and generated wavelengths is relatively unconstrained. This allows the generated output wavelengths to be selected at the design stage of the PCF for a desired pump laser, subject to the conservation of energy.

As discussed in Section 3.5.2, the maximum pump power that can be used to generate FWM pairs in a photon source of this type is ultimately limited by the effect of multiple-pair generation events. In order to achieve a sufficient high output rate of photons from the source, a high repetition rate, pulsed pump laser was required. Using short pulses to increase the peak power also helps to reduce the contribution of noise photons generated by Raman scattering (see Section 2.2.2). The pump source that was selected for use was an amplified, mode-locked, 1064 nm fibre laser (*Fianium*, Femtomaster1060-0.1). This provided a variable average pump power of up to 120 mW in 4.5 ps duration, bandwidth-limited pulses, at a rate of 80 MHz. Yb-doped fibre lasers such as this are able to provide relatively high average power compared to other laser systems whilst also being compact and low cost. Fibre lasers also offer the significant advantage of being stable and low maintenance as their beams are generated in the guided mode of the fibre so there is no need for realignment. This choice of pump wavelength also meant that for an idler at 1550 nm, the corresponding signal wavelength would be at 810 nm. This wavelength lies within the ideal range for detection with high efficiency, silicon-based single photon detectors.

In order to generate idler photons at the required wavelength of 1550 nm with a 1064 nm pump, the pump wavelength should lie in the normal dispersion region of the PCF (see Section 2.2.4). PCF-B was chosen from a pre-existing set of fibres that closely matched the required dispersion parameters for phase-matched FWM at the desired wavelengths. Fig. 4.1(a) shows an SEM image of this fibre. The structure of PCF-B was based on a standard hexagonal cladding hole array with a solid core of 5 µm diameter. The pitch of the cladding (Λ) was 2.92 µm and the ratio of the cladding hole diameter to the pitch (d/Λ) was 0.34.

The low air filling fraction of this PCF meant that it also satisfied the condition for endlessly single-mode guidance (see Section 2.1.3). Single-mode guidance of the generated idler and signal photons ensured that the output heralded photons from the source would be in a pure spatial mode. Generating the photons in a single spatial mode of the PCF also meant that they could later be easily coupled into standard single-mode fibre (SMF) using low loss fusion splicing (see Section 2.4). Having only a single mode available in the fibre across the whole wavelength range of interest also precluded the possibility of an unintentional intermodal phase-matched process generating light near the wavelengths of interest. Since the photon source is designed to have maximum transmission at the desired signal and idler wavelength and the detectors are sensitive to single photon levels of light, even a relatively low intensity source of uncorrelated photons at these wavelengths would be a significant cause of noise.

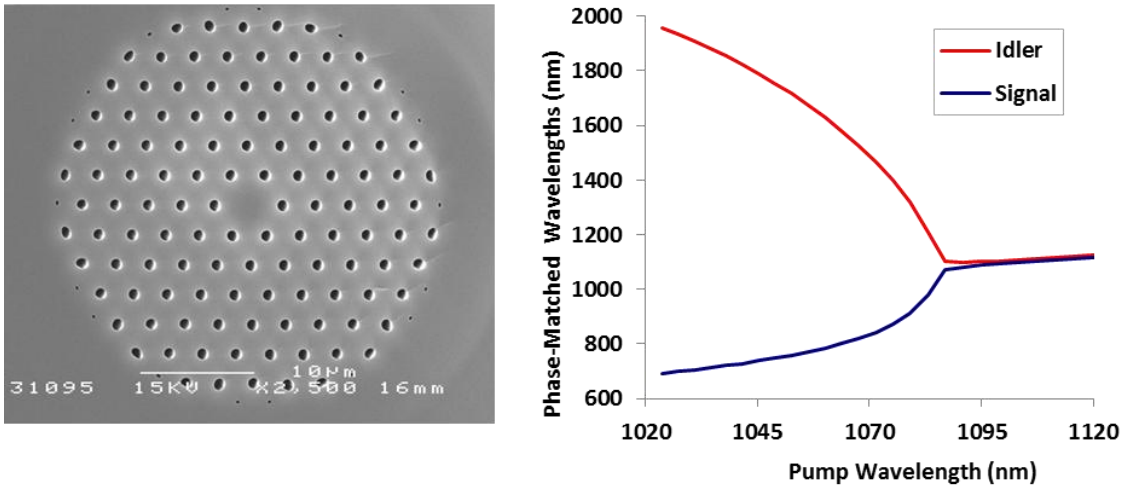

(a) (b)

Figure 4.1: (a) SEM image of the cross-section of PCF-B. The light grey region is silica and the dark grey regions are air holes; (b) Phase-matching curve for the structure, calculated from measured dispersion data using Eqs. (2.48) and (2.49). The curves show the anticipated generated signal and idler wavelengths for a given pump wavelength.

The calculated phase-matching plot for PCF-B is shown in Fig. 4.1(b). This shows the signal and idler wavelengths that are expected to be generated through FWM, and how these vary with the central pump wavelength. The ZDW for this PCF was calculated to be at 1087 nm. The phase-matching results shown are for the co-polarised case, where the pump, signal and idler are all polarised on the same axis. Since the PCF is designed to be symmetric it has only nominal birefringence, so the phase-matching conditions for co-polarised FWM will be identical for the two orthogonal polarisation modes. As shown in Section 2.2.4, the phase-matching conditions are dependent on the pump power used. The results shown in

Fig. 4.1(b) correspond to a peak pump power of 12 W, although the effect of pump power on the generated wavelength is minimal for a pump wavelength far into the normal dispersion region, as is the case here. This particular PCF was chosen because the calculated phase-matching results indicated that a 1064 nm pump pulse would lead to the generation of a signal and idler at around 810 nm and 1550 nm respectively.

To check that the calculated phase-matching results for the PCF were accurate, the generated output of the fibre was observed on an optical spectrum analyzer (OSA – *Ando*, AO-6315B). Unfortunately, the short pulse-length fibre laser that was chosen to pump the finished photon source had insufficient maximum peak pump power to be able to observe any nonlinear output from this PCF on the OSA. In order to observe the signal and idler wavelengths directly, a different laser with a higher peak power, also operating at 1064 nm, was used for comparison. The laser chosen was a Q-switched, Nd:YAG microchip laser (*Teem Photonics*, NP-10820) producing nanosecond pulses (0.6 ns FWHM) at a repetition rate of 7.2 kHz. The average output power of the laser was 65 mW. Using a microscope objective lens the laser was coupled into the guided mode of a 6 m section of the PCF, with a coupling efficiency of around 60%. This corresponds to a maximum of around 9 kW peak power in the fibre, compared to 200 W for the fibre laser. The output of the PCF was then connected directly to the OSA and the generated signal and idler peaks were observed. The measured optical spectra of the pump and the generated signal and idler peaks are shown in Fig. 4.2.

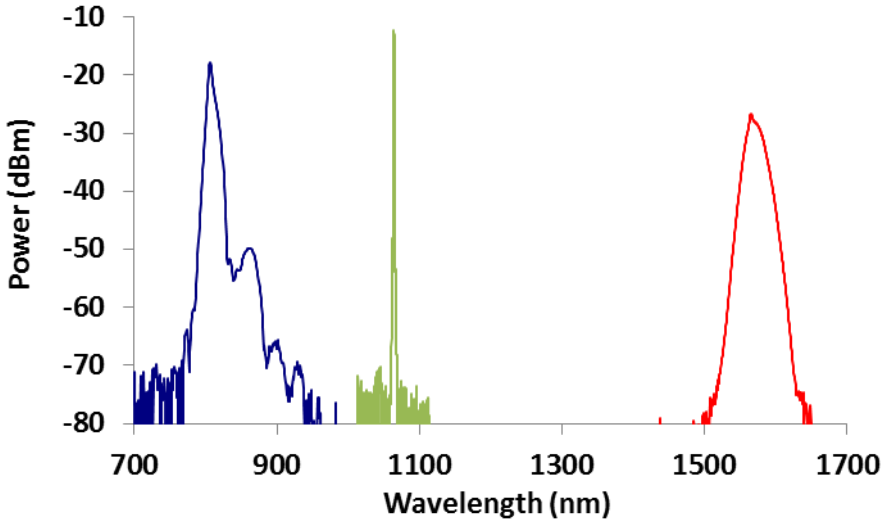

Figure 4.2: Measured FWM spectrum of PCF-B, pumped using a nanosecond pulsed microchip laser. The different coloured sections show separate high resolution scans for the signal (blue), pump (green) and idler (red). The measurement resolution was 2 nm for the signal and idler wavelength measurements and 0.2 nm for the pump wavelength.

The small peaks that can be seen on the long wavelength side of the signal peak correspond to the peak wavelengths expected for the second, third and fourth order Raman-shifted light (the first Raman peak is obscured by the bandwidth of the signal peak). The signal and idler wavelengths were found to be 805 nm and 1563 nm respectively using this pump source. This indicated that the fibre was a suitable choice to generate the desired wavelengths. However, further measurements still needed to be made of these using the picosecond fibre laser as the pump source. Due to the extremely narrow spectral filtering that is required to ensure indistinguishability of the output photons, it was necessary to have an accurate measurement of the signal and idler wavelengths with the pump laser that was intended to be used in the final device, so that appropriate filtering components could be selected. The wavelength of the picosecond fibre laser was found to be 1063.2 nm, again using the OSA. The calculated phase-matching curve shown in Fig. 4.1(b) shows the steep gradient of around 5 for the generated signal wavelength and 15 for the idler in the phase-matching conditions. A change of around 0.5 nm in the pump central wavelength is therefore predicted to shift the signal and idler wavelengths by several nanometres to 803 nm and 1571 nm. However, due to the steep gradient of the curve at this wavelength, comparison between the two lasers is quite sensitive to both small changes in the pump wavelength and any error in the calculation of the curve itself.

4.2 A Heralded Single Photon Source with Free-Space Filtering

In order to verify the principle of operation for the fibre-based single photon device, preliminary work was conducted using free-space bulk optics for filtering and wavelength separation of the generated photon pair. The output from this source was then characterised using two single photon avalanche diode detectors (SPAD). This preliminary work also allowed the peak FWM wavelengths to be determined, in order for appropriate filtering components to be selected for the subsequent all-fibre device. The experimental setup is shown in Fig. 4.3.

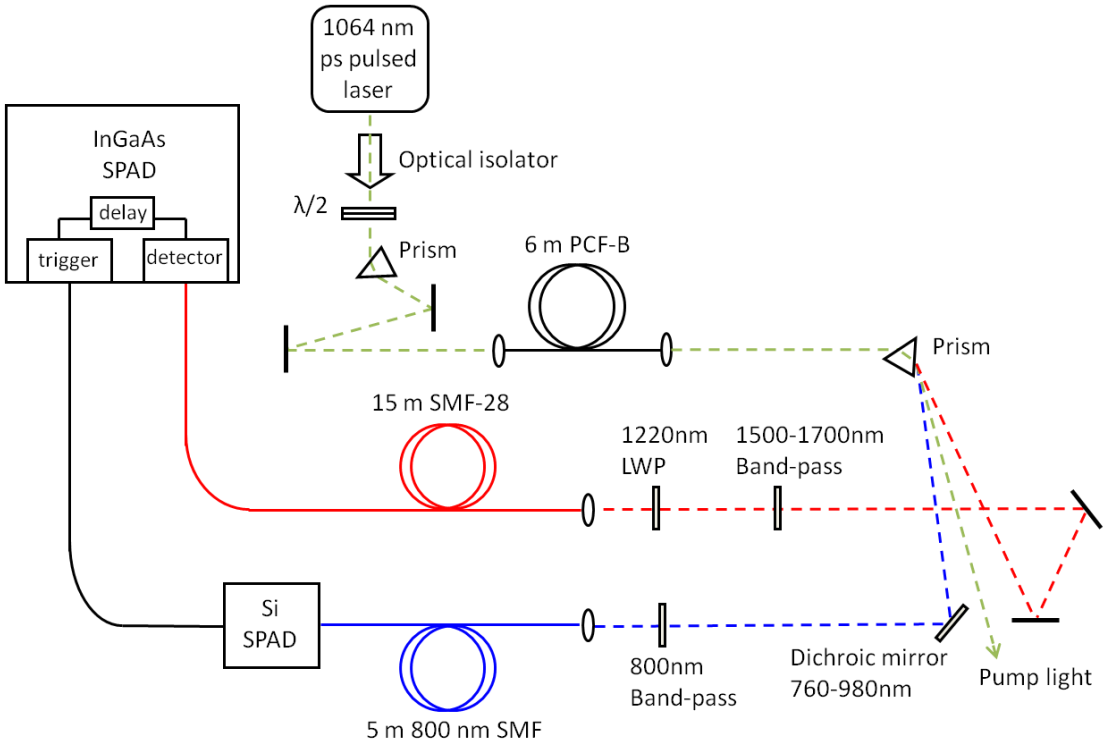

Figure 4.3: Schematic for the single photon source using entirely free-space filtering. λ/2 is a half-wave plate, LWP is a long-wave pass filter, SPAD are single photon avalanche diode detectors and SMF is conventional single-mode fibre.

The pump laser used was the same 1064 nm fibre laser described previously in Section 4.1. An optical isolator was required at the output of the laser in order to reduce the intensity of any backscattered light, such as that from the reflection at the end face of the PCF, from going back into the laser. This could otherwise affect the stability of the laser output and potentially damage it.

After going through the isolator the pump beam passed through a half-wave plate to rotate its polarisation state to be p-polarised at the surface of the prism in order to minimise the Fresnel reflection from the surface and maximise the power available to couple into the PCF. After passing through the prism the beam was coupled into the PCF using an anti-reflection coated aspheric singlet lens. The use of a prism here was essential as it removed any photons emitted by the laser at wavelengths close to the signal and idler wavelengths that were intended to be generated. The launch optics reduced the total amount of laser power available at the input end of the fibre to around 70 mW, due to losses in the isolator and from reflection from the surface of the prism. The measured coupling efficiency into the PCF was around 60% of the available 70 mW.

The 6 m section of PCF-B generated pairs of photons at wavelengths governed by the phase-matching conditions shown in Fig. 4.1(b). It should be noted that the walk-off length for 5 ps pulses in this fibre is only around 30 cm. This meant that the three interacting pulses (signal, idler and pump fields) will only remain aligned and interacting in the PCF over this length, due to the fact that they are travelling with different group velocities. Eq. (2.65) describes how the number of generated photon pairs is expected to depend on both the pump power and fibre length. The equation shows that the average number of pairs generated per laser pulse rises quadratically with increasing fibre length. The super-linear increase in signal and idler intensity occurs due to the fact that the four-wave mixing rate depends on the intensity of all four of the interacting fields (although the pump fields are degenerate in this case) and therefore the generation rate in later sections of the PCF is enhanced by the pairs generated at an earlier point in the fibre. However, as discussed in Section 2.2.7, Eq. (2.65) only remains valid in the range where the generated signal and idler fields can continue to interact with the pump pulse.

Although the pair generation rate only rises linearly with PCF length beyond the first 30 cm, the long interaction length in a 6 m length reduces the amount of laser power required to attain a desired generation rate. For the purposes of a free-space proof of principle demonstration, a higher generation rate is preferable, both for ease of setup and to observe a clear output despite the inherently high losses of the free-space filtering arrangement. Although there will be some walk-off between the signal and idler pairs due to the long PCF, this timing jitter is small relative to the temporal gate width of the single photon detectors, so this should not have any impact when testing the single photon source in isolation. The consideration of walk-off becomes critical when considering the interaction of multiple photon sources (see Section 3.5.3).

The output signal and idler beams from the PCF were collimated using an aspheric singlet lens before passing to another prism. This prism separated the signal, idler and pump wavelengths onto three different paths. The signal and idler beams then passed through filters designed to remove any remaining scattered pump light and other wavelengths before coupling them back into conventional SMF, with a lens mounted on a 3-axis translation stage.

Assuming that the pump laser is operated at the maximum power of 100 mW, there would be $\sim 7 \times 10^9$ pump photons output from the PCF, along with the single pair of generated photons of interest. In order to be able to detect the single pair of photons there needs to be of the

order of 100 dB of rejection of the pump frequency, in order to assure that the probability of detecting a pump photon is low compared to the generated photons of interest. Much of the required loss at 1064 nm comes from the two filters in the idler arm and single band-pass filter and dichroic mirror in the signal arm. The inefficiency of the detectors at the pump wavelength also meant that the probability of detecting photons these photons was lower than for the generated signal and idler photons. The remainder of the required filtering came from the spectral selection provided by the combination of the dispersed output of the prism being collected into single-mode fibre. Even with an aspheric singlet lens increasing the coupling efficiency of the beam to the fibre, the coupling is still strongly dependent on the position of the incoming beam relative to the fibre, meaning that only a narrow spectral range would be transmitted to the detector. The wavelength of light coupled into the fibre from the prism could be adjusted by horizontal translation of the lens perpendicular to the propagation direction of the fibre. For this preliminary work it was not necessary for the filtering to be so narrow as to achieve spectral indistinguishability of the single photons.

The output of the single-mode fibres for the signal and idler photons were then connected to SPADs to detect the photons and characterise the source. The signal photons, at around 810 nm, were detected using a silicon-based SPAD (*Perkin Elmer,* SPCM-AQR-14), operating in the 350 - 1050 nm range with an efficiency of 55% at the wavelength of interest. Since the source was designed to output the 1550 nm idler photons, the detected signal photons were used to produce a heralding signal. This detector was therefore an important part of the single photon source as it provided the electronic herald signal output. The high detection efficiency at this wavelength is therefore crucial because it affects the performance of the source; only idler photons that have their corresponding herald detected contribute to the successful operation of the source.

For the longer idler wavelength, at around 1550 nm, the detector was an InGaAs based SPAD (*Id Quantique,* ID200). The detection efficiency could be varied in the range 10-30% by controlling the internal bias voltage used to drive the detector. The drawback of using higher detection efficiencies is that the higher bias voltage raises the dark count rate. These are false counts that occur even when no light is present at the detector. Also, whilst the bias level required for a detection efficiency of 10% was specified by the manufacturer, the required detector bias for a 30% detection efficiency had to be deduced by monitoring the measured

count rates as the bias was increased. For these reasons, the measurements made to characterise the source were performed at the lower detector efficiency of 10%.

An important distinction between the two detectors is that whilst the performance of the detector in the signal arm directly affects the performance of the source, the detector in the idler arm does not. For practical applications the output of the source is the photons from the idler arm, along with the electronic heralding signal from the Si SPAD. While any application of the source would most likely require some form of detector at the idler wavelength, and may well be concerned with achieving this detection with low loss, any such detection losses would be part of the application rather than a characteristic of the source. The use of the InGaAs detector here is only for the purpose of characterising the source. While the lower detection efficiency at this wavelength can result in these characterisation measurements being more challenging to make, since this loss is not a part of the source it can be accounted for in the figures for the source performance.

In the signal arm a 5 m section of SMF with a cut-off wavelength of 750 nm (*Corning*, SM800) was used to deliver the photons to the detector. A longer 15 m length of standard telecommunications fibre (*Corning,* SMF-28e), was used in the idler arm. The additional 10 m of fibre introduced a delay of around 50 ns between the arrivals of the two photons at their respective detectors. Upon arrival of a signal photon at the Si SPAD the output electrical pulse, signalling a detection, was sent to the trigger input for the InGaAs SPAD. The additional delay introduced by the extra length of fibre allowed time for the electrical signal to reach the second detector, and its internal electronics to trigger and activate the detection element. The minimum electronic gate width of 2.5 ns (corresponding to an active time of around 1 ns for the detecting element) was chosen, both to minimise the amount of accidental background light detected, and to allow any features of the input light spaced closely in time to be resolved.

4.3 Characterisation of the Single Photon Source

Using single photon detectors at the end of both the signal (heralding) and idler (output) arms of the single photon source, it is possible to look for correlations between detection events in the two, due to generation of FWM pairs. Ensuring that these correlations could be observed above any background noise present, particularly detector dark counts and Raman-shifted light at 1550 nm, was one of the main aims for this free-space demonstration.

The Si SPAD was operated in a free running mode, allowing photons to be detected regardless of their arrival time. The count rate from this detector gave the measured singles count rate in the signal arm. This is the number of signal photons that reach the detector, regardless of whether the corresponding idler photon is also detected. If the optical losses in the signal arm are known this can be used to calculate the generation rate of photon pairs. The detector cannot distinguish between one photon and multi-photon detection events, or any other sources of optical noise that make it through the filtering elements to the detector. These sources of noise can therefore cause false heralding events, where a single photon state is not output from the idler arm as expected.

The heralding signal from the Si SPAD was used as the electronic trigger for the InGaAs SPAD, which was operated in a gated mode. Detection events on the InGaAs SPAD therefore correspond to coincident detections between two photons - a signal photon, and an idler photon that arrived within the 1 ns optical gating window of the InGaAs SPAD. The extra 10 m of optical fibre in the idler arm ensured that for a signal and idler generated simultaneously in the PCF, the idler would always arrive at the detector after the signal photon had already been detected and the InGaAs detector had time to activate. The InGaAs SPAD had an adjustable electronic delay feature, allowing an additional delay of up to 25 ns to be applied between the arrival of a trigger pulse and the activation of the detector element. This delay could be adjusted in 0.1 ns intervals, allowing the delay to be fine-tuned such that the detection of a signal photon would allow the gate of the InGaAs SPAD to be open when the idler photon arrived within the 1 ns detection window.

Scanning the adjustable delay across the range of 25 ns whilst observing the detection rate of the InGaAs SPAD showed the number of idler photons present in two important regions – idler photons detected from the same laser pulse that generated the heralding signal, and uncorrelated photons detected on the subsequent pulse of the laser. The measured

coincidence count rates, at the delay values corresponding to these points, is shown in Fig. 4.4 for pump powers of 21.5 mW and 53.0 mW at the input end of the PCF. The background coincidence count rate between these times was seen to be ~10 counts per second (C/s) for the pump power of 21.5 mW and 50 C/s with a 53 mW pump.

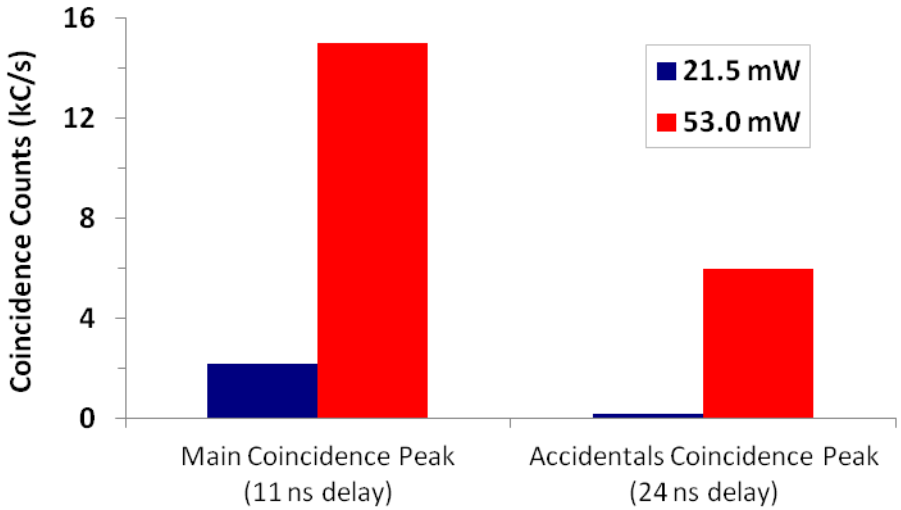

Figure 4.4: Measured coincidence count rates at the two settings for the InGaAs SPAD electronic delay, where peaks in the count rate were observed.

The measured coincidence count rate results showed a large peak centred at around 11 ns. This corresponds to the case where the electronic delay was appropriately adjusted such that the idler photon detected was generated at the same time as the signal photon that caused the heralding signal. This is referred to as the main coincidence peak. The smaller peak that was observed near 24 ns is known as the accidentals peak. The separation between these two peaks is determined by the laser pulse repetition frequency (PRF). In this case the 80 MHz PRF gives laser pulses spaced by around 12.5 ns in time. The accidentals peak results when the idler arm detector is activated to coincide with the arrival of the photons generated on a subsequent pulse of the laser to that which caused the heralding signal. Although only a single accidental peak could be seen within the 25 ns delay time window, peaks identical to this one are expected to be observed for every 12.5 ns of delay time, both before and after the main coincidence peak. At all delay times between these two peaks the low observed coincident count rate corresponded to the background count rate when the detector was activated at a time in between the expected arrival time for photons generated by laser pulses.

As the detected photons in the accidentals peak were not generated as part of the same FWM pair as the detected signal photon, they are uncorrelated photons. There are several possible contributions to the uncorrelated noise in the accidentals peak and the background count level. The detector has an inherent level of dark counts which will add to the measured count rate. This is a form of detector noise where a count is generated without a photon present due to the spontaneous creation of a thermally excited charge carrier triggering an avalanche current. While this noise cannot be entirely eliminated, the probability of such events is reduced by using a reasonably low detector bias, and by minimising the time the detector element is active by using the minimum detector gate time. The source was operated in a fully darkened room to minimise the contribution of stray photons from the room lighting to the background count rate. Under these conditions the background count rate was found to be ~50 C/s at the highest pump power used.

This type of detector can also be susceptible to an effect known as after-pulsing where the generation of an avalanche current through photo-detection leads to a significantly increased probability of a dark count for some time after. In order to avoid such false counts the detector includes an electronic dead-time, where the detector is purposely not activated for some time after the detection. During this work the dead-time used was 5 µs. This limits the maximum potential measured count rate to 200 kC/s, with some discrepancy between the measured and actual count rates occurring as this value is approached. The coincidence count rates observed were significantly below this value, so the results should not be affected by this dead-time. Comparison of the measured count rates with a detector dead-time of 10 µs showed no observable difference, indicating that a 5 µs dead-time was sufficient to eliminate the effects of after-pulsing with these detector settings.

The sources of noise described above are also present in the accidentals peak. However, here there are also further contributions to the uncorrelated photons due to the bright pump pulse. Possible sources of noise due to the laser include photons at the pump wavelength that have passed through the various filtering stages, photons from the pump LED in the fibre laser at 980 nm and photons generated by undesired nonlinear processes in the fibre due to the high intensity pump pulse, especially Raman-shifted pump light. The final, and most important contribution to the accidentals peak comes from additional photon pairs, generated by the FWM process, that are uncorrelated with the photon that caused the heralding signal. With

the exception of the dark counts, most of these noise sources are related to the pump power level.

In principle the noise sources associated with leakage of pump photons to the detector and Raman-shifted light could be reduced by additional spectral filtering. The Raman effect can also be suppressed by cooling of the fibre [101]. However, the generation rate of pairs of photons on subsequent pulses of the lasers is related to the average pair generation probability and cannot be reduced, except by reducing the pump power. This source of uncorrelated photons ultimately limits the potential brightness of the source, as the probability of generating an uncorrelated photon pair on a subsequent pulse of the laser is approximately the same as the probability of generating two pairs on a given laser pulse (see Section 3.5.2). Although the noise photons seen in the accidentals peak shown in Fig. 4.4 are widely separated in time from the correlated photon pairs of interest, and can clearly be avoided through temporal gating in the activation time of the detector, these noise photons will be present on every pulse of the laser, including on the same laser pulse that generated the heralding signal, where they cannot be separated temporally from the true heralded single photon. Thus the magnitude of the accidentals peak from a subsequent laser pulse indicates the level of noise photons present in the main coincidence peak. The coincidence-to-accidentals ratio (CAR) is an important figure of merit for such a system and is given by

$$\frac{C-A}{A}, \tag{4.1}$$

where C is the maximum measured count rate of the main coincidence peak and A is the measured count rate of one of the accidental peaks (taken to be the laser pulse directly after that which produced the heralding signal in the case of Fig. 4.4). This ratio shows the relative proportion of uncorrelated noise relative to the true coincidence counts from heralded single photons. These uncorrelated detections will reduce the potential visibility of any subsequent quantum interference experiment, which rely on the indistinguishability that a pure single photon state provides (see Section 3.3). Although the CAR required will vary depending on the desired application, for the purposes of source characterisation, the brightness is usually given for a CAR of 10. The results for two pump powers in Fig. 4.4 show that the CAR can be increased by lowering the pump power, although this also reduces the source brightness. Ultimately, the upper limit on the CAR will be limited by background noise in the system.

The measured singles count rates in the signal (N_s) and idler (N_i) arms are dependent on the pair generation rate (r), as well as the effective transmission coefficient in the signal and idler arms (η_s and η_i), and the efficiency of the Si and InGaAs SPADs (η_{Si} and η_{InGaAs}), through

$$N_s = r\eta_s\eta_{Si} + B_s, \tag{4.2}$$

and

$$N_i = r\eta_i\eta_{InGaAs} + B_i, \tag{4.3}$$

where B_s and B_i are the measured background count rates in the signal and idler arm respectively. Due to the necessity of gating the InGaAs SPAD it was not possible to measure N_i in this preliminary experiment. The coincidence count rate for the main coincidence peak C is dependent on the generation rate r as well as the transmission and detection efficiency of both of the arms, and is given by

$$C = r\eta_s\eta_{Si}\eta_i\eta_{InGaAs} + A, \tag{4.4}$$

where A is the accidentals coincidence rate. The accidentals coincidence rate is given from the measured singles count rates by

$$A = \frac{N_s}{\mathrm{PRF}} \times \frac{N_i}{\mathrm{PRF}} \times \mathrm{PRF} = \frac{N_s N_i}{\mathrm{PRF}}. \tag{4.5}$$

An important figure of merit for a heralded single photon source is the heralding fidelity. This is the probability that a single photon is output from the source, given that a heralding signal was output. The heralding fidelity H, is defined by

$$H = \frac{C - A}{N_s\eta_{InGaAs}} \approx \eta_i. \tag{4.6}$$

If the noise level in the signal arm B_s, is low then heralding fidelity is given approximately by the optical loss in the idler arm, although it is also dependent on the spectral filtering profile in the case of narrowband filtering (see Section 5.3.3). It is essential to minimise losses in the idler arm for this reason, as well as to improve the brightness of the source, given by Eq. (4.4). Although the effect of loss in the signal arm is not so detrimental to the source performance, as it will not affect H, loss in this arm should still be minimised if possible, as it will similarly affect the source brightness.

As discussed in Section 3.4.3, the heralding process removes the vacuum component of the output photon state, which would otherwise dominate due to the low pair generation rate. The effect of loss in the idler arm will cause empty output pulses to be heralded, reintroducing this effect of the vacuum component to some extent. As with the case of noise photons, this will reduce the fidelity of operation of subsequent processes that depend on a pure single photon state. This is the reason that the heralding fidelity is important measure of source quality.

The large coincidence peak shown in Fig. 4.4 demonstrates that correlated photon pairs are being generated by this setup, and can be discriminated from other background sources of noise. The CAR can be controlled through the pump power, although at a CAR of 11 the output of the source was only 2.2 kC/s heralded single photons from an 80 MHz pump rate (as seen in Fig.4.4 with a pump power level of 21.5 mW). In the ideal case of low loss and noise the CAR should be given by the ratio of the PRF to *r*, which can be seen from Eq. (4.1), (4.4), and (4.5).

For a 20 mW pump power level the trigger rate of the InGaAs SPAD, which corresponds to the measured singles count rate in the signal arm, was around 250 kHz. If most of these counts were due to the signal photons from FWM pairs then each should give a corresponding idler photon in the case of perfect heralding fidelity. The fact that the measured two-fold coincidence count rate is significantly lower demonstrates the high level of loss in the system due to this filtering arrangement. Disregarding the effects of noise here and accounting for the detector efficiencies, the transmission in the idler arm can be estimated from this information to be around 8%. Although the count rates here appear low this is due to the high levels of loss in the signal and idler arms rather than the generation rate of photon pairs. In Chapter 5, the use of narrowband fibre based filtering will be shown to significantly improve both the brightness and heralding fidelity of the source.

4.4 Measurement of the Signal and Idler Wavelengths

In order to determine the required specifications for future filtering components for this source, the wavelength of the generated signal and idler photons had to be accurately measured. As described previously in Section 4.2, the spectral filtering of this source could be tuned by adjusting the position of the coupling lens before the output single-mode fibre, using the micrometer controlled translation stage in order to couple in light that had been dispersed by the prism into the fibre. The filtering setup first had to be calibrated by relating the recorded micrometer position readings to the transmitted wavelength of the filtering.

In order to produce the required calibration curves, light from a broadband supercontinuum source (see Section 2.2.8) was launched to the input end of PCF-B by butt-coupling the fibres. The output wavelength transmitted through the prism based filtering was measured using an OSA (in place of the SPAD detectors in each arm) as the micrometer position was scanned. The calibration curves showed a linear dependence of the filtered wavelength on micrometer position over the narrow wavelength range of interest with a measurement error of around ±1 nm.

After this, calibration light from the 1064 nm picosecond pump pulse was again launched into PCF-B in order to generate the FWM peaks of interest. The micrometer markings on the translation stage were recorded as the filtering was scanned across the central operating frequencies (the position where the peak count rates were observed), first for the signal arm and then for the idler. The count rate in the signal arm was monitored using the Si SPAD in its free running mode to show how the singles count rate in the signal arm varied with the central wavelength of the filtering. For the measurement of the idler wavelength the InGaAs SPAD was operated with the maximum allowable internal trigger rate of 1 MHz, as this detector cannot be operated in a free running mode. Scanning the filtering in this way allowed the shape of the generated FWM sidebands to be determined. The measured, calibrated signal and idler spectra are shown in Fig. 4.5, along with the measured calibration curves.

The measured central wavelengths for the signal and idler peaks, shown in Fig. 4.5 were found to be 804 nm and 1572 nm. These are in excellent agreement with the predicted shift due to the change in the pump wavelength. The measured full-width half-maximum bandwidths were 4 nm for signal wavelength and 30nm for the idler in the single photon regime, although the resolution of this measurement was not recorded. The measured signal and idler

bandwidths both significantly exceeded the range required for a spectrally pure output (see Section 3.5.1). Given the 4.5 ps pulse duration of the pump source, the required spectral bandwidths were calculated from Eq. (3.14) to be 0.15 nm for the signal wavelength and 0.6 nm for the idler. Narrowband filtering of the FWM outputs would therefore be necessary in order to ensure spectral indistinguishability of the output idler photon state.

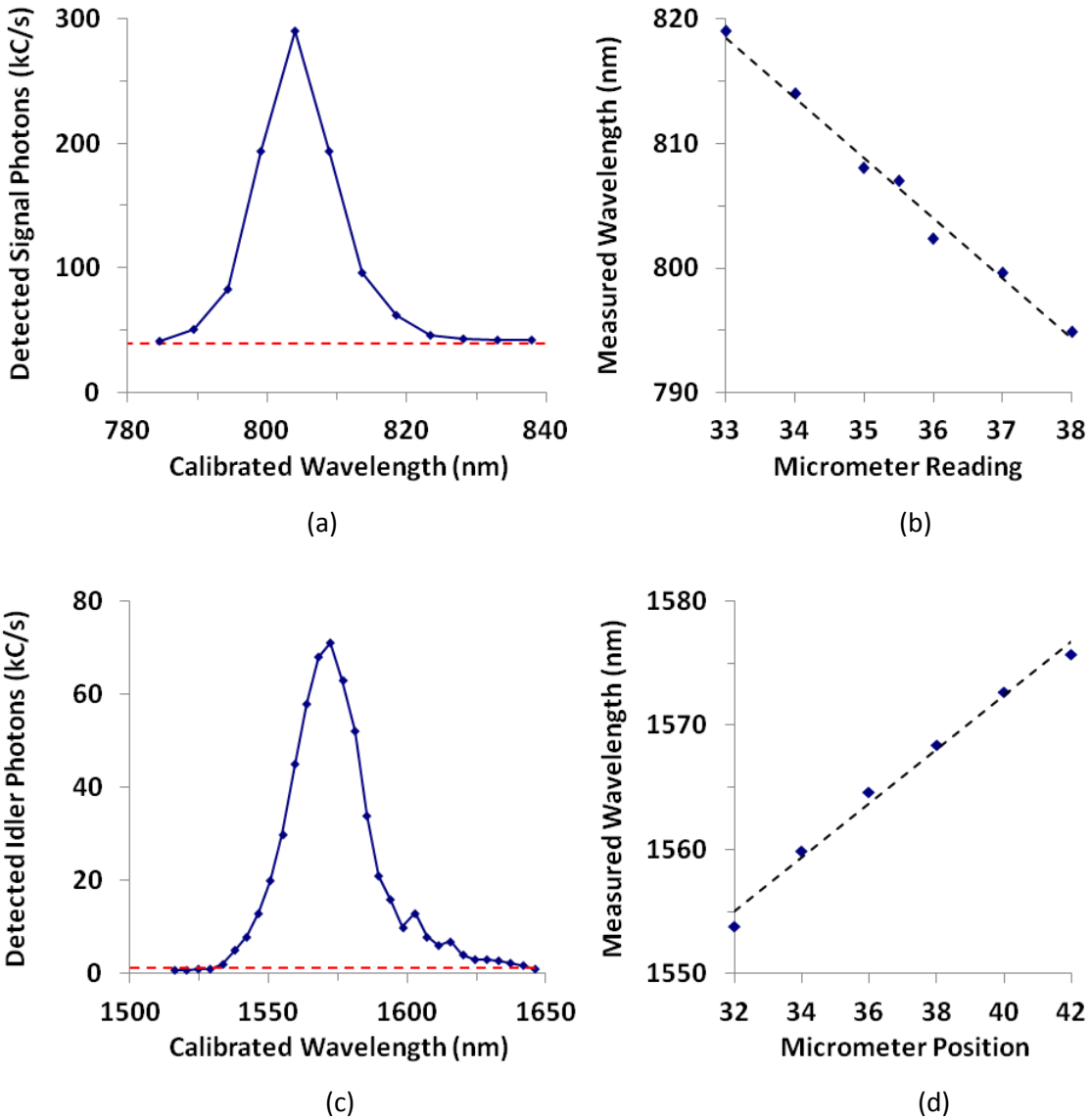

Figure 4.5: Single photon count rates detected as the transmission wavelength of the spectral filtering was scanned. (a) shows the measured spectrum for the signal arm of the source and was calibrated using the linear fit to the calibration data shown in (b). Similarly, the idler arm spectrum and calibration curve can be seen in (c) and (d). The dashed red lines in (a) and (c) indicate the measured background count rates.

It should be noted that during this spectral measurement of the signal bandwidth, the 10 nm band-pass filter at 800 nm was still present in the setup, as shown in Fig. 4.3. Unfortunately it

was not possible to perform the measurement without this filter. When the filter was removed the measured peak count rates were around 4.5 MHz, approaching the saturation limit of the detector, and several sources of noise were visible in the spectra.

In order to measure the signal wavelength without the need for a bulk narrowband filter, which could affect the result, the prism-based filtering was exchanged for a tuneable grating monochromator (*Optometrics,* DMC1-04). The experimental setup for this measurement is shown in Fig. 4.6.

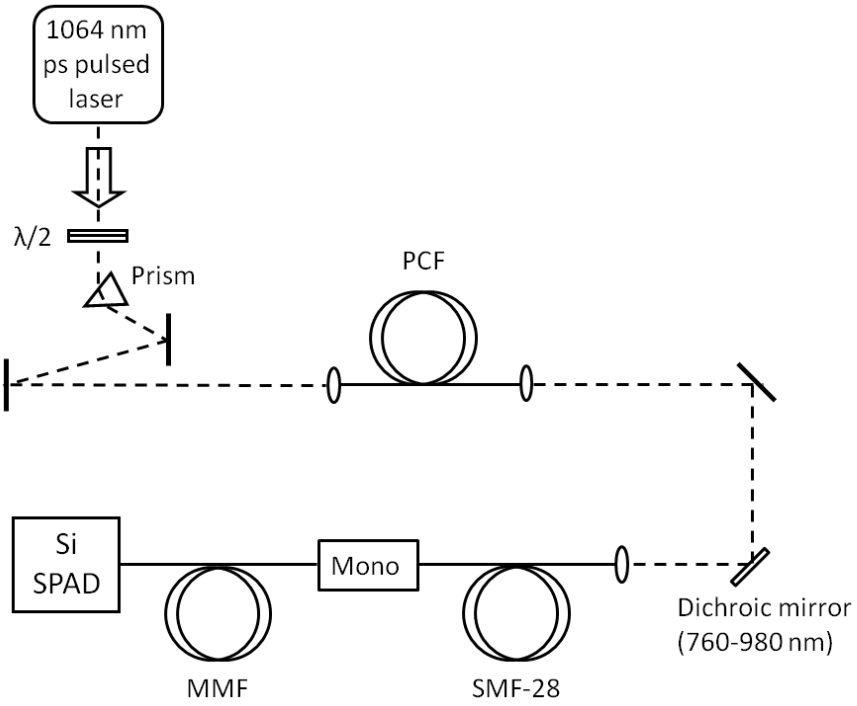

Figure 4.6: Experimental setup for wavelength measurement using a monochromator (mono). The multimode collection fibre (MMF) was attached to the monochromator with a fibre connector and the output of the SMF-28 fibre was positioned on a 3-axis translation stage aligned with the input slit of the monochromator.

The broadband filtering provided by the dichroic mirror remained, but the prism and the narrowband 800 nm filter were removed. The photon count rate at the Si-SPAD was recorded as the monochromator was scanned across a range from 780 – 820 nm. The results at the wavelength of interest are shown in Fig. 4.7(a). As with the previous spectral measurements, the monochromator reading was calibrated by launching supercontinuum light through the filtering and measuring the transmitted wavelength of the light using an OSA. The calibration data is shown in Fig. 4.7(b). The measured OSA spectra indicated that the monochromator filtering resolution was around 0.5 nm.

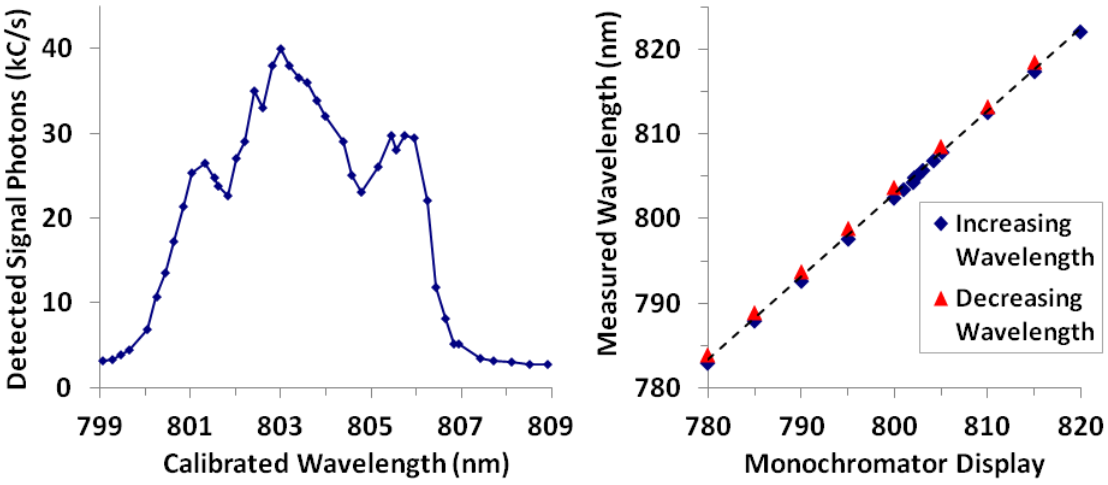

Figure 4.7: (a) Detected single photon count rate in the signal arm as the monochromator grating was rotated. The monochromator dial readings have been converted to wavelengths using a measured calibration curve shown in (b).

The peak signal wavelength found by this method was 803.0 nm, in agreement with the result found using the prism, despite the presence of the narrowband filter in that case. The measured FWHM bandwidth of the signal peak was found to be around 6 nm in this case, although there was some uncertainty over this measurement due to the side peaks observed, which can be seen in Fig. 4.7(a). These may have been due to the outlying structure of the fundamental mode field profile observed for the PCF.

4.5 Conclusion

This chapter demonstrates the feasibility of a fibre-based heralded single photon source using a relatively low-cost, low power picosecond fibre laser pump source. The laser had a high repetition rate of 80 MHz giving a high potential maximum rate at which photon pairs could be generated. The pump pulse duration chosen indicated that in order to achieve spectrally pure heralded single photons filtering bandwidths of 0.15 nm and 0.6 nm would be required for the signal and idler respectively. A suitable PCF for generating signal and idler pairs at wavelengths near 810 nm and 1550 nm (PCF-B) was demonstrated. This idler wavelength was selected to allow for future integration with telecoms systems. The corresponding signal photon wavelength would then also lie within the range of Si-based photon detectors, allowing for efficient detection of the heralding photons.

In Section 4.2, a 6 m length of PCF-B was pumped with the chosen fibre laser in order to demonstrate the generation photon pairs. These pairs were separated and filtered using bulk optics, before arriving in separate output fibres at single photon detectors.

The source performance was characterised by analysing the rate of coincident detections as a function of the detection time of the idler photons relative to the heralding signals. Important indicators of source performance, such as the CAR and heralding fidelity were defined and discussed. The detection of correlated pairs demonstrated that this preliminary device was functioning as intended. However, due to the high losses in the set-up, the brightness of the source was low, only 2.2 kC/s detected heralded photons (at a detection efficiency of 10%) near the optimum CAR of 10, with a pump power of 21.5 mW. The measured singles count rate in the signal arm was around 250 kC/s at this pump power level, indicating that loss in the idler arm of the source was high. From this data the heralding fidelity, and consequently the loss in the idler arm, were both calculated to be around 8%.

The generated signal and idler wavelengths of the PCF-B were measured using two different methods and found to be at 803 nm for the signal, and 1572 nm for the idler, in close agreement with the results predicted based on the phase-matching curve for the fibre. The accurate measurement of these wavelengths enabled the selection of suitable narrowband filtering for integration with this PCF as part of the all-fibre photon source, described in Chapter 5.

Chapter 5

An All-Fibre Heralded Single Photon Source

In Chapter 4 a heralded photon source based on FWM in a PCF was demonstrated. The results showed that an all-fibre photon source with a comparable brightness to existing parametric down-conversion sources should be feasible given the available pump power. At the upper limit of the available pump power the emergence of a large accidentals peak (as seen in Fig. 4.4) suggested that the generation rate of photon pairs was sufficiently high that the probability of generating multiple pairs of photons on a single pulse of the laser was significant. In the case of this source the available laser power exceeded the requirements to reach the useful limit of the source brightness, defined by the point where the CAR is equal to 10 (see Section 3.5.2).

Although important as proof of principle, the source described in Chapter 4 would not be suitable for use in experiments requiring heralded single photon states. While the generation rate of photon pairs in the PCF was sufficiently high, the detected output heralded photon rate was only ~2 kC/s (at a CAR of 11), due to the low transmission efficiency between the point of photon pair generation and the detectors. Even accounting for the poor efficiency of the detector this meant that < 0.05% of the laser pump pulses generated a useful output from the system. The high loss in the idler arm of the system also meant that the heralded output from the device was a poor approximation to the idealised single photon state, which should have no vacuum component as described in Section 3.4.3.

This Chapter describes the development and characterisation of an all-fibre source of heralded single photons. Some of this work has been published in the journal Optics Express [149]. In addition to the substantial improvements in the brightness and heralding fidelity of the source over the previously described free-space source, the indistinguishability of the output photons is considered. Sections 5.1 and 5.2 describe the construction of a photon source where the separation of the signal and idler photons and narrowband tuneable filtering are all achieved using fibre-based components. Section 5.3 deals with the characterisation of the source, including measurements of the source brightness, CAR, and heralding fidelity, and the measurement of the optical loss of the system. Section 5.4 describes the necessary reduction of the PCF length due to the walk-off conditions for the fibre, in order to ensure temporal indistinguishability of the output photons. The final version of the all-fibre photon source is shown in Section 5.5. Finally, in Section 5.6 the polarisation state of the heralded photons output from the source is investigated.

5.1 A Fibre-Based Broad Bandwidth Heralded Photon Source

As an intermediate step between the free-space preliminary work and an all-fibre heralded single photon source, a device consisting partially of fibre-based components was constructed. The pump rejection, wavelength separation, and filtering in the idler arm was implemented in fibre, while the filtering in the signal arm relied on free-space bulk optics. The purpose of the change to fibre-based filtering was to demonstrate that the required rejection of the pump light could be achieved with significantly lower loss than in the case of free-space filtering. At this stage the spectral filtering was still broadband (relative to the FWM peak bandwidth), as using narrowband filters would introduce the additional difficulty of having to ensure that the wavelengths are matched, and would also reduce the number of generated FWM pairs within the filtering bandwidth. A schematic representation of this device is shown in Fig. 5.1.

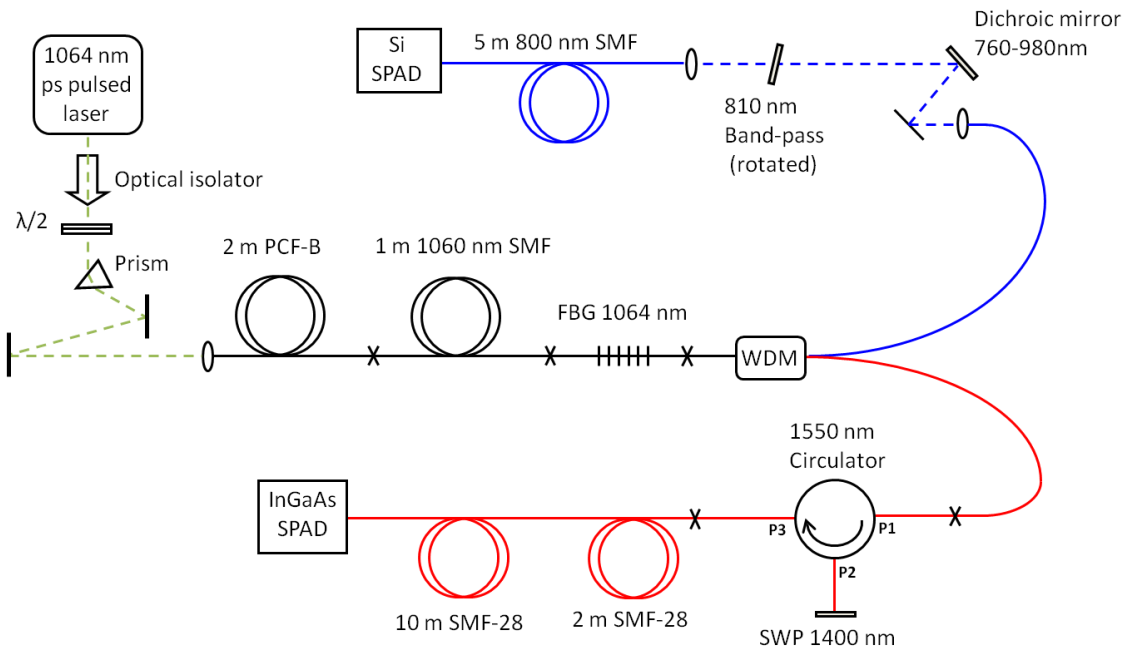

Figure 5.1: Schematic representation of the photon source with broad bandwidth filtering. FBG is a fibre Bragg grating, WDM is a wavelength division multiplexer and SWP is a short-wave pass filter. These components are described further throughout this section. P1, P2 and P3 denote the 3 output ports of the circulator.

Signal and idler pairs were generated via FWM in a 2 m section of PCF-B (described previously in Section 4.1). The launch optics were the same as for the previous source (see Section 4.2), including the picosecond pulsed pump laser (*Fianium,* Femtomaster1060-0.1). In order to ensure low loss transmission of the photon pairs through the device, the various fibre components were joined by fusion splicing. The loss was carefully monitored as each new component was added, starting from the PCF and working towards the end of the signal and idler arms, in order to ensure that the splices were optimised. This was done by launching light from a stable low power source (a broadband SLED source for measurement in the idler arm or 780 nm diode laser for the signal arm) into the input of the PCF and recording the power at the output of the device on a photodiode power meter, comparing the power before and after each new component was added.

In order to minimise splice losses, the components shown in Figure 5.1 were selected so that their fibre types were matched. After the PCF, the first part of the device (shown in black in the figure) was 1060 nm conventional SMF (*Corning*, HI1060), while the fibre in the idler arm (shown in red) was conventional 1550 nm telecoms fibre (*Corning*, SMF-28). Since the fibre types were matched, the splicing between conventional fibres could be performed using a

standard arc splicer (*Fujikura*, FSM-40PM) and preset splicing parameters, giving typical measured losses of < 0.1dB.

As discussed in Section 2.4, achieving low loss splices between PCF and standard fibre is usually more difficult than for two conventional fibres. For this reason a 1 m section of 1060 nm single mode fibre (SMF) was included after the PCF to allow the splice to be attempted several times and optimised, without wasting the pigtails on the fibre Bragg grating that followed. The splice between the PCF and the section of 1060 nm SMF was made using a filament fusion splicing system (*Vytran*, FFS-2000). Several of the available splicing parameters had to be altered from the standard settings for conventional SMF to SMF splicing in order to achieve low loss. The filament temperature was reduced, as well as the overlap distance of the two fibres when they were pushed together. While this resulted in a splice that was mechanically weaker than usual, losses ~0.5 dB could be consistently achieved, and the minimum loss splice that was kept for the device shown in Fig. 5.1 was 0.2 dB at 1550 nm.

It was later found that low loss splices between this PCF and SMF could be achieved using the same arc splicer as for the SMF to SMF splices. Again, the splicing temperature was reduced by lowering the power in the arc discharge, and the overlap between the fibres as they were fused was also reduced. After the initial fusing of the PCF and SMF, the re-arc function of the splicer was used repeatedly in order to reduce the mode field mismatch, as described in Section 2.4. The arc was offset by 7 µm from the central position over the gap towards the PCF side in order to encourage the controlled collapse of the cladding structure during the re-arc procedure. The loss was monitored and found to decrease from a typical initial value of around 0.5 dB after the initial fusing of the fibres to a minimum of < 0.2 dB after 5-10 re-arcs. The application of additional arcs after this point would cause the loss to begin to rise again. This technique was used to reproduce the splice between the PCF and SMF in later versions of the source (such as that shown later in Fig. 5.17) as it was faster and easier to use than the filament fusion splicer, and achieved lower loss splices with greater consistency.

After the PCF, a fibre Bragg grating (FBG) with a central wavelength of 1063.8nm provided an initial 30 dB rejection of the pump light within a 2 nm bandwidth of the central wavelength, preventing any further undesired nonlinear interactions in the system. The insertion loss at the signal and idler wavelengths for this component was less than 0.1 dB. The prism that was used in the previous system to separate the signal and idler wavelengths was replaced with a custom wavelength separation system (shown as WDM in Fig. 5.1). This component consisted

of two fused-fibre wavelength division multiplexers (WDM) spliced together, as shown in Fig. 5.2. The first WDM separated the idler wavelength into one fibre and the signal and pump wavelengths into a second fibre. The second WDM then separated the signal and pump wavelengths into two separate fibres. The pump light was terminated inside the component.

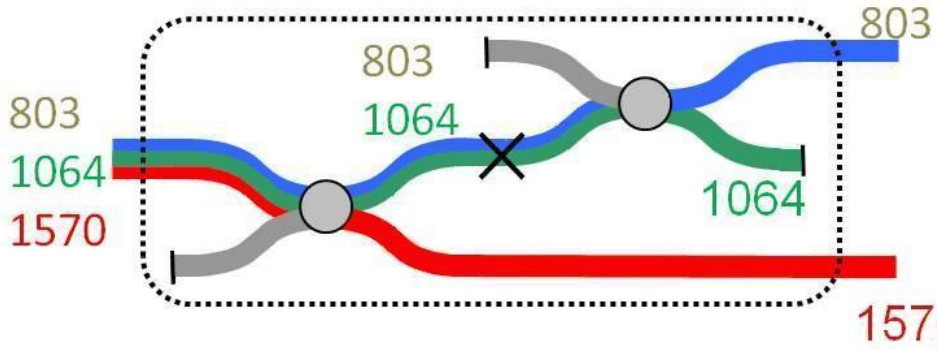

Figure 5.2: Schematic of the WDM system, showing how the three wavelengths are separated from a single fibre at the input to three separate fibres, by the use of two fused-fibre couplers. The dotted black outline represents the component packaging and the black cross denotes a splice. The input fibre and signal wavelength output fibre were HI1060, the idler output fibre was SMF-28.

The specified insertion loss of this component was 0.05 dB for an idler wavelength of 1573 nm and 0.65 dB at the signal wavelength of 803 nm. In addition to separating the signal and idler into two different fibres this component also provided an additional 25 dB reduction in the pump power on both the signal and idler paths.

After the WDM system, light in the signal arm was then output into free-space and collimated by an aspheric singlet lens. Spectral filtering in the signal arm still relied on free-space optics at this stage, with a dichroic mirror and band-pass filter providing the necessary additional pump rejection before the light was coupled back into a length of SMF. The dichroic filter was the same as that described in Section 4.2 for the previous source with free-space filtering. The band-pass filter had a 10 nm bandwidth centred at 810 nm, and was rotated to an angle of around 30° from normal incidence in order to shift its central wavelength slightly to 804 nm.

In the idler arm, filtering was provided by a 1550 nm 3-port circulator (*Opneti,* CIR-3-2-1-15-NE). The second port of the circulator was butt-coupled to a short-wave pass (SWP) filter with a cut-off wavelength of 1400 nm. The SWP filter reflected the idler wavelength back into the fibre, whilst transmitting light at the pump and Raman wavelengths. Light reflected back into the second port of the circulator was output from the third port, so

this arrangement acted as a broadband filter at the idler wavelength, with the bandwidth determined by the reflection profile of the SWP filter, and by the performance of the circulator outside its specified operating bandwidth. The circulator loss at 1550 nm was measured by coupling light into the component from a 1550 nm laser diode and measuring the transmitted power using a photodiode power meter. The input coupling efficiency of the laser to the fibre was assumed to be ~90%, which could be consistently achieved using a section of plain SMF-28 fibre with the same launch optics and light source. The measured insertion loss at 1550 nm was consistent with the specified values for the component of 0.4 dB for port 1 to port 2 and 0.5 dB for port 2 to port 3. The wavelength dependence of the transmission was also measured by coupling in light from a broadband SLED source with a wavelength range of 1180-1630 nm (*Agilent*, 83437A), and measuring the output spectrum from port one to two (and similarly for port two to three) using an OSA. The relative transmission was then calculated by comparing the measured spectrum transmitted through the component to that transmitted through a section of SMF-28. Both paths of the circulator showed similar transmission characteristics. The transmission profile, for port 1 to port 2, is shown in Fig. 5.3.

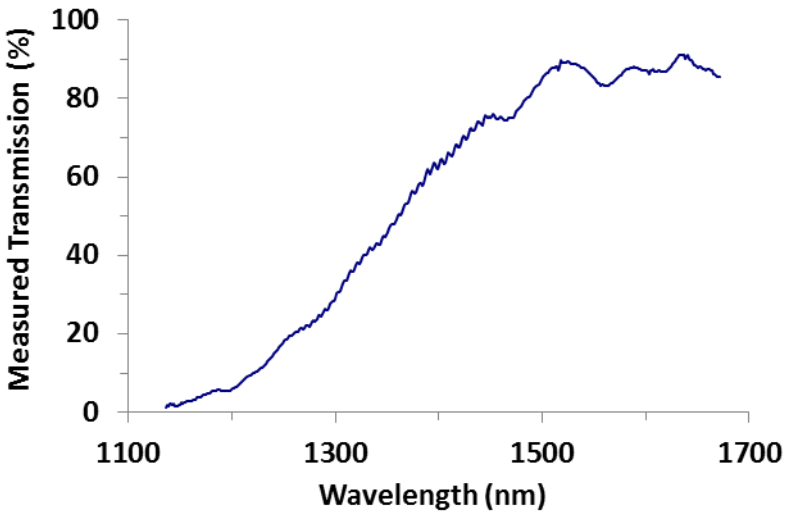

Figure 5.3: Measured transmission spectrum for the 1550nm circulator from port 1 to port 2.

Achieving low loss in the idler arm was critical in order to ensure a high purity single photon state could be produced after moving to narrowband filtering, as the heralding fidelity of the system was mainly dependent on this loss, as shown in Eq. (4.6). While low loss in the signal arm was also desirable in order to achieve a high brightness source as shown in Eq. (4.4), loss

here would not reduce the purity of the source since FWM events where the signal photon is subsequently lost would not produce a heralding signal.

Once the device had been fully spliced together, the total loss from the input of the PCF to the output of the idler arm was measured. This was done by coupling in light from a CW 1550 nm fibre-coupled laser diode source (*Thorlabs*, S1FC1550), as shown in Fig. 5.4. The output power was measured using a photodiode power meter first at the output of port two of the circulator and subsequently at the output of the 12 m section of SMF-28 after the SWP filter was placed against the port two fibre. Both of these results were compared against the maximum power transmission that could be achieved through a 2 m section of the same PCF structure used in the device, in order to account for the loss due to input coupling. The overall measured transmission was 68% (-1.7 dB), in good agreement with the individual losses measured as each component was added as shown in Fig. 5.4. The higher loss on the second pass through the circulator was due to the loss of the filter and the coupling efficiency between the SWP filter and the fibre.

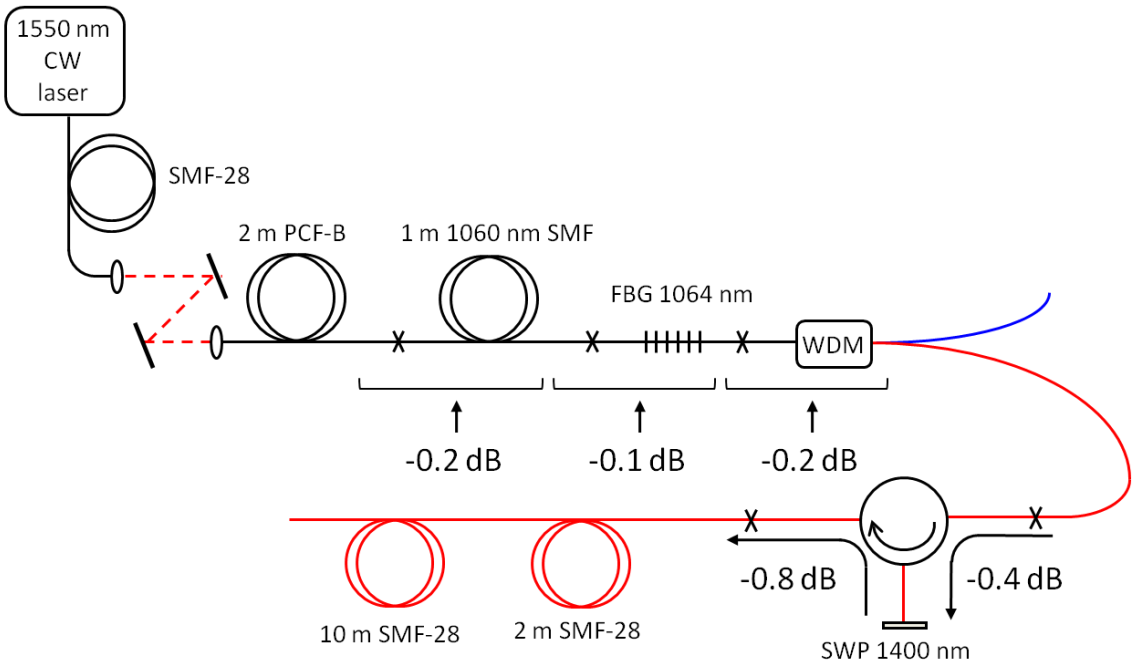

Figure 5.4: Experimental setup for measurement of the total loss in the idler arm. The indicated values show the separately measured loss values for each individual component.

The performance of the single photon source shown in Fig. 5.1 was characterised using a similar technique to that described for previous source in Section 4.3. Again, the Si SPAD at

the output of the signal arm operated in a free-running mode, and the output from this detector was used to trigger the InGaAs SPAD at the output of the idler arm, operated in a gated mode. The activation time of the idler detector relative to the triggering signal was again scanned over a range of 25 ns using the adjustable electronic delay feature of the idler arm detector, in order to observe the main coincidence peak and the accidentals peak. In this measurement the coincidence count rate was recorded over the entire delay range rather than just sampling the two peak values and one point on the background. The detector efficiency of the InGaAs SPAD was set to 10% for this measurement. The resulting count rate on this detector, corresponding to the measured coincidence count rate of signal and idler pairs, is shown in Fig. 5.5.

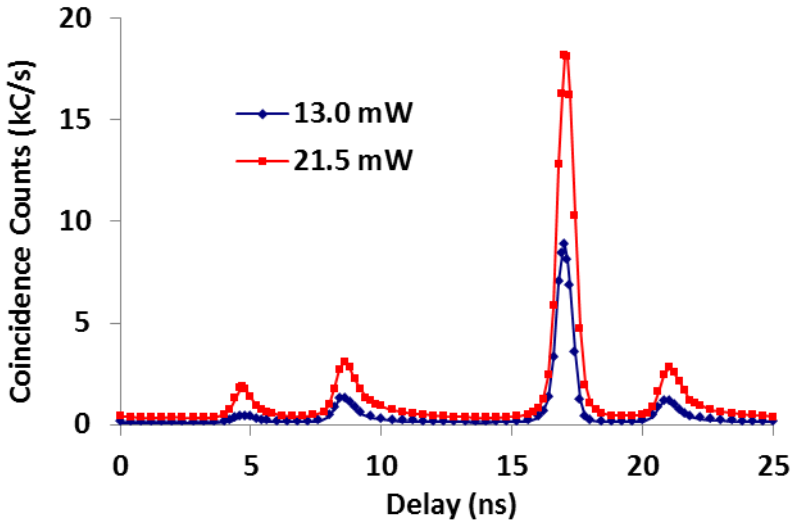

Figure 5.5: Variation of coincidence count rate with delay for the source with broad bandwidth filtering. The results are shown for pump powers of 13.0 mW and 21.5 mW. The additional peaks at 9 ns and 21 ns are due to noise from the pump laser.

The large peak shown at a delay of 17 ns is the main coincidence peak, and the accidentals peak can be seen at 5 ns delay. Two other peaks were also present near 9 ns and 21 ns, spaced from each other by the laser repetition period. When the SWP filter was removed from port two of the circulator, so that no light was reflected back in to the device, the main coincidence peak and accidentals peak disappeared as expected but these other two peaks remained. In order to ensure that light was not still being reflected back in to the circulator from the end-face of the fibre, the port two fibre was broken without cleaving to produce a rough interface and was also placed into an index matched liquid. These peaks were still present, implying that they were due to noise photons breaking through the circulator directly

from port one to port three. Due to the difference in the arrival time of these noise photons caused by the difference in the path length from bypassing the fibre on the second port of the circulator, this source of noise could be easily distinguished from the main coincidence peak and accidentals peak. These peaks were successfully removed in later versions of the photon source as described in Section 5.3.2.

As shown in Fig. 5.5, with 21.5 mW of pump power the measured coincidence count rate was 18 kC/s. Accounting for the detector efficiency of 10% this corresponds to an output heralded single photon rate of 1.8×10^5 s^{-1}. This was an improvement over the previous source with prism-based filtering discussed in Chapter 4 by nearly a factor of 10. Crucially, the reduced loss in the idler arm also meant that the heralding fidelity was significantly improved. The chance of outputting a single photon given that there was an electrical trigger was 44% in the higher power case.

5.2 Implementation of Narrowband Filtering

Although the device described in Section 5.1 showed a high coincidence count rate and excellent heralding fidelity, it could not be considered a useful heralded single photon source for quantum information applications at this stage. The broadband filtering in the idler arm allowed idler photons of slightly different wavelengths (by which they could be distinguished) to be heralded and output. The heralded photons would thus be in a mixed quantum state, rendering them useless for observing the type of quantum interference described in Section 3.3.

In order to achieve spectral indistinguishability of the output idler photons, narrowband filtering was required in the idler arm (see Section 3.5.1). Additionally, energy-matched narrowband filtering was also necessary in the signal arm, in order to ensure that only the idler photons that passed the spectral filtering would be heralded by their corresponding signal partner. Without the matching narrowband filtering in the signal arm the false heralds would dramatically reduce the achievable heralding fidelity of the source.

As discussed in Section 3.5.1, the spectral purity of the heralded single photon state can become absolute only as the filtering bandwidth in the idler arm tends to zero. However, for practical purposes the purity becomes sufficiently high to observe high visibility interference effects when the temporal coherence length of the idler photons becomes approximately

equal to the pump pulse duration. For the pump laser in this source the required temporal coherence length for the idler photons should therefore be 4.5 ps. As stated previously in Section 4.4, this corresponds to a required idler filtering bandwidth of 0.6 nm. The corresponding energy matched filtering bandwidth required at the signal wavelength was 0.15 nm.

In the case of free-space interference filters, achieving a transmission profile with a sufficiently narrow pass band would usually lead to an unacceptably high loss that would significantly reduce the heralding fidelity. For this reason, fibre-based filtering using a circulator was chosen for the source, as this allowed narrowband fibre Bragg gratings (FBGs) to be used to define the filtering bandwidth. The typical reflectivity of these components can exceed 99%.

For the initial version of the photon source described in this section, FBGs of bandwidth of 0.8 nm and 0.2 nm at the idler and signal wavelengths respectively were used to provide filtering. These were later reduced to 0.6 nm and 0.15 nm for the source described in Section 5.5, in order to ensure that the filtering bandwidth would be adequate to achieve sufficiently high spectral purity. In practice the difference between the two filtering bandwidths is likely to be small, particularly as the criteria for the bandwidth at which the photons are deemed spectrally pure is somewhat arbitrary.

As discussed in Section 4.4, the methods used to measure the wavelength of the FWM peaks in the single photon regime could only provide a resolution ~0.5 nm. Although the resolution when measuring in the FWM peaks with higher pump power was better, in this case there was some uncertainty in the shift of the peak wavelengths that would be expected, both due to a difference in the central wavelengths of the two pump lasers, and from the additional phase-mismatch from SPM due to the significantly different peak pump powers (see Section 2.2.4). In order to ensure that the signal and idler wavelengths that were selected by the FBG filters were matched to each other (by the condition of energy conservation) and to the wavelengths of maximum gain for the FWM interaction, it was necessary to tune them. The central wavelength of reflection for an FBG can be shifted either by a change in temperature, or through the application of mechanical strain. For temperature tuning, the grating wavelength will be shifted due to the change in the spatial period of the structure from the thermal expansion of the silica, as well as the temperature dependence of the refractive index. The temperature dependence of the wavelength shift is typically ~10 pm/°C

[150], too small to be of practical use here. In contrast, tuning FBGs with mechanical strain (again due to the change in the grating period) can readily achieve a tuning range of 10 nm or more [151]. For this reason, the FBGs were stretched in order to tune them to longer wavelengths.

In order to determine the wavelength tuning range that could be achieved under tension, an FBG with a specified central wavelength of 1117 nm was tested. The was fixed at one end by turning the fibre pigtail 10 times around a 1" metal post and securing with adhesive tape. On the other side of the grating region a length of fishing line was attached to the other fibre pigtail using an epoxy resin. The FBG was positioned horizontally above the bench and tension was applied by means of weights hanging on the fishing line that was run across a pulley. Light from a supercontinuum source was launched into one end of the grating and the position of the dip in the spectrum, corresponding to the central wavelength of the grating reflection, was observed at the other end using an OSA.

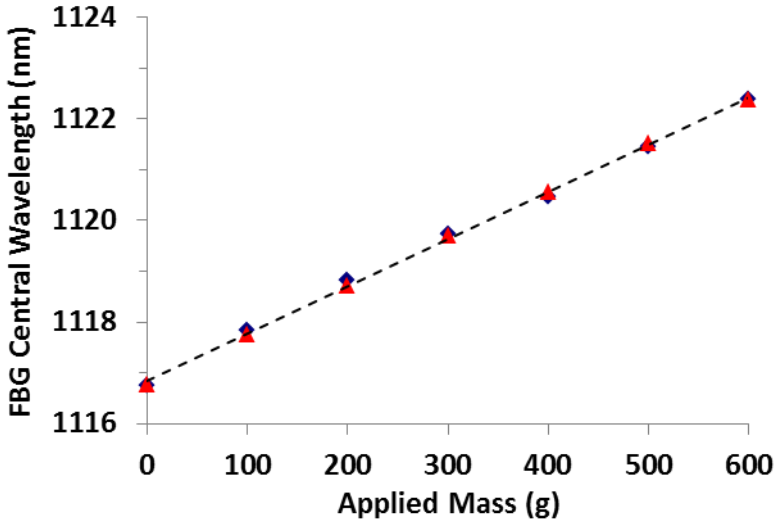

Figure 5.6: Measured calibration curve showing the response of an FBG central reflection wavelength to stress. In this case the stress was applied using weights and the stress is expressed in terms of the applied mass.

The results of the wavelength tuning showed that a suitable tuning range could be achieved for FBGs using mechanical stress. However, the method used here to strain the FBG was deemed unsuitable for use in the photon source, firstly because the fine tuning of the wavelength with small masses would be awkward, and secondly because applying too large a stress to the fibre caused inelastic deformation of the epoxy bond, causing the fibre to from a tight coil upon removal of the stress. An alternative method of straining the FBG was chosen,

where the fibre pigtails were fixed at both ends by coiling. The fibre pigtail between the circulator and FBG region was coiled 5 times around a rubber spool of diameter 70 mm. The larger radius of coiling was chosen at this end to avoid the possibility of bend loss (see Section 2.1.5). The other pigtail of the FBG was wrapped 10 times around the 1" metal post, since the consideration of induced bend loss was unimportant at this point in the system. The metal post was mounted on a screw thread driven translation stage that could be moved over a 20 mm range to provide the required strain for tuning the FBGs. The slight flexibility of the rubber spool meant that the applied stain on the FBG changed gradually over a large movement range of the translation stage meaning that the tuning was not excessively sensitive. The maximum tuning range that could be achieved (using an 801 nm central wavelength FBG) was ~5 nm, as the fibre began to slip beyond this point. Stability measurements showed that the tuned gratings could maintain their central wavelength over a 24 hour period, even tuned near to the limit that could be achieved without slipping. Narrowband FBGs with central wavelengths of 801 nm and 1569 nm (when untuned) were incorporated in to the signal and idler arms of the photon source system, as shown in Fig. 5.7.

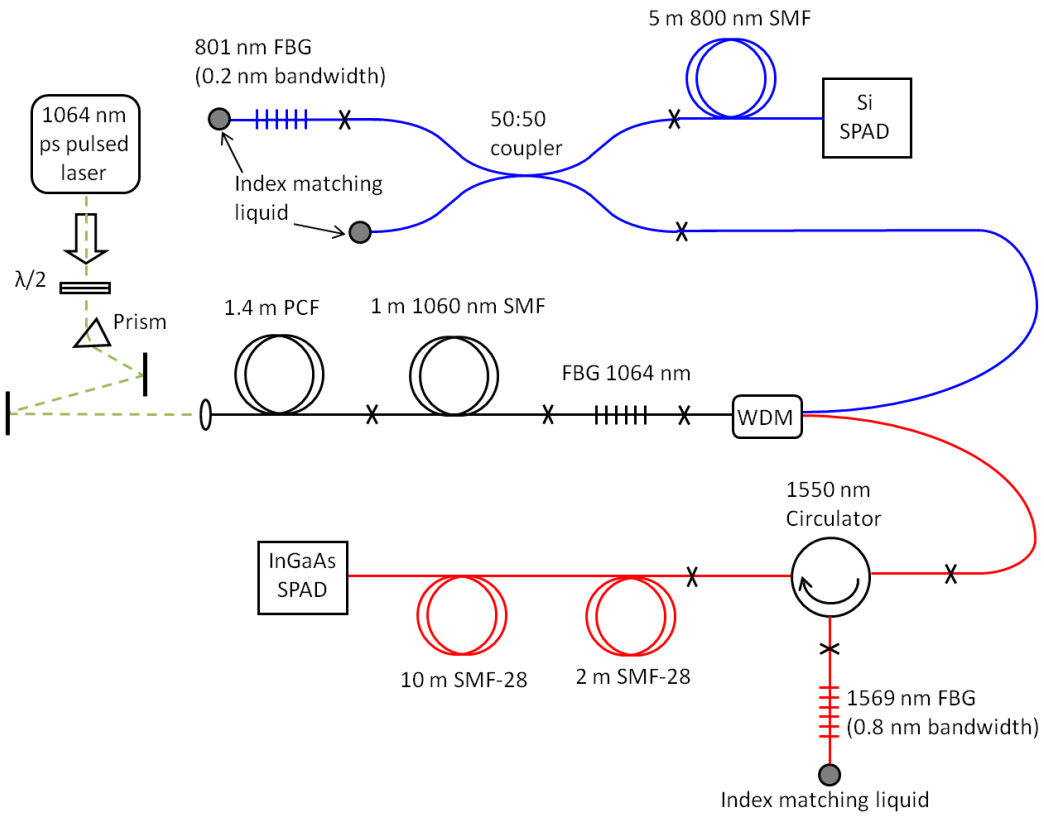

Figure 5.7: Schematic diagram of the all-fibre single photon source, with spectral filtering implemented using tuneable narrowband filtering.

The narrowband FBGs could both be tuned independently to longer wavelengths using the technique described earlier in this section. The ends of both gratings were placed into index matching liquid to avoid problems due to noise photons that had been transmitted through the gratings being reflected back into the system from the end-faces of the fibres. In order to accommodate narrowband filtering using an FBG in the signal arm, the free-space filtering was replaced with a 50:50 fibre coupler. In the arrangement shown in Fig. 5.7, this component acts in a similar manner to a circulator, although with a higher total loss of 6 dB due to the light having to take the correct path on the two transitions through the component in order to reach the detector. The choice to use this component rather than a circulator was due to the difficulty in obtaining low insertion loss circulators at this wavelength.

In addition to the introduction of narrowband filtering, the length of the PCF in the source was also reduced from 2 m to 1.4 m. This was still in excess of the calculated walk-off length for the fibre of 35 cm, and would eventually need to be reduced further (see Section 5.4). However, at this stage the PCF length was not reduced to this length as the addition of narrowband filtering would result in lower measured count rates for the same pump power. As discussed previously in Section 3.5.2, ideally the photon source should be operated in at a pump power level where the CAR is around 10. At a fixed pump power, when the filter bandwidth is significantly reduced the probability of pair generation within the filtering bandwidth is also reduced, since the pairs will be generated across the entire range over the entire spectral range over which there is gain for FWM. Therefore, in order to achieve the optimal CAR the required pump power increases as the filtering bandwidth is reduced.

5.3 Characterisation of the Narrowband Source and Reduction of Noise

5.3.1 Pump Power Dependence of the Source Brightness

The same method described in Section 5.1 was again used to characterise the source performance. A Labview program (*National Instruments*, LabVIEW) was written to interface with the InGaAs detector in order to automate the measurement process, allowing more data points to be collected in a shorter period of time than in the previous measurements. This adjusted the electronic delay of the detector across a specified range whilst stopping at each point for 5 seconds and taking an average of the measured coincidence count rate over that period. This helped to reduce the statistical uncertainty in the measurement that resulted from the lower overall count rates in the case of narrowband filtering. Before the coincident count rate measurements were made, the narrowband FBGs had to be tuned to the required wavelengths. This was done manually by first adjusting the grating in the signal arm in order to maximise the singles count rate in that arm, ensuring that the signal grating wavelength was matched to the FWM peak. After this the electronic delay in the InGaAs SPAD was adjusted such that the detector was activated to coincide with the main coincidence peak. The idler FBG could then be tuned to maximise the coincidence count rate, ensuring that the idler grating was both energy matched to signal wavelength and adjusted to the idler FWM peak wavelength.

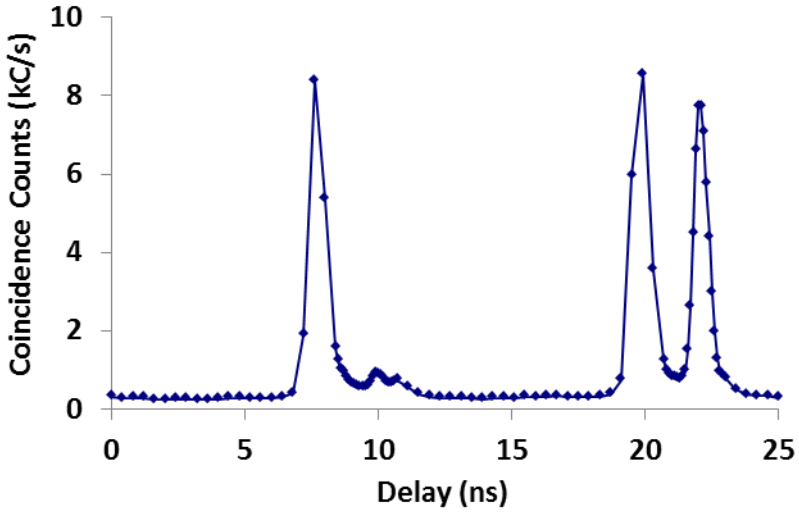

Figure 5.8: Variation of coincidence count rate with delay for the all-fibre single photon source at a pump power of 62 mW.

A typical example of the measured coincidence count rate for the source is in shown Fig. 5.8. The figure shows a main coincidence peak at 22 ns, and an accidentals peak at 10 ns. The two large peaks at 7.5 and 20 ns are the noise peaks due to the breakthrough of light in the idler arm circulator as discussed in Section 5.1. Note that the change in the absolute position of the peaks and the relative delay offset between the noise peaks and the main coincidence and accidentals peaks is due to the difference in fibre length at the output of port two of the circulator because of the addition of the narrowband FBG.

The CAR of the source at the pump power shown was 8.5, similar to that shown in Fig. 5.5 for the broadband filtered source at a pump power of 21.5 mW, allowing a straightforward comparison between the sources before and after the change to narrowband filtering. Achieving a similar CAR with the narrowband filtered source required an increase in the average pump power to 62 mW (measured at the end face of the PCF before launch). This was close to the maximum attainable pump power of 70 mW that could be achieved due to inefficiency in the launch optics, especially the isolator. While the available pump power was sufficient for this PCF length these results show that it would become a limiting factor when the PCF was reduced to the walk-off length.

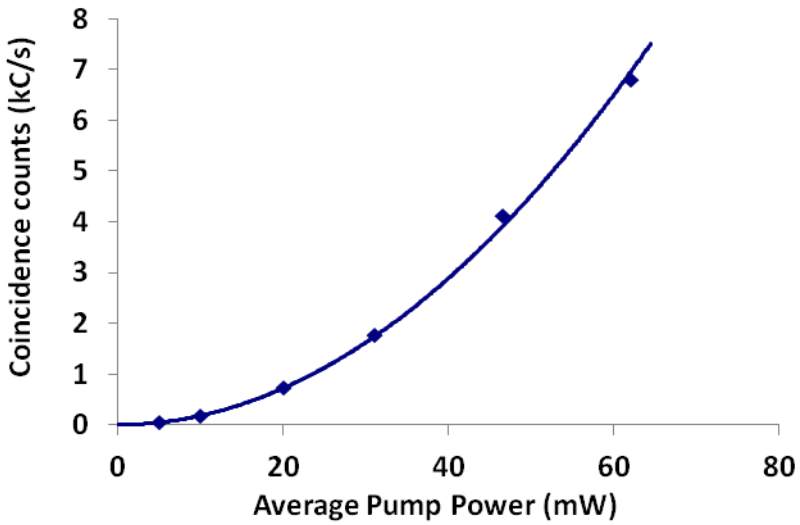

Figure 5.9: Measured main coincidence peak count rate as a function of input pump power for the narrowband filtered photon source.

The variation in the measured coincidence count rate at different pump power levels was also investigated. At each pump power level the measured count rate for the accidentals peak was subtracted from the main coincidence peak to give an adjusted coincidence count rate. Since the accidentals peak contains all of the uncorrelated processes that are also present in the main coincidence peak, this then represents just the counts due to the correlated photon pairs of interest. The results, shown in Fig. 5.9, were numerically fitted with a line of purely quadratic form aP^2, where a is the fitted coefficient and P is the average pump power. The fitting gave an R^2 value of 0.998, showing good agreement with the P^2 dependence of the FWM gain predicted from theory (see Section 2.2.5). The CAR was 7.5 at the highest pump power level of 62 mW, increasing to around 50 with 10 mW of pump power. The CAR could not be determined at the lowest pump power level used due to the recorded counts in the accidentals peak dropping to zero in the measurement time frame. The heralding fidelity of the source was ~40% at all pump power levels above 10 mW. Below this the heralding fidelity dropped, to 35% at 10 mW and 20% at 5 mW, as the background count rates from the Si-detector due to dark counts and stray background light in the room became comparable in magnitude to that from detected FWM photons.

5.3.2 Reduction of the Noise Contribution to the Idler Arm

From the measured coincidence data shown in Fig. 5.8, it is clear that the magnitude of the noise peaks relative to the main coincidence and accidentals peaks increased significantly compared to the broadband filtered source. This is due to both the increase in the total amount of noise arising from the higher pump power level and the reduction in the measured signal and idler rates due to the effect of narrowband filtering. The close timing proximity of the noise peaks to the photons of interest meant that time gating of the detector was no longer certain to entirely eliminate this noise source. Furthermore, at the 62 mW pumping level the background count rate of around 300 C/s (seen in the regions between the peaks in Fig. 5.8) accounted for around 30% of the total in the accidentals peak, meaning that it was one of the primary sources of uncorrelated photons in the main coincidence peak as well. In order to determine the nature of the noise photons that were passing directly through the idler arm circulator, a free-space filtering section was introduced at the end of the idler arm, between the two sections of SMF-28 fibre, just before the detector. Light was coupled out of the 2 m fibre patch cord and collimated with a microscope objective lens, before being reflected from two mirrors and coupled back into the 10 m fibre section. This allowed various

additional spectral filters to be added into the free space section while the measured coincidence counts from the source were monitored.

As shown in Fig. 5.10, the addition of an extra long-wave pass filter, blocking at 1064 nm with the cut-off at around 1065 nm, totally removed the noise peaks as well as reducing the background count rate to almost zero. This confirmed that the noise was due to insufficient blocking of the pump light in the device, as the only other noise source that might be expected to be bright enough to break through the circulator in this way was Raman-shifted pump light, and that wavelength would not be blocked by this filter.

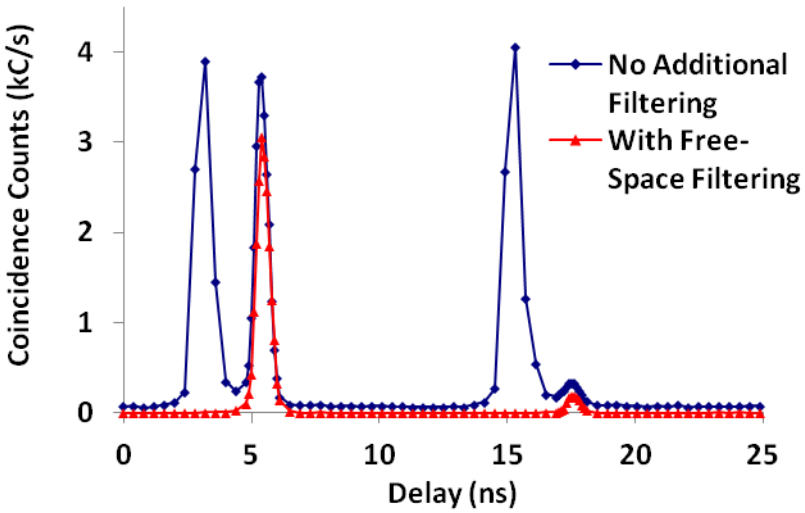

Figure 5.10: Effect of additional spectral filtering on the noise peaks seen in the coincidence count rate data, associated with circulator breakthrough.

As the source of the noise was confirmed to be leaked pump photons, additional filtering could easily be implemented by incorporating an additional FBG of central wavelength 1064 nm in both arms of the device after the WDM, avoiding the need for lossy free-space filtering. This arrangement was possible due to the fact that the WDM was designed to have minimal transmission at 1064 nm into both outputs, meaning that the two pump rejection FBGs before and after the WDM did not form a resonant cavity.

After splicing the pump rejecting FBGs into the system, the coincidence count rate as a function of the detector electronic delay was again measured in order to verify that the excess background noise had been removed. The results at average pump powers of 70 mW and 31 mW are shown in Fig. 5.11.

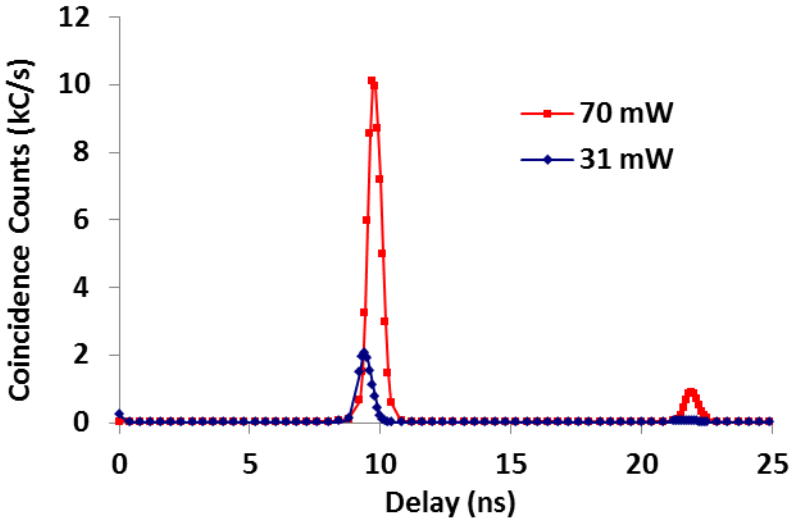

Figure 5.11: Variation of coincidence count rate with delay for the narrowband filtered all-fibre source with additional Bragg gratings added for improved pump light rejection from the output. Results are shown for pump powers of 31 mW and 70 mW.

The addition of the 1064 nm FBG in the idler arm can clearly be seen to eliminate the noise peaks that were associated with circulator breakthrough, as expected. The background coincidence count rate in between the main coincidence and accidentals peaks was also reduced to ~30 C/s at the highest pump power level. Using the maximum available pump power of 70 mW the target CAR of 10 was reached with a measured count rate of 10.1 kC/s for the main coincidence peak. Accounting for the presence of accidental noise photons and the InGaAs detector efficiency of 10% for this measurement, this corresponds to 9.2×10^4 true heralded single photons per second output from the device.

5.3.3 Heralding Fidelity and Loss Measurements

As discussed in Section 4.3, achieving a high heralding fidelity is important for photon sources in most QI applications, as the presence of heralded pulses with no corresponding idler photon will otherwise reduce the photon number purity of the output state. The heralding fidelity that can be achieved is determined by the passive loss in the system for the idler photons between the point of generation and detection. The total loss for the idler and signal photons was again measured for this new device using a similar technique to that described in Section 5.1, with a 780 nm CW laser diode providing the light required for the signal arm loss measurement. The peak transmission efficiency in the idler arm (excluding detector efficiency) was found to be 68% (-1.6 dB), which defines the upper bound of the heralding fidelity. The signal arm efficiency was lower at 7% (-11.5 dB) but the loss in this arm should only affect the output count rate and not the heralding fidelity.

In addition to the peak transmission efficiency measurement, the transmission profile of the filtering in both arms was investigated. Broadband supercontinuum light, of the type described in Section 2.2.8, was launched to the input of the device and the spectra at the signal and idler outputs of the source were recorded using an OSA.

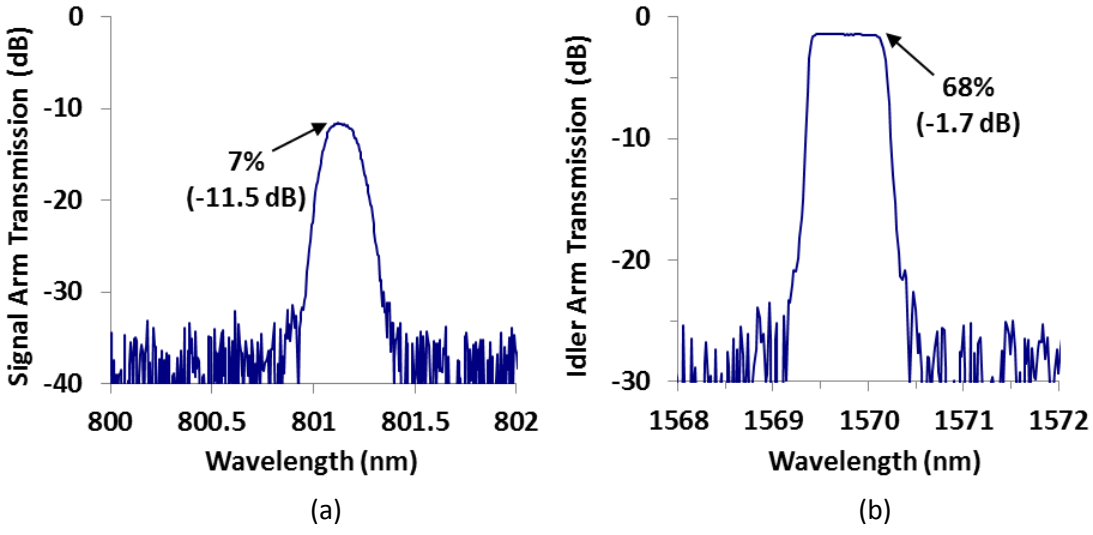

Figure 5.12: Measured transmission profiles of the all-fibre source with narrowband filtering for: (a) The signal arm; (b) The idler arm.

As shown in Fig. 5.12, the spectral transmission in both arms was dominated by the profile of the narrowband FBGs. As these gratings were tuned at the time of this measurement to maximise the singles and coincidence count rates, the central positions of the gratings

provides an indirect measurement of the wavelengths of the FWM peaks. In particular, the idler grating centre at 1570 nm corresponds to the wavelength of the heralded photons that will be output from the source.

The values for the main coincidence and accidentals peak count rates at several different levels of pump power are summarised in Table 5.1. The heralding fidelity of the source, calculated at each pump power using Eq. (4.6), is also shown.

Pump Power (mW)	Main Coincidence Peak (kC/s)	Accidentals Peak (C/s)	Detector Trigger Rate (kC/s)	CAR	Heralding Fidelity (%)
70	10.1	888	178	10.4	51.6
64	8.3	653	150	11.8	51.4
52	5.4	274	101	18.6	50.7
31	2.0	43	40	46.5	50.3

Table 5.1: Summary of the measured coincidences, singles count rates, CAR and heralding fidelity for the all-fibre photon source at different pump power levels.

As expected, the heralding fidelity was found to be nearly independent of the pump power over the range studied, with a value of 52% at the highest pump power level. The slight variation was most likely due to the increased difficulty of optimising the peak wavelength of the idler arm FBG with lower coincidence count rates. This heralding fidelity was nearly 10 times greater than the 6% measured for the previously described source with free-space filtering (see Section 4.3), and is close to the highest value demonstrated for a spectrally filtered, heralded single photon source output into fibre [97]. However, in this case the filtering was narrower than in [97] due to the requirements for achieving spectral purity with a pulsed pump (see Section 3.5.1). The heralding fidelity that was achieved with this all-fibre source compares favourably with other demonstrated narrow bandwidth sources operating at telecoms wavelengths [152].

Although the heralding fidelity of 52% shown here is high for a narrowband filtered source, there is still some discrepancy between this and the maximum value ~65% that might be expected from the passive loss measurement. There are several reasons why this may be the case.

Firstly, error in the transmission measurement may mean that the passive loss is in fact higher than believed. This was due to the manner in which the loss was measured, by repeatedly maximising the coupling efficiency of a test light source to the device and taking an average of the measured transmission, which is inherently less reliable than a typical fibre cut-back loss measurement. In this case, a cut-back measurement of the loss could not be performed due to the relatively short length of PCF available on the input end of the device and the inability to launch light in the reverse direction through the device due to the circulator. The transmission values obtained by this method were typically (65 $\pm$ 10) %.

Secondly, the effective transmission of the FBG filtering for the heralded photons may be lower than the measured peak transmission due to filter edge effects. For instance, when considering an idealised case with no loss and energy matched Gaussian filtering in both arms (centred at the peak idler and signal wavelengths), the effective transmission is a factor of $\sqrt{2}$ lower than the 100% peak transmission value [121]. This is because signal photons with wavelengths near the edge of the filter bandwidth, that pass through with non-unity probability will herald idler photons that also have non-unity transmission probability, and will sometimes be blocked. Even though this is unlikely to have much of an effect here due to the sharp cut-off of the FBG profile, even for perfectly sharp filter edges the effective transmission can still be reduced in the case of a broadband pump. The idler and signal arm filters can only be chosen to be perfectly energy matched for a single monochromatic pump wavelength (chosen to be the peak pump wavelength). For other wavelengths within the pump bandwidth it is possible for signal photons which are near the edge of the filtering bandwidth to herald a photon which lies outside the idler filter range.

Finally, for a given effective transmission efficiency, the heralding fidelity can be further reduced by the presence of noise in both the idler and signal arms. Noise in the idler arm is accounted for in Eq. (4.6) by the accidental coincidence rate term A, and noise in the signal arm is incorporated via the background contribution B_s to the singles count rate in the signal arm N_s, given by Eq. (4.2). The noise in the idler arm was known to be low from the measurement of the CAR, and the background count rate in the signal arm outside of the laser pulses (detector dark counts and counts from the room lights) can be accounted for. However uncorrelated noise photons in the signal arm coinciding with the laser pulses (e.g. leaked pump light) cannot be differentiated from the signal photons generated by FWM by the

measurement described in Section 5.3.1. Such noise photons in the signal arm, if present, would produce additional false heralding signals, lowering the measured heralding fidelity.

5.3.4 Measurement of the Idler Singles Count Rate

The measured values for the CAR of the source, shown in Table 5.1, demonstrate that uncorrelated photons constitute a relatively small proportion of the total measured coincidences. However, this data does not show how much of the accidental count rate is due to uncorrelated multiple pair generation events through FWM, compared to other noise sources, such as residual pump photons or Raman-shifted pump light. This is important to know, as the accidentals count rate ultimately limits the source brightness that can be achieved. If additional sources of noise beyond the generation of multiple FWM pairs were present then the CAR could potentially be improved by eliminating them.

In order to gauge the proportion of the accidentals count rate that was due to multiple pair generation events, the unheralded single photon count rate for the idler arm of the source was measured. As the InGaAs SPAD in the idler arm was unable to operate in a free-running mode it had to be triggered directly from the laser pulse train. This was done by sending a small fraction of the pump power (the beam reflected from the surface of the prism in the launch optics) to a fast photodiode (*Thorlabs,* DET10A) to provide the necessary timing signal. The InGaAs SPAD could accept a maximum trigger rate of 4.5 MHz so the electronic pulse train from the photodiode was down sampled using a digital delay generator (*SRS*, DG645) so that only $1/20^{th}$ of the laser pulses produced a triggering signal. The SPAD was operated with a detection efficiency of 10%. As in the case of the heralded coincidence measurements, the count rate from the InGaAs SPAD was recorded as the electronic delay between the detector activation and the arrival of the triggering signals was varied. The results are shown in Fig. 5.13.

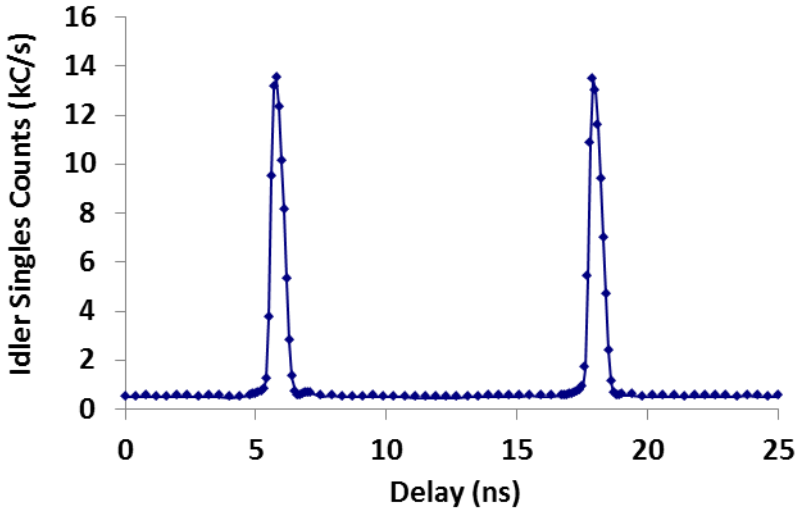

Figure 5.13: Measured singles count rate in the idler arm as the InGaAs detector internal delay was varied. The detector was triggered from the laser pulse train at a rate of 4 MHz.

The measured idler singles count rate data consisted of a series of peaks, with their separation in time determined by the laser pulse repetition frequency (PRF). As each pump pulse was equally likely to generate an idler photon, all of these peaks were identical. The measured singles count rate for the idler arm was 13.5 kC/s at a detector trigger rate of 4 MHz and a pump power of 60 mW. Using Eq. (4.3), combined with the previously determined value for the effective transmission coefficient (η_i) of 0.52, the pair generation rate r was found to be 4.7 MC/s for an 80 MHz PRF at this pump power level. This measurement of r allowed the effective transmission coefficient in the signal arm (η_s) to be calculated from Eq. (4.2). This was found to be 0.037. This then allowed the pair generation rate for the previous coincidence count measurements (shown in Table 5.1) to be determined via Eq. (4.2) using the singles count rates in the signal arm.

For the data listed in Table 5.1, at the maximum pump power of 70 mW the generation rate of photon pairs from FWM mixing was 7.6×10^6 s^{-1} or 0.094 generated pairs per pulse. In the ideal case where the accidentals peak consisted only of photons due to FWM, the expected CAR is given by

$$\left(\mathrm{CAR}\right)_{\mathrm{ideal}} = \frac{C_P}{C_A} = \frac{\mathrm{PRF}}{r}\ , \tag{5.1}$$

where C_P and C_A are the coincidence count rate of the main coincidence peak and accidentals peak respectively. Therefore, assuming that there was no noise present in the count rates, the

expected CAR at for this generation rate would be 10.6. This places an upper limit on the CAR that can be achieved at this pump power due to the inevitable effect of multiple pair generation. If other sources of noise are also contributing to the coincidence count rates then the experimentally measured CAR will be

$$(\mathrm{CAR})_{\mathrm{exp}} = \frac{C_P + C_{noise}}{C_A + C_{noise}}, \tag{5.2}$$

where C_{noise} represents the additional noise contribution to the coincidence count rates. As shown in Table 5.1, the experimentally measured CAR value was found to be 10.4, reduced by the presence of noise. Using this, along with the calculated value of 10.6 for $(\mathrm{CAR})_{\mathrm{ideal}}$ found from the generation rate *r*, the magnitude of C_{noise} was found to be 2.6% of C_A. This shows that the level of noise photons in the idler arm for this source was negligible and the observed accidental coincidence peak was dominated by photons generated by FWM.

5.4 Achieving Temporal Indistinguishability of the Output Photons

As described in Section 3.5.3, due to group velocity mismatch between photons at the pump and generated wavelengths the output heralded photon state tends to a single temporal mode only when the PCF is reduced in length to the walk-off length. In order to produce pure state heralded photons it is therefore important that the PCF used for FWM did not exceed this length. The walk-off length for PCF-B was calculated from a previously measured group velocity delay curve for the fibre, shown in Fig. 5.14. This data had been obtained using the stage-scanning technique for dispersion measurement, which is described later in Section 7.5.

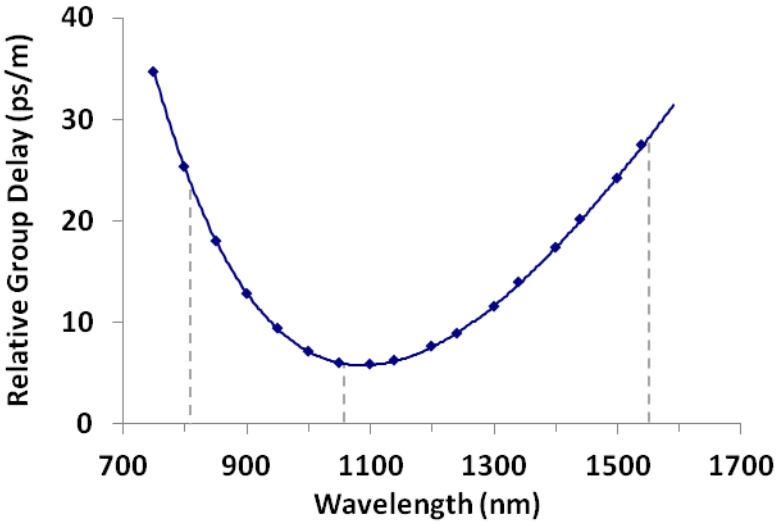

Figure 5.14: Measured relative group delay for light in PCF-B as a function of wavelength. The dashed lines indicate the signal, idler and pump wavelengths of interest.

As seen in Fig. 5.14, the signal and idler group velocities were similar to each other but both varied considerably from that of the pump wavelength. Using the measured group velocity data with Eq. (2.68), the walk-off length for this fibre was found to be 35 cm. The PCF was reduced down to this length from an initial value of 1.35 m by repeatedly cutting off sections ~20 cm in length, and was then reduced in length further beyond this point until only 15 cm remained. At each length the pump laser was coupled into the PCF and the coincidence count rate analysis, described in Section 5.3.1, was performed. In each case the maximum laser pump power of 70 mW was used and the narrowband FBGs were tuned in order to optimise the count rates.

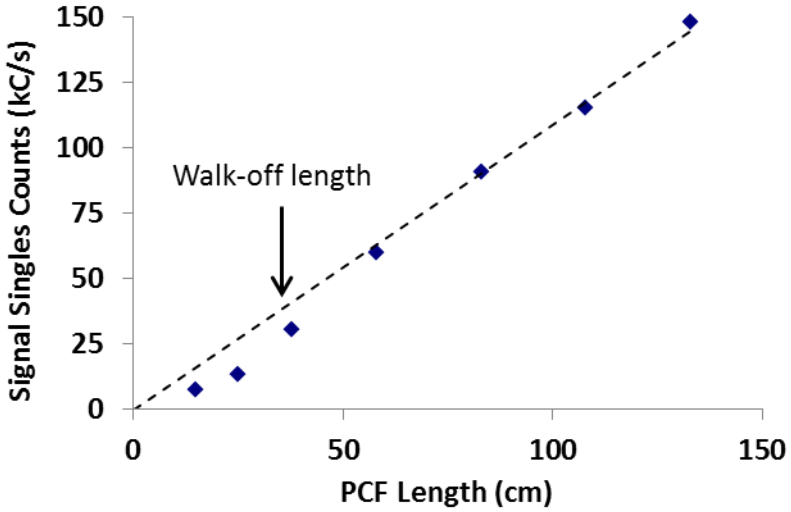

Figure 5.15: Measured singles count rate for the all-fibre source as the input PCF length was reduced. The dashed line that passes through the origin is a linear fit to the final four data points shown, corresponding to the longest PCF lengths where the FWM gain was expected to vary linearly with fibre length. The walk-off length calculated from the measured group delay data is also shown.

The measured singles count rate in the signal arm was reduced as the PCF was cut-back, as shown in Fig. 5.15. As expected, when the PCF exceeded the walk-off length, both the singles and coincidence count rates fell linearly with fibre length (see Section 2.2.7). When the fibre was below the walk-off length, the count rates were seen to decrease more rapidly, as the FWM gain varies as the square of the length in this regime.

At a PCF length of 38 cm, close to the fibre walk-off length, the main coincidence count rate at the maximum pump power was 1040 C/s with a singles count rate in the signal arm of 30 kC/s. The CAR was 43, indicating that at the required PCF length the source brightness was no longer limited by the generation of multiple photon pairs by FWM, but by the available peak pump power from the laser source. In Section 6.4.3 it will be shown that a CAR of 10 was achieved using this PCF with use of another fibre laser with similar properties but a higher available average power.

As the heralding fidelity of the source was predominantly determined by the optical loss in the idler arm it was expected to remain constant as PCF length was reduced. However, as shown in Fig. 5.16, the heralding fidelity was found to reduce from 52% to 23% as the fibre length decreased from 1.35 m to 15 cm.

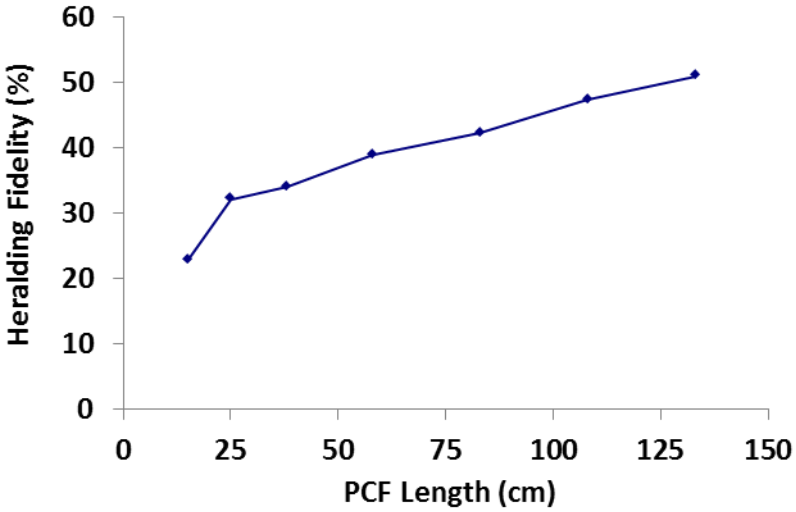

Figure 5.16: Variation in the measured heralding fidelity of the all-fibre photon source as the PCF length was reduced.

One possible contribution to this decline in heralding fidelity was mismatch of the tuned central wavelength of the narrowband FBG in the idler arm to the ideal position. As the PCF length and photon pair generation rate reduced, it became progressively more difficult to determine the point at which the FBG was tuned correctly such that the coincidence count rate was maximised. For the shortest PCF length of 15 cm the main coincidence peak count rate was only 180 C/s. Changes in the coincidence count rate from varying the FBG strain were then almost totally obscured by random statistical fluctuations in the measured count rates. This is evident from the sharp drop in heralding fidelity at the shortest length. However, systematic error in the optimisation of the spectral filtering is unlikely to explain the reduction at the higher count rate levels for the PCF, seen above the walk-off length.

As the optical loss in the idler arm should not be significantly affected by the reduction of the PCF length, the heralding fidelity was most likely reduced by some source of optical noise present in the signal arm. Introducing an additional free-space 10 nm band-pass filter (used previously in the broad-bandwidth source described in Section 5.1) at the output of the signal arm did not have any effect on the heralding fidelity, suggesting that the noise source was at the signal wavelength. Although there was a prism in the launch optics in order to filter the laser pulse of any undesirable additional wavelengths, due to the high transmission of the system for light at the signal wavelength and the sensitivity of the Si SPAD even relatively a small number of photons with these wavelengths could constitute a significant noise source. Such photons could be generated for example by two-photon absorption in the laser or

components in the launch optics, followed by subsequent fluorescence. As the PCF length was reduced the number of signal photons generated by FWM would also be reduced and the relative contribution of these noise photons to the total signal arm count rate would increase. This could lead to the reduction in the heralding fidelity observed. A bright source of noise emitted from the laser, which was not rejected from the device by the filtering, was observed to be present in the pump beam. A small adjustment to the mirror in the launch optics immediately before the PCF, in order to select a different dispersed wavelength component, resulted in the measured signal count rate increasing due to noise that was uncorrelated with photons in the idler arm. As there was no minima in the signal count rate between the point at which the noise was coupled into the system and the position at which the coupling of 1064 nm light to the system was optimised, this noise source was probably not entirely removed from the pump light by the launch optics, even when the input coupling was optimised.

In order to improve the spectral filtering of the pump light before it was launched into the device the distance between the prism and the PCF was subsequently increased from around 50 cm initially to more than 1 m. For the final version of the source described in Section 5.5, the heralding fidelity was found to remain at a constant value of 20% on cut-back from 2.5 m down to 35 cm. The lower heralding fidelity in this case was due to higher passive loss in the idler arm.

5.5 Reduction of Loss in the Signal Arm of the Source

Although the reduction in the PCF length was necessary in order to ensure a pure generated single photon state, it meant that the available pump power became a limiting factor and the source brightness was reduced. One approach to improving the output rate of heralded photons was to increase the transmission efficiency in the signal arm of the device, which was only 7% (-11.5 dB) for the source described in Section 5.2. The 50:50 coupler, used for spectral filtering in the signal arm, was replaced with an 80 nm bandwidth circulator with a central operating wavelength of 850 nm (*Thorlabs*, CIR-0850-40-APC). Its specified loss at 810 nm was 3 dB in total for transmission from port one to port two and port two to port three.

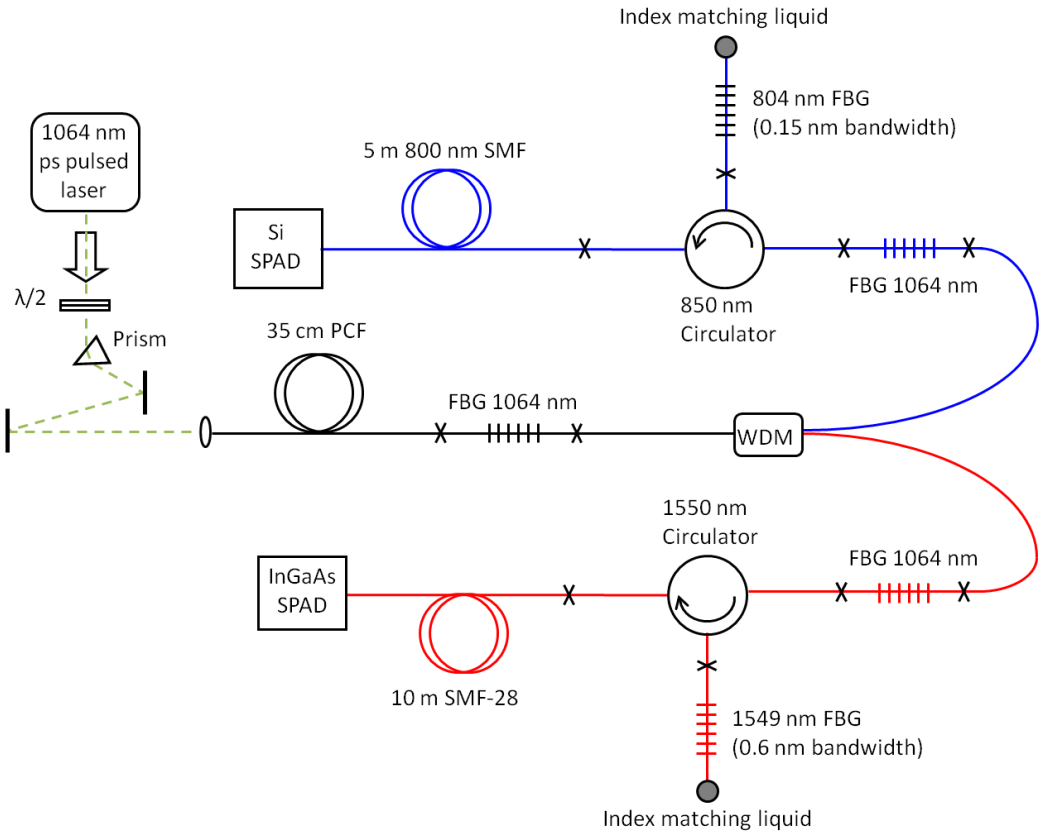

Figure 5.17: Schematic diagram showing the final layout of the all-fibre, narrowband filtered, single photon source.

In addition to the change to the filtering setup in the signal arm, many of the other components were replaced in the source. A new section of PCF-B was spliced to the input end of the device, as the previous PCF had been totally removed after the cut-back procedure described in Section 5.4. This initially had a length of 2.5 m but was eventually reduced to a length of 35 cm after performing a similar measurement in which the PCF length was cut-back in sections. In this case the heralding fidelity was found to independent of the fibre length, probably due to the increased distance in the free-space launch optics between the prism and the input of the PCF. The narrowband FBGs in both the signal and idler arms were replaced with new gratings with different central wavelengths, as the new section of PCF generated FWM peaks centred at 806 nm and 1559 nm. The WDM system was also replaced by a new component with operating wavelengths of 804 nm and 1570 nm. This new WDM had slightly a higher loss of 0.2 dB at the idler wavelength than the previous one, but was otherwise similar.

As the various components in the source were not added in series starting with the PCF, it was not possible to accurately determine the total loss by summing the measured losses from

each individual component and splice in this case. The total loss in both arms was measured using the technique described in Section 5.1 and shown in Fig. 5.4. Light from either a 1550 nm CW laser or a supercontinuum source filtered to give an 806 nm was input to the device and the output power from port two of the respective circulator was measured. This result was then compared against the output power that was transmitted from the light source through a similar section of the PCF alone in order to determine the loss of the device. The transmission in the signal arm was found to be significantly improved to around 25% (-6 dB). Unfortunately the loss in the idler arm was measured to have increased from that of the previous source after splicing together all of the new components. The transmission in the idler arm was measured to be 43% (-3.7 dB). This resulted in a decrease in the heralding fidelity for the source to 20%. It was unclear from this measurement which component or splice in the system was responsible for this increase in the loss. Determining the origin of this loss by rebuilding the source in series whilst monitoring the transmission was left as one of the objectives of future work.

Even with the increased loss in the idler arm, the heralding fidelity of 20% shown here compares favourably with other spectrally filtered fibre sources (see Table 3.1). This heralding fidelity is still relatively low compared to modern parametric down-conversion sources utilising high transmission free-space band-pass filters and optimised for coupling to single-mode fibre, which can reach fidelity of >80% [100]. However, this PCF source generates photons filtered to a narrow bandwidth that could not be easily achieved using free-space components without introducing a high level of loss. The low loss, narrowband, fibre-based filtering incorporated in the PCF-based source described in this chapter allows the source to be pumped using a relatively cheap picosecond pulsed fibre laser, rather than an expensive and bulky Ti:Sapphire pump laser. Also, as this source consists entirely of spliced fibre components, from the point of photon pair generation to detection, it is likely to be very reliable and more stable than sources incorporating free-space optics.

Although the number of heralded idler photons output from the source would clearly be reduced by the extra loss of the idler arm, overall the brightness of the source was still increased due to the improvement in the signal arm of the device. With the InGaAs detection efficiency set at 10% the count rate of the main coincidence peak was measured to be 2.3 kC/s with a singles count rate in the signal arm of 113 kC/s at the maximum pump power. The accidentals peak count rate was 60 C/s giving a CAR of 35, which was closer to the target CAR

of 10, but still limited by the available power of the pump laser. While the main coincidence count rate observed for this source appears low compared to those seen in PDC sources, this can be partially explained by the lower detection efficiency here of 10%, compared to ~50% for PDC sources operating at around 800 nm. As the CAR of this PCF-based source was greater than 10 the brightness could also be improved by using a higher peak power pump laser source, as demonstrated in Chapter 6.

5.6 Polarisation Purity of the Heralded Single Photon State

Given the reduction of the PCF to the walk-off length and the implementation of narrowband spectral filtering for the source, the output photon state should be restricted to only a single temporal mode. As discussed in Section 3.5.4, in this case the generated photons are all expected to possess the same well defined polarisation state, despite the non-polarisation maintaining nature of the PCF in which they are generated. This would mean that by adjusting the polarisation state of the idler photons it should be possible to totally extinguish the output of the device using an appropriately oriented polariser. In order to adjust the polarisation state of the idler photons, the output idler arm fibre of the device was coiled onto a fibre polarisation controller in order to implement a quarter-wave plate, half-wave plate, and then another quarter-wave plate. Adjustment of the polarisation controller would then allow any arbitrary single input polarisation state to be transformed into any desired output state [153]. An all-fibre linear polariser (*Thorlabs*, IFP1550SM-FC) was then added to output of the source between the polarisation controller and the InGaAs SPAD. Accounting for the extra length of fibre in the idler arm due to the polariser, the detector delay was chosen to look at the main coincidence peak, in order to observe what proportion of the heralded idler photons were transmitted through the polariser. By adjusting to the polarisation controller to maximise and minimise the measured coincidence count rate, the polarisation extinction ratio that could be achieved was 27. This shows that the heralded single photons were predominantly prepared in a single pure polarisation state, which would later be required in order to observe HOM interference using photons from this source (see Section 6.4.4).

5.7 Conclusion

This chapter describes the manufacture and characterisation of an all-fibre source of heralded single photons at telecoms wavelength. The free-space filtering described in Chapter 4 was replaced by narrowband fibre-based filtering, implemented using tuneable FBGs. These provided the tight spectral filtering required for a pure heralded photon state to be realised with low loss. A transmission of 68% was achieved from the point of photon pair generation in the PCF to the output of the idler photons from the system. From this, a heralding fidelity of 50% was observed for the source. This high heralding fidelity for a filtered source with a pulsed pump should make this device useful for QI applications which rely on multiple sources outputting a photon simultaneously, where error free operation of every source is required for a successful result.

Although narrowband spectral filtering discards a large proportion of the pairs generated by FWM, this can be compensated with a higher pump power. Given the reduction in the PCF length, the brightness of the source was significantly improved compared to the source with free-space filtering (see Section 4.2). For the desired CAR of 10 an output photon rate of 9.2×10^4 s^{-1} was achieved for a PCF of length 1.4 m. By reducing the pump power the CAR could be increased to more than 45, which is also important for QI applications, where the generation of multiple pairs of photons on the same laser pulse is detrimental to the performance. Measurement of the unheralded idler photon singles count rate showed that sources of noise in the idler arm, such as Raman-shifted pump light were negligible, and the accidentals coincidence count rate was dominated by the generation of additional pairs of photons via FWM, uncorrelated with the heralding signal.

The PCF in the source was reduced to its walk-off length, as seen by observing the variation in the photon count rate as the fibre length was altered. This change meant that the maximum source brightness that could be achieved was limited to 2×10^4 output photons per second by the available pump power, and the CAR of 10 could no longer be reached. However, limiting the PCF length to this length meant that the generated single photon state would be in a pure temporal mode. The purity of the polarisation state of the photons was also investigated and polarisation extinction of 27 was demonstrated for the source output. The purity of the generated photon state is confirmed in Chapter 6, where HOM interference was observed using the output from this source.

Chapter 6

Interference of Photons from PCF and PPLN Based Sources

While the work described in this thesis so far has solely focussed on producing a PCF-based source of heralded single photons, this is by no means the only option employed for generating photons for QI applications. As discussed in Section 3.4.3, there are many potential nonlinear materials that could be used as part of a probabilistic source based on parametric processes. One such material that has shown particular promise in recent years is periodically poled lithium niobate (PPLN) [154]. Although the photons generated in this material can be difficult to interface with single mode fibres, this can be improved by the formation of waveguides through selective doping of a bulk PPLN crystal. Sources based on this material have demonstrated high count rates from comparatively low pump powers, and output heralded photon states with high purity [155].

This chapter describes an experiment that was conducted with the aim of observing quantum interference between photons generated from the nonlinear interaction in a PPLN waveguide with those produced from the PCF-based source discussed in Chapter 5. This was of fundamental interest, as although interference effects in both types of sources have individually been studied previously, HOM interference between photons from these two different types of sources has not been observed before. From a more practical point of view, interference between the different types of sources may be of importance in future QIP applications (see Section 3.6.2).

Section 6.1 introduces some basic background information on PPLN sources, before the motivation for this project is discussed in Section 6.2. This section also includes some of the challenges involved in ensuring that the photons output from the two different source types were suitably matched in terms of their wavelength, polarisation, spatial and temporal modes. The properties of the actual PPLN source used in this work are then given in Section 6.3. Finally, the interference experiment between the PPLN and PCF is described in Section 6.4. The work described in this chapter was done in collaboration with researchers from the University of Bristol, and the University of Nice who produced the PPLN photon source. The work of producing and characterising the PPLN source (described in Section 6.3) was conducted by Laurent Labonté of the University of Nice, while the interference experiment (presented in Section 6.4) was a joint effort between L. Labonté, myself, and Alex Clark and Bryn Bell of the University of Bristol.

6.1 Overview of PPLN and Parametric Down-Conversion

Lithium Niobate ($LiNbO_3$) is a ferroelectric crystal, meaning that the crystal unit cell has a permanent electric dipole, characteristic of the material. In contrast with isotropic materials such as silica, in single crystals of $LiNbO_3$ these electric dipoles can be aligned, leading to material polarisation (see Section 2.2.1) even in the absence of an applied electric field, giving the possibility of inverting its nonlinear coefficient. This factor, combined with a wide transparency window for the material across the visible and near infrared (300 nm – 5 μm) makes it a useful medium for second-order nonlinear interactions, which can be observed with high conversation efficiencies [154].

As with the Kerr nonlinearity described previously in Section 2.2.1, the $\chi^{(2)}$ component of the electric susceptibility leads to a variety of nonlinear effects such as second-harmonic generation (SHG), and parametric amplification, but in the context of heralded photon generation sources, the most important process is spontaneous parametric down-conversion (PDC). The theoretical description of PDC [156] is broadly similar to that of FWM discussed in Section 2.2.3, the main difference being that $\chi^{(2)}$ processes involve the interaction of three photons, so a single photon at the pump frequency is annihilated to generate a signal and idler pair. As with FWM the signal photon will have a higher frequency than the corresponding idler (except in the case of degenerate PDC where they are equal), although the constraint of energy conservation means that in PDC both the signal and idler frequencies are down-shifted

from the pump. As described in Section 3.4.3, since photons are generated simultaneously in pairs by PDC, the detection of a signal photon can be used to herald the presence of the corresponding idler photon (or vice versa).

Similarly to FWM (see Section 2.2.4), the efficient generation of photons from PDC depends not only on the strength of the nonlinearity but also on achieving phase-matching between light at the three different interacting wavelengths. As in the case of phase-matching for XFWM in a birefringent fibre (see Section 2.2.6), in a bulk lithium niobate crystal birefringence can be used to compensate for the material dispersion and achieve phase-matching. With type-I phase-matching the signal and idler are both polarised orthogonally to the pump, or for type-II phase-matching the signal and idler can be made orthogonal to each other. This arrangement can be used to produce sources of entangled photons [157]. In addition to the birefringence, the refractive index in $LiNbO_3$ is strongly temperature dependent, allowing the phase-mismatch to be controlled by adjusting the crystal temperature over a range from room temperature up to ~250°C.

For $LiNbO_3$ efficient generation of light in parametric processes can also be achieved through the technique of quasi-phase-matching (QPM) by periodic poling. Periodically poled crystals are designed so that the intrinsic material polarisation alternates in sign between adjacent regions of the sample. This can be achieved through the application of high voltage electric pulses (typically ~20 kV/mm [158]) across a sample, which causes the electric dipoles in the material to align with the applied field. This polarisation will remain imprinted on the sample even after the field is removed. By choosing an electrode with an appropriate 'striped' geometry to apply the field, a periodically poled structure with a well-defined repetition period can be produced [159]. This is illustrated in Fig. 6.1.

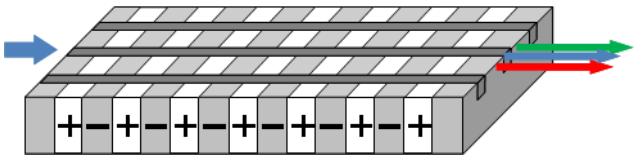

Figure 6.1: Schematic representation of a PPLN crystal showing the alternating regions formed by poling. The dark strips represent rectangular waveguide channels in the crystal in which pump light can be confined and PDC can occur.

As described in the case of FWM in Section 2.2.4, usually nonlinear frequency conversion only occurs efficiently when the requirement of phase-matching is satisfied. However, for the case of QPM in periodically poled materials, such as PPLN, the poling period is chosen such that the

sign of the nonlinear coefficient is reversed at the position in the crystal where the intensities of the generated signal and idler would otherwise begin to decline due to the accumulated phase-mismatch [160]. This allows the intensity of the generated light to continue to increase along the entire length of the crystal (see Fig. 6.2). The presence of the grating like periodic structure in PPLN leads to a QPM condition of the form [157]

$$\vec{k}_p = \vec{k}_s + \vec{k}_i + \frac{2\pi}{\Lambda} \cdot \vec{u}\,, \tag{6.1}$$

where k_j are the wavevectors for the pump, signal, and idler field, Λ is the poling period, and u is a unit vector perpendicular to the poling alignment in the material. Through careful choice of the poling period Λ the poled grating can balance the material dispersion of the crystal, even in the case of widely spaced wavelengths where phase-matching is otherwise difficult to achieve. In addition, periodic poling can enable phase-matching with pump, signal and idler co-polarised, where the relevant nonlinear coefficient of the material for the interaction (d_{33}), is highest [161]. As mentioned previously, the high temperature sensitivity of PPLN can be used to adjust the phase-matching conditions, which can allow some for some tuning of the central wavelengths of the generated photon pairs in order to achieve a single photon source with a particular desired operating wavelength.

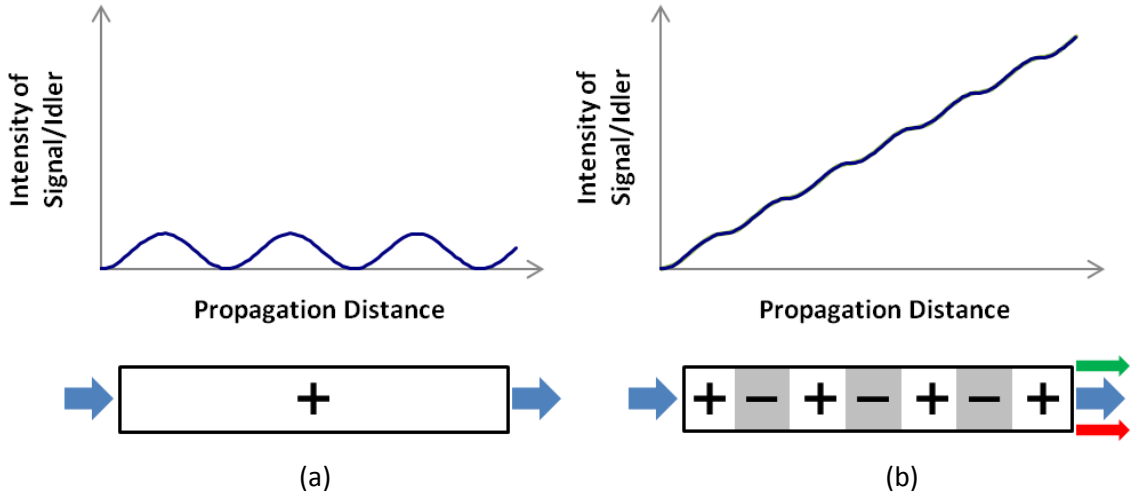

Figure 6.2: (a) Generated power at the signal and idler wavelengths from PDC in an un-poled crystal. The power is unable to build up due to the lack of phase-matching; (b) In a periodically poled crystal the QPM resulting from the change in the sign of the nonlinear coefficient allows the power to accumulate with propagation length in an approximately linear fashion.

In addition to its suitability for QPM, PPLN can be selectively doped to write high index channels into the crystal. Crucially, this allows waveguides to be formed, allowing the PDC interaction to be realised in a guided wave configuration. This means that many of the difficulties of earlier photon sources based on PDC in bulk crystals, such as the spatial collection of the generated photons, spatial walk-off of the beams, and stability issues for free space optics can be avoided. The high index channels can be formed by exchange of lithium atoms with hydrogen [154] or in-diffusion of materials such as titanium, typically by patterning the dopant material onto the crystal surface and heat treating [157].While the manufacturing process typically limits the waveguide length to only a few centimetres, the inherently higher strength of $\chi^{(2)}$ based nonlinear processes allows efficient conversion rates between the pump generated photons over a very short range, enabling heralded single photon sources with low pump power requirements [162].

6.2 Integration of Different Types of Photon Sources

As discussed in Section 6.1, PPLN waveguides can achieve photon pair generation with high efficiency over extremely short lengths. Additionally, the pump power requirements of such sources tends to be low, and photon pairs in both heralded single photon and entangled pair configurations are easily realised using quasi-phase-matching. For these reasons PPLN sources appear to be an attractive option for future optical QIP tasks. Miniaturised optical components for this purpose, such as controllable phase-shifters, were recently demonstrated in a deposited silica waveguide on a silicon substrate [163]. In the future, PPLN sources could be incorporated with these types of components in order to realise both quantum optical logic gates and the required photon sources to utilise them, integrated on a single chip.

While PPLN sources may be well suited for on-chip applications, for transmission of photonic qubits over large distances in quantum communications optical fibres will be crucial. As fibre-based photon sources can be easily integrated with single mode transmission fibres they seem a natural choice for future quantum optical networks. While it is unclear at this stage which, if any, of the currently realised single photon sources technologies will prove to be most suitable for these future applications, it may well be the case that the ideal solution will encompass multiple types of sources. Since future optical networks that incorporate both the transmission and optical processing of photonic qubits may include both fibre and PPLN

photon sources, a key question is whether photons from these two different types of source are compatible.

The QIP applications described in Section 3.6 rely on sources of photonic qubits in order to operate. These protocols are quite general and make no stipulations as to the nature of the source from which the photons were produced. However, interaction between photons in the scheme of linear optical quantum computation is achieved via quantum interference effects that depend critically on the indistinguishability of the photons. The indistinguishability of two single photons is commonly demonstrated through measurement of the HOM interference visibility that can be observed between them when both are incident together on the input ports of a beam-splitter (see Section 3.3). To date however, there has been no demonstration of interference between the photons from a fibre-based source with those from a PPLN source, which would show the potential for future integration of the sources in QIP systems.

The HOM effect was first demonstrated by Mandel et al. through the interaction at a beam-splitter between 700 nm wavelength photons from a degenerate pair, produced by PDC in a bulk potassium dihydrogen phosphate crystal [76]. A HOM dip with visibility of 90% was measured, with imperfect spatial overlap (and therefore distinguishability) of the photons at the beam-splitter accounting for the non-unity visibility. Later sources based on degenerate PDC in $\chi^{(2)}$ crystals, in which background noise photon levels were reduced and the spatial overlap of the interfering photons was guaranteed though single-mode collection fibres, improved the interference visibility to ~99% [96].

While degenerate parametric processes provide a convenient method for preparation of indistinguishable photons, they are not the only means by which high visibility HOM interference can be observed. Non-classical interference has also been demonstrated between heralded single photons from independent photon sources, including the output from two bulk crystal sources [164], the heralded photon states from two separate fibre sources [120], and between the photons from independent PPLN sources [165]. In the case of the fibre source experiment, a raw HOM dip visibility of 88% was reported, limited primarily by the effect of multiple pair generation events in the individual sources. After correcting for this background coincidence contribution, the net visibility was found to be 95%, close to the anticipated maximum for the chosen spectral filtering. Similarly, the raw visibility of 93% demonstrated for the interference between the separate PPLN sources [165] was limited by higher order pair emission. The net visibility in this case was 99%.

While there have been many demonstrations of HOM interference between separate but identical photon sources, the interference of photons from dissimilar sources has so far received little attention. One notable study by Polyakov et al. [166] investigated the interference of photons from a quantum dot with those produced by a periodically poled $\chi^{(2)}$ crystal. The low measured raw visibility of only 16% was attributed to decoherence of the quantum dot. However, by post-selecting coincidences within a narrow temporal gate, visibility of 70% could be achieved at the expense of discarding 90% of the collected coincidence events.

From an experimental perspective, observing HOM interference between dissimilar sources, such as those based on PCF and PPLN, is challenging because of the requirement of achieving indistinguishability of the interacting photons in all degrees of freedom (see Section 3.5). Matching of the spatial modes of two sources in this experiment was ensured by coupling the output from the PPLN source into single-mode optical fibre. While this process introduces some loss into the system it allows the interaction to occur in a single-mode fibre coupler, which guarantees an overlap of the mode profiles of the photons from the sources without requiring alignment. This also allowed the PPLN source to take advantage of narrowband fibre-based filtering that was matched to that described in Section 5.2 for the PCF-based photon source, in order to approach an idealised spectrally pure state (see Section 3.5.1). Matching of the polarisation states of light from the two sources was achieved using fibre polarisation controllers at the output of both sources.

Ensuring that the heralded photons output from the sources are synchronised in time, in order to ensure temporal overlap at the fibre coupler, is more difficult. As discussed in Section 5.4, the PCF in the fibre source was kept below the walk-off length to minimise timing jitter of the photons relative to the pump pulse. Typically in this type of interference experiment with two sources, the pump pulses from the laser are split at a beam-splitter in order to provide synchronous pumping. This option could not be used in this case as the pump power requirements of each source were too high, and the laser power could not be further increased due to the detrimental effects of self-phase modulation (SPM) in the fibre laser amplifier (see Section 2.2.1). The solution was to use a dual output pump laser (*Fianium*, custom design based on model FP1060-0.1), with the seed pulse from a single oscillator split between two independent fibre amplifiers, giving more power (in nearly bandwidth limited pulses) than a single-beam design could provide.

Selecting an appropriate pump laser was also important in order to achieve phase-matching at desirable generated wavelengths. Section 4.1 describes the advantages of working with a 1064 nm fibre pump laser, and of generating signal and idler light near 810 nm and 1550 nm respectively. In order to spectrally match the sources it is clearly necessary to match the wavelengths for peak parametric gain in the sources, as well as the filtering. Since PDC produces signal and idler photons of lower frequency than the pump, energy conservation would lead to heralding photons with a wavelength of 3.4 μm when generating photons at 1550 nm directly from a 1064 nm pump, which would be difficult to detect. In order to match the PPLN output wavelengths to that of the PCF source, the 1064 nm laser was first frequency doubled to 532 nm using a second-harmonic generation (SHG) bulk crystal. The PPLN source was designed to allow QPM between this wavelength and signal and idler pairs at 810 and 1550 nm in the fundamental mode of the waveguide.

6.3 A PPLN-Based 1550 nm Single Photon Source

The PPLN heralded single photon source, used to investigate the potential for HOM interference, was designed to generate signal and idler photon pairs at 810 nm and 1550 nm respectively from a pump wavelength of 532 nm via QPM PDC (see Section 6.1). As with the PCF-based photon source described in Chapter 5, the signal photons generated from this interaction were detected using an efficient Si-based SPAD in order to provide heralding for the idler photons. The heralding signal could then be used to trigger an InGaAs-based SPAD in order to measure the coincidence count rate between the signal and idler photons when the electronic delay between the detectors was appropriately chosen to measure the main coincidence peak (see Section 5.3.1). The performance of the source was first investigated using a 532 nm CW pump in order to select a PPLN waveguide with phase-matching properties that would most closely match the signal and idler wavelengths to those of the fibre source. This preliminary work also ascertained the pump power at 532 nm that would be required to observe sufficiently high singles and coincidence count rates in the interference experiment in the case of narrowband filtering.

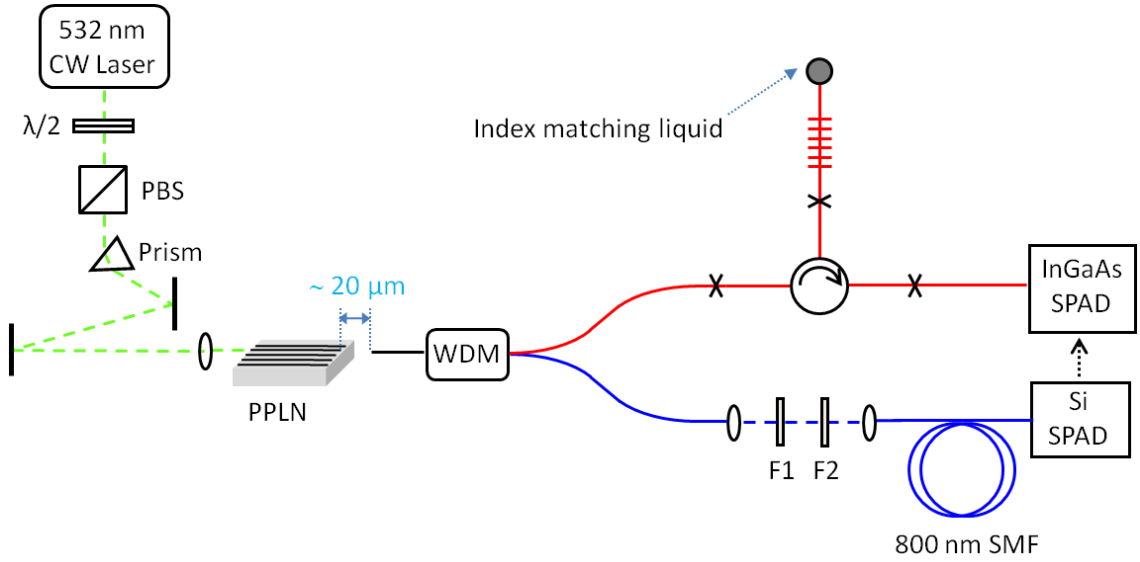

Figure 6.3: Experimental set up for the preliminary study of the PPLN photon source, using a 532 nm CW laser. Filtering in the (red) idler arm is achieved with a circulator and narrowband FBG, while in the (blue) signal arm 10 nm and 0.5 nm bandwidth free-space filters (F1 and F2) are used. PBS is a polarising beam splitter and WDM is a wavelength division multiplexing system, similar to that used in the PCF-based source.

The setup for the preliminary investigation of the PPLN source with a CW pump source is shown in Fig. 6.3. The PPLN crystal contained an array of different waveguides, each with slightly different geometric parameters, leading to different phase-matching conditions. The waveguides were produced using the soft proton exchange method [154] to introduce H+ ions to the PPLN lattice, forming channels of raised refractive index penetrating to a depth ~2 µm below the surface. The crystal length was 30 mm. The different waveguide channels ranged in width from 4 to 8 µm, giving channels with various effective indices for the guided modes. There were five such groups of waveguide channels with these widths, written into separate regions of the PPLN crystal with different poling periods, ranging from 6.9 to 7.5 µm. The waveguide that was selected for use in the interference experiment had a width of 6 µm and a poling period of 7.2 µm.

In the launch optics, a polarising beam-splitter was used to ensure that the pump beam was linearly polarised and aligned to the correct crystal axis of the PPLN, and a half-wave plate was used to adjust the pump power. The waveguides were designed for phase-matching with co-polarised pump, signal and idler beams. A prism was also included in the launch optics in order to avoid coupling into the PPLN any light that may have been emitted by the laser at the signal or idler wavelengths. An 11 mm focal length lens then coupled the pump beam into the PPLN waveguide. Care needed to be taken when optimising this input coupling as the

waveguide was multimode at the pump wavelength. The phase-matching conditions were only satisfied for pump light in the second order mode generating signal and idler beams in the fundamental mode, so any pump power launched into other modes would be wasted.

The end-faces of the PPLN crystal had been polished in order to allow efficient input and output coupling of light from the waveguides. At the output face the signal and idler photons were collected into 1060 nm SMF. The end of the SMF was positioned ~20 μm from the PPLN and coupling between the SMF and the correct waveguide of the PPLN was achieved using a magnified video image of the PPLN and fibre from above. The coupling loss was measured to be 5 dB. The signal and idler photons were then separated into two output fibres using a WDM system, similar in design to that described in Section 5.1. The tuneable narrowband filtering in the idler arm of the system was realised using identical components to those described in Section 5.2 for the PCF source. In the signal arm filtering was achieved using two bulk filters placed in a free-space 'U-bench' arrangement. The narrowband filtering in this arm was from a 0.5 nm bandwidth filter, slightly rotated to give a central wavelength of 804.5 nm. An additional 10 nm bandwidth filter with a central wavelength of 800 nm was used to ensure sufficient rejection of the pump light. The combined insertion loss of the two filters and the U-bench setup was ~3 dB.

For 6.2 mW of CW pump power at 532 nm the measured singles count rate in the signal arm was 95 kC/s and the measured coincidence count rate was 800 C/s at a detector efficiency of 25% for the InGaAs SPAD. Clearly the heralding fidelity for the PPLN source in this case was significantly lower than that demonstrated previously for the PCF-based source. This is to be expected because of the relatively high output coupling loss from the PPLN in this configuration. Also, the filtering bandwidth in the signal arm here is broader than the required 0.15 nm for a time-bandwidth limited output. While narrowband filtering is not essential in this arm, since the signal filtering bandwidth is not energy matched to the idler filtering this will lead to additional false heralding events. This can be seen from the relatively high measured singles count rate compared to the measured two-fold coincidence count rate. For the purposes of the HOM interference measurement (see Section 6.4) a low heralding fidelity should not be a significant problem, as this relies on observing the four-fold coincidence count rate between all four SPADs, meaning events where an idler photon is not detected will be discarded in post-selection in any case.

In addition to requirement of producing pure state idler photons, as required for high visibility HOM interference, the other important goal for this experiment was achieving high measured two-fold coincidence count rates for each of the sources, as this would determine the rate of four-fold coincidences between the photons from the two sources, and ultimately how long the experiment would take to run. While some previously demonstrated photon sources based on PDC in PPLN have required only microwatts of average pump power to operate [167], for this source the power requirements were much higher. This is due to the fact that the efficiency of the PDC process depends on the overlap between the mode fields of the interacting signal, idler, and pump fields. Since PPLN-based sources are often designed to generate entangled pairs via degenerate PDC, the overlap between the generated modes can lead to very high efficiency. For this source however the resulting mode overlap is far lower due to the widely separated signal and idler wavelengths required to match the heralded single photons from this source to those of the PCF-based source. Additionally, the multimode nature of the waveguide limited the efficiency with which pump light could be launched to the required mode, further increasing the power requirements. The preliminary work showed that ~10 mW of pump power at 532 nm would be required for the PPLN source in order to operate with the optimum CAR of 10, the point at which the probability of generating multiple pairs of photons per laser pulse begins to become significant (see Section 3.5.2).

As described in Section 6.2, for the HOM interference experiment the 532 nm light for PDC in the PPLN had to be generated from a dual-output 1064 nm fibre laser. The characteristics of this laser were similar to the picosecond pulsed pump source described previously in Section 4.1, apart from the higher average power. The specified pulse duration was 4.5 ps, and the central wavelength and bandwidth were measured to be 1064.0 nm and 1 nm respectively. The pulse repetition rate was 80 MHz. The average power in the two laser outputs was adjustable independently up to a maximum of 250 mW. The laser incorporated internally spliced fibre isolators for both outputs.

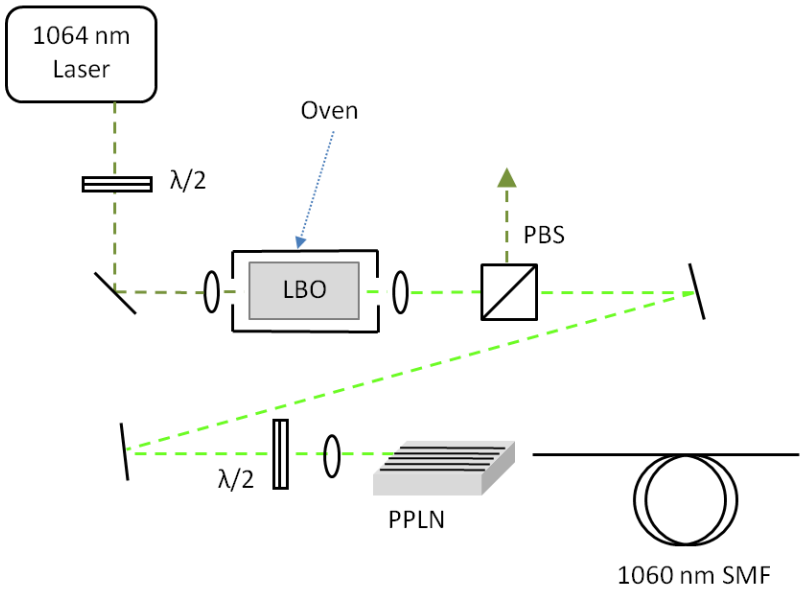

Figure 6.4: Pumping scheme for the PPLN source. The CW pump was been replaced by the second-harmonic output of an LBO crystal, pumped with a pulsed 1064 nm laser. The polarising beam-splitter (PBS) rejects the residual 1064 nm after the SHG crystal.

In order to pump the PPLN with this source a $\chi^{(2)}$ nonlinear lithium triborate (LBO) crystal was used for SHG, as shown in Fig. 6.4. The LBO crystal was 20 mm long and anti-reflection coated for operation at both 1064 nm and 532 nm. The crystal was held in an oven at 148°C for efficient SHG via type-I noncritical phase-matching. The 50 mm focal length lenses at the input and output of the crystal were selected to optimise the conversion efficiency of the SHG process. As the 532 nm light generated through SHG was polarised orthogonally to the residual 1064 nm beam, the 1064 nm light was rejected after the LBO crystal using a Glan-Thompson polariser. A half-wave plate was used to adjust the polarisation state of the 532 nm light before it was coupled into the PPLN.

After moving to the 1064 nm laser source, the generated signal and idler wavelengths of the PPLN were measured in order to ensure that they could be matched to those generated by the PCF-based source.

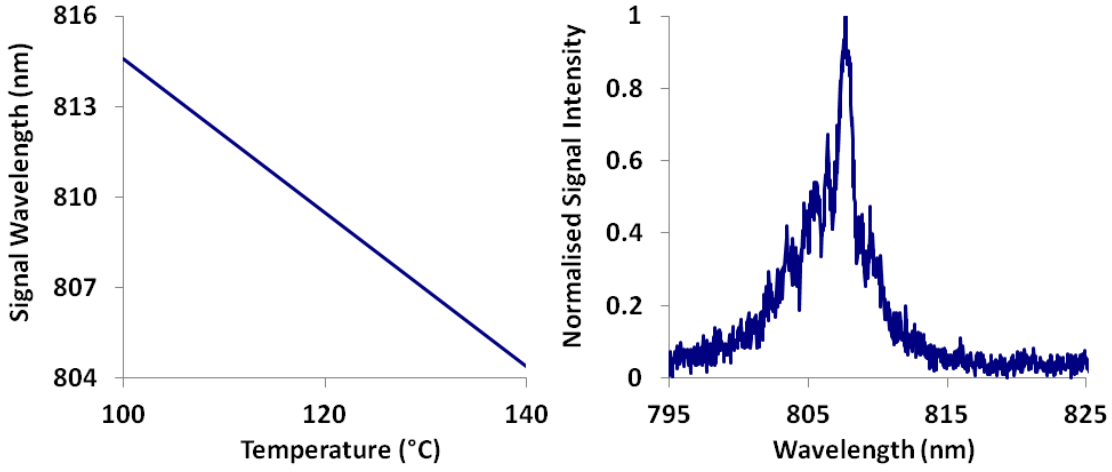

Figure 6.5: (a) Calculated dependence of the generated signal wavelength on the PPLN temperature; (b) Measured output of the signal arm of the PPLN source at 120°C.

The peak signal wavelength for PDC in the PPLN was predicted by numerical modelling [168] over a range of experimentally accessible crystal temperatures. The results are shown in Fig. 6.5(a). To attain the required temperature tuning the PPLN was mounted on a resistive heating element with a connected temperature controller and the crystal was surrounded by thermal insulation, apart from two small holes to allow the optical beam in and out. This allowed continuous adjustment of the crystal temperature up to 120°C. An example of the output signal peak from the PPLN source (without the narrowband filters included) at a temperature of 120°C, measured using a sensitive liquid nitrogen cooled CCD based spectrometer (*Jobin Yvon*, Symphony and Triax), is shown in Fig. 6.5(b). The measurements demonstrated that this temperature tuning should allow the operating wavelengths of the PPLN source to be adjusted close to that of the PCF-based source.

6.4 Investigation of the HOM Interference Visibility

In order to look for the experimental signature of quantum interference between photons, the single photon output of the PCF source (described in Section 5.5) and the output from the PPLN source with 1064 nm pumping (see Section 6.3) were coupled into the two inputs of a fused-fibre coupler. Section 6.4.1 outlines the experimental setup and subsequent sections describe how indistinguishability of the photons was achieved. The results of the experiment are discussed in Section 6.4.5.

6.4.1 Interfacing the Photon Source Outputs

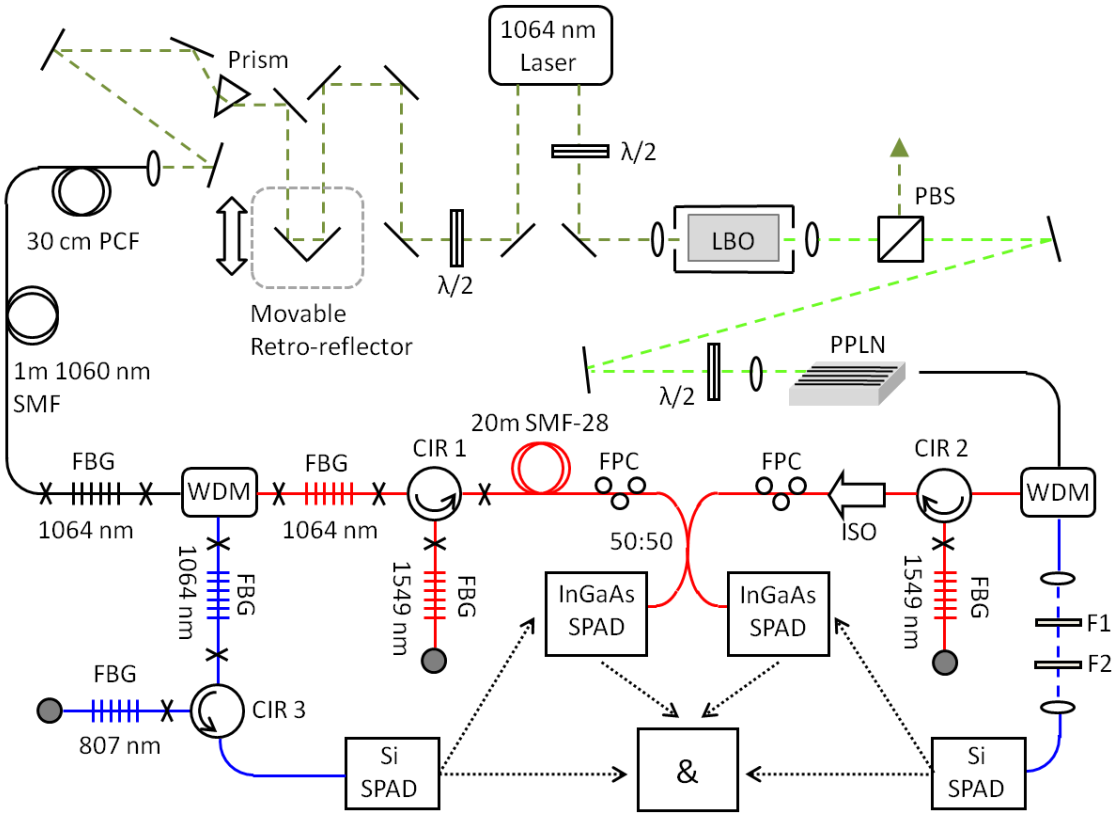

Figure 6.6: Joint setup of both the PCF-based photon source (left side of diagram) and PPLN source (right side of diagram) for the HOM interference measurement. ISO is an isolator, FPC are fibre polarisation controllers, 50:50 is a fused-fibre coupler and '&' is FPGA-based coincidence counting electronics. Dotted arrows indicate the transmission of electrical signals for the purposes of triggering and coincidence counting.

The experimental setup used to observe HOM interference between photons from the two sources is shown in Fig. 6.6. The left side of the figure shows the PCF source, of which very little was changed from that shown in Fig. 5.17. The narrowband gratings in the signal and idler arm were replaced with new FBGs at central wavelengths of 807 nm and 1549 nm with the same bandwidths as the previous gratings, 0.15 nm at the signal wavelength and 0.6 nm for the idler. This change was necessary due to the shift in the peak FWM gain resulting from the change to a new pump laser with a slightly longer central wavelength, measured to be 1064.0 nm using an OSA. The right side Fig. 6.6 shows the PPLN source, as described in Section 6.3. The only change here was the addition of a 1550 nm optical isolator directly after the idler arm circulator. The purpose of this was to provide further rejection of light at the pump wavelength from this arm. In the future this could be replaced with an FBG to provide

the required wavelength filtering with minimal loss, in order to improve the count rates. At the end of the idler arms of both sources were fibre polarisation controllers to allow the polarisation state of the idler photons to be matched at the point of interaction.

The outputs of both sources were connected to the two input ports of a 50:50 fused-fibre coupler (*Thorlabs*, 10202A-50-FC). The two output ports of the coupler were connected to InGaAs SPADs. Each of these detectors was gated using the heralding signal from one of the Si SPADs at the output of the signal arms of the sources. If only one of the two photon sources was operating, one of the InGaAs SPADs was triggered and, as described in Section 4.3, the measured count rate gave the two-photon coincidence count rate for the source, albeit with the count rate reduced by half due to the effect of the 50:50 coupler.

The outputs from the InGaAs detectors (indicating when idler photons were measured) were connected to an electronic coincidence counting system, along with the heralding signals from the Si SPADs. The coincidence counter was a custom made system, produced at the University of Bristol, based on a field-programmable gate array (FPGA) electronic circuit. The FPGA system was controlled using a Labview program, recording detection events for each of the four input channels whenever a rising electronic edge from the corresponding detector was received. Additionally, the system looked for simultaneous arrival of signals from the two InGaAs detectors (corresponding to a four-fold coincidence event in this detector arrangement) as well as simultaneous signals from the two Si based detectors, which was later used to normalise the four-fold count measurements. Two pulses were judged by the system to be coincident if their rising edges arrived within <6 ns of each other and distinct if separated by >9 ns, with nearly 100% accuracy [169]. As the laser repetition period was 12 ns, this was sufficient to distinguish when the successful operation of both sources occurred on the same pulse of the pump laser. The FPGA system therefore allowed the singles count rate in the signal arms, the two-fold coincidence count rates in both sources, and the four-fold count rate between all four detectors, as well as the events where both sources produced a heralding signal to be recorded concurrently and accumulated over a desired period of time.

Since HOM interference is dependent on the interacting photons being indistinguishable in all degrees of freedom it was necessary to match the filtering wavelength in the idler arms of the two sources, the polarisation state of the single photons at the point in the 50:50 fused fibre coupler where the exchange of energy between the two fibre cores occurred, and the arrival

time of the photons at the coupler. Matching of the spatial degree of freedom was already guaranteed by the single-mode nature of the coupler.

6.4.2 Matching the Arrival Times of the Single Photons

In order to ensure that heralded photons from the two sources arrived at the coupler at the same time, the optical path length of the sources had to be appropriately chosen. As the probability of a successful operation of one source was independent of the other on any given pulse of the laser, there was no need to ensure that the lengths of the two sources were identical. The aim was to the match the arrival time of single photons from one source, generated on a given laser pulse, to the arrival time of photons from the other source that were generated on another pulse of the pump laser, separated in their time of arrival by some multiple of the pump repetition period.

A time-correlated, single photon counting system (*PicoQuant*, PicoHarp 300) was used in order to measure the relative timing offset between the detection of idler photons from the PPLN source and the pulse train from the laser. This timing analysis system was triggered using start pulses taken from the electronic oscillator output of the laser. The detection output from the InGaAs detector (that was triggered using the heralding signal from the PPLN source) was used as a stop pulse. The device repeatedly measured the time interval between received start and stop pulses, forming a histogram of the relative time delay between the laser pulses and idler photon detection events from the accumulated data. Since no particular laser pulse was more likely to produce a detection event than any other, this histogram consisted of a periodic series of peaks, at delay times separated by the laser pulse repetition period. From this data it was only possible to determine the relative delay between the laser pulse train and the detection of idler photons, as the total path length for idler photons in the photon source was not known with sufficient accuracy.

After measuring the timing offset of the PPLN source from the laser pulse train, the same procedure was performed for the PCF source. The optical setup was not changed at all between the two measurements in order to avoid changing the source length. Also, the same InGaAs detector was used in both measurements in order to avoid any error in the length matching of the sources due to differences in the output fibre lengths of the two arms of the 50:50 coupler. The triggering of the InGaAs detector therefore had to be changed for the purposes of this measurement, such that it was triggered with the heralding signals from the

Si SPAD at the output of the PCF source, in order to detect the corresponding idler photons from this source.

When the timing measurement was repeated for the PCF source, the histogram again showed a series of peaks separated by the laser pulse repetition period. The offset between the peaks in the two sets of data, and therefore the difference in the arrival times of the idler photons at the coupler, was ~1 ns when the retroreflector was at the central position of its available range. This mismatch in arrival time was too large to compensate by moving the retroreflector, which had a maximum travel range of 75 mm in each direction, allowing the delay to be adjusted by only ±0.5 ns. A 30 cm section of fibre was removed from the 20 m of SMF-28 at the output of the PCF source in order to more closely align the arrival times of the idler photons. Subsequently, repeating the measurement of the PCF source delay showed that the arrival of the idler photons from the PCF source at the coupler could be made to occur before or after the idler photons from the PPLN source with the retroreflector at the two extremes of the movement range. This showed that the idler photons from the sources would be overlapped in time at the 50:50 coupler for some position of the retroreflector within the accessible range. The measured relative timing data for the two sources is shown in Fig. 6.7 for a retroreflector position of -20 mm relative to its central position.

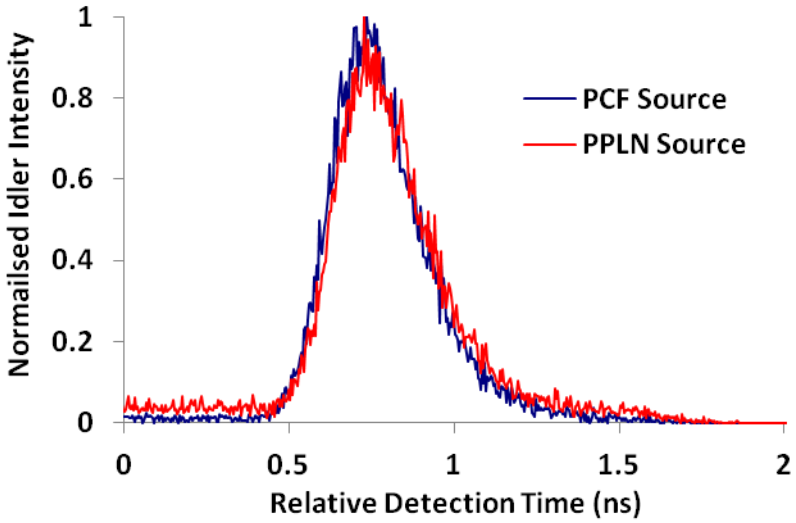

Figure 6.7: Measurement of the timing offset between the laser pulse train and the detection of idler photons, shown for both the PPLN and PCF sources for a retroreflector position of -20 mm.

The timing analysis system was able to measure the timing offset with a resolution of around 4 ps. However, as seen in Fig. 6.7 the measured FWHM of the timing peaks was much broader,

around 300 ps. The resolution was limited by the timing jitter of the electronic output from the InGaAs SPAD. The accuracy of this timing measurement was important as it determined the range of positions of the retroreflector that would need to be investigated in order to locate the HOM dip. The anticipated HOM interference was only expected to occur for photons overlapped to better than the photon coherence time ~5 ps. Assuming that 5 data points would be required within the range defined by the coherence time gave the required step size for scanning the retroreflector as 0.15 mm. From the relative timing measurement, the overlap of photons from the two sources at the coupler was predicted to occur for a retroreflector position between -10 mm and -30 mm from the central point of its range. Searching over this entire range would involve acquiring four-fold coincidence data at more than 100 different stage positions. Due to the low four-fold coincidence count rate, measurement of the required number of idler photons took around 40 minutes at each stage position, so even this 20 mm range would require a considerable amount of time to search.

6.4.3 Matching of the Single Photon Spectra

In addition to ensuring the simultaneous arrival of photons from the two sources it was also necessary to make the photons from the two sources spectrally indistinguishable. As discussed in Section 6.3, the phase-matching conditions for PDC in the PPLN source were temperature dependent, whilst for the PCF source the peak idler wavelength for the FWM gain was fixed by the dispersion properties of the PCF and the pump laser wavelength. Ideally it would therefore be preferable to select the wavelength for the interacting photons based on the peak idler wavelength of the PCF source and then match the peak idler wavelength of the PPLN source to this value by temperature tuning.

The spectrum of the unfiltered signal arm output from the PCF source was measured using the same sensitive CCD spectrometer that was used to determine the operating wavelengths of the PPLN source. This measurement was made by observing the transmitted output past the narrowband FBG in the signal arm, at maximum pump power, when the grating was tuned away from the peak of the FWM gain. The measured peak (unfiltered) signal wavelength was 807.5 nm. The PPLN waveguide that was initially selected was for use in the interference experiment generated signal photons matched to this wavelength at a crystal temperature of around 80°C. Unfortunately this operating temperature (and consequently the waveguide) proved to be unsuitable due to the problem of photorefractive damage [44]. This effect results

from the generation of free carriers in a material by an applied optical field. The resultant electric field distribution from these carriers modifies the refractive index profile of the material, which in waveguides it can lead to undesirable time-varying, inter-modal coupling that reduces the efficiency of nonlinear processes [170]. When operating the PPLN source at 80°C, this resulted in an observed instability in the measured coincidence count rates from one second to the next.

The onset of photorefractive damage is known to be suppressed at higher temperatures and the effect is significantly reduced at temperatures of more than 100°C [171]. A different waveguide on the PPLN chip was selected that generated signal and idler wavelengths that would be matched to the PCF source at higher temperatures. The shortest signal wavelength that could be achieved in this case was 808.8 nm at the maximum crystal temperature of 120°C that could be attained using the heater, close to, but not quite matched with the peak signal wavelength of 807.5 nm for the PCF source.

Since the PPLN source proved to be far more stable at the higher temperature, the sources were matched in wavelength by tuning the narrowband spectral filtering in the PCF source slightly away from the signal and idler peaks in order to match the two sources at wavelengths of 808.8 nm and 1553.8 nm respectively. In order to accurately match the idler wavelengths of each photon source, light from a supercontinuum source (see Section 2.2.8) was launched into the output end of the narrowband idler FBGs. The spectrum of the light transmitted through the idler arm circulator for each source was measured using an OSA. The transmitted spectra for both sources contained a narrow dip corresponding to the light reflected by the grating. By tuning the narrowband FBG in the idler arm of the PCF source, the central wavelength of the idler arm filtering of the two sources was matched to within 0.1 nm. When this spectral measurement was repeated several days later the same central wavelengths were measured for the two idler arm FBGs, indicating that the stress tuning of the gratings, described in Section 5.2, was stable over this period.

When the narrowband FBGs in the PCF source were adjusted to the peak signal and idler values, the measured coincidence count rate of the main coincidence peak was found to be 16.1 kC/s (without the inclusion of the 50:50 coupler at the source output). This measurement was made using maximum available pump power of 145 mW at the input end of the PCF, and a detection efficiency of 25%. The corresponding singles count rate in the signal arm was

245 kC/s and the accidentals peak count rate was measured to be 1.7 kC/s at this pump power level. The corresponding heralding fidelity and CAR were 23% and 8.5 respectively.

After changing the filtering to match the wavelengths to those of the PPLN source, the measured main coincidence peak was reduced to around 12.3 kC/s. Although adjusting the wavelength of the PCF source in this way led to a reduction in the four-fold coincidences between the sources, the stability of the PPLN source was improved. A stability measurement of the two-fold (idler and signal) coincidence count rates for each source is shown in Fig. 6.8.

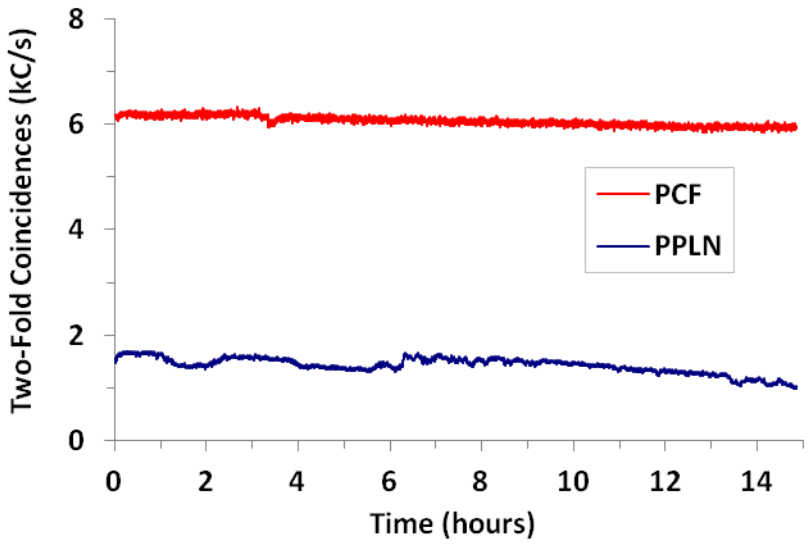

Figure 6.8: Measured count rates recorded by the two InGaAs detectors (shown in Fig. 6.6), over a period of 15 hours. The data sets from the two sources are labelled according to which photon source was used to provide the heralding trigger signal.

The two-fold count rates, shown Fig. 6.8, were measured simultaneously, using the arrangement shown in Fig. 6.6, which included the 50:50 coupler between the source outputs and the detectors. For this reason the measured two-fold coincidence count rates shown are only half the true source output. The presence of the coupler also meant that some of the measured two-fold coincidences would be due to coincident detections of a signal photon from one source and an uncorrelated idler photon from the other source, as idler photons from the both sources could arrive at either of the two InGaAs detectors in this arrangement. However, due to the relatively low probability of both sources generating a heralding signal on the same pulse of the pump laser, this contribution to the observed two-fold count rates was negligible.

6.4.4 Matching of the Photon Polarisation States

The final degree of freedom that needed to be matched for the two sources was the polarisation state of the heralded idler photons. As described in Section 5.6, for the PCF source each idler photon would be generated in the same initial polarisation state, with that polarisation then evolving deterministically during propagation through the rest of the fibre components, due to bending induced birefringence (see Section 2.1.4), before arriving at the 50:50 coupler. Similarly for the PPLN source, while the generated signal and idler were initially generated co-polarised with the pump their polarisation state would change during propagation to some other well defined but unknown polarisation state at the coupler.

In order to match the polarisation state of the two sources, an all-fibre linear polariser, based on a periodic double-helical core structure (*Thorlabs*, IFP1550SM-FC), was inserted between one of the output ports of the 50:50 coupler and the InGaAs detector that was triggered by the PCF photon source. The pump laser input to the PPLN source was blocked so that only idler photons from the PCF source would contribute to the detector counts. By adjusting the fibre polarisation controller at the output end of the fibre source before the 50:50 coupler it was possible to maximise and minimise the measured idler photon count rate, giving a measured polarisation extinction ratio of 8.5.

As stated in Chapter 5, the polarisation extinction with this same source was previously measured to be 27 when using the lower power (but otherwise similar) picosecond pump laser source. This was not investigated further, but may have been due to noise photons launched into the photon source or generated in the PCF by Raman scattering due to the higher pump power, which would not necessarily be co-polarised with the idler photons generated by FWM. As poor polarisation extinction would lead to a reduction in the expected HOM interference visibility, an additional fibre polarisation controller and fibre polariser were added to the output of the PCF source, just before the previous fibre polarisation controller, in order to purify the transmitted polarisation state. This change to the experimental setup is illustrated in Fig. 6.9. With the addition of this component the attainable polarisation extinction ratio was improved to more than 30. The insertion loss associated with this extra component was around 2 dB. After the photons passed through the first polariser (Pol 1), the second polarisation controller (FPC 2) was adjusted in order to minimise their transmission

through the second polariser (Pol 2) such that the photon polarisation state at this polariser was known to be linear (and orthogonal to the transmission axis of the polariser).

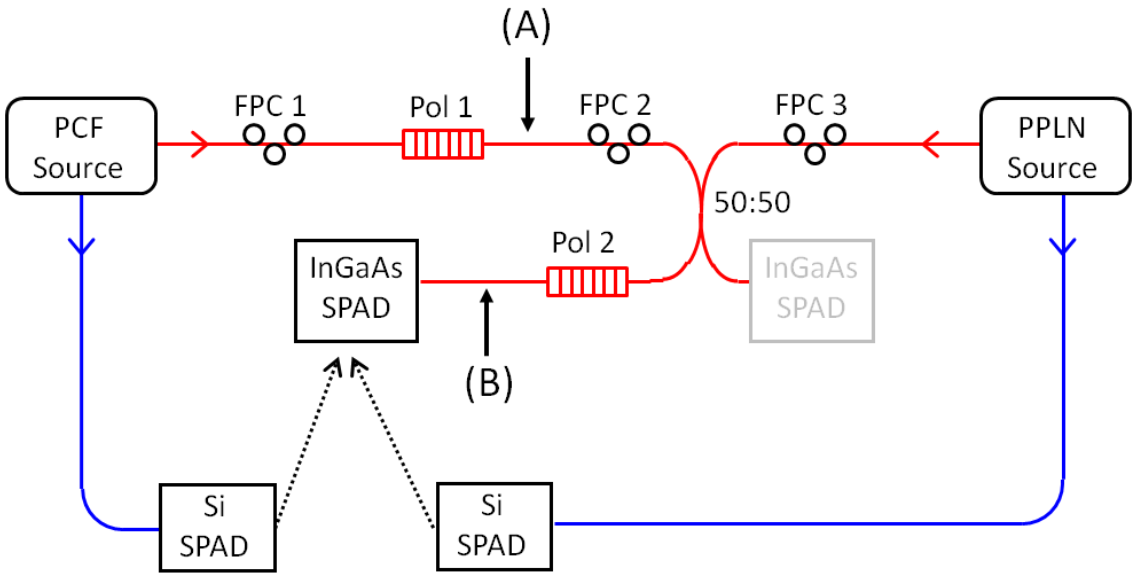

Figure 6.9: Schematic representation of the polarisation control setup used to match the polarisation state of photons from the two sources at the 50:50 coupler. FPC represent the fibre polarisation controllers and Pol are in-fibre polarisers. FPC 1 and 2 were adjusted in order to maximise the number of measured idler photons from the PCF source at position (A), and minimise the number at position (B).

After adjusting the polarisation state of the PCF source, the PPLN source output had to be matched to it. The laser output to the PCF source was blocked while on the PPLN side the laser beam was unblocked. The same InGaAs detector was used to detect the idler photons from the PPLN source (through the 50:50 coupler) so that the procedure could be done without changing the optical setup at all. The electronics set up was changed such that the InGaAs detector was triggered by the heralding signal from the PPLN source, with the electronic delay appropriately chosen to ensure the detector was active to coincide with the arrival of idler photons. The fibre polarisation controller in the PPLN source (FPC 3) was then also used to minimise the number of idler photons passing through the polariser (Pol 2). As the polarisation state of the idler photons at the polariser was then matched for the two sources, and both followed the same path from the coupler to the polariser, the polarisation state would also be matched at the interaction region of the coupler. Although the polarisation state at the coupler was most likely not linearly polarised, it only needed to be the same for both sources in order to observe interference. After matching the two sources the polariser

after the 50:50 coupler (Pol 2) was removed, taking care not to move any fibres before the coupler in the system, which could alter the polarisation state of the photons at the coupler.

6.4.5 Measurement of the HOM Dip

After matching the polarisation state and spectral filtering for the two sources, the position of the retroreflector was scanned whilst observing the four-fold coincidence count rate between the detectors using the FPGA coincidence counting electronics, described previously in Section 6.4.1. When the retroreflector position matched the arrival time of idler photons at the 50:50 coupler to within the coherence time of the single photon state this four-fold coincidence rate was expected to reduce due to the effect of HOM interference. The two-fold coincidence count rates of both sources were also recorded in order to check the stability of the output heralded photon count rates from both sources across the duration of the measurement.

The retroreflector was scanned over the identified range of interest from -30 mm to - 10 mm, with a step size of 1.5 mm (see Section 6.4.2). At each position the retroreflector had to be held for enough time to gather a representative of sample of the four-fold count rate at that point. The probability of obtaining a particular number of four-fold coincidences in a given time window can be obtained by the Poisson distribution (see Section 3.4.1). A characteristic property of this distribution is that the standard deviation of the measured number of counts in a given time window is equal to the square root of the mean number of counts expected in that time window.

For reliable photon counting statistics it is desirable to wait for long enough to measure at least 100 four-fold coincidences at points outside the dip, since this means that the average fluctuations in the measured count rate would be limited to 10% of the mean value. In the first instance, when searching for the position of the dip, measuring a sufficiently large number of four-fold coincidences is particularly important, as the visibility could potentially be low if photon states are not optimally matched, which could lead to the interference feature being obscured by the inherent statistical variations in the count rate. The relatively low two-fold coincidence count rates of the sources led to a four-fold coincidence count rate of around 2.5 C/min, meaning that at each data point it took around 40 minutes to obtain the required number of four-fold coincidences. Instead of waiting for this entire time at a single stage position before proceeding to the next, the data was acquired by running the stage scan

repeatedly, stopping for around 1 minute at each data point. The required statistics were achieved by summing the results at each data point from each individual short run. This avoided the potential problem of sections of the measurement being unusable if the four-fold count rate dropped due to problems with the stability of the sources. The HOM dip was observed to occur at a retroreflector position of -24.7 mm, close to the centre of the expected range. Once the HOM dip was located, the pump power was lowered for both sources in order to reduce the influence of noise photons on the background four-fold count rate and the dip measurement was repeated with a longer accumulation time at each data point. The results are shown in Fig. 6.10.

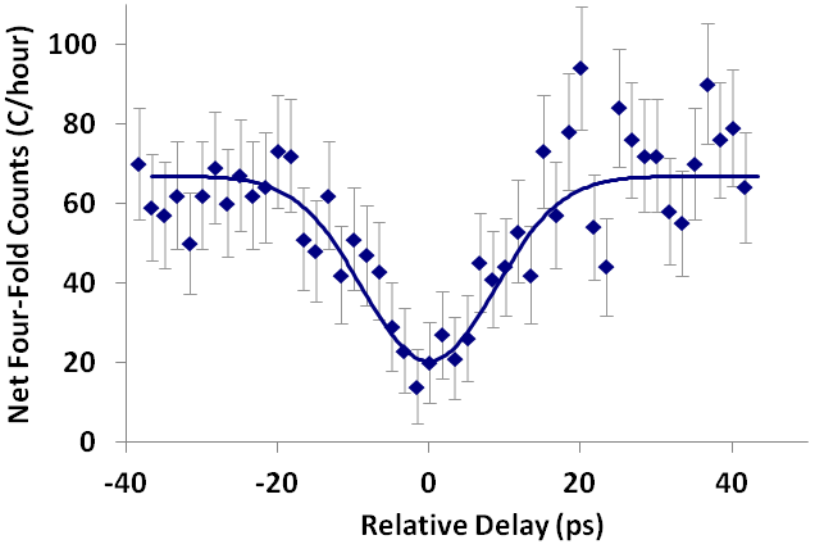

Figure 6.10: Net four-fold coincidence count rate for the two sources after subtracting the background four-fold count rate due to each source individually from the raw four-fold count data. The solid line shows a Gaussian fit.

The data shown in Fig. 6.10 was adjusted by subtracting the background four-fold coincidence count rates for both of the sources from the measured raw four-fold coincidences. These background count rates were measured by moving the retroreflector away from the position corresponding to the dip minima and monitoring the detected four-fold coincidence count rate with the idler output from each source blocked in turn. Ideally this background count rate should be zero for single photon inputs to the coupler. However, measured background four-fold counts were present, suggesting that either the probability of multiple pair generation events in the sources was high, or that some other form of noise, such as leaked pump or Raman-shifted pump light was reaching the detectors. The measured raw four-fold

count rate away from the dip position was around 90 per hour. With the PPLN source output blocked, the measured four-fold coincidence count rate was around 14 per hour, while with the PCF source blocked the count rate was 4 per hour. With both sources blocked, no four-fold coincidences were observed within a one hour period. Further work will be required to establish the cause of these relatively high background count rates. If it is due to insufficient rejection of the pump or Raman-shifted light then the visibility of the measured HOM dip could potentially be improved by the addition of extra filtering at these wavelengths.

The net four-fold coincidence data was fitted with a Gaussian curve of the form shown in Eq. (3.22). The measured visibility according to the fitting parameters was found to be 70%. The visibility of the raw four-fold coincidences data without subtraction of the background rates was 55%. These results both demonstrate HOM interference with a visibility beyond the classical limit of 50%. Although the measured visibility of the HOM dip was lower than in many experiments involving interference between photons from identical sources, which commonly achieve >85% (see Section 6.2), it should be possible to improve it further by identifying and reducing any remaining distinguishability between the photons. One possible limiting factor for the visibility could be the degree of walk-off of the photon pairs from the pump during generation that is still remaining in the system. While the level of walk-off in the PPLN waveguide requires further investigation, the temporal purity of the PCF source could be immediately improved by further reducing the PCF length.

Another possibility for improving the visibility of the HOM would be to reduce any remaining spectral distinguishability of the sources by sharing a single narrowband idler FBG between them, thus ensuring the filtering was matched. This could be implemented by splicing the second port of the two idler arm circulators in the sources to either end of a single grating. As photons rejected by the filtering of one source would be input into the other source in this arrangement, the optical delay in the idler arms of the two sources would need to be carefully selected such that only the idler photons from one of the sources were passing through the narrowband FBG at any given time.

As seen from Fig. 6.10, the FWHM width of the HOM dip, and therefore the coherence length of the single photons was 20 ps. This was broader than expected given the pulse duration of the pump laser and the chosen spectral filtering. This may indicate that the spectral filtering used was actually narrower than required to observe the interference feature, increasing the coherence length of the photons. This could also be due to the relatively large error in the

measured four-fold count rate in this data. If the visibility of the interference feature could be improved it should allow for a more accurate measurement of the dip width. An increase in the dip width beyond the range defined by the spectral filtering is also consistent with temporal broadening of the heralded photons; again suggesting that walk-off in one or both of the sources may be a limiting factor of the demonstrated visibility.

6.5 Conclusion

This chapter has described an experiment used to observe non-classical HOM interference between heralded single photons from two very different types of source, the all fibre source described previously in Chapter 5, and a source based on the generation of correlated signal and idler pairs by parametric down-conversion in a PPLN waveguide. In order to realise synchronised pumping of the two sources, a dual output 1064 nm fibre laser was used, with the input power for the PPLN source frequency doubled in a $\chi^{(2)}$ nonlinear crystal in order to match the source output wavelengths to that of the fibre-based system.

The higher pump power of this laser meant the photon source was no longer limited by the available pump power and could be operated close to the optimal CAR of 10. With 145 mW of pump power at the input of the source, heralded idler photons were detected at a rate of 16.1 kC/s with a 25% detector efficiency, corresponding to 6.4×10^4 heralded photons per second output from the source. The detected two-fold coincidence count rate for the source was also measured over a period of 15 hours and was seen to be very stable, with short term variations of less than 1% of the average value over 10 second intervals and a long term decline in the average measured count rate of only 1% over the entire measurement.

In order to observe HOM interference between the PCF and PPLN-based sources, the spectral state of the output photons was carefully matched through tuning of the narrowband FBG filters. The polarisation state of the photons was also adjusted to be matched at the point of interaction between the photons at a fused-fibre coupler. Upon scanning the position of a moveable retroreflector, in order to alter the arrival time of photons from the PCF source at the coupler, a dip was observed in the measured four-fold coincidence count rate between the sources, due to HOM interference. The raw visibility of the observed interference feature was 55%. Subtracting the background four-fold count rate due to each source individually, yielded a net visibility of 70%. Future work will aim to improve this visibility further by more closely matching the properties of the photons from the two sources and investigating the

nature of the background four-fold count rates from the sources with the aim of improving the raw measured visibility.

As discussed in Section 3.3 HOM interference is dependent on indistinguishability of the involved photons. The observation of this effect therefore establishes the purity of the single photon states generated by the PCF-based source. Furthermore, this demonstration that these types of source can be engineered to generate compatible photons for interaction may enable future integration of different varieties of photon sources within a single QI system.

Chapter 7

Birefringent PCF for Naturally Narrowband Photon Generation

The goal of the work presented throughout this thesis has been to produce a fibre-based source of photons with an output approaching as closely as possible to that of a pure photon state. The technique adopted in Chapter 5, of spectrally filtering the photons generated by FWM and selecting only a subsection of the ensemble of photon states generated across the FWM gain bandwidth, mirrors the approach taken historically in photon sources based on PDC in $\chi^{(2)}$ crystals.

In addition to the co-polarised FWM process used thus far to generate correlated photon pairs, FWM can also occur in a cross-polarised configuration (see Section 2.2.6), where the generated pair photons are polarised orthogonally to the pump beam. In a birefringent PCF the properties of the structure can be tailored to allow for the generation of idler photons with a naturally narrow bandwidth by XFWM. This can make the pair generation process more pump power efficient, since none of the generated photon pairs need be discarded through spectral filtering. Furthermore, under these conditions the spectral correlations that are normally present between the generated signal and idler photons are removed and the idler photons can be left in a pure quantum state after heralding (see Section 3.5.5). This makes them suitable for observing high visibility quantum interference or as a resource for quantum information processing applications.

This chapter describes the design and fabrication of birefringent PCF suitable for generating narrowband photons at 1550 nm, for use as a source of heralded single photons. Section 7.1 describes the factors affecting the choice of design parameters in order to generate an appropriate output photon state, as well summarising some of the previously demonstrated experiments on naturally narrowband photon generation. In Section 7.2 a numerical modelling technique is used to predict the required fibre geometry to achieve narrowband photon generation. A manufactured PCF matching these parameters is described in Section 7.3. This PCF was then characterised, with a spectral measurement of the signal and idler peaks in Section 7.4, and a measurement of the group delay properties of the fibre is discussed in Section 7.5.

7.1 Design Considerations for a Birefringent PCF

The operation of the fibre-based photon source described previously in Chapter 5 was based on co-polarised FWM in a nominally non-birefringent PCF. Due to the broadband nature of the FWM gain by which photon pairs are produced, narrowband filtering is necessary to remove the spectral correlation between signal and idler photons. The high measured heralded photon count rates and low optical losses of the implemented fibre filtering for the device demonstrated that such a source can prove useful in quantum information applications. However, one drawback for the system was the relatively high pump power requirements associated with the narrowband filtering. This is because the tight spectral filtering causes the majority of the generated photon pairs to be discarded, as seen in Fig. 7.1, reducing the brightness of the source. This then has to be compensated by increasing the pump power.

As described in Section 2.2.6, in birefringent fibre it is possible to generate signal and idler pairs at the desired wavelengths of 810 nm and 1550 nm using XFWM, where the modal index contrast between the two axes of the fibre required for phase-matching can be controlled by the level of asymmetry in the fibre structure. In addition, by appropriately matching the group velocity of the chosen pump wavelength to that of either the idler or signal photons the bandwidth of the generated photons can be greatly reduced. Such a fibre could be a useful replacement for PCF-B in the all-fibre photon source, as increasing the proportion of the generated photons falling within the filtering bandwidth should reduce the pump power requirements, even after accounting for the reduced efficiency of the cross-polarised nonlinear process (see Section 2.2.6). If this group velocity matching is sufficiently accurate

then the generated signal and idler photons will be spectrally uncorrelated, giving a pure output heralded photon state even in the absence of narrowband filtering. This would allow the circulators used for spectral filtering to be removed from the source, further reducing the loss and improving the source brightness.

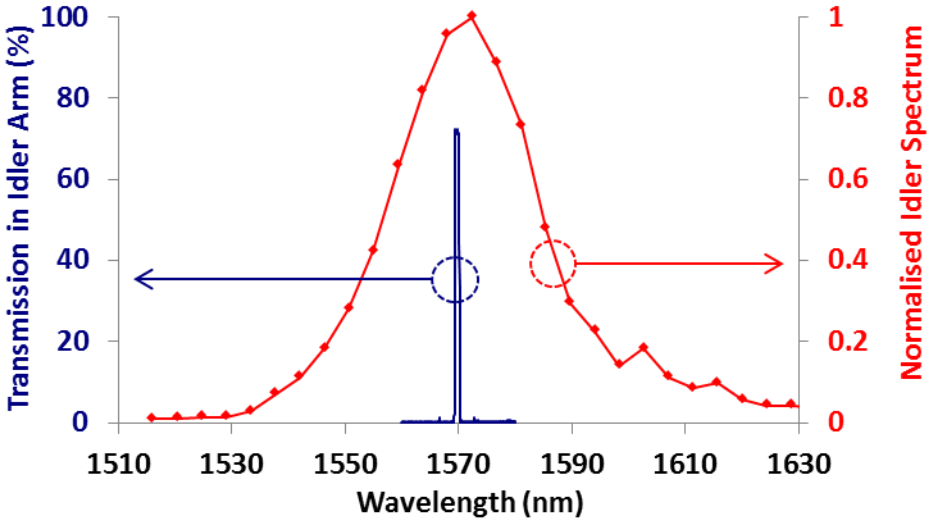

Figure 7.1: Comparison between the bandwidth of the previously measured idler peak (shown in Fig. 4.5(c)) and the transmission profile of the idler arm for the heralded photon source described in Chapter 5.

There are two possible approaches to generating a naturally narrowband, factorable two-photon state by XFWM, as described in Section 3.5.5. The first approach relies on counterbalancing the spectral correlation of the generated photon pair introduced by the constraint of energy matching to the pump wavelength with the contribution to the correlation from the phase-matching conditions of the fibre. This technique has been experimentally demonstrated, for the case of FWM in birefringent fibre [172]. However, this technique is not well suited to use in the picosecond pulsed pumping regime, as dictated by the choice of pump laser here. This is because for femtosecond pumping with a Ti:Sapphire, as was used in the previous demonstrations, the spectral bandwidth of the laser can be ~10 nm. This allows the laser pulse duration to be easily increased through low loss spectral filtering in order to optimise the laser pulse properties to obtain the desired factorable state for a given crystal or fibre with fixed phase-matching conditions. In the case of picosecond pulses the spectral bandwidth of the pulses is far narrower, making such tuning of the laser pulse properties technically challenging.

The alternative approach for generating spectrally uncorrelated signal and idler photons is to match the group velocity of either the signal or idler to that of the pump pulse. This corresponds to pump wavelengths on the phase-matching diagram where the gradient of either the idler or signal wavelength curve is zero respectively. Generation of spectrally uncorrelated pairs has been demonstrated experimentally, by our group and others, using this approach.

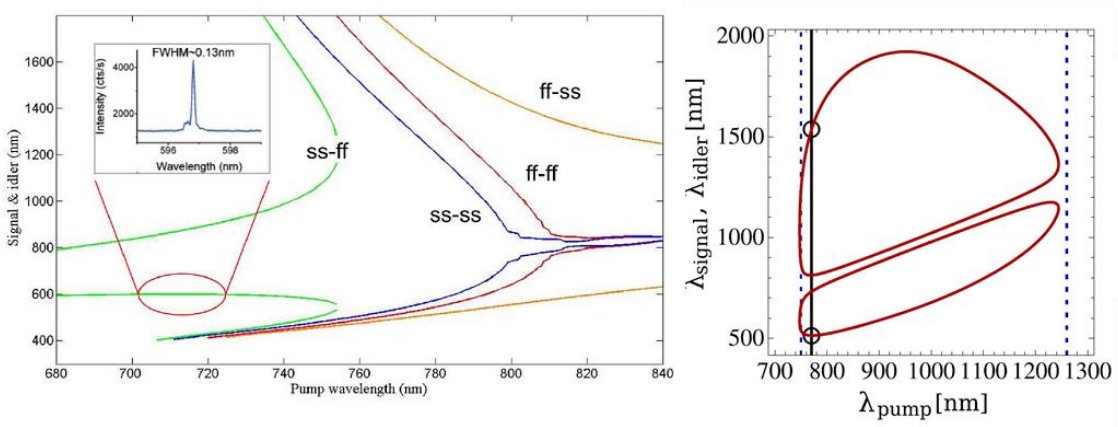

(a) (b)

Figure 7.2: (a) Phase-matching diagram for a birefringent PCF designed for the generation of naturally narrowband signal photons pumping in the normal dispersion region of a PCF (Image from [173]); (b) Phase-matching diagram demonstrating the generation of pure state idler photons in a non-birefringent PCF. The dashed lines show the ZDWs of the fibre (Image from [174]).

In birefringent PCF, naturally narrowband signal photons with a wavelength of 597 nm were generated from a 705 nm Ti:Sapphire laser [173] by taking advantage of the zero-gradient point of the signal phase-matching curve in the normal dispersion regime of the fibre when pumping on the slow axis of the fibre and generating photon pairs through XFWM on the fast axis (see Fig. 7.2(a)). In this case the relatively low birefringence of the fibre meant that generated signal and idler wavelengths were relatively closely spaced to the pump, meaning that Raman-shifted pump light could be a problematic source of noise. The significant shift in the ZDW of the PCF that would be required to generate 1550 nm idler photons from a 1064 nm pump makes this configuration of XFWM an unattractive option for the work in this thesis. Spectrally uncorrelated photon pairs have also been demonstrated with an idler wavelength at 1542 nm [174]. In this case the fibre was non-birefringent and the phase-matching for FWM relied on the zero gradient point for the signal wavelength on the outside edge of the phase-matching curves in the anomalous dispersion regime of the fibre

(see Fig. 7.2(b)). Again, pumping in this case was with a Ti:Sapphire laser at 771 nm, which would mean a significant shift in fibre ZDW would be required to take advantage of this phase-matching point with a 1064 nm fibre laser. While the signal photon at 514 nm was narrowband in this case, the steep gradient of the idler phase-matching conditions at this point would lead to a heralded idler photon with a broad bandwidth. If this was used as a single photon source for transmission of heralded single photons across telecoms networks, this broad bandwidth could lead to problems due to the dispersion of the transmission fibre.

In order to meet the requirements of a 1550 nm narrowband idler generated from a 1064 nm pump laser, a birefringent PCF was designed to be pumped on the fast axis of the fibre and generate signal and idler pair photons on the slow axis of the fibre. The fibre was designed such that at the 1064 nm pump wavelength, the phase-matching curve for the idler wavelength was at a minimum, corresponding to the point at which the group velocity of the signal wavelength on the slow axis of the fibre was matched to the group velocity of the pump wavelength on the fast axis. This would lead to a naturally narrowband idler, as the signal photon would be highly localised in time and hence posses all of the uncertainty in frequency of the photon pair.

Further improvement in the pump power requirements for XFWM may also be possible due to the effect of group velocity matching of the pump with the generated signal photons. In the case of co-polarised FWM, the requirement of generating the heralded single photon in pure temporal state (see Section 3.5.3) limits the maximum possible PCF length that can be used in any experiment due to the effect of pulse walk-off (see Section 2.2.7). For XFWM in the configuration described, the signal photons will not walk-off from the pump pulse. As the PCF length is increased, the temporal coherence length of the heralded idler photons is expected to increase, with an associated reduction in the spectral bandwidth, such that they remain in a pure state. The theoretical maximum visibility for quantum interference that such photons are expected to exhibit actually improves as the PCF length is increased [175]. As the gain for FWM increases with the square of the interaction length in the low gain limit (see Section 2.2.5), and the allowable PCF length for interaction is no longer limited, in principle the required laser power could be further reduced by using a long length of PCF. However, previous experimental studies (using PCF produced at the University of Bath) showed that changes in the phase-matching conditions along the fibre, due to non-uniformity introduced in the manufacturing process, limited the maximum useable length to around 1 m [173]. In that

case the birefringence required to achieve phase-matching was relatively small, in contrast to the PCF proposed here where the required birefringence is much larger in order to generate widely separated signal and idler wavelengths. This may mean that the phase-matching conditions for this fibre are less susceptible to the small scale fluctuations in the fibre geometry that limited the maximum useable lengths of fibre in previous experiments [55].

7.2 Modelling of the Phase-Matching Conditions for XFWM

The PCF structure that was chosen for XFWM was a solid core fibre with a hexagonal array of air holes forming the cladding, similar to PCF-B described in Section 4.1. The necessary birefringence for satisfying the phase-matching requirements for XFWM was provided by enlarging two of the cladding holes, one on either side of the core. This resulted in an asymmetrical PCF structure with an elliptic core shape. Numerical modelling was used in order to determine the parameters for the structure that would be required in order to generate naturally narrowband idler photons at a wavelength of 1550 nm from a 1064 nm pump laser.

Previous work on birefringent fibres designed for XFWM (relating to the phase-matching plot shown in Fig. 7.2(a)), provided a starting point for the fibre parameters from which to work. There are three important PCF parameters that will affect the XFWM process, the pitch Λ, the ratio of the cladding hole diameter relative to the pitch d/Λ, and the ratio of the diameter of the enlarged holes around the core relative to the other cladding holes D/d. Control of these parameters allowed the wavelengths of the generated signal and idler to be selected, whilst simultaneously matching the group velocity at the signal wavelength on the slow axis of the fibre to that of the pump beam on the fast axis of the fibre to produce spectrally uncorrelated photon pairs (see Section 3.5.5). Reducing the PCF core size (by reducing the pitch) or increasing the fibre air filling fraction (by increasing d/Λ) will both result in the ZDW of the fibre being shifted to shorter wavelengths, along with the optimum wavelength required for pumping. The required cladding structure for XFWM with pumping at 1064 nm was known to lie somewhere between that of PCF-B, with a ZDW of 1086 nm and a d/Λ of 0.33, and that of the PCF shown in Fig. 7.2(a) with a d/Λ value of 0.75, where the required pump wavelength for a narrowband idler was around 850 nm. In order to reduce the size of the parameter space that needed to be investigated by modelling, the diameter of the cladding holes was kept constant at 1.2 µm. The pitch was varied in order to adjust d/Λ within the required range to change the optimum pump wavelength required for narrowband photon generation.

While changes in the value of d/Λ were expected to shift the optimum pump wavelength position, it was not expected to produce significant changes in the wavelength of the phase-matched idler when pumping close to minima of the phase-matching curve. However, the strength of the birefringence (related to the diameter of the enlarged holes around the core, D) was expected to strongly effect the idler wavelength though its inclusion in the δn term in the phase-matching conditions given by Eq. (2.67). As it was not obvious prior to the modelling to what extent the strength of the birefringence would influence the ZDW, or whether changes in d/Λ would alter the generated idler wavelength, the study had to proceed in an iterative fashion. First the value of d/Λ was fixed at 0.4 while phase-matching curves were calculated for D/d in the range of 1 - 2.5. The value of D/d giving an idler wavelength closest to the required value of 1550 nm was then kept fixed while d/Λ was varied in the range 0.4 - 0.5 to find the optimum position for the pump wavelength. This process was repeated several times, updating the value of the fixed parameter based on the previous results until both the idler wavelength and optimum pump wavelength were closely matched to their target values.

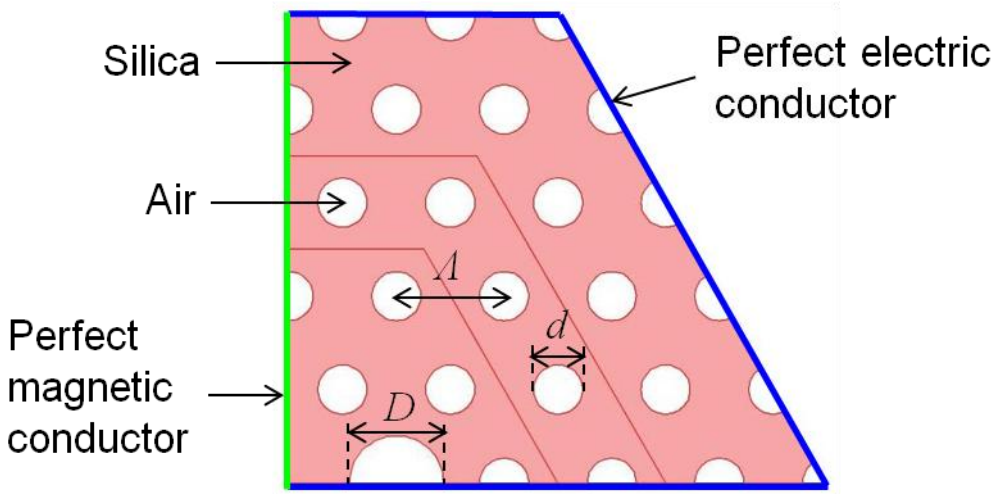

Figure 7.3: Diagram showing the modelled PCF structure. The modelling parameters and boundary conditions are also shown.

The numerical modelling study was conducted using commercial finite element analysis software (COMSOL Multiphysics). A matlab script was used to control COMSOL so that different PCF structures could quickly be defined and evaluated, simply by inputting values for the parameters of the structure, Λ, d/Λ and D/d. Due to the symmetry of the PCF it was only necessary to model one quarter of the total structure, reducing the required processing time.

The modelled area of the structure, shown in Fig. 7.3, contained 5 rings of air holes and one of the two enlarged air holes around the core. The core region of the PCF was in the lower left-hand corner of the image, with the centre of the fibre corresponding to the right-angled vertex of the simulation boundary.

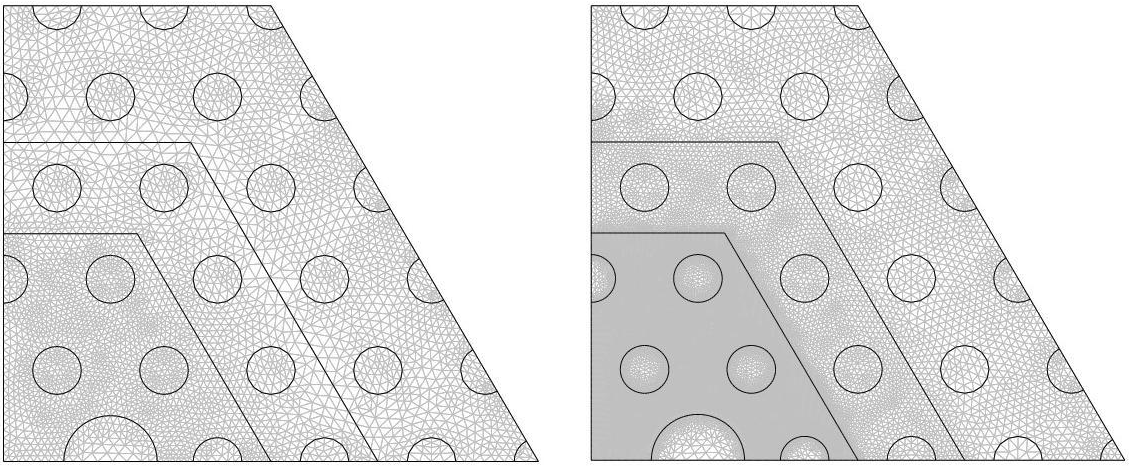

(a) (b)

Figure 7.4: Image showing the meshing used for the finite element analysis: (a) at 2 µm; and (b) at 600 nm.

The refractive index of the air hole regions was defined to be equal to 1, while for the silica glass regions the refractive index was dependent on the wavelength chosen for the simulation, defined by the Sellmeier equation (Eq. (2.16)). Automatic meshing was used to divide the structure into the small triangular elements required for finite element analysis, with the value of the electric field at each intersection between these regions adjusted by the program in order to find solutions for the total electric field distribution in the structure satisfying Maxwell's equations (see Fig. 7.4). The number of elements in the mesh varied with the wavelength under consideration, from 5×10^4 elements at 2 µm up to 2×10^5 elements at 600 nm. The program automatically adjusted the size of the triangular elements, giving a higher density of elements in areas close to silica-air boundaries. The density of elements was also selected to be higher in the region bounded by the first two rings of air holes and reduced further out into the cladding. This was expected to improve the accuracy of the simulation for a given number of elements, as the outer rings of cladding holes are not likely to strongly affect the properties of the fibre.

The boundary conditions for the two edges of the simulation corresponding to the outer region of the cladding were set as perfect electrical conductors. For the two inner edges

adjacent to the core one side was set to be a perfect electrical conductor and the other a perfect magnetic conductor. These boundary conditions ensured that the solution to this reduced structure was equivalent to that which would be obtained for the complete PCF structure. Furthermore, the perfect electric conductor constrained the solutions such that the component of the electric field parallel to the boundary must be zero on these edges. For physical guided core modes this means that at the outer cladding edges the total amplitude of the electric field must fall to zero, whilst in the core region the electric field must be polarised perpendicular to this boundary (this automatically satisfies the condition that the parallel component of the magnetic field on the other boundary adjacent to the core must be zero). Setting the boundary conditions adjacent to the core as shown in Fig. 7.3 therefore finds one of the two possible orthogonal polarisation modes of the birefringent structure. Each simulation was run twice, with the positions of the perfect electric and magnetic conduction boundaries adjacent to the core reversed in the second instance, in order to obtain results for the other polarisation mode.

For each of the two possible polarisation modes the program searched for spatial modes of the structure over a range of wavelengths from 600 nm to 2 µm. For each such calculated mode the electric field distribution was obtained, as well as the effective index of the mode. For all the PCF structures investigated (ranging in d/Λ from 0.4 to 0.5) the program was only able to find a single mode in which the electric field was confined to the core region, corresponding to the fundamental mode of the structure as shown in Fig. 7.5(a). The electric field distribution of all other calculated modes displayed areas of high electric field in the cladding region near to the simulation boundary, an example of which can be seen in Fig. 7.5(b). This is a result of the finite size of the simulation and these would not correspond to guided modes of a real structure. The simulations therefore suggest that these structures may be single mode at the wavelengths of interest, although the value of d/Λ is close to the anticipated cut-off for single-mode behaviour (see Section 2.1.3).

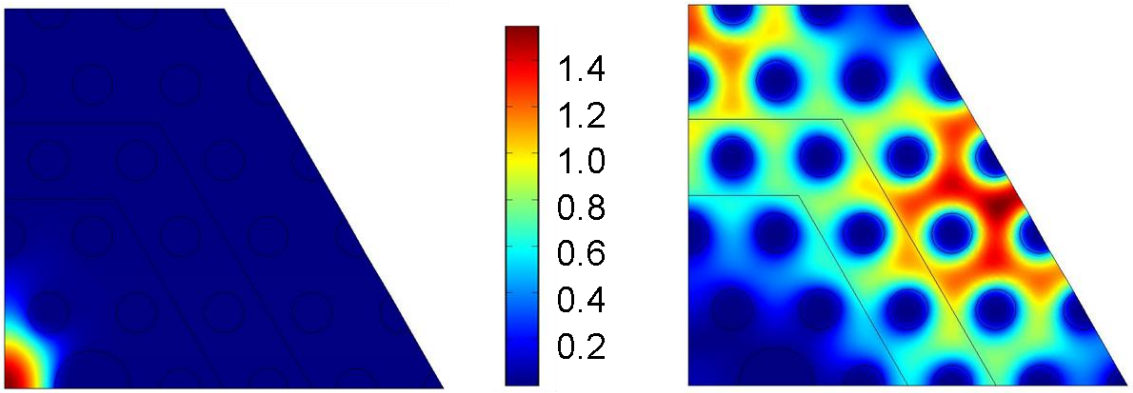

Figure 7.5: (a) Modelled electric field profile of the fundamental guided mode of the structure. (b) Unphysical modelled cladding mode.

The composite image in Fig. 7.6(a) shows the shape of the electric field profile for the fundamental mode polarised on the *s*-axis of the fibre. The highly elliptical shape of the core due to the enlarged cladding holes is clearly apparent. For the orthogonally polarised mode on the *f*-axis the electric field distribution appeared similar, as this is defined by the core shape. However, the group velocity dispersion for the two fibre axes, calculated from the effective mode indices determined by COMSOL (Fig. 7.6(b)), demonstrates the difference between the two modes due to the birefringence.

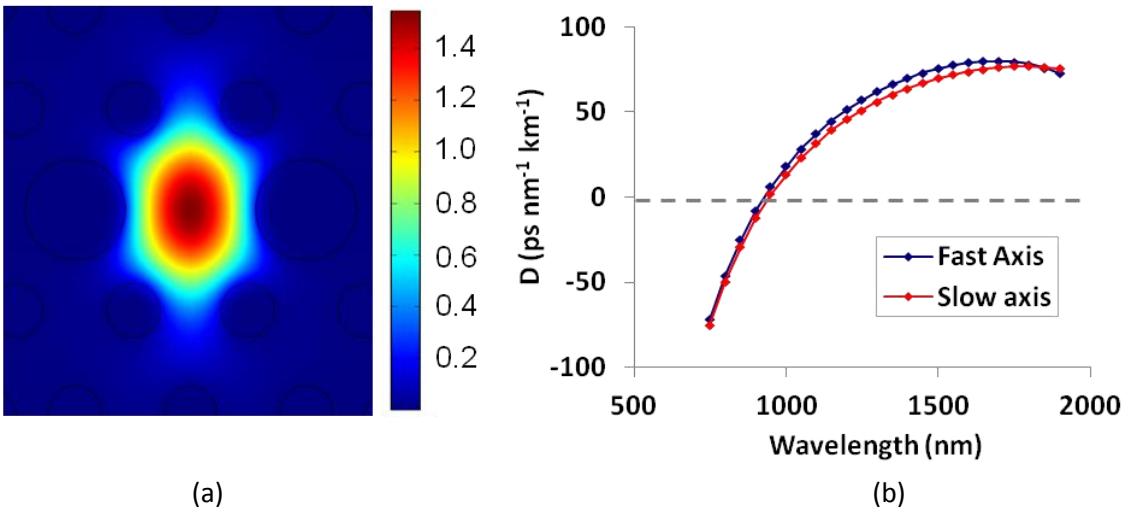

Figure 7.6: (a) Depiction of the fundamental mode of the whole PCF structure, polarised on the *s*-axis of the fibre. (b) Calculated plot of the dispersion parameter D for the vertical and horizontally polarised modes in this structure.

Using the calculated effective mode indices, the phase-matching curves for the XFWM and co-polarised FWM process could be calculated for each PCF structure of interest. For each

fibre this calculation was performed over a range of pump wavelengths from 800 nm to 1.15 µm by searching for pairs of signal and idler wavelengths (constrained by the energy matching condition, described in Eq. (2.48)), that minimised the phase-mismatch κ given by Eq. (2.49). The effective indices for the signal, idler and pump at each wavelength were taken from the interpolated curves of numerical data for either the fast or slow axis of the fibre depending on which of the phase-matching curves was being calculated.

Of primary interest from the calculated phase-matching plots was the minimum occurring for the idler wavelength for the XFWM process when pumping on the *f*-axis of the fibre (see Section 2.2.6). For each modelled PCF structure, the pump wavelength at which the minimum point occurred and the anticipated generated idler wavelength were automatically recorded.

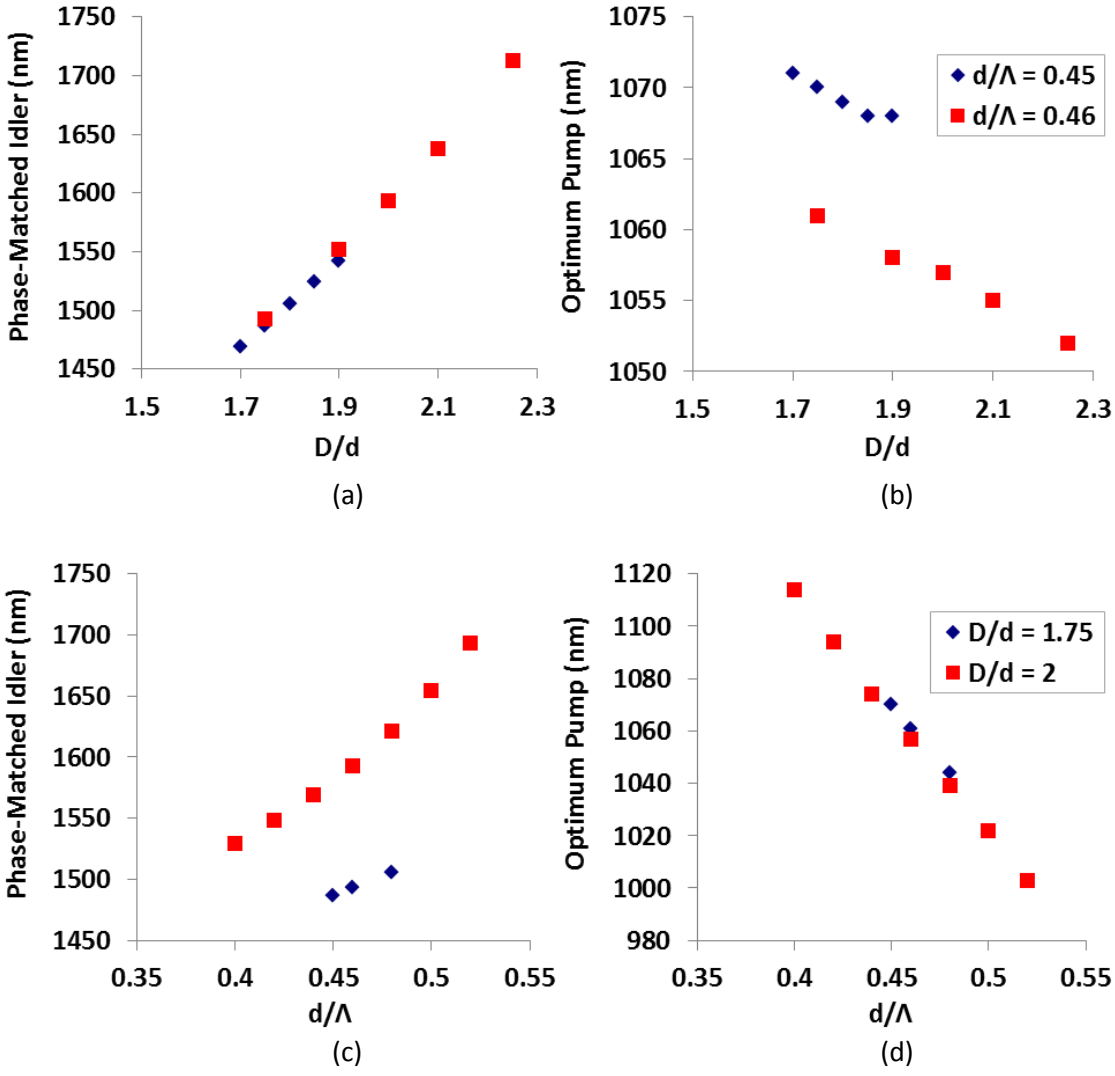

Figure 7.7: (a)-(d) Summary of the modelling results demonstrating how the narrowband phase-matched idler wavelength and the required pump wavelength vary with d/Λ and D/d.

The calculated phase-matching plots for XFWM in the *ff→ss* configuration, summarised in Fig. 7.7, showed that the idler wavelength could be varied over a range of at least 200 nm around the target wavelength of 1550 nm without the enlarged holes becoming too large and leaving narrow silica bridges between them and the adjacent cladding holes. The required pump wavelength of 1064 nm would be met by a value of d/Λ close to the cut-off for endlessly single-mode guidance (in non-birefringent structures). Fig. 7.7(d) demonstrates that the optimum pump wavelength required for a naturally narrowband idler was expected to be quite sensitive to variation in the air filling fraction of the fibre, with a shift of around 10 nm in the required pump wavelength for a change in d/Λ of 0.01. The variation in the idler wavelength with d/Λ and the change in the required pump wavelength with D/d were found to be less important. This suggested that the best approach to produce a fibre with the required properties would be to first manufacture a set of fibres with a fixed value for D in order to find the draw parameters required to meet the target value of d/Λ. It would then be possible to produce more fibre whilst varying the value of D in order to find the correct idler wavelength without changing the optimum pump wavelength. The modelling indicated that the ideal phase-matching conditions for a narrowband idler at 1550 nm pumped by a 1064 nm laser occurred at a pitch of 2.64 µm, d/Λ of 0.455 and D/d of 1.9, as shown in Fig. 7.8.

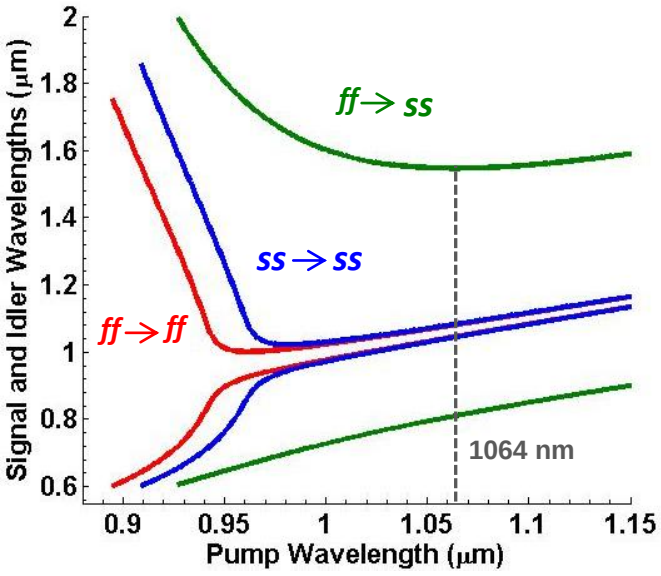

Figure 7.8: Calculated phase-matching plot for the optimum PCF structure.

7.3 Fabrication of Birefringent PCF

A series of birefringent PCFs were manufactured in order to try to match the fibre properties to those predicted by modelling for the required XFWM behaviour, described in Section 7.2. A single PCF preform was prepared using the stack and draw technique (see Section 2.3) from which all the subsequently produced fibres described in this chapter were derived. The stack consisted of five rings of glass capillaries in a hexagonal arrangement, the same as the modelled structure. The capillaries used to form the cladding holes had an outer diameter (OD) of 1.30 mm and an inner diameter (ID) of 0.67 mm. The solid core was formed by replacing the central capillary in the structure with a solid rod of 1.30 mm OD. Thinner walled capillaries with an OD of 1.30 mm and an ID of 1.21 mm were used for the two holes around the core that would be enlarged in the final fibre. The stack was placed in a jacketing tube of OD 26 mm and drawn down to canes of OD 4.2 mm on a fibre drawing tower. The OD of these capillaries and cane were chosen such that the OD of the final fibre would be ~140 µm for the required pitch after the structure was placed in a second jacketing layer of OD 10 mm and drawn to fibre.

When drawing PCF from the manufactured preforms there were several variables that needed to be optimised in order to achieve the desired fibre structure. The cladding hole size and size of the enlarged holes around the core were adjusted during the draw through two independent applied pressures P_{clad} and P_{core}, as described in Section 2.3. In addition the OD of the fibre (and hence the pitch of the PCF structure) could be controlled by adjusting the draw speed for the fibre coming off the fibre drawing tower. For the initial batch of fibres both P_{clad} and P_{core} were kept constant at values of 8.7 kPa and 8.5 kPa respectively. Fibres were drawn over a range of draw speeds from 20-30 m/min with a preform feed rate of 5mm/min, giving fibre OD in the range from 130-150 µm, as measured by the laser diameter monitor of the tower. Subsequent measurements of the produced fibres using a scanning electron microscope (SEM) were used to relate the OD of the fibre to the pitch of the structure as shown in Fig. 7.9(a).

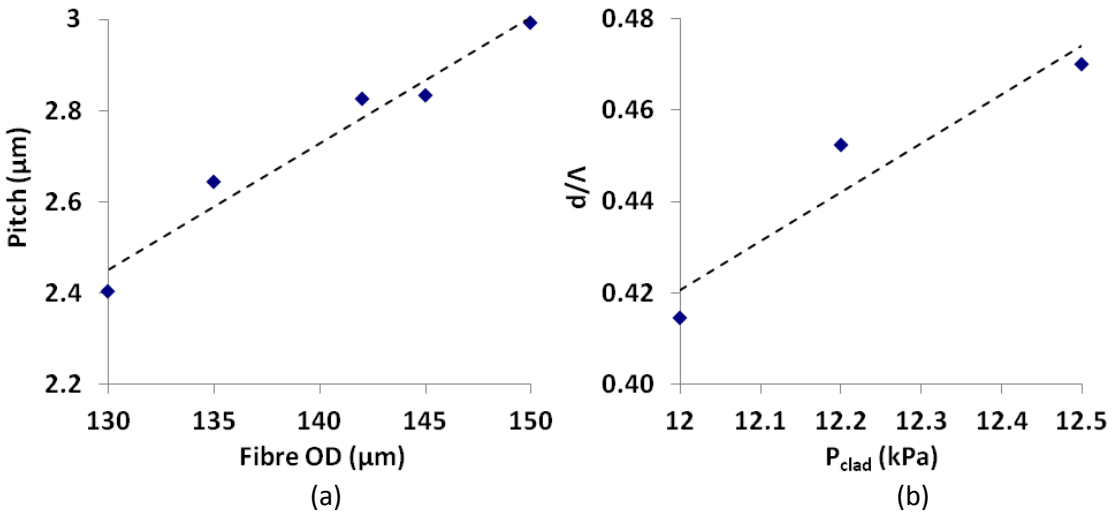

Figure 7.9: (a) Linear fit of the measured variation in the manufactured PCF pitch with outer diameter. (b) Linear fit of the measured variation in d/Λ at differing values of cladding pressure.

Another batch of fibres was produced with P_{clad} scanned and P_{core} fixed at 8 kPa, in order to locate the required value for d/Λ of 0.455 as shown in Fig. 7.9(b). The fibre OD was kept at 135 µm, which was found previously to give a PCF pitch close to the modelled value of 2.64 µm. Again, the manufactured fibres were investigated using an SEM in order to measure the ratio d/Λ. While the d/Λ parameter could be adjusted within the required range, some scatter was evident in the measured values, from the linear fit, as P_{clad} was changed. Given the sensitivity with which this parameter affected the optimum pump wavelength for XFWM in the modelling described in Section 7.2, this may make the ideal fibre difficult to achieve without the advantage of a tuneable laser source. The structure of the manufactured PCFs showed some non-uniformity of the holes in the cladding, which may also have contributed to the variation of d/Λ. Typical examples of the PCF structure are shown in Fig. 7.10. The non-uniformity was present in the preform, which meant that it could be seen in all the fibres that were produced. This non-uniformity was not expected to have a significant effect on the phase-matching conditions as the cladding holes and pitch were quite regular within the central region of the fibre where the electric field intensity was highest. One potential improvement that could be made in the future would be to produce a more uniform preform, which may lead to better control over d/Λ.

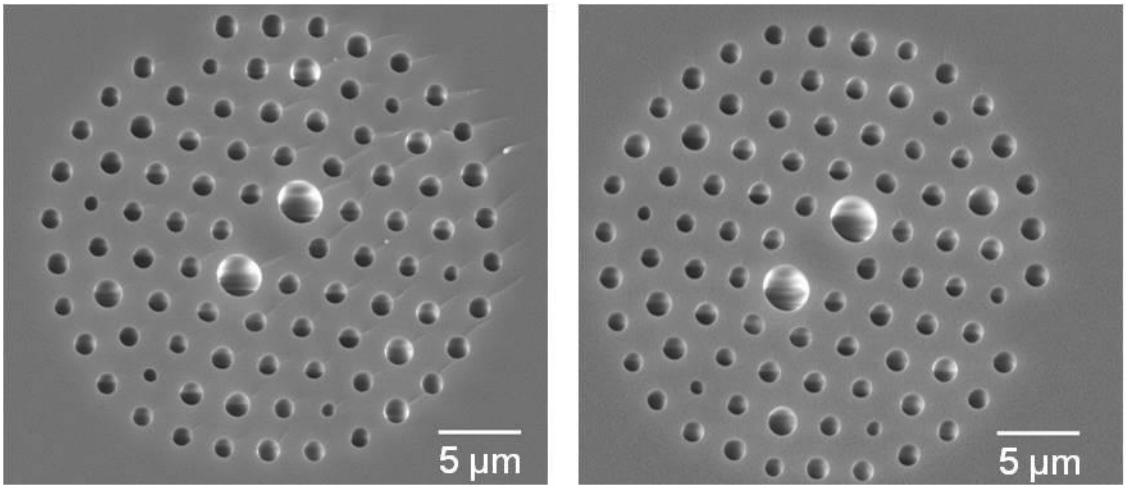

(a) (b)

Figure 7.10: SEM images of: (a) PCF-C; (b) PCF-D.

Once the manufacturing parameters required for the correct value of d/Λ were found, a final batch of fibres were produced by varying P_{core} for fixed values of P_{clad}. The relative size of the enlarged holes D/d, along with the other fibre parameters was measured by SEM, and is shown in Fig. 7.11(a). As expected, varying D did not significantly affect the rest of the cladding structure, which is evident in Fig. 7.11(b).

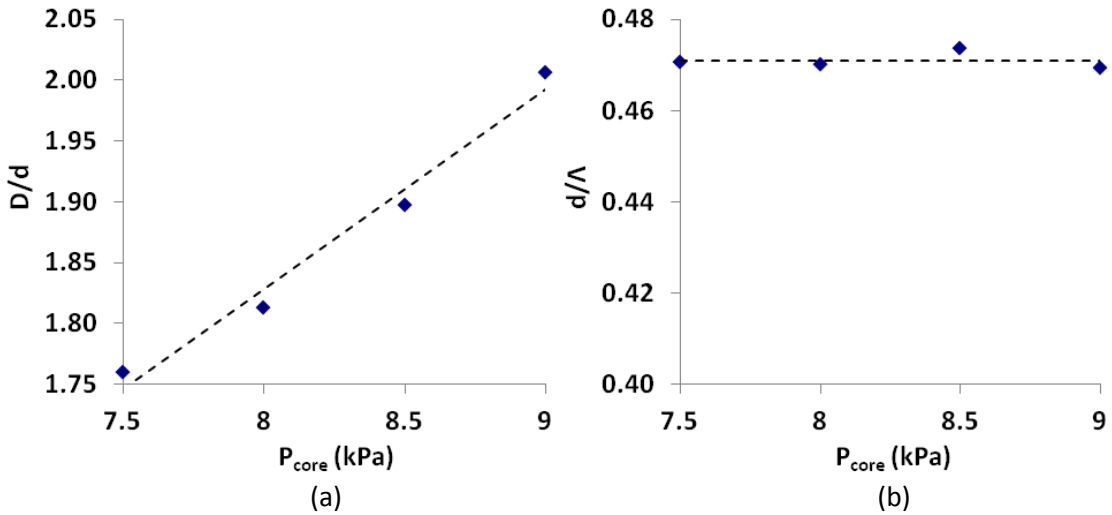

(a) (b)

Figure 7.11: (a) Linear fit of the measured variation in D/d at differing values of the pressure in the core; (b) Demonstration of the stability in the measured values of d/Λ for differing core pressures, at a constant cladding pressure.

7.4 Measurement of the XFWM Spectra

7.4.1 XFWM in the High Pump Power Regime

The nonlinear spectra generated from a 1064 nm pump was investigated for the manufactured PCFs in order to determine which of the fibres would generate photons through XFWM at the desired idler wavelength. The fibres with structures most closely matching the ideal modelled structure, found in Section 7.2, were tested in the high pump power regime to see if the XFWM peaks could be observed using an OSA. The experimental set up for this measurement is shown in Fig. 7.12.

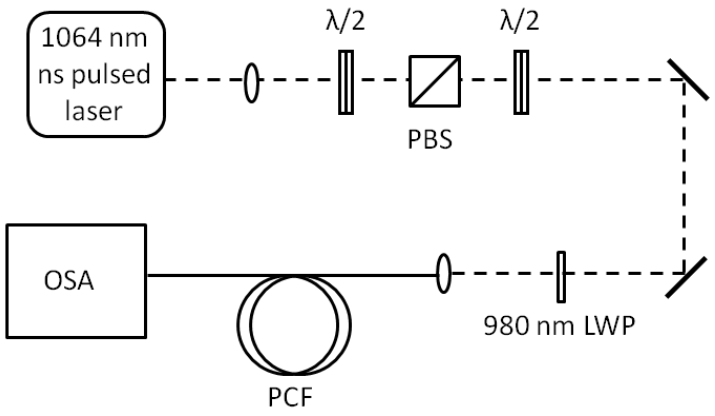

Figure 7.12: Experimental setup to measure the XFWM spectrum from a section of birefringent PCF. LWP is a long-wave pass filter with a cut-off at 980 nm.

The pump laser used was a the same low repetition rate, nanosecond-pulsed, microchip laser (*Teem Photonics*, NP-10820) used to verify the FWM peak wavelengths of PCF-B in Section 4.1. A half-wave plate and polarising beam-splitter (PBS) were used to adjust the pump power reaching the PCF and a second half-wave plate was used to adjust the polarisation state of the pump input into the PCF. As the XFWM process of interest was dependent on the pump power only on the *f*-axis of the PCF, by adjusting the pump polarisation the power in the signal and idler XFWM peaks could be maximised. A 980 nm LWP filter (*Semrock*, RazorEdge LP01-980RS) was added to filter the pump beam before launch to the PCF. Measured spectra taken without this filter showed a distinctive peak near 800 nm, which was unaffected by changes in the input pump polarisation state. Adding the filter removed this peak, showing that it was probably due to photons generated by the laser pump diode.

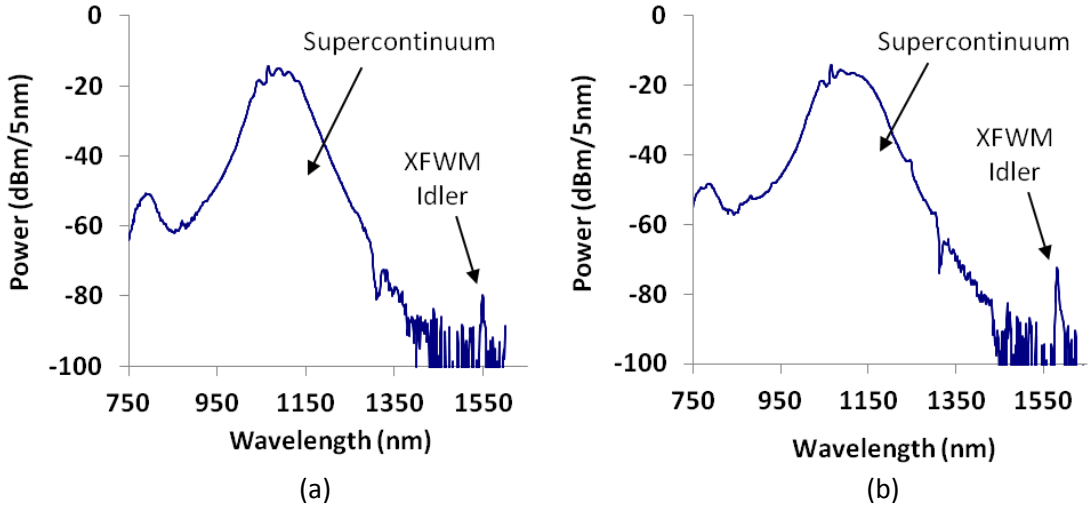

Figure 7.13: Measured output spectra from a nanosecond pulsed pump source: (a) for a 1 m section of PCF-C; (b) For 1 m of PCF-D.

1 m sections of the fabricated series of PCFs, described in Section 7.3, were tested, and PCF-C and PCF-D (SEM images shown in Fig. 7.10) generated spectral peaks near the idler wavelength of interest. The measured OSA spectra for these fibres with 40 mW of pump power incident on the fibres are shown in Fig. 7.13. This corresponded to 10 mW of pump power in the fibre. PCF-C was of interest for further study due to the generated idler wavelength of 1550 nm from a 1064 nm pump, matching the target specifications for the photon source described in Section 4.1. PCF-D was also of interest as the idler wavelength here of 1580 nm was close to the operating wavelength of the photon source discussed previously in Chapter 5, so this fibre could be a useful replacement for PCF-B in that source.

The separation of the central wavelengths of the idler peaks between PCF-C and PCF-D was around 30 nm, due to the difference in D/d for the two fibres. D/d was measured to be 2.03 for PCF-C and 2.16 for PCF-D. Even for the somewhat non-uniform preform used to produce these fibres, the value of D/d was observed to be well correlated with changes in the P_{core}. This suggests that in the future it may be possible to reliably produce more PCF with the generated idler wavelength accurate to within 10 nm of a desired value.

In addition to the XFWM idler peak of interest, the measured spectra in Fig. 7.13 also showed photons generated at other wavelengths over a wide range about the pump. This is due to supercontinuum generation on the orthogonal axis of the fibre (see Section 2.2.8).

In principle, as the photon pairs generated by XFWM were polarised orthogonally to the supercontinuum light it should be possible to extinguish the noise from the supercontinuum using a polariser. In practice, noise photons from the supercontinuum were still observed on the same axis as the XFWM peaks even after adding an additional PBS between the OSA and the output of the PCF. This was most likely due to the intense supercontinuum light being scattering onto the orthogonal fibre axis by Rayleigh scattering or cross-polarised Raman scattering. This meant that the signal peak was obscured and could not be observed by this method.

7.4.2 Measurement of XFWM Spectra in the Single Photon Regime

Since the supercontinuum generation is a cascaded process, its bandwidth will be reduced at lower pump powers. The wavelength of the XFWM peaks should not be significantly affected by pump power, so at low pump power the spectral overlap between the supercontinuum light and the XFWM peaks will be reduced. In order to observe both the signal and idler peaks without supercontinuum noise photons present, a spectral measurement was performed using the lower peak power, 1064 nm, picosecond pulsed fibre laser that was described previously in Section 4.1.

From the fibre source count rates observed in Chapter 4 and Chapter 5, for the case of co-polarised FWM using this laser, it was anticipated that the output power from XFWM in the PCFs would be too low to be observed using an OSA. In order to measure the XFWM spectra at the signal wavelength, the output light from the PCF was coupled into a free-space grating monochromator (*Optometrics*, DMC1-04) in order to implement narrowband spectral filtering, as shown in Fig. 7.14.

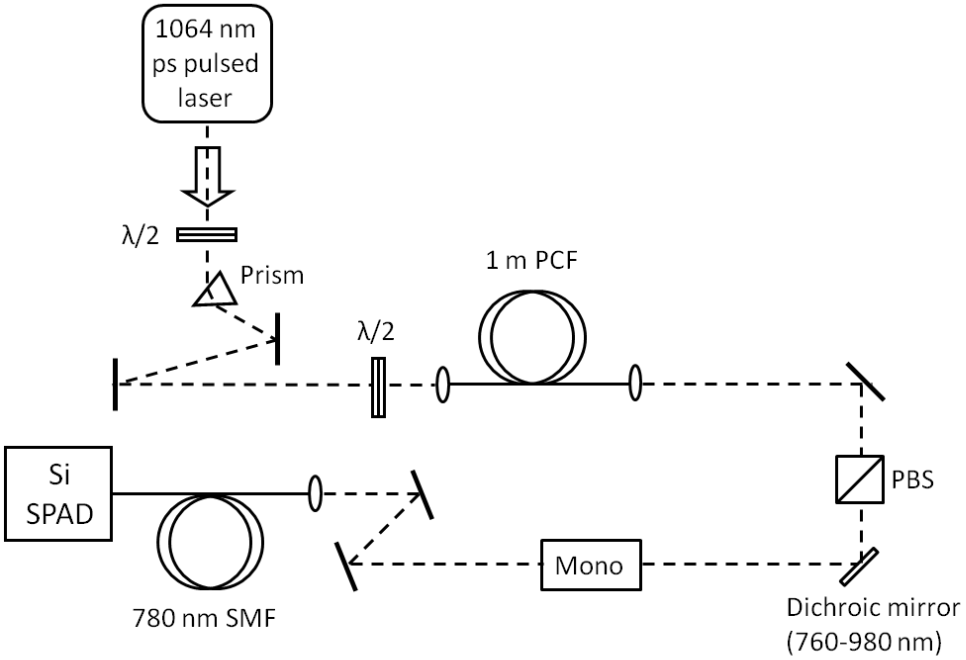

Figure 7.14: Experimental setup to measure the XFWM signal peak in the low power regime. Wavelength selectivity was provided by a grating monochromator.

The lens at the output end of the output end of the PCF was adjusted such that the output beam was focussed to its minimum spot size at the input slit of the monochromator. As the beam would then diverge inside the monochromator after the minima, this would ensure the beam spot size incident on the grating would be as large as possible in order to achieve a high resolution of filtering. The overall coupling efficiency from an input SMF, through the monochromator and into the output SMF fibre before the detector was measured to be 10% at 780 nm.

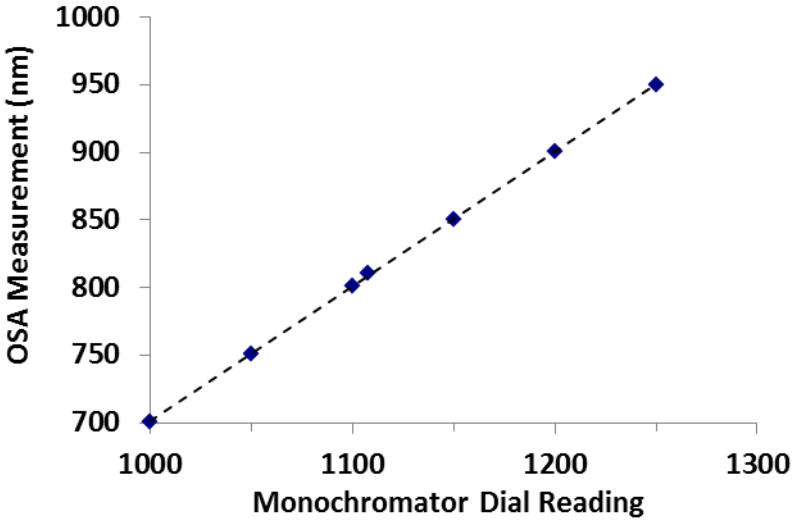

Figure 7.15: Calibration curve for the monochromator, comparing the dial reading to the true transmitted wavelength. The dashed line shows a linear fit.

As the transmitted wavelength reported by the monochromator dial reading was known to be unreliable, it first had to calibrated by launching supercontinuum light into the input of the PCF and measuring the wavelength at the output using an OSA. This calibration curve is shown in Fig. 7.15. Although the transmission wavelength reported by the monochromator dial showed a significant offset of 300 nm from the true transmitted wavelength, the relationship between them was linear and repeatable, allowing for this to be easily accounted for. This calibration measurement also showed that the resolution of the monochromator filtering set up was ~2 nm, as seen from the bandwidth of the transmitted light measured on the OSA.

As the XFWM process was only phase-matched for pump power launched on the fast axis of the PCF, generating signal and idler pairs on the slow axis, it was necessary to correctly orient the half-wave plate before the PCF and the PBS after it in order to observe the generated signal peak. In the far field, the light polarised along the direction of the short axis of the beam ellipse corresponds to the output of the slow axis of the PCF. This was therefore aligned with the marked transmission axis of the PBS in order to select light output on the desired fibre axis. In the first instance this was alignment was performed by eye by observing the shape of the of the beam profile using an infrared viewer. Once the PBS was set to approximately the right position, the half-wave plate before the PCF was adjusted in order to minimise the pump power transmitted through the PBS, monitored using a power meter. This minimum would occur when the pump was launched onto the fast axis as required for the XFWM. Small adjustments were also made to the polariser orientation in order to minimise the observed

transmitted pump power, taking care not to move the polariser too far from the previously determined position.

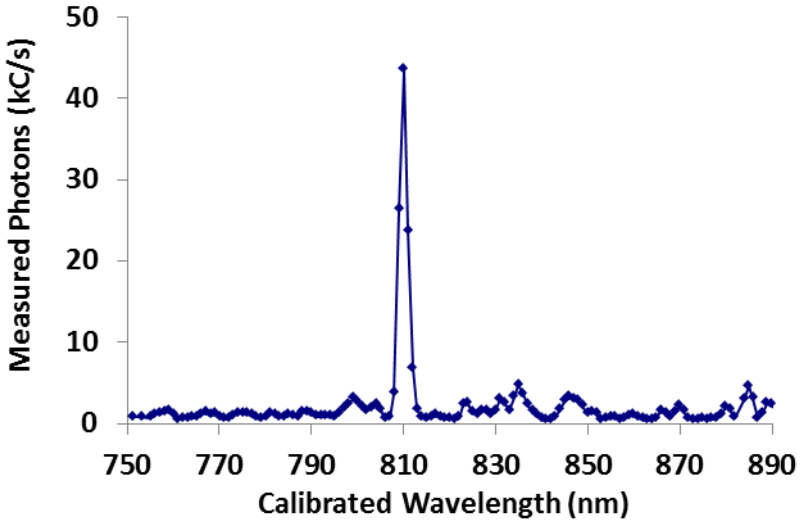

Figure 7.16: Measured output spectrum for PCF-C, showing low background noise over a broad spectral range.

Once the polarisation optics were correctly aligned the spectral measurement of the signal peak was performed by observing the filtered, fibre coupled output from the monochromator using a Si SPAD as the grating inside the monochromator was rotated. The measured single photon count rate from the SPAD over a range from 750 – 890 nm (after calibration) is shown in Fig. 7.16 for a 1 m section of PCF-C with a launched pump power of 27 mW. A narrow peak of 45 kC/s was seen at 810 nm, corresponding to the XFWM signal wavelength which was energy matched (for a 1064 nm pump) to the spectral feature at 1550 nm previously observed in Section 7.4.1 for this fibre. Away from this peak the background count level was around 1 kC/s, demonstrating that noise due to supercontinuum generation was negligible in the low power regime. As there were no notable spectral features observed in the measured wavelength range aside from the signal peak, the measurement was repeated over a narrower range, allowing more data points to be collected on the peak. The results of this measurement for both PCF-C and PCF-D are shown in Fig. 7.17. In both cases the FWHM bandwidth was 2 nm, showing that measurement was probably limited by the resolution of the monochromator filtering. However, even this represents a reduction from the FWHM signal bandwidth of 6 nm measured previously for the case of co-polarised FWM in PCF-B shown in Fig. 4.7(a).

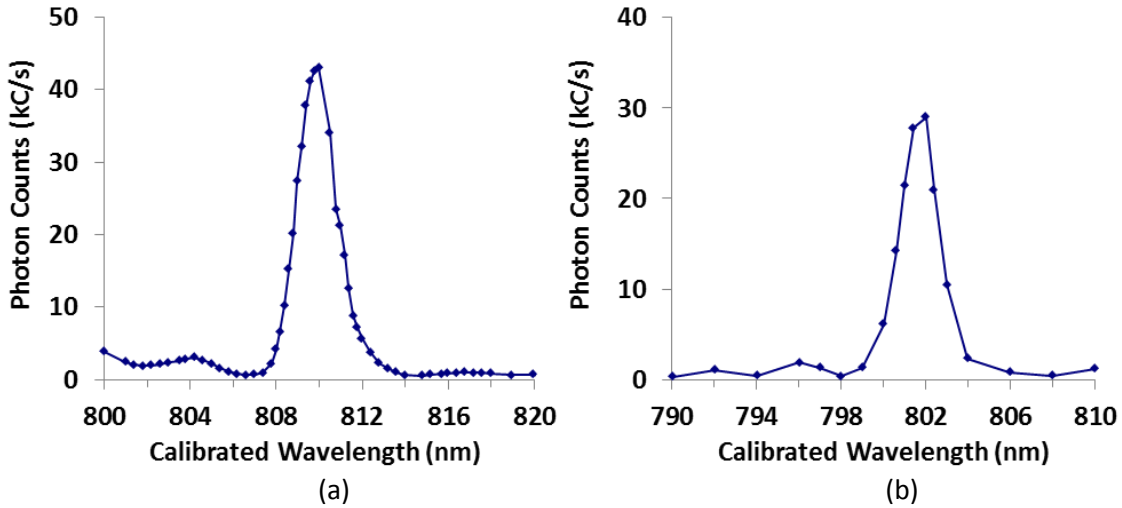

Figure 7.17: (a) Low power spectral measurement of PCF-C showing a signal peak at 810 nm; (b) Measured signal peak at 802 nm for PCF-D.

Both signal and idler bandwidths were expected to be reduced compared to those generated by co-polarised FWM in the normal dispersion region of a fibre at similar wavelengths. However, the idler was expected to be the more narrowband of the pair for the chosen phase-matching conditions in the anomalous dispersion region.

The procedure used to measure the idler bandwidth was similar to that used for the signal. However, instead of using the manually controlled monochromator, as shown in Fig. 7.14, an OSA with an optical output was used as a tuneable spectral filter. Idler photons transmitted though the PBS were collected in multimode fibre (MMF) and input to the OSA. The OSA was used on a double-pass monochromator setting with the filtering bandwidth set to 0.1 nm. This determined the resolution of the idler peak measurement. The OSA output was sent through another section of MMF to an InGaAs SPAD, which was triggered from the laser pulse train as described in Section 5.3.4. Due to the high detector dark count associated with the triggering rate of 4 MHz, and the low transmission efficiency of the OSA (~1%) the idler photons were unable to be observed using this pump laser without the benefit of heralding via the signal photons.

Although the idler peaks of PCF-C and PCF-D could not be seen when pumping with the low peak power, picosecond pulsed laser, they were able measured using this detection arrangement when pumping with the attenuated output from the higher power nanosecond pulsed microchip laser, described in Section 4.1. As the sensitivity of the detection provided by the InGaAs SPAD was much higher than that of the OSA in used in Section 4.1 the idler peaks

for the two PCFs could be clearly observed with an order of magnitude less pump power, with 4 mW incident on the PCF in each case. The measured spectra are shown in Fig. 7.18.

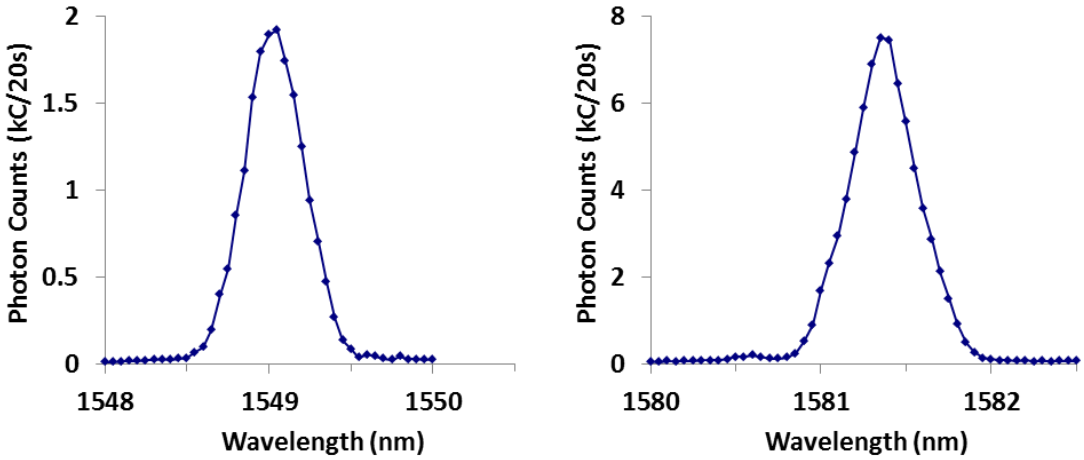

Figure 7.18: (a) Measured idler peak for PCF-C using a nanosecond pulsed pump source; (b) Measured idler peak for PCF-D.

The central wavelengths of the idler peaks were measured to be at 1549.0 nm for PCF-C, and 1581.4 nm for PCF-D for this laser, in agreement with the previously measured values found in Section 7.4.1. The measured FHWM bandwidth was 0.5 nm in both cases. The expected bandwidth for the generated idler photons will depend on the PCF length as well as the pump pulse duration and spectral bandwidth. In this instance, the laser pulse output was not time-bandwidth limited, which will significantly broaden the generated idler peaks compared to the same pump pulse duration in the bandwidth limited case. In order to demonstrate that the idler bandwidth was reduced in these birefringent PCFs, a 1 m section of PCF-B was also measured for comparison, using the same experimental setup shown here with a pump power of 4 mW.

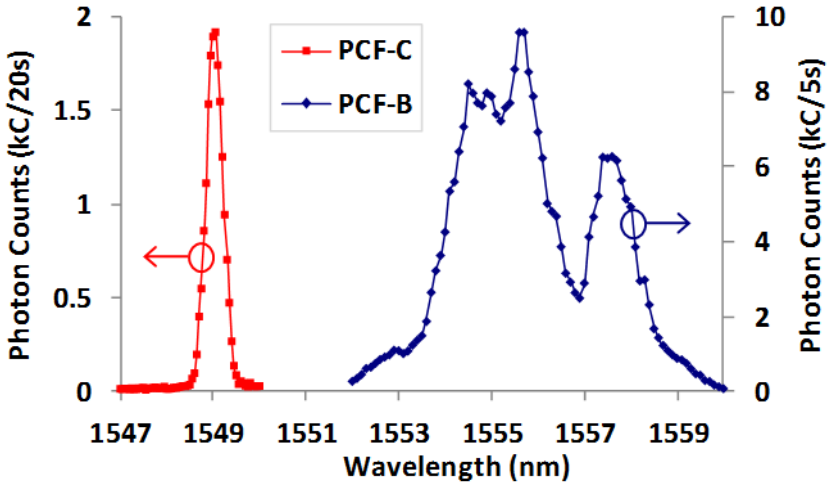

Figure 7.19: Measured idler peak for co-polarised FWM in a section of PCF-B. The fibre length was 1 m and the pump power was 4 mW. The previously measured idler spectrum for XFWM in PCF-C at the same pump power is also shown for comparison.

The FWHM of the spectral profile for the idler peak generated by co-polarised FWM was broader than that generated by XFWM by at least a factor of 5. Significant variations in the output power at different wavelength were also apparent for this PCF and the shape of the spectral profile was found to vary as the input pump power was varied. Again, this was most likely due to the poor quality of the pump pulses produced by this laser.

7.5 Characterisation of the Group Velocity Dispersion

As shown in Section 7.4.2, the manufactured birefringent PCF generated signal and idler peaks with significantly reduced bandwidth compared to co-polarised FWM at the same wavelengths using a similar PCF structure. However, it could not be determined from these spectral measurements whether the phase-matching conditions for the PCF structure were close to those required to generate naturally narrow bandwidth idler photons from a time-bandwidth limited 1064 nm pump source. One potential way to investigate this would be to pump the fibre using a tuneable laser, so that the bandwidth of the idler photons could be measured as the pump wavelength was varied, in order to determine the optimal wavelength where the generated photon bandwidth was minimised. An alternative approach, which was adopted here, is to identify the point at which the slope of the phase-matching curve for the idler becomes zero. This can be found by a dispersion measurement of the PCF, as the required phase-matching position is known to coincide with the group velocity of the pump on the *f*-axis of the fibre being matched to the group velocity of the signal wavelength on the

s-axis (see Section 3.5.5). Measurements of the group delay for both PCFs were performed using a Mach-Zehnder interferometer arrangement as shown in Fig. 7.20.

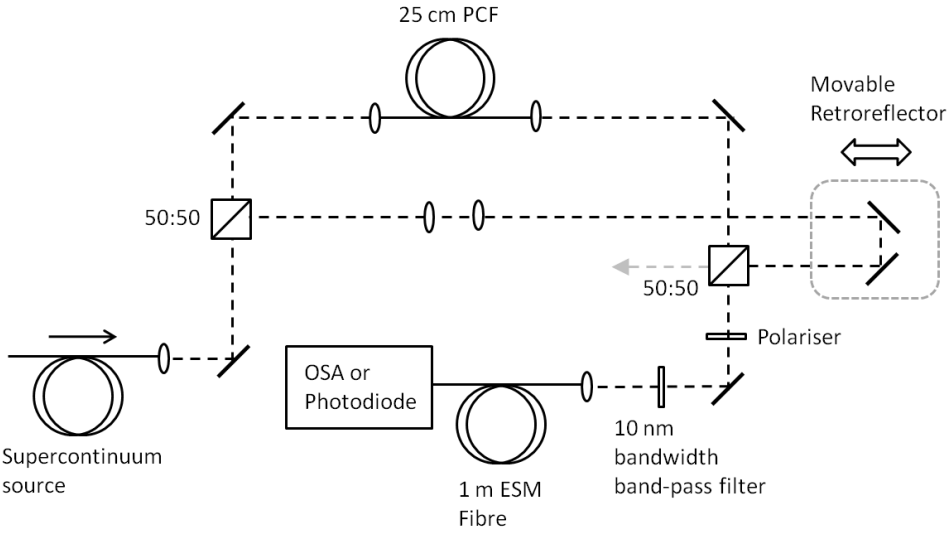

Figure 7.20: Experimental setup for the PCF dispersion measurement.

The input light source used for this experiment was a collimated, pulsed supercontinuum. Light from the source was split at a 50:50 beam-splitter into the two arms of the interferometer. One arm was free-space, while the other included a 25 cm section of the PCF under investigation. The effect of the dispersion of the lenses used to couple light into and out of the PCF was removed by including two similar lenses in the free-space arm. The length of the free-space arm could be scanned over a range of 5 cm using a retroreflector mounted onto a stepper-motor controlled translation stage. After the propagation of light through each arm the beams were recombined at a second 50:50 beam-splitter. The spatial overlap of the beams was ensured by subsequently coupling them both into a section of ESM fibre (see Section 2.1.3). A classical interference pattern was observed at the output of this ESM fibre by a photodiode as the retroreflector was moved. The relative group delay caused by the PCF could be then inferred from the retroreflector position required to balance the interferometer.

The group delay data was obtained using two different methods. The first technique was the 'stage scanning' method. In this case the interference pattern was measured for a single narrow wavelength range (selected using a 10 nm wide band-pass filter at the desired central wavelength) by measuring the output power from the ESM fibre on the photodiode as the position of the retroreflector was scanned. A polariser in a rotatable mount was also included

at the output of the interferometer in order to allow the group velocity for light on each axis of the PCF to be measured independently by rotating it to the required position. A typical example of the measured interference pattern at a single wavelength for a single polarisation component is shown in Fig. 7.21.

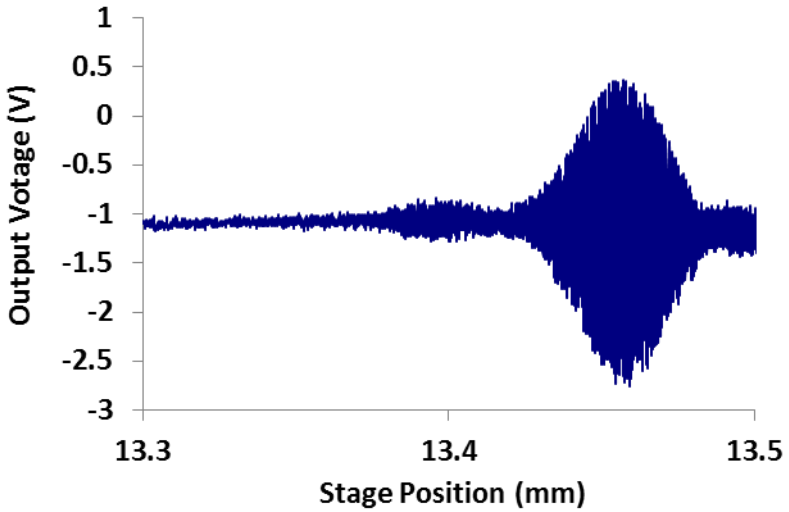

Figure 7.21: Example of the interference fringe pattern observed using the stage scanning method of dispersion measurement.

A series of closely spaced interference fringes contained within a slowly varying envelope function can be seen. The point at which the visibility of the interference fringes is maximised, in this case at 13.46 mm, corresponds to the stage position at which the group delay in the PCF, at the wavelength selected by the band-pass filtering, is balanced by the additional length of the free-space arm. By repeating this measurement with a variety of different spectral filters, the PCF group delay as a function of wavelength could be obtained.

The second method by which the group delay data was measured was using a 'wavelength scanning' technique [176]. In this case the retroreflector position was fixed and no spectral filtering (band-pass filter) was included. The output polariser was again used to select only light propagating on a single axis of the PCF. The spectrum of the output light from the interferometer coupled into the ESM fibre was measured using an OSA. A typical spectrum for a single polarisation is shown in Fig. 7.22.

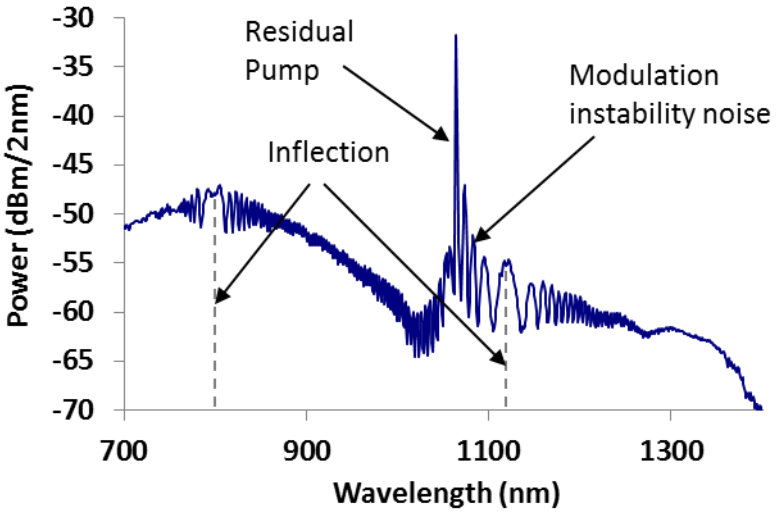

Figure 7.22: Example of the measured spectrum observed when using the wavelength scanning method of dispersion measurement.

Interference fringes can be seen in the data, centred on the wavelengths at which the interferometer is balanced for the given stage position. The interference fringes become more widely spaced close to these wavelengths, with a point of inflection occurring at the balanced point. Due to the shape of the group index curve for PCFs, there will be two such balanced wavelengths at each stage position, one on either side of the ZDW. The group delay profile for PCF can then be found by repeating this measurement with the retroreflector set at different positions. The main advantage of this method is that due to the short time required to take a spectral measurement with an OSA, and the fact that two data points are acquired from each measured spectrum, data points can be acquired more rapidly. The drawback is that this technique cannot be used for wavelengths separated from the pump by < 50 nm. This is because the significant spectral features seen in this region due to the residual pump light and associated noise such as peaks from modulation instability make it difficult to determine where the point of inflection is located. As the group delay at the pump wavelength was one of the points of interest, the stage scanning method was used to collect data points near the pump wavelength, while the wavelength scanning method was used to rapidly acquire the data for the rest of the spectrum. The group delay curves for both the *s*-axis and *f*-axis of PCF-C and PCF-D are shown in Fig. 7.23.

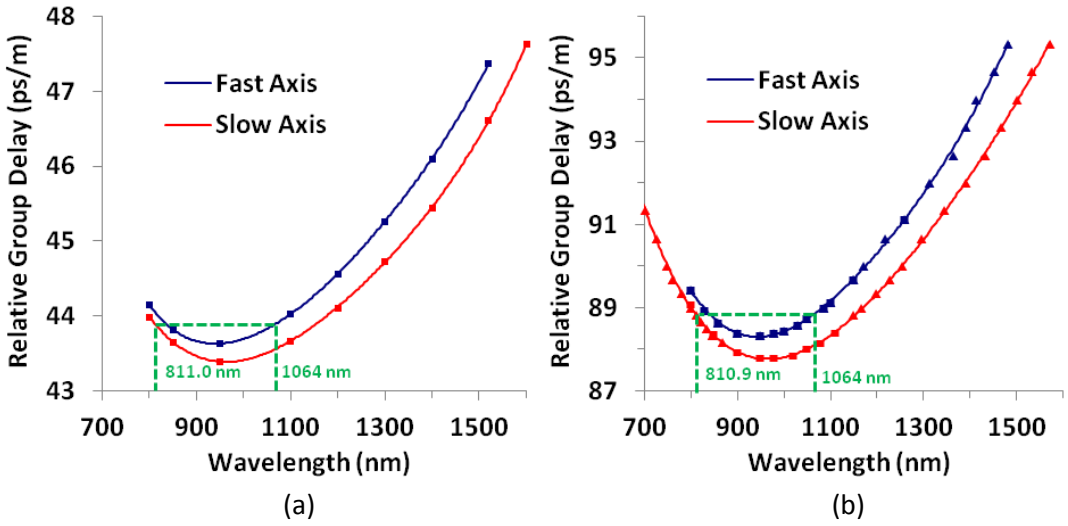

Figure 7.23: Measured group delay for the *f* and *s*-axes of (a) PCF-C; and (b) PCF-D. The square data points were obtained using the stage scanning technique and the triangular data points were obtained via the wavelength scanning method. A polynomial fit to these data points is also shown. The dashed lines illustrate the matching of the pump and signal group velocities.

Using a polynomial fit to the measured data, the wavelength of the signal photons on the *s*-axis of the PCF that was matched in group velocity to a wavelength of 1064 nm on the *f*-axis of the fibre, was determined. This group velocity matching was found to occur for a signal wavelength of 811.0 nm for PCF-C and 810.9 nm for PCF-D. The result for PCF-C was therefore closely matched to the measured peak signal wavelength of 810 nm generated by this fibre (found in Section 7.4.2). This demonstrates that this fibre should be well suited to the generation of narrowband idler photons at the desired wavelength.

As the cladding structures were the same for both of these PCFs, the wavelengths at which the signal and pump group velocities were matched were similar for both, as anticipated by the theoretical modelling of the structure (see Section 7.2). While this meant that the group velocity of the measured signal and pump wavelengths for PCF-D were not so closely matched (for this pump source), the previously measured narrow signal and idler bandwidths demonstrated that this PCF could still be useful as part of a spectrally filtered single photon source, such as that described in Chapter 5. The measured dispersion profiles for both fibres indicate that with an appropriate tuneable laser source it should be possible to realise high visibility quantum interference between idler photons produced by either of these PCF structures, even in the absence of spectral filtering.

7.6 Conclusion

This chapter describes the development of birefringent PCF suitable for the generation of narrowband idler photons at telecoms wavelengths by XFWM. Numerical modelling was used to determine required parameters for the PCF structure that would generate idler photons at 1550 nm from a 1064 nm pump source, whilst simultaneously matching the group velocity of the pump wavelength on the *f*-axis of the fibre to that of the signal wavelength on the *s*-axis. The required PCF structure was determined to have a pitch of 2.64 μm, d/Λ of 0.455 and D/d of 1.9.

A series of PCFs were manufactured in order to produce a structure close to the modelled parameters. Two promising fibres, PCF-C and PCF-D, were identified and found to output spectral peaks at 1550 nm and 1580 nm respectively with a high pump power laser. As the signal peaks could not be observed by this measurement, due to the presence of generated supercontinuum light, they were measured by use of single photon detector using a lower pump power. The observed signal peaks were found to be narrower than in the previously measured case of co-polarised FWM, although the measurement was limited by the filtering resolution of 2 nm. The idler bandwidth could not be measured in the low power regime due to the signal-to-noise ratio of the available detector, however, the idler bandwidth for XFWM did show a factor of 5 reduction compared to that of co-polarised FWM with a higher power, non-bandwidth limited pump pulse. The suitability of the PCFs for generating narrowband photons was also determined indirectly through a measurement of the relative group delay of the fibres. This showed that the group velocity of the pump wavelength was closely matched to that of the measured signal wavelength for both fibres, as required to generate signal and idler photons free from spectral correlation.

The manufactured PCF will be useful for incorporation into the all-fibre single photon source described in Chapter 5. The narrowband nature of the XFWM peaks will mean that fewer of the generated photon pairs will need to discarded by spectral filtering, reducing the pump power requirements of the system. Use of a birefringent PCF for the pair generation could improve upon the previously demonstrated polarisation purity of the single photon source described in Section 6.4.4. These fibres may also be suitable for the generation of factorable two photon states, allowing pure single photon states to be heralded without the need for

spectral filtering. Future work will be required to confirm this by looking for HOM interference between the idler photons output from two separate sections of this fibre.

Chapter 8

Conclusions and Future Work

This chapter concludes this thesis, with a summary of some of the main experimental results obtained in Section 8.1, and possible future improvements to the manufactured source and potential applications discussed in Section 8.2.

8.1 Summary

This thesis has described the development of an all-fibre high brightness source of pure heralded single photons, with a wavelength near 1550 nm, for use in QI applications. An initial demonstration of the generation of correlated pairs of photons through FWM in a PCF was presented in Chapter 4. The source showed promise, with a high output rate of photon pairs. The measured coincident detection rate of signal and idler photons was 10.1 kC/s for an average pump power of 19.2 mW and a detector efficiency of 10% at the idler wavelength. The CAR at this pump power level was 10.4, close to the optimum value. While the output of the photons in fibre guaranteed they would be in a single spatial mode, at this stage the broad bandwidth of the free-space spectral filtering that was used meant that a high purity heralded single photon state could not be realised from this output.

The preliminary work of Chapter 4 was later extended in Chapter 5, with the narrowband filtering required for spectral purity implemented using tuneable FBGs. Additionally, the section of PCF used for the generation of correlated pairs was also reduced below the walk-off length of the fibre in order to ensure that the heralded single photons output from the source

were in a single temporal mode. The polarisation extinction ratio of the heralded single photons was measured to be 27. Initial loss measurements demonstrated that a transmission of 68% could be achieved for the idler photons from the point of generation to detection giving a measured heralding fidelity of 52%. Due to the decrease in the PCF length and the introduction of narrowband filtering, the maximum pump power available from the laser described in Chapter 5 became the limiting factor of the output heralded photon rate. This was measured to be 2.3 kC/s with an idler arm detection efficiency of 10% at the maximum available pump power of 70 mW.

Later work, described in Chapter 6, using a higher power laser as a pump for the photon source enabled the optimal CAR level of 10 to be reached. With an average pump power of 145 mW, pure state, heralded photons were output from the source at a detected rate of 16.1 kC/s (with a detector efficiency of 25% in this case). The purity of the generated heralded photon state was verified by observing a non-classical HOM dip (with 70% net visibility and 55% raw visibility) between the output of this source and that of a source based on PPLN. As HOM interference had not previously been observed between sources of these types, this experiment also demonstrated the potential for integration of different varieties of single photon sources in future QI applications.

Finally, in Chapter 7 a birefringent PCF structure was modelled in order to determine the design parameters required to realise phase-matching for a XFWM process, generating narrow bandwidth idler photons at 1550 nm using a 1064 nm pump laser. Based on the results of this modelling, a series birefringent PCFs were fabricated, and observed to generate idler photons at the required wavelength. Due to detector limitations, the bandwidth of the idler photons could not be measured directly when pumping with the same low power, bandwidth-limited laser that was used previously for the photon source (described in Chapter 5). However, the bandwidth was shown to be reduced by a factor of 5, compared to co-polarised FWM in a similar PCF structure when using a higher power pump laser. Dispersion measurements of the manufactured fibres demonstrated that the group velocity for the pump wavelength was closely matched to that of the measured signal wavelength, indicating that the required pump wavelength for generating naturally pure state idler photons occurred near the desired value of 1064 nm.

8.2 Future Work

While the all-fibre photon source, outlined in Chapter 5, was already a useful source for QI experiments in its current form, as demonstrated by the results of Chapter 6, there are several improvements that could be implemented in the near future to enhance the source performance. As described in Section 5.4, while the heralding fidelity of the source was initially measured to be 52%, this declined upon cut-back of the PCF to the walk-off length. This was attributed to noise photons generated by the pump laser, as this variation in the heralding fidelity with fibre length was not observed after increasing the distance between the PCF and pump filtering prism. However, this high heralding fidelity was not observed with the required shorter length of PCF, due to an increase in the measured passive loss in later versions of the source. Although the origin of loss was not identified due to time constraints, the components in the idler arm of the source could be separated and spliced back together in sequence whilst monitoring the increase in loss due to the addition of each component, as described in Section 5.1. Reproducing the low loss reported for the original source would not only lead to an improvement in the heralding fidelity but also in the source brightness.

A further possibility for future work is to incorporate the fabricated birefringent PCF with the photon source, in place of the non-birefringent PCF used currently. While the strength of the nonlinear interaction is inherently lower for the XFWM process, this should be compensated by enabling a longer length of fibre to be used, due to group velocity matching. Furthermore, even if the idler photons are not generated in an absolutely pure spectral state, the reduction in their bandwidth will mean fewer of the generated pairs need be discarded by spectral filtering, reducing the pump power requirements. Low loss splices are more difficult to perform between birefringent PCF and conventional SMF due to the poor overlap between the mode fields of the fibres. However, they can be realised by making use of a selective collapse of the larger air holes to form an adiabatic transition to a symmetric structure. Techniques for achieving this type of transition with low loss have been previously demonstrated by our group and others [177,178].

In addition to improving the performance of the single photon source, splicing the birefringent PCF to the input of this device would allow the bandwidths of the generated signal and idler for this fibre to be measured directly by adjustment of the narrowband tuneable spectral filtering provided by the FBGs. The measurement of this bandwidth would allow the spectral

purity of the generated idler photons to be estimated, enabling the fabrication of further birefringent PCF with a dispersion profile more closely tailored to the desired pump source wavelength.

As described in Section 2.2.6, the XFWM process will only be phase-matched for the generation of signal and idler photons on a single axis of the birefringent PCF. Because of this, the incorporation of this fibre with the photon source may also benefit the measurement of the HOM interference visibility, discussed in Chapter 6, by improving the polarisation extinction of the generated photons, meaning that an additional polariser is no longer required. The brightness increase and improvement in heralding fidelity resulting from the removal of this component, as well as the other potential improvements to the source described in this chapter, should improve the measured rate of four-fold coincidences for the HOM experiment giving a higher number of total coincidences measured for a given experiment run time. This should improve the observed visibility, both by reducing the inherent statistical uncertainty in the measured number of photons, and by allowing operation at a lower pump power, reducing the influence of any noise photons from the pump contributing to the four-fold coincidences measured at the dip minima.

The stability of the source demonstrated in Chapter 6, along with the alignment-free nature of an all-fibre optical setup means that, in the future, the source described in Chapter 5 could also be spliced directly to the output of a fibre laser and packaged as a single compact unit. The operating wavelength near 1550 nm, combined with the fact that the photons are generated in fibre mean that this source is well-suited to the low loss transmission of the generated photons and integration with existing telecoms networks. Such a maintenance free, turn-key source of heralded single photons, output into single mode fibre, would be of considerable interest as a light source for future research and commercial applications in the field of quantum communications.

Appendix A

List of Fibres

Fibre name in thesis	Stock name	Λ (µm)	d/Λ	D/d
PCF-A	181006A	2.91	0.35	N/A
PCF-B	310703E	2.92	0.34	N/A
PCF-C	180809C	2.94	0.442	2.03
PCF-D	180809D	2.98	0.436	2.16

References

[1] R. A. Millikan, “A Direct Photoelectric Determination of Planck's “*h*”,” *Phys. Rev.* **7,** 355 (1916).

[2] M. Planck, “On the Law of Distribution of Energy in the Normal Spectrum,” *Annalen der Physik* **4,** 553 (1901).

[3] T. H. Maiman, “Stimulated Optical Radiation in Ruby,” *Nature* **187,** 493 (1960).

[4] P. A. Franken, A. E. Hill, C. W. Peters and G. Weinreich, “Generation of Optical Harmonics,” *Phys. Rev. Lett.* **7,** 118 (1961).

[5] A. C. S. van Heel, “A New Method of transporting Optical Images without Aberrations,” *Nature* **173,** 39 (1954).

[6] R. H. Stolen, J. E. Bjorkholm and A. Ashkin, “Phase-matched three-wave mixing in silica fiber optical waveguides,” *Appl. Phys. Lett.* **24,** 308 (1974).

[7] J. C. Knight, T. A. Birks, P. St. J. Russell and D. M. Atkin, “All-silica single-mode optical fiber with photonic crystal cladding,” *Opt. Lett.* **21,** 1547 (1996).

[8] C. H. Bennett and G. Brassard, “Quantum Cryptography: Public key Distribution and Coin Tossing,” *International Conference on Computers, Systems and Signal Processing* (Bangalore, India - 1984).

[9] V. Giovannetti, “Quantum-Enhanced Measurements: Beating the Standard Quantum Limit,” *Science* **306,** 1330 (2004).

[10] J. L. O’Brien, “Optical Quantum Computing,” *Science* **318,** 1567 (2007).

[11] J. Hecht, *City of Light: The Story of Fiber Optics* (Oxford University Press, 1999).

[12] G. P Agrawal, *Nonlinear Fiber Optics*, 4th Ed. (Academic Press, 2007).

[13] A. W. Snyder and J. D. Love, *Optical Waveguide Theory* (Chapman and Hall, 1983).

[14] J. Buck, *Fundamentals of Optical Fibers* (John Wiley & Sons, 1995).

[15] D. Gloge, "Weakly Guiding Fibers," *Appl. Opt.* **10,** 2252 (1971).

[16] Encyclopedia of laser physics and technology: http://www.rp-photonics.com/modes.html

[17] B. J. Ainslie and C. R. Day, "A Review of Single-Mode Fibers with Modified Dispersion Characteristics," *IEEE J. Lightwave Technol.* **4,** 967 (1986).

[18] D. Marcuse, *Theory of Dielectric Optical Waveguides*, 2nd Ed. (Academic Press, 1991).

[19] T.A. Birks, P.J. Roberts, P.St.J. Russell, D.M. Atkin and T.J. Shepherd, "Full 2-D photonic bandgaps in silica/air structures," *Electron. Lett.* **31,** 1941 (1995).

[20] F. Luan, A. K. George, T. D. Hedley, G. J. Pearce, D. M. Bird, J. C. Knight and P. St. J. Russell, "All-solid photonic bandgap fiber," *Opt. Lett.* **29,** 2369 (2004).

[21] R. F. Cregan, B. J. Mangan, J. C. Knight, T. A. Birks, P. St. J. Russell, P. J. Roberts and D. C. Allan, "Single-mode photonic band gap guidance of light in air," *Science* **285,** 1537 (1999).

[22] T. A. Birks, J. C. Knight and P. St. J. Russell, "Endlessly single-mode photonic crystal fiber," *Opt. Lett.* **22,** 961 (1997).

[23] N. A. Mortensen, "Effective area of photonic crystal fibers," *Opt. Express* **10,** 341 (2002).

[24] T. A. Birks, D. Mogilevtsev, J. C. Knight, P. St. J. Russell, J. Broeng, P. J. Roberts, J. A. West, D. C. Allen, J. C. Fajardo, "The analogy between photonic crystal fibres and step index fibres," *Proceedings of the Optical Fiber Communication Conference* (OFC, California), FG4 (1999).

[25] M. Delgado-Pinar, A. Díez, S. Torres-Peiró, M. V. Andrés, T. Pinheiro-Ortega and E. Silvestre, "Waveguiding properties of a photonic crystal fiber with a solid core surrounded by four large air holes," *Opt. Express* **17,** 6931 (2009).

[26] R. Ulrich, S. C. Rashleigh and W. Eickhoff, “Bending-induced birefringence in single-mode fibers,” *Opt. Lett.* **5,** 273 (1980).

[27] R. B. Dyott, *Elliptical Fiber Waveguides* (Artec House, 1995).

[28] J. Noda, K. Okamoto and Y. Sasaki, “Polarization-maintaining fibers and their applications,” *J. Lightwave Technol.* **4,** 1071 (1986).

[29] C. Xiong and W. J. Wadsworth, “Polarized supercontinuum in birefringent photonic crystal fibre pumped at 1064 nm and application to tuneable visible/UV generation,” *Opt. Express* **16,** 2438 (2008).

[30] G. A. Thomas, B. L. Shraiman, P. F. Glodis and M. J. Stephan, “Towards the clarity limit in optical fibre," *Nature* **404,** 262 (2000).

[31] P. J. Roberts, F. Couny, H. Sabert, B. J. Mangan, T. A. Birks, J. C. Knight and P. St. J. Russell, “Loss in solid-core photonic crystal fibers due to interface roughness scattering,” *Opt. Express* **13,** 7779 (2005).

[32] L. Faustini and G. Martini, “Bend loss in single-mode fibers”, *J. Lightwave Technol.* **15,** 671 (1997).

[33] K. G. Hougaard, A. Bjarklev, E. Knudsen, S. B. Libori, J. Riishede, P. M. W. Skovgaard and J. Broeng, “Coupllng to Photonlc Crystal Fibers,” *Proceedings of the Optical Fiber Communication Conference* (OFC, California) 627 (2002).

[34] D. C. Hutchings, M. Sheik-Bahae, D. J. Hagan and E. W. Van Stryland, “Kramers-Kronig Relations in Nonlinear Optics,” *Opt. Quantum Electron*. **24,** 1 (1992).

[35] D. Marcuse, *Light Transmission Optics*, 2nd Ed. (Van Nostrand Reinhold, 1982).

[36] L. G. Cohen, “Comparison of Single-Mode Fiber Dispersion Measurement Techniques,” *J. Lightwave Technol.* **3,** 958 (1985).

[37] D. Davidson, *Optical-Fiber Transmission* (Howard W. Sams & Co, 1987).

[38] R. Lundin, “Dispersion flattening in a W fiber,” *Appl. Opt.* **33,** 1011 (1994).

[39] J. M. Dudley and J. R. Taylor, *Supercontinuum Generation in Optical Fibers* (Cambridge University Press, 2010).

[40] K. Saitoh and M. Koshiba, “Empirical relations for simple design of photonic crystal fibers,” *Opt. Express* **13,** 267 (2004).

[41] G. J. Pearce, T. D. Hedley and D. M. Bird, “Adaptive curvilinear coordinates in a plane-wave solution of maxwell's equations in photonic crystals,” *Phys. Rev. B.* **71,** 195108 (2005).

[42] F. A. Fernández and Y. Lu, *Microwave and optical waveguide analysis by the finite element method* (Research Studies Press, 1996).

[43] J. C. Knight, J. Arriaga, T. A. Birks, A. Ortigosa-Blanch, W. J. Wadsworth and P. St. J. Russell, “Anomalous Dispersion in Photonic Crystal Fiber,” *IEEE Photonic. Tech. L.* **12,** 807 (2000).

[44] R. W. Boyd, *Nonlinear Optics*, 2nd Ed. (Academic Press, 2003).

[45] R. H. Stolen and C. Lin, “Self-phase modulation in silica optical fibers,” *Phys. Rev. A* **17,** 1448 (1978).

[46] R. H. Stolen, E. P. Ippen and A. R. Tynes, “Raman Oscillation in Glass Optical Waveguide,” *Appl. Phys. Lett.* **20,** 62 (1972).

[47] X. Li, P. L. Voss, J. Chen, K. F. Lee and P. Kumar, “Measurement of co- and cross-polarized Raman spectra in silica fiber for small detunings,” *Opt. Express* **13,** 2236 (2005).

[48] J. D. Harvey, R. Leonhardt, S. Coen, G. K. L. Wong, J. C. Knight, W. J. Wadsworth and P. St. J. Russell, “Scalar modulation instability in the normal dispersion regime by use of a photonic crystal fiber,” *Opt. Lett.* **28,** 2225 (2003).

[49] W. J. Wadsworth, N. Joly, J. C. Knight, T. A. Birks, F. Biancalana and P. St. J. Russell, “Supercontinuum and four-wave mixing with Q-switched pulses in endlessly single-mode photonic crystal fibres," *Opt. Express* **12,** 299 (2004).

[50] K. Garay-Palmett, H. J. McGuinness, Offir Cohen, J. S. Lundeen, R. Rangel-Rojo, A. B. U’Ren, M. G. Raymer, C. J. McKinstrie, S. Radic and I. A. Walmsley, “Photon pair-state preparation with tailored spectral properties by spontaneous four-wave mixing in photonic-crystal fiber,” *Opt. Express* **15,** 14870 (2007).

[51] L. J. Wang, C. K. Hong and S. R. Friberg, “Generation of correlated photons via four-wave mixing in optical fibres,” *J. Opt. B: Quantum Semiclass. Opt.* **3,** 346 (2001).

[52] R. H. Stolen and J. E. Bjorkholm, “Parametric Amplification and Frequency Conversion in Optical Fibers,” *IEEE J. Quantum Elect.* **18,** 1062 (1982).

[53] J. Y. Y. Leong, P. Petropoulos, J. H. V. Price, H. Ebendorff-Heidepriem, S. Asimakis, R. C. Moore, K. E. Frampton, V. Finazzi, X. Feng, T. M. Monro and D. J. Richardson, “High-Nonlinearity Dispersion-Shifted Lead-Silicate Holey Fibers for Efficient 1-µm Pumped Supercontinuum Generation,” *J. Lightwave Technol.* **24,** 183 (2006).

[54] R. G. Smith, “Optical Power Handling Capacity of Low Loss Optical Fibers as Determined by Stimulated Raman and Brillouin Scattering,” *Appl. Opt.* **11,** 2489 (1972).

[55] M. Halder, J. Fulconis, B. Cemlyn, A. Clark, C. Xiong, W. J. Wadsworth and J. G. Rarity, “Nonclassical 2-photon interference with separate intrinsically narrowband fibre sources,” *Opt. Express* **17,** 4670 (2009).

[56] P. N. Morgan and J. M. Liu, “Parametric Four-Photon Mixing Followed by Stimulated Raman Scattering with Optical Pulses in Birefringent Optical Fibers,” *IEEE J. Quantum Elect.* **21,** 1011 (1991).

[57] J. M. Stone and J. C. Knight, “Visibly ‘white’ light generation in uniform photonic crystal fiber using a microchip laser,” *Opt. Express* **16,** 2670 (2008).

[58] J. Herrmann,U. Griebner, N. Zhavoronkov, A. Husakou, D. Nickel, J. C. Knight, W. J. Wadsworth, P. St. J. Russell, and G. Korn, “Experimental Evidence for Supercontinuum Generation by Fission of Higher-Order Solitons in Photonic Fibers,” *Phys. Rev. Lett.* **88,** 173901 (2002).

[59] I. Cristiani, R. Tediosi, L. Tartara and V. Degiorgio, “Dispersive wave generation by solitons in microstructured optical fibers," *Opt. Express* **12,** 124 (2004).

[60] T. Li, Ed., *Optical Fiber Communications: Fiber Fabrication, Vol. 1* (Academic Press, 1985).

[61] K. M. Kiang, K. Frampton, T. M. Monro, R. Moore, J. Tucknott, D. W. Hewak, D. J. Richardson and H. N. Rutt, "Extruded singlemode non-silica glass holey optical fibres," *Electron. Lett.* **38,** 546 (2002).

[62] W. H. Reeves, *Photonic crystal Fibre: the ultra-flattened dispersion regime,* Ph.D. thesis (University of Bath, 2003).

[63] C. Xiong, *Nonlinearity in Photonic Crystal Fibres,* Ph.D. thesis (University of Bath, 2008).

[64] L. Xiao and W. Jin, "Fusion Splicing Photonic Crystal Fibers and Conventional Single-Mode Fibers: Microhole Collapse Effect," *J. Lightwave Technol.* **25,** 3563 (2007).

[65] J. Lægsgaard and A Bjarklev, "Reduction of coupling loss to photonic crystal fibers by controlled hole collapse: a numerical study," *Opt. Commun.* **237,** 431 (2004).

[66] L. Xiao, W. Jin and M. S. Demokan, "Fusion splicing small-core photonic crystal fibers and single-mode fibers by repeated arc discharges," *Opt. Lett.* **32,** 115 (2007).

[67] M. Fox, *Quantum Optics: An Introduction* (Oxford University Press, 2006).

[68] D. P. DiVincenzo, "The Physical Implementation of Quantum Computation," *arXiv:quant-ph/0002077v3* (2000).

[69] J. I. Cirac and P. Zoller, "Quantum Computations with Cold Trapped Ions," *Phys. Rev. Lett.* **74,** 4091 (1995).

[70] L. M. K. Vandersypen, M. Steffan, G. Breyta, C. S. Yannoni, M. H. Sherwood and I. L. Chuang, "Experimental realization of Shor's quantum factoring algorithm using nuclear magnetic resonance," *Nature* **414,** 883 (2001).

[71] L. B. Ioffe, V. B. Geshkenbein, M. V. Feigel'man, A. L. Fauchère, and G. Blatter, "Environmentally decoupled *sds* -wave Josephson junctions for quantum computing," *Nature* **398,** 679 (1999).

[72] E. Knill, R. Laflamme and G. J. Milburn, "A scheme for efficient quantum computation with linear optics," *Nature* **409,** 46 (2001).

[73] R. Loudon, *The Quantum Theory of Light*, 3rd Ed. (Oxford University Press, 2000).

[74] L. Mandel and E. Wolf, *Optical Coherence and Quantum Optics* (Cambridge University Press, 1995).

[75] P. Rohde, W. Mauerer and C. Silberhorn, "Spectral structure and decompositions of optical states, and their applications," *New J. Phys.* **9,** 91 (2007).

[76] C. K. Hong, Z. Y. Ou and L. Mandel, "Measurement of Subpicosecond Time Intervals between Two Photons by Interference," *Phys. Rev. Lett.* **59,** 2044 (1987).

[77] H. Fearn and R. Loudon, "Quantum Theory of the Lossless Beam Splitter," *Opt. Commun.* **64,** 485 (1987).

[78] Z. Y. Ou, *Multi-Photon Quantum Interference* (Springer, 2007).

[79] J. G. Rarity and P. R. Tapster, "Fourth-order interference in parametric downconversion," *J. Opt. Soc. Am. B* **6,** 1221 (1989).

[80] L. Mandel, "Quantum effects in one-photon and two-photon interference," *Rev. Mod. Phys.* **71,** S274 (1999).

[81] T. B. Pittman, D. V. Strekalov, A. Migdall, M. H. Rubin, A. V. Sergienko and Y. H. Shih, "Can Two Photon Interference be Considered the Interference of Two Photons?" *Phys. Rev. Lett.* **77,** 1917 (1996).

[82] G. M. Hockney, P. Kok and J. P. Dowling, "Suitability versus fidelity for rating single-photon guns," *Phys. Rev. A* **67,** 032306 (2003).

[83] B. Lounis and M. Orrit, "Single-photon sources," *Rep. Prog. Phys.* **68,** 1129 (2005).

[84] H. J. Kimble, M. Dagenais and L. Mandel, "Photon Antibunching in Resonance Fluorescence," *Phys. Rev. Lett.* **39,** 691 (1977).

[85] P. Maunz, D. L. Moehring, S. Olmschenk, K. C. Younge, D. N. Matsukevich and C. Monroe, "Quantum interference of photon pairs from two remote trapped atomic ions," *Nature Phys.* **3,** 538 (2007).

[86] T. Basché, W. E. Moerner, M. Orrit and H. Talon, "Photon antibunching in the fluorescence of a single dye molecule trapped in a solid," *Phys. Rev. Lett.* **69,** 1516 (1992).

[87] A. Kiraz, M. Atatüre and A. Imamoğlu, “Quantum-dot single-photon sources: Prospects for applications in linear optics quantum-information processing,” *Phys. Rev. A* **69,** 032305 (2004).

[88] A. Gruber, A. Dräbenstedt, C. Tietz, L. Fleury, J. Wrachtrup and C. von Borczyskowski, “Scanning Confocal Optical Microscopy and Magnetic Resonance on Single Defect Centers,” *Science* **276,** 2012 (1997).

[89] E. Moreau, I. Robert, J. M. Gérard, I. Abram, L. Manin and V. Thierry-Mieg, “Single-mode solid-state single photon source based on isolated quantum dots in pillar microcavities,” *Appl. Phys. Lett.* **79,** 2865 (2001).

[90] D. C. Burnham and D. L. Weinberg, “Observation of simultaneity in parametric production of optical photon pairs,” *Phys. Rev. Lett.* **25,** 84 (1970).

[91] S. Friberg, C. K. Hong and L. Mandel, “Measurement of Time Delays in the Parametric Production of Photon Pairs,” *Phys. Rev. Lett.* **54,** 2011 (1985).

[92] C. K. Hong and L. Mandel, “Experimental realization of a localized one-photon state,” *Phys. Rev. Lett.* **56,** 58 (1986).

[93] P. G. Kwiat, K. Mattle, H. Weinfurter, A. Zeilinger, A. V. Sergienko and Y. Shih, “New High-Intensity Source of Polarization-Entangled Photon Pairs,” *Phys. Rev. Lett.* **75,** 4337 (1995).

[94] A. Dragan, “Efficient fiber coupling of down-conversion photon pairs,” *arXiv:quant-ph/0407113v1* (2004).

[95] C. Kurtsiefer, M. Oberparleiter and H. Weinfurter, “High-efficiency entangled photon pair collection in type-II parametric fluorescence,” *Phys. Rev. A* **64,** 023802 (2001).

[96] T. B. Pittman, B. C. Jacobs and J. D. Franson, “Heralding single photons from pulsed parametric down conversion,” *Opt. Commun.* **246,** 545 (2005).

[97] S. Fasel, O. Alibart, S. Tanzilli, P. Baldi, A. Beveratos, N. Gisin and H. Zbinden, “High-quality asynchronous heralded single-photon source at telecom wavelength,” *New J. Phys.* **6,** 163 (2004).

[98] K. Banaszek, A. B. U'Ren and I. A. Walmsley, "Generation of correlated photons in controlled spatial modes by downconversion in nonlinear waveguides," *Opt. Lett.* **26,** 1367 (2001).

[99] M. Fiorentino, S. M. Spillane, R. G. Beausoleil, T. D. Roberts, P. Battle, and M. W. Munro, "Spontaneous parametric down-conversion in periodically poled KTP waveguides and bulk crystals," *Opt. Express* **15,** 7479 (2007).

[100] A. B. U'Ren, C. Silberhorn, K. Banaszek and I. A.Walmsley, "Efficient Conditional Preparation of High-Fidelity Single Photon States for Fiber-Optic Quantum Networks," *Phys. Rev. Lett.* **93,** 093601 (2004).

[101] X. Li, J. Chen, P. Voss, J. Sharping and P. Kumar, "All-fiber photon-pair source for quantum communications: Improved generation of correlated photons," *Opt. Express* **12,** 3737 (2004).

[102] J. Fan, A. Migdall and L. J. Wang, "Efficient generation of correlated photon pairs in a microstructure fiber," *Opt. Lett.* **30,** 3368 (2005).

[103] J. E. Sharping, J. Chen, X. Li and P. Kumar, "Quantum Correlated twin photons from microstructured fibre," *Opt. Express* **12,** 3086 (2004).

[104] J. G. Rarity, J. Fulconis, J. Duligall, W. J. Wadsworth and P. St. J. Russell, "Photonic crystal fiber source of correlated photon pairs," *Opt. Express* **13,** 534 (2005).

[105] A. Ling, J. Chen, J. Fan and A. Migdall, "Mode expansion and Bragg filtering for a high-fidelity fiber-based photon-pair source," *Opt. Express* **17,** 21302 (2009).

[106] E. A. Goldschmidt, M. D. Eisaman, J. Fan, S. V. Polyakov and A. Migdall, "Spectrally bright and broad fiber-based heralded single-photon source," *Physical Review A* **78,** 013844 (2008).

[107] W. Grice, R. Bennink, P. Evans, T. Humble and J. Schaake, "Bright Photon Pair Source with High Spectral and Spatial Purity," *International Conference on Quantum Information* (OSA, Ottawa) QWD4 (2011).

[108] J. A. Slater, J. S. Corbeil, S. Virally, F. Bussières, A. Kudlinski, G. Bouwmans, S. Lacroix, N. Godbout and W Tittel, "Microstructured fiber source of photon pairs at widely separated wavelengths," *Opt. Lett.* **35,** 499 (2010).

[109] C. Söller, O. Cohen, B. J. Smith, I. A. Walmsley and C. Silberhorn, “High-performance single photon generation with commercial-grade optical fiber,” *Phys. Rev. A* **83,** 031806(R) (2011).

[110] J. Chen, X. Li, and P. Kumar, “Two-photon-state generation via four-wave mixing in optical fibers,” *Phys. Rev. A* **72,** 033801 (2005).

[111] Q. Lin, F. Yaman and G. P. Agrawal, “Photon-pair generation in optical fibers through four-wave mixing: Role of Raman scattering and pump polarization,” *Phys. Rev. A* **75,** 023803 (2007).

[112] O. Alibart, J. Fulconis, G. K. L. Wong, S. G. Murdoch, W. J. Wadsworth and J. G. Rarity, “Photon pair generation using four-wave mixing in a microstructured fibre: theory versus experiment,” *New J. Phys.* **8,** 67 (2006).

[113] P. Meystre and M. Sargent, *Elements of Quantum Optics*, 4th Ed. (Springer, 2007).

[114] D. F. Walls and G. J. Milburn, *Quantum Optics*, 2nd Ed. (Springer, 2008).

[115] P. P. Rohde and T. C. Ralph, “Modelling photo-detectors in quantum optics,” *J. Mod. Optic.* **53,** 1589 (2006).

[116] M. A. Nielsen and I. L. Chuang, *Quantum Computation and Quantum Information* (Cambridge University Press, 2000).

[117] J. G. Rarity, P. R. Tapster and E. Jakeman, “Observation of sub-poissonian light in parametric downconversion,” *Opt. Commun.* **62,** 201 (1987).

[118] P. J. Mosley, J. S. Lundeen, B. J. Smith, P. Wasylczyk, A. B. U'Ren, C. Silberhorn and I. A. Walmsley, “Heralded Generation of Ultrafast Single Photons in Pure Quantum States,” *Phys. Rev. Lett.* **100,** 133601 (2008).

[119] Y. H. Shih and M. H. Rubin, “Four photon interference experiment for the testing of the Greenberger-Horne-Zeilinger Theorem,” *Phys. Lett. A* **182,** 16 (1993).

[120] J. Fulconis, O. Alibart, W. J. Wadsworth and J. G. Rarity, “Quantum interference with photon pairs using two micro-structured fibres,” *New J. Phys.* **9,** 276 (2007).

[121] J. G. Rarity, “Interference of Single Photons for Separate Sources,” *Ann. NY Acad. Sci.* 755, 624 (1995).

[122] H. C. Lim, A. Yoshizawa, H. Tsuchida and K. Kikuchi, “Distribution of polarization-entangled photon-pairs produced via spontaneous parametric down-conversion within a local-area fiber network: Theoretical model and experiment,” *Opt. Express* **16,** 14512 (2008).

[123] R. Hanbury Brown and R. Q. Twiss, “Correlation between Photons in two Coherent Beams of Light,” *Nature* **177,** 27 (1956).

[124] H. Takesue and K. Shimizu, “Effects of multiple pairs on visibility measurements of entangled photons generated by spontaneous parametric processes,” *arXiv:0907.4535v1* (2009).

[125] P. R. Tapster and J. G. Rarity, “Photon Statistics of Pulsed Parametric Light,” *J. Mod. Optic.* **45,** 595 (1998).

[126] H. de Riedmatten, I. Marcikic, W. Tittel, H. Zbinden and N. Gisin, “Quantum interference with photon pairs created in spatially separated sources,” *Phys. Rev. A* **67,** 022301 (2003).

[127] A. L. Migdall, D. Branning and S. Castelletto, “Tailoring single-photon and multiphoton probabilities of a single-photon on-demand source,” *Phys. Rev. A* **66,** 053805 (2002).

[128] X. Ma, S. Zotter, J. Kofler, T. Jennewein and A. Zeilinger, “Experimental generation of single photons via active multiplexing,” *Phys. Rev. A* **83,** 043814 (2011).

[129] R. H. Hadfield “Single-photon detectors for optical quantum information applications,” *Nature Photon.* **3,** 696 (2009).

[130] K. Inoue, “Polarization Effect on Four-Wave Mixing Efficiency in a Single-Mode Fiber,” *IEEE J. Quantum Elect.* **28,** 883 (1992).

[131] D. F. V. James, P. G. Kwiat, W. J. Munro and A. G. White, “Measurement of qubits,” *Phys. Rev. A* **64,** 052312 (2001).

[132] W. P. Grice, A. B. U’Ren and I. A. Walmsley, “Eliminating frequency and space-time correlations in multiphoton states,” *Phys. Rev. A* **64,** 063815 (2001).

[133] P. J. Mosley, *Generation of Heralded Single Photons in Pure Quantum States*, Ph. D. thesis (University of Oxford, 2007).

[134] A. Einstein, B. Podolsky, and N. Rosen, “Can Quantum-Mechanical Description of Physical Reality Be Considered Complete?” *Phys. Rev.* **47,** 777 (1935).

[135] J.S. Bell, “On the Einstein Podolsky Rosen Paradox,” *Physics* **1,** 195 (1964).

[136] A. Aspect, P. Grangier and G. Roger, “Experimental Tests of Realistic Local Theories via Bell's Theorem,” *Phys. Rev. Lett.* **47,** 460 (1981).

[137] W. Tittel, J. Brendel, H. Zbinden and N. Gisin, “Violation of Bell Inequalities by Photons More Than 10 km Apart,” *Phys. Rev. Lett.* **81,** 3563 (1998).

[138] A. N. Boto, P. Kok, D. S. Abrams, S. L. Braunstein, C. P. Williams and J. P. Dowling, “Quantum Interferometric Optical Lithography: Exploiting Entanglement to Beat the Diffraction Limit,” *Phys. Rev. Lett.* **85,** 2733 (2000).

[139] D. R. Hjelm, L. Lydersen and V. Makarov, “Quantum Cryptography,” *arXiv:quant-ph/1108.1718v1* (2011).

[140] N. Gisin, G. Ribordy, W. Tittel and H. Zbinden, “Quantum cryptography,” *Rev. Mod. Phys.* **74,** 145 (2002).

[141] W. K. Wootters and W. H. Zurek, “A single quantum cannot be cloned,” *Nature* **299,** 802 (1982).

[142] G. Brassard, N. Lütkenhaus, T. Mor and B. C. Sanders, “Limitations on Practical Quantum Cryptography,” *Phys. Rev. Lett.* **85,** 1330 (2000).

[143] P. Shor, “Algorithms for quantum computation: Discrete logarithms and factoring,” *Proceedings of the Symposium on the Foundations of Computer Science,* (IEEE Computer Society, Los Alamitos, California) 124 (1994).

[144] L. K. Grover, “Quantum Mechanics Helps in Searching for a Needle in a Haystack,” *Phys. Rev. Lett.* **79,** 325 (1997).

[145] R. P. Feynman, “Simulating physics with computers,” *Int. J. Theoretical Phys.* **21,** 467 (1982).

[146] P. Kok, W.J. Munro, K. Nemoto, T.C. Ralph, J. P. Dowling and G.J. Milburn, “Linear optical quantum computing,” *arXiv:quant-ph/0512071v2* (2006).

[147] J. L. O'Brien, G. J. Pryde, A. G. White, T. C. Ralph and D. Branning, "Demonstration of an all-optical quantum controlled-NOT gate," *Nature* **426,** 264 (2003).

[148] A. S. Clark, J. Fulconis, J. G. Rarity, W. J. Wadsworth and J. L. O'Brien, "All-optical-fiber polarization-based quantum logic gate," *Phys. Rev. A* **79,** 030303(R) (2009).

[149] A. R. McMillan, J. Fulconis, M. Halder, C. Xiong, J. G. Rarity and W. J. Wadsworth, "Narrowband high-fidelity all-fibre source of heralded single photons at 1570 nm," *Opt. Express* **17,** 6156 (2009).

[150] J. Lauzon, S. Thibault, J. Martin and F. Ouellette, "Implementation and characterization of fiber Bragg gratings linearly chirped by a temperature gradient," *Opt. Lett.* **19,** 2027 (1994).

[151] M. L Rocha, F. Borin, H. C. L. Monteiro, M. R. Horiuchi, M. R. X. de Barros, M. A. D. Santos, F. L. Oliveira and F. D. Simões, "Mechanical Tuning of a Fiber Bragg Grating for Optical Networking Applications," *JMOe* **4,** 1 (2005).

[152] M. Halder, A. Beveratos, R. T. Thew, C. Jorel, H. Zbinden and N. Gisin, "High coherence photon pair source for quantum communication," *New J. Phys.* **10,** 023027 (2008).

[153] H. C. Lefevre, "Single-mode fibre fractional wave devices and polarisation controllers," *Electron. Lett.* **16,** 778 (1980).

[154] L. Chanvillard, P. Aschiéri, P. Baldi, D. B. Ostrowsky, M. de Micheli, L. Huang and D. J. Bamford, "Soft proton exchange on periodically poled LiNbO3: A simple waveguide fabrication process for highly efficient nonlinear interactions," *Appl. Phys. Lett.* **76,** 1089 (2000).

[155] O. Alibart, D. B. Ostrowsky, P. Baldi and S. Tanzilli, "High-performance guided-wave asynchronous heralded single-photon source," *Opt. Lett.* **30,** 1539 (2005).

[156] A. Ling, A. Lamas-Linares and C. Kurtsiefer, "Absolute emission rates of spontaneous parametric down-conversion into single transverse Gaussian modes," *Phys. Rev. A* **77,** 043834 (2008).

[157] A. Martin, V. Cristofori, P. Aboussouan, H. Herrmann, W. Sohler, D. B. Ostrowsky, O. Alibart and S. Tanzilli, "Integrated optical source of polarization entangled photons at 1310 nm," *Opt. Express* **17,** 1033 (2009).

[158] M. Yamada, N. Nada, M. Saitoh and K. Watanabe, “First-order quasi-phase matched $LiNbO_3$ waveguide periodically poled by applying an external field for efficient blue second-harmonic generation,” *Appl. Phys. Lett.* **62,** 435 (1993).

[159] J. Webjörn, V. Pruneri, P. St. J. Russel, J. R. M. Barr and D. C. Hanna, “Quasi-phase-matched blue light generation in bulk lithium niobate, electrically poled via periodic liquid electrodes,” *Electron. Lett.* **30,** 894 (1994).

[160] J. A. Armstrong, N. Bloembergen, J. Ducuing and P. S. Pershan, “Interactions between Light Waves in a Nonlinear Dielectric,” *Phys. Rev.* **127,** 1918 (1962).

[161] S. Tanzilli, W. Tittel, H. De Riedmatten, H. Zbinden, P. Baldi, M. De Micheli, D. B. Ostrowsky, and N. Gisin, “PPLN Waveguide for Quantum Communication,” *Eur. Phys. J. D* **18,** 155 (2002).

[162] O. Alibart, D. B. Ostrowsky, P. Baldi, and S. Tanzilli, “High-performance guided-wave asynchronous heralded single-photon source,” *Opt. Lett.* **30,** 1539 (2005).

[163] J. C. F. Matthews, A. Politi, A. Stefanov, and J. L. O’Brien, “Manipulation of multiphoton entanglement in waveguide quantum circuits,” *Nature Photon.* **3,** 346 (2009).

[164] R. Kaltenbaek, B. Blauensteiner, M Żukowski, M. Aspelmeyer and A. Zeilinger, “Experimental interference of independent photons,” *Phys. Rev. Lett.* **96,** 240502 (2006).

[165] P. Aboussouan, O. Alibart, D. B. Ostrowsky, P. Baldi and S. Tanzilli, “High-visibility two-photon interference at a telecom wavelength using picosecond-regime separated sources,” *Phys. Rev. A* **81,** 021801(R) (2010).

[166] S. V. Polyakov, A. Muller, E. B. Flagg, A. Ling, N. Borjemscaia, E. Van Keuren, A. Migdall, and G. S. Solomon, “Coalescence of Single Photons Emitted by Disparate Single-Photon Sources: The Example of InAs Quantum Dots and Parametric Down-Conversion Sources,” *Phys. Rev. Lett.* **107,** 157402 (2011).

[167] S. Tanzilli, H. De Riedmatten, W. Tittel, H. Zbinden, P. Baldi, M. De Micheli, D. B. Ostrowsky and N. Gisin, “Highly efficient photon-pair source using periodically poled lithium niobate waveguide,” *Electron. Lett.* **37,** 26 (2001).

[168] K. van de Velde, H. Thienpont and R. van Geen, “Extending the effective index method for arbitrarily shaped inhomogeneous optical waveguides,” *J. Lightwave Technol.* **6,** 1153 (1988).

[169] J. C. F. Matthews, A. Politi, D. Bonneau, and J. L. O'Brien, “Heralded entanglement for quantum enhanced measurement with photons,” *arXiv:1005.5119v1* (2010).

[170] F. Laurell and G. Arvidsson, “Frequency doubling in Ti:MgO:$LiNbO_3$ channel waveguides,” *J. Opt. Soc. Am. B* **5,** 292 (1988).

[171] J. Rams, A. Alcázar-de-Velasco, M. Carrascosa, J. M. Cabrera and F. Agulló-López, “Optical damage inhibition and thresholding effects in lithium niobate above room temperature,” *Opt. Commun.* **178,** 211 (2000).

[172] B. J. Smith, P. Mahou, O. Cohen, J. S. Lundeen, and I. A. Walmsley, “Photon pair generation in birefringent optical fibers,” *Opt. Express* **17,** 23589 (2009).

[173] A. Clark, B. Bell, J. Fulconis, M. Halder, B. Cemlyn, O. Alibart, C. Xiong, W. J. Wadsworth and J. G. Rarity, “Intrinsically narrowband pair photon generation in microstructured fibres,” *arXiv:1102.4415v1* (2011).

[174] C. Söller, B. Brecht, P. J. Mosley, L. Y. Zang, A. Podlipensky, N. Y. Joly, P. St.J. Russell and C. Silberhorn, “Bridging visible and telecom wavelengths with a single-mode broadband photon pair source,” *arXiv:0908.2932v3* (2010).

[175] O. Cohen, J. S. Lundeen, B. J. Smith, G. Puentes, P. J. Mosley and I. A. Walmsley, “Tailored photon-pair generation in optical fibers,” *Phys. Rev. Lett.* **102,** 123603 (2009).

[176] Q. Ye, C. Xu, X. Liu, W. H. Knox, M. F. Yan, R. S. Windeler and B. Eggleton, “Dispersion measurement of tapered air-silica microstructure fiber by white-light interferometry,” *Appl. Opt.* **41,** 4467 (2002).

[177] J. Ju, H. F. Xuan, W. Jin, S. Liu and H. L. Ho, “Selective opening of airholes in photonic crystal fiber,” *Opt. Lett.* **35,** 3886 (2010).

[178] A. Witkowska, K. Lai, S. G. Leon-Saval, W. J. Wadsworth and T. A. Birks, “All-fiber anamorphic core-shape transitions,” *Opt. Lett.* **31,** 2672 (2006).